

Synthesis, Physical, Structural and Biological Properties of Some Gold(III) Amide Complexes: Towards Novel Metallotherapeutic Drugs

Submitted in fulfilment of the requirements for the degree of

Doctor of Philosophy of Science

By

Colin Rylott Wilson

B.Sc. (Hons) (UKZN)

November 2012

School of Chemical and Physical Sciences

University of KwaZulu-Natal

Pietermaritzburg

COLLEGE OF AGRICULTURE, ENGINEERING AND SCIENCE

DECLARATION - PLAGIARISM

I, Colin R. Wilson, declare that

1. The research reported in this thesis, except where otherwise indicated, is my original research.
2. This thesis has not been submitted for any degree or examination at any other university.
3. This thesis does not contain other persons' data, pictures, graphs or other information, unless specifically acknowledged as being sourced from other persons.
4. This thesis does not contain other persons' writing, unless specifically acknowledged as being sourced from other researchers. Where other written sources have been quoted, then:
 - a. Their words have been re-written but the general information attributed to them has been referenced
 - b. Where their exact words have been used, then their writing has been placed in italics and inside quotation marks, and referenced.
5. This thesis does not contain text, graphics or tables copied and pasted from the Internet, unless specifically acknowledged, and the source being detailed in the thesis and in the References sections.

Signed:

Date:

Colin R. Wilson

I hereby certify that this is correct.

Signed:

Prof. O. Q. Munro

Supervisor

Acknowledgements

First of all I would like to thank my supervisor Professor Munro for all of his encouragement, enthusiasm and detailed insight to all aspects pertaining to my project. Without your advice and guidance this project would have not been possible.

I would like to thank Prof Mark Muller, Alex Fagenson and Wanvipa Ruangpradit from the University of Central Florida for their assistance with the biological aspects of the project.

I am very grateful to Professor Field for imparting his knowledge and expertise in the field of chemistry whenever required.

I would like to thank Mr Craig Grimmer for NMR analysis and allowing me to 'pick' his brain on organic synthetic methodologies almost daily.

I would like to thank the technical staff, Mr Shaun Ball and Fiezal Shiek for always being helpful in assisting with any request in the lab or stores.

I wish to thank the National Research Foundation for their financial support through a DST NRF Innovation doctoral scholarship.

My sincere gratitude goes to my family and friends, especially my grandparents, for their support and understanding.

I dedicate this thesis to my parents.

Research outputs

Publications:

- 1.) Wilson, C. R.; Munro, O. Q., Unconventional hydrogen bonding and pi-stacking in two substituted pyridine carboxamides. *Acta Crystallogr C*, **2010**, *66*, o513-o516.
- 2.) Munro, O. Q.; Wilson, C., Amide hydrogen bonding: control of the molecular and extended structures of two symmetrical pyridine-2-carboxamide derivatives. *Acta Crystallogr C*, **2010**, *66*, o535-o539.

Conferences:

Poster presentation at the 11th European Biological Inorganic Chemistry Conference (EUROBIC 11).

Title: Synthesis, Physical, Computational and Biological Studies of some Amido Gold(III) Chelates.

List of abbreviations

ATP	-	Adenosine Triphosphate
BSA	-	Bovine serum Albumin
CD	-	Circular dichroism
COSY	-	Correlation spectroscopy
C-PCM	-	Conductor-like polarisable continuum model
CSD	-	Cambridge structural database
ctDNA	-	Calf thymus DNA
CTEP	-	Cancer Therapy Evaluation Program
Da	-	Daltons
DCCI	-	Dicyclohexylcarbodiimide
DCM	-	Dichlormethane
DCTDC	-	Division of Cancer Treatment, Diagnosis and Centres
DEPT135	-	Distortionless enhancement by polarization transfer
DFT	-	Density functional theory
DMSO	-	Dimethyl Sulfoxide
DNA	-	Deoxyribonucleic acid
dsDNA	-	Double stranded DNA
DTP	-	Developmental Therapeutics Program
EB	-	Ethidium bromide

ECP	-	Effective core potential
EL	-	Electro-luminescent
EMSA	-	Electrophoretic gel mobility shift assays
ES	-	Electro spray ionization
ESMS	-	Electrospray mass spectroscopy
EtOH	-	Ethanol
GGA	-	Generalised gradient approximation
GSH	-	Glutathione
HF	-	Hartree-Fock
HMBC	-	Heteronuclear multiply bond correlation
HOBt	-	1-hydroxybenzotriazole
HOMO	-	Highest occupied molecular orbital
HSAB	-	Hard soft acid base theory
HSQC	-	Heteronuclear single quantum coherence
IM	-	Intramuscularly
IP	-	Intraperitoneally
IR	-	Infrared
IV	-	Intravenously
kDNA	-	Kinetoplast DNA
LDA	-	Local density approximation

LMCT	-	Ligand-to-metal-charge-transfer
LSDA	-	Local spin density approximation
LUMO	-	Lowest unoccupied molecular orbital
mAMSA	-	4'-(9-acridinylamino)methanesulfon-m-anisidide
MeOH	-	Methanol
MLCT	-	Metal-to-ligand-charge-transfer,
MO	-	Molecular orbitals
MOA	-	Mechanisms of action
MPS	-	Mean plane separation
MS	-	Mass spectrometry
MTD	-	Maximum tolerated dose
MTT	-	3-(4,5-Dimethylthiazol-2-YI)-2,5-Diphenyltetrazolium Bromide
NADPH	-	Nicotinamide adenine dinucleotide phosphate
NCI	-	National cancer institute
NOC-DNA	-	nicked open circular-DNA
NIH	-	American National Institute of Health
NMR	-	Nuclear magnetic resonance
OLEDs	-	Organic light emitting diodes
PBS	-	Phosphate-buffered saline
PO	-	Orally

Ppm	-	Parts per million
RNA	-	Ribonucleic acid
RMSD	-	Root-mean-square deviation
RPMI	-	Roswell Park Memorial Institute Media
SC	-	Subcutaneously
SC-DNA	-	Supercoiled DNA
SDS	-	Sodium dodecyl sulfate
SRB	-	Sulforhodamine B
TBE	-	Tris borate EDTA
TCA	-	Tricarboxylic acid
TD- SCF	-	Time dependent self-consistent field
TD-DFT	-	Time dependent Density functional theory
THF	-	Tetrahydrofuran
TOF	-	Time of flight
TGI	-	Total growth inhibition
TBS	-	Tris buffered saline
UV	-	Ultra violet
VSEPR	-	Valence Shell electron pair repulsion

List of Figures

Figure 1.2.1: Gold nuggets.....	2
Figure 1.2.2: Hybrid orbitals formed from mixing d_{z^2} and an s orbital ψ_1 and ψ_2 and the hybrid orbitals formed from mixing ψ_2 and a p_z orbital.....	5
Figure 1.2.3: VSEPR view of d^8 square planar metal complexes showing the expected low spin configuration.....	6
Figure 1.2.4: Molecular structures of a five co-ordinate gold(III) complex, $[\text{Au}\{\text{N}_2\text{C}_{10}\text{H}_7(\text{CHMePh})\text{-6}\}\text{C}_{13}]$, (A) and a six co-ordinate gold(III) complex, $[\text{Au}(\text{L})\text{Cl}_2]\text{AuCl}_4$ (where $\text{L} = 1,8\text{-bis}(\text{hydroxyethyl})\text{-}1,3,6,8,10,13\text{-hexaazacyclotetradecane}$) (B). The compounds are redrawn from the CSD co-ordinates RADLAJ and TEMMED respectively and rendered as sticks.....	7
Figure 1.3.1: Reaction scheme and percentage yields for some Au^{3+} -catalysed cyclizations. Redrawn from reference 24.	7
Figure 1.3.2: Chemical structures of $\text{Au}[\text{TPP}]^+$ (A), $[\text{Au}(\text{C}^{\wedge}\text{N}^{\wedge}\text{C})\text{Cl}]$ (B), $[\text{Au}(\text{sal}_2\text{pn})]\text{Cl}$ (C) and $[\text{Au}(\text{C}^{\wedge}\text{N})\text{Cl}_2]$ (D) used in the catalytic synthesis of propargylamines.....	8
Figure 1.3.3: Reaction scheme used in the synthesis of propargylamines. Redrawn from ref 22.....	9
Figure 1.3.4: Chemical structures of gold(III) alkynyl-based organic light-emitting devices.	9
Figure 1.3.5: Oxygen sensitive Emission of Che's organogold(III) complex (A). Ortep view of the complex in question (B). Hydrogen production properties of the complex under different reaction conditions (C). Reaction scheme showing the oxidative cyanation of tertiary amines (D). Reaction scheme showing the oxidation of secondary amines by the complex (E).Adapted from reference 33.....	10
Figure 1.4.1.1 Chemical structure of Aflatoxin.....	13
Figure 1.4.2.1: Diagram showing the relaxation of the DNA supercoiled structure by topoisomerase I and the trapping of the cleavage complex by a drug. Adapted from reference 42.....	16
Figure 1.4.2.2: Chemical structures of quinolone alkaloid based topo I poisons.....	17

Figure 1.4.2.3: Crystal structure of topo I-DNA-drug complex redrawn from the co-ordinates in PDB1T8I. The topo I enzyme has been coloured in red, the DNA in blue and the drug, topotecan, has been rendered as pink spheres. Molecular graphics generated with the UCSF Chimera package.....	18
Figure 1.4.2.4: Schematic diagram showing the mechanism through which topo II exhibits its function and the critical points in its function where inhibitors with well-studied mechanisms of action arrest or inhibit the catalytic cycle. Etoposide is a poison; ICRF-187, merbarone, and aclarubicin are catalytic inhibitors that operate in mechanistically distinct ways. Adapted from reference's 53 and 54.....	19
Figure 1.4.2.5: Crystal structure of topo II-DNA-drug complex redrawn from the co-ordinates in PDB 3QX3. The topo II enzyme has been coloured in red, the DNA in blue and the drug, topotecan, has been rendered as pink spheres. Reproduced from reference 54. Molecular graphics generated with the UCSF Chimera package.....	21
Figure 1.5.1.1: Crystal structures showing a rhodium intercalator, $\Delta\text{-}\alpha\text{-}[\text{Rh}\{(R,R)\text{-Me}_2\text{trien}\}(\text{phi})]^{3+}$ (where $(R,R)\text{-Me}_2\text{trien}$ = 2 <i>R</i> ,9 <i>R</i> -diamino-4,7-diazadecane and phi = 9.10-Diaminophenanthrene), left, and a rhodium inserter $\Delta\text{-}[\text{Rh}(\text{bipy}_2\text{chrysi})]^{3+}$ (where bipy = 2,2'-bipyridine and chrysi = 5,6-chrysene quinone diimine), right, bound to DNA. Adapted from reference 58.....	23
Figure 1.5.2.1: Crystal structure of Hoechst 33342 bound to DNA via the minor groove redrawn from the co-ordinates in PDB 129D. DNA is coloured blue and Hoechst 33342 is rendered as spheres and coloured pink. Molecular graphics generated with the UCSF Chimera package.....	24
Figure 1.5.3.1: Crystal structure of an iron metallo-supramolecular cylinder (pink) non-covalently bound to a DNA three-way junction (blue), left, redrawn from the co-ordinates in PDB 3FX8. ⁶³ Molecular structure of the iron metallo-supramolecular cylinder, right. Molecular graphics generated with the UCSF Chimera package.....	25
Figure 1.5.4.1: Crystal structure of a cisplatin (pink) intrastrand crosslink within a DNA helix (blue) redrawn from the co-ordinates in PDB 1AIO. Molecular graphics generated with the UCSF Chimera package.....	26
Figure 1.6.1.1: Chemical structures of gold(I) compounds for treatment of rheumatoid arthritis.....	27
Figure 1.6.1.2: Chemical structure of $\text{Au}(\text{d}2\text{pypp})_2\text{Cl}$	28
Figure 1.6.2.1: Chemical structures of gold(III) dithiocarbamate complexes.....	29

Figure 1.6.2.2: Chemical structures of [AuCl(dmamp)], (A) and [Au(O ₂ CMe)(dmamp)], (B).	30
Figure 1.6.2.3: Photographs of electrophoresis gels showing the changes in mobility of the RF I (upperband) and RF II (lowerband) forms of the Col E1 plasmid after treatment with [Au(SCN)(dmamp)] (left) and cisplatin (right). Left (from left to right): [Au(SCN)(dmamp)] at 75, 150, 300, 600, and 1500 μ M and plasmid control. Right (from left to right): cisplatin at 6.25, 9.4, 18.8, 37.5, 50, 75, and 100 μ M and plasmid control. Adapted from ref 87.....	31
Figure 1.6.2.4: Chemical structures of thiosalicylate and salicylate gold(III) derivatives synthesized by Dinger <i>et al</i>	32
Figure 1.6.2.5: Chemical structures of cytotoxic gold(III) porphyrin complexes reported by Che <i>et al</i>	33
Figure 1.6.2.6: <i>In vivo</i> anti-cancer activity of [Au(TPP)+] toward nasopharyngeal carcinoma cells. Adapted from reference 78.....	34
Figure 1.6.2.7: Laser confocal micrographs of the HeLa cells treated with [Au(TPP)+] (0.5 μ M) at time intervals of (a) 0 h and (b) 15 h. Healthy cells are marked by a yellow circle and apoptotic cells are marked by a red circle. Reproduced from ref 2.....	35
Figure 1.6.2.8: Chemical structures of various gold(III) complexes.....	36
Figure 1.6.2.9: Chemical structures of [Au(cyclam)](ClO ₄) ₂ Cl (left), [Au(en) ₂]Cl ₃ (middle) and [Au(dien)Cl]Cl ₂ (right).	37
Figure 1.6.2.10: Chemical structures of [Au(sal ₂ en)](PF ₆) (left) and [Au(sal ₂ pn)]Cl·2.5H ₂ O (right).....	38
Figure 1.7.1: Chemical structures and naming scheme of the ligands used in this work.....	39
Figure 1.7.2: Resonance hybrid structure of a general amide bond.....	39
Figure 1.7.3: Diagram of [Au(HL)Cl ₂] (H ₂ L = 2,2'-bis(2-pyridylcarboxamide)-1,1'-binaphthyl).....	40
Figure 1.7.4: Chemical structures of bis(amide) gold(III) complexes.....	41
Figure 1.7.5: Chemical structures of the complexes synthesized by Yang <i>et al</i>	42

Figure 1.7.6: Chemical structures of the compounds relating to the recent patent.....	42
Figure 1.8.1: Chemical structure of the ruthenium-based anti-cancer agents NAMI-A and KP1019 which are currently undergoing clinical trials.....	43
Figure 2.2.1: labelling scheme used for aroyl-2-pyridinecarboxylic acids.....	52
Figure 2.4.1.3: Numbering scheme employed for NMR characterisation of H ₂ L3, black letters correspond to ¹ H NMR signals and blue numbers correspond to ¹³ C NMR signals.....	55
Figure 2.4.1.4: Fully labelled thermal ellipsoid view (50% probability surfaces) of the molecular structure of H ₂ L3. All hydrogen atoms are shown as sticks. The four intramolecular hydrogen bonds present are rendered as a broken black line (N1···H100, 2.23 Å; N1···N2, 2.681(2) Å; N1···H100–N2, 113(1)°; O2···H100, 2.14 Å; O2···N2, 2.830(2) Å; O2···H100–N2, 137(2)°; O1···H12, 2.39 Å; O2···C12, 2.882(2) Å; O2···H100–N2, 113(1)°; N4···H200, 2.26 Å; N4···N3, 2.684(2) Å; N4···H200–N3, 111(2)°.....	56
Figure 2.4.2.1: Numbering scheme employed for NMR characterisation of HL6, black letters correspond to ¹ H NMR signals and blue numbers correspond to ¹³ C NMR signals.....	58
Figure 2.4.2.2: Numbering scheme employed for NMR characterisation of HL7, black letters correspond to ¹ H NMR signals and blue numbers correspond to ¹³ C NMR signals.....	59
Figure 2.4.2.3: Numbering scheme employed for NMR characterisation of HL9, black letters correspond to ¹ H NMR signals and blue numbers correspond to ¹³ C NMR signals.....	60
Figure 2.4.2.4: Numbering scheme employed for NMR characterisation of HL10, black letters correspond to ¹ H NMR signals and blue numbers correspond to ¹³ C NMR signals.....	61
Figure 2.4.2.5: Numbering scheme employed for NMR characterisation of HL11, black letters correspond to ¹ H NMR signals and blue numbers correspond to ¹³ C NMR signals.....	62
Figure 2.4.2.6: Numbering scheme employed for NMR characterisation of HL12, black letters correspond to ¹ H NMR signals and blue numbers correspond to ¹³ C NMR signals.....	63

Figure 2.4.2.7: Numbering scheme employed for NMR characterisation of HL9, black letters correspond to ^1H NMR signals and blue numbers correspond to ^{13}C NMR signals.....	64
Figure 2.4.2.8: Fully labelled thermal ellipsoid view (50% probability surfaces) of the molecular structure of HL9. All hydrogen atoms are shown as sticks. The three intramolecular hydrogen bonds present are rendered as broken black lines (N1...H100, 2.25 Å; N1...N2, 2.655(1) Å; N1...H100-N2, 109(1)°; N3...H100, 2.17 Å; N3...N2, 2.640(1) Å; N3...H100-N2, 114(1)°; O1...H7, 2.33 Å; O1...C7, 2.918(1) Å; O1...H7-C7, 121(1)°.....	65
Figure 2.4.2.9: Numbering scheme employed for NMR characterisation of HL14, black letters correspond to ^1H NMR signals and blue numbers correspond to ^{13}C NMR signals.....	66
Figure 2.5.1.1: Numbering scheme employed for NMR characterisation of $[\text{Au}(\text{HL1})\text{Cl}_2]$, black letters correspond to ^1H NMR signals and blue numbers correspond to ^{13}C NMR signals.....	68
Figure 2.5.1.2: Numbering scheme employed for NMR characterisation of $[\text{Au}(\text{HL2})\text{Cl}_2]$, black letters correspond to ^1H NMR signals and blue numbers correspond to ^{13}C NMR signals.....	69
Figure 2.5.1.3: Numbering scheme employed for NMR characterisation of $[\text{Au}(\text{HL3})\text{Cl}_2]$, black letters correspond to ^1H NMR signals and blue numbers correspond to ^{13}C NMR signals.....	70
Figure 2.5.1.4: Numbering scheme employed for NMR characterisation of $[\text{Au}(\text{L4})\text{Cl}_2]$, black letters correspond to ^1H NMR signals and blue numbers correspond to ^{13}C NMR signals.....	71
Figure 2.5.2.1: Numbering scheme employed for NMR characterisation of $[\text{Au}(\text{L5})\text{Cl}](\text{PF}_6)$, black letters correspond to ^1H NMR signals and blue numbers correspond to ^{13}C NMR signals.....	73
Figure 2.5.2.2: Numbering scheme employed for NMR characterisation of $[\text{Au}(\text{L6})\text{Cl}](\text{PF}_6)$, black letters correspond to ^1H NMR signals and blue numbers correspond to ^{13}C NMR signals.....	74
Figure 2.5.2.3: Numbering scheme employed for NMR characterisation of $[\text{Au}(\text{L7})\text{Cl}](\text{PF}_6)$, black letters correspond to ^1H NMR signals and blue numbers correspond to ^{13}C NMR signals.....	75

Figure 2.5.3.1: Numbering scheme employed for NMR characterisation of $[\text{Au}(\text{L}8)\text{Cl}](\text{PF}_6)$, black letters correspond to ^1H NMR signals and blue numbers correspond to ^{13}C NMR signals.....77

Figure 2.5.3.2: Numbering scheme employed for NMR characterisation of $[\text{Au}(\text{L}9)\text{Cl}](\text{PF}_6)$, black letters correspond to ^1H NMR signals and blue numbers correspond to ^{13}C NMR signals.....78

Figure 2.5.3.3: Numbering scheme employed for NMR characterisation of $[\text{Au}(\text{L}10)\text{Cl}](\text{PF}_6)$, black letters correspond to ^1H NMR signals and blue numbers correspond to ^{13}C NMR signals.....79

Figure 2.5.3.4: Numbering scheme employed for NMR characterisation of $[\text{Au}(\text{L}11)\text{Cl}](\text{PF}_6)$, black letters correspond to ^1H NMR signals and blue numbers correspond to ^{13}C NMR signals.....80

Figure 2.5.3.5: Numbering scheme employed for NMR characterisation of $[\text{Au}(\text{L}12)\text{Cl}](\text{PF}_6)$, black letters correspond to ^1H NMR signals and blue numbers correspond to ^{13}C NMR signals.....81

Figure 2.5.3.6: Numbering scheme employed for NMR characterisation of $[\text{Au}(\text{L}13)\text{Cl}](\text{PF}_6)$, black letters correspond to ^1H NMR signals and blue numbers correspond to ^{13}C NMR signals.....82

Figure 2.5.3.7: Numbering scheme employed for NMR characterisation of $[\text{Au}(\text{L}14)\text{Cl}](\text{PF}_6)$, black letters correspond to ^1H NMR signals and blue numbers correspond to ^{13}C NMR signals.....83

Figure 2.5.4.1: Numbering scheme employed for NMR characterisation of $[\text{Au}(\text{L}15)\text{Cl}]$, black letters correspond to ^1H NMR signals and blue numbers correspond to ^{13}C NMR signals.....84

Figure 2.5.4.2: Numbering scheme employed for NMR characterisation of $[\text{Au}(\text{L}16)\text{Cl}]$, black letters correspond to ^1H NMR signals and blue numbers correspond to ^{13}C NMR signals.....85

Figure 3.3.2.1: Negative ionisation mass spectral data of $[\text{Au}(\text{L}10)\text{Cl}_2]\text{AuCl}_2^-$ showing the presence of both $[\text{AuCl}_2]^-$ and $[\text{AuCl}_4]^-$ as counterions.....95

Figure 3.3.2.2: Schematic diagram depicting the different methods of synthesis used to generate the gold(III) chelates represented in this work. The green arrow shows the synthetic route employed for the synthesis of gold(III) chelates with mixed gold(I) and

gold(III) counterions while the blue arrows show the synthetic scheme used in the successful synthesis of the PF₆⁻ salt of the gold(III) complexes. Ligand HL10 is used as an example in the scheme.....96

Figure 4.1.1: Approximate absorption regions of some common functional groups. Diagram adapted and modified from 'Introduction to Spectroscopy' 4th Edition.....99

Figure 4.1.3.1: IR spectra overlay of H₂L3 (black) and [Au(HL3)Cl₂] (green).....103

Figure 4.2.1: The spins of nuclei in the absence (left) and in the presence (right) of a magnetic field. Diagram adapted and modified from 'Organic Chemistry' 4th Edition.....104

Figure 4.2.2.1: ¹H NMR spectra (500.01 MHz) of symmetric H₂L3 (blue) and its asymmetric mono(amido) gold(III) complex (black), [Au(L3)Cl](PF₆) (inset structure) recorded in DMSO-*d*₆. Signal integrals and peak assignments are based on the schemes for H₂L3 and [Au(HL3)Cl₂] given in the Experimental Section. Arrows track the splittings and shifts for protons *a* and *f* that accompany chelation of gold(III) and the loss of symmetry in [Au(HL3)Cl₂] relative to the free ligand. Intramolecular hydrogen bonds and a mid-range C-H···π interaction are shown with dashed lines and interaction distances (structure inset).....108

Figure 4.2.2.2: ¹H NMR spectra (400 MHz) of asymmetric ligand HL12 (blue) and its mono(amido) gold(III) complex (black), [Au(L12)Cl](PF₆) (inset structure) recorded in CDCl₃ and DMSO-*d*₆ respectively. Signal integrals and peak assignments are based on the schemes for HL12 and [Au(L12)Cl](PF₆) given in the Experimental Section.....109

Figure 4.2.2.3: Diagrammatic representation of the α-proton designations for ligands HL5–HL16 and their gold(III) metal compounds. Metal compound [Au(L12)Cl](PF₆) is used as an example.....110

Figure 4.2.2.4: Intramolecular hydrogen bonding between protons *f* and *g* with the carbonyl oxygen of the amide bond for compound [Au(L10)Cl](PF₆).....112

Figure 4.2.2.5: Diagram showing the ¹⁹F coupled ¹H spectrum of AuL13 (black trace) and the ¹⁹F decoupled proton spectrum (blue trace). The figure inset graphically shows the proton (blue) and carbon (red) atoms of the phenyl ketone ring that the fluorine atom couples with.....113

Figure 4.2.2.6: Selected regions of the spectral window showing the decomposition of [Au(L6)Cl](PF ₆) in DMSO- <i>d</i> ₆ over a 48 h period.....	115
Figure 4.3.1: Electronic energy levels and the two of the possible transitions in organic molecules. Diagram adapted from ‘Organic Chemistry, Fourth Edition’. ²	116
Figure 4.3.2.1: Overlaid electronic spectra of H ₂ L3 (green line) and [Au(HL3)Cl ₂] (blue line) showing the π-π* region (A and B) for both molecules and the LMCT band (inset C) for [Au(HL3)Cl ₂].....	118
Figure 4.4.1: Chemical structure of the hydrolysis product originating from a bis(pyrrole-imine) gold(III) compound. ¹⁹	121
Figure 4.4.2: Chemical structures of reduced glutathione (GSH) and oxidised glutathione (GSSH).....	122
Figure 4.4.3.1: Spectra of [Au(HL3)Cl ₂] recorded as a function of time in TBS at a complex concentration of 1.16 x 10 ⁻⁵ M, pH 7.34 and at 37 °C. All spectra were corrected for any background offset by setting A ₆₀₀ = 0.....	124
Figure 4.4.3.2: Double exponential decay curve for [Au(HL3)Cl ₂] at 295 nm in TBS at a complex concentration of 1.16 x 10 ⁻⁵ M, pH 7.34 and at 37 °C over a period of 48 h. Non-linear equation used: $Y = A1 \times 10^{(-A2*t)} + A3 \times 10^{(-A4*t)}$ where t = time, A1 and A3 are Y spans; A2 and A4 are rate constants. R is 0.9987, A1 is 0.18(1), A2 is 0.024(2) h ⁻¹ , A3 is 0.10(1) and A4 is 0.15(3) h ⁻¹	125
Figure 4.4.3.3: UV/Vis absorption spectrum for complex [Au(L6)Cl](PF ₆) at a concentration of 2.32 x 10 ⁻⁵ M, pH 7.34 and at 37 °C. The spectra were recorded over a period of 12 h displaying a 57% drop in absorbance at 365 nm.....	126
Figure 4.4.3.4: UV/Vis absorption spectrum taken over a period of 24 h at 37 °C in TBS, pH 7.34, for complex [Au(L12)Cl](PF ₆) (1.52 x 10 ⁻⁵ M) displaying a 2% drop in absorbance.....	127
Figure 4.4.3.5: UV/Vis spectra of [Au(L12)Cl](PF ₆) in the presence of a tenfold increase in concentration of imidazole over a period of 24 h (A) and in the presence of a tenfold increase in concentration of glutathione (B) over 12 h. Both sets of spectra were recorded at 37 °C in TBS at pH 7.34. All spectra were corrected for any background offset by setting A ₆₀₀ = 0.....	128

Figure 4.5.1: Structures and log $P_{o/w}$ values of an anti-biotic (amoxicillin), two anti-cancer chemotherapeutic drugs (doxorubicin and RDC11) and an anti-psychotic drug (chlorprothixene).....	130
Figure 4.5.3.1: Plot of the mean growth percent values versus their log $P_{o/w}$ values showing the unconventional correlation. The correlation coefficient of the fit is 0.985.....	135
Figure 4.6.1: Chemical structures of three proven metal-based DNA intercalators.....	137
Figure 4.6.3.1: UV/Visible spectrum of $[\text{Au}(\text{L10})\text{Cl}](\text{PF}_6)$ in pH 7.34 TBS at 37 °C showing the hypochromism and bathochromic shift of the LMCT band upon addition of consecutive aliquots of ctDNA. Inset displays a plot of $(\epsilon_a - \epsilon_f)/(\epsilon_b - \epsilon_f)$ vs [ctDNA] and the non-linear fit of the data resulting in the determination of K_b and s	142
Figure 4.6.3.2: UV/Visible spectrum of $[\text{Au}(\text{L12})\text{Cl}](\text{PF}_6)$ in pH 7.34 TBS at 37 °C showing the hypochromism and bathochromic shift of the LMCT band upon addition of consecutive aliquots of ctDNA. Inset displays a plot of $(\epsilon_a - \epsilon_f)/(\epsilon_b - \epsilon_f)$ vs [ctDNA] and the non-linear fit of the data resulting in the determination of K_b and s	143
Figure 4.6.3.3: Emission spectrum of EB in pH 7.34 TBS at 37 °C, showing the reduction in intensity upon increasing the concentration of $[\text{Au}(\text{L12})\text{Cl}](\text{PF}_6)$. Inset displays a plot of emission intensity as a percentage vs $[[\text{Au}(\text{L12})\text{Cl}](\text{PF}_6)]$ and the IC_{50} fit of the data.....	145
Figure: 5.1.1: Diagram of a single molecular unit of $[\text{Au}(\text{L-N,N}')\text{Cl}_2]$, showing the co-ordination geometry of the gold(III) centre. Redrawn from the CSD ¹ co-ordinates of Yang <i>et al.</i> 's structure.....	149
Figure: 5.1.2: Diagram of a single molecular unit of $[\text{Au}(\text{XL})\text{Cl}_2]$, showing the co-ordination geometry of the gold(III) centre. Redrawn from the CSD ¹ co-ordinates of Che <i>et al.</i> 's structure. ²	150
Figure: 5.1.3: Diagram of a single molecular unit of $[\text{Au}(\text{Quingly})\text{Cl}]\text{Cl}$ (A) and $[\text{Au}(\text{Quinala})\text{Cl}]\text{Cl}$ (B), showing the co-ordination geometry of the gold(III) centre. Redrawn from the CSD ¹ co-ordinates of Yang <i>et al.</i> 's structures. ⁵	151
Figure: 5.4.1: Labelled views of the single crystal X-ray structures of gold(III) compounds $[\text{Au}(\text{HL1})\text{Cl}_2]$, $[\text{Au}(\text{HL2})\text{Cl}_2]$, $[\text{Au}(\text{HL3})\text{Cl}_2]$ and $[\text{Au}(\text{L4})\text{Cl}_2]$. Hydrogen atoms are rendered as sticks and bonds are represented as cylinders. Thermal ellipsoids are represented as 50% probability surfaces for $[\text{Au}(\text{HL1})\text{Cl}_2]$, $[\text{Au}(\text{HL2})\text{Cl}_2]$, and $[\text{Au}(\text{HL3})\text{Cl}_2]$	154

Figure 5.4.2: Key intermolecular H-bonds (labeled atoms) for [Au(HL1)Cl₂]. Atoms and bonds are shown as sticks. Hydrogen bonds are shown as broken magenta cylinders.....158

Figure 5.4.3: View of the hydrogen-bonding and π - π stacking interactions between molecules of [Au(L4)Cl₂]. The distance between the two ring centers of gravity (Cg) is indicated. Atoms and bonds are shown as spheres and sticks, respectively. Hydrogen bonds are shown as broken magenta cylinders and individual molecules are colored according to their symmetry operators. A mean plane separation (MPS) for the stacked rings cannot be determined as the rings are not parallel.....159

Figure 5.4.4: Partially labeled view of the centrosymmetric π -stacked dimer formed by [Au(HL3)Cl₂]. The isoquinoline ring planes are parallel; the distance between the isoquinoline ring centers of gravity (Cg1...Cg1ⁱ) is indicated. The dimer is additionally stabilised by C-H...Cl hydrogen bonds: H22...Cl2ⁱ, 2.960(1) Å; C22...Cl2ⁱ, 3.864(4) Å; C22-H22...Cl2ⁱ, 159.5(3)°. Crystallographic symmetry code: (i) -x, 1-y, 1-z.....160

Figure: 5.4.6: Labelled views of the single crystal X-ray structures of gold(III) compounds [Au(L5)Cl](PF₆)-[Au(L7)Cl](PF₆). Hydrogen atoms are rendered as sticks and bonds are represented as cylinders. Thermal ellipsoids are represented as 50% probability surfaces.....163

Figure 5.4.7: Partially labeled view of the centrosymmetric unconventionally hydrogen bonded dimer formed by [Au(L5)Cl](PF₆). The dimer is stabilized by C-H...Cl hydrogen bonds: H1...Cl1ⁱ, 2.746(1) Å; C1...Cl1ⁱ, 3.503(6) Å; C1-H1...Cl1ⁱ, 137.1(3)°. Crystallographic symmetry code: (i) -x,-y,-z.....167

Figure 5.4.8: Partially labeled view of the centrosymmetric π -stacked dimer formed by [Au(L7)Cl](PF₆). The isoquinoline ring planes are parallel; the distance between the isoquinoline ring centers of gravity (Cg1...Cg1ⁱ) is indicated. The mean plane separation (MPS) and lateral shift (LS) of the stacked isoquinoline rings (calculated from the coordinates of Cg1 and Cg1ⁱ) are depicted graphically on the triangle to the right of to the top-down view of the dimer (lower left).....168

Figure: 5.4.9: Labelled views of the single crystal X-ray structures of gold(III) compounds [Au(L8)Cl](PF₆), [Au(L9)Cl](AuCl₂), [Au(L11)Cl](PF₆)-[Au(L13)Cl](PF₆) and [Au(L15)Cl]. Hydrogen atoms are rendered as sticks and bonds are represented as cylinders. Thermal ellipsoids are represented as 50% probability surfaces.....171

Figure 5.4.10: Partially labelled view of a discrete unconventionally hydrogen-bonded centrosymmetric dimer of [Au(L12)Cl](PF₆). Hydrogen atoms are represented as sticks; all other atoms are represented as thermal ellipsoids (50% probability). The dimer is stabilised by C–H···O hydrogen bonds: H6···O1ⁱ, 2.49 Å; C6···O1ⁱ, 3.318(5) Å; C6–H6···O1ⁱ, 145°. Crystallographic symmetry code: (i) 1-x,1-y,-z.....177

Figure 5.4.11: Partially labelled view of a both types of unconventionally hydrogen bonded centrosymmetric dimers of [Au(L12)Cl](PF₆). Hydrogen atoms are represented as sticks; all other atoms are represented as thermal ellipsoids (50% probability). The dimer on the left is stabilised by bifurcated C–H···O hydrogen bonds: H6···O1ⁱ, 2.50 Å; C6···O1ⁱ, 3.240(5) Å; C6–H6···O1ⁱ, 135°; H6···O2ⁱ, 2.60 Å; C6···O2ⁱ, 3.443(5) Å; C6–H6···O2ⁱ, 147°. Crystallographic symmetry code: (i) -x,-y,-z. The dimer on the right is stabilized by C–H···Cl hydrogen bonds: H1···Clⁱⁱ, 2.79 Å; C1···Clⁱⁱ, 3.516(4) Å; C6–H6···O1ⁱⁱ, 134°. Crystallographic symmetry code: (ii) 2-x,1-y,-z.....178

Figure 5.4.12: A: Spacefull (left) and stick (right) representation of the centrosymmetric π -stacked dimer between two quinoline rings in compound [Au(L12)Cl](PF₆). The metrics of the interaction are as follows: Cg1···Cg2, 3.819 Å; MPS, 3.307 Å; LS, 1.911. B: Partially labeled view of the centrosymmetric π -stacked dimer formed by [Au(L15)Cl]. The metrics of the interaction are depicted in the triangle inset on the left hand side while the inset on the right displays the interaction from a point of view perpendicular to a mean plane through an isoquinoline ring.....179

Figure 5.4.13: Centrosymmetric ‘sandwich’ structure observed for compound [Au(L9)Cl](AuCl₂) showing a linear gold(I) anion symmetrically sandwiched between two gold(III) cations (left). A top view of the ‘sandwich’ structure viewed perpendicular to a co-ordination motif mean plane.....181

Figure 6.1.1: Chemical structures of some gold(III) alkynyl complexes studied by Yam and co-workers.....189

Figure 6.1.2: Free energy diagram for the reaction in chloroform. All energy levels in kcal/mol. TS1 is transition state 1 and TS2 is transition state 2. Adapted from reference 28.....190

Figure 6.4.1: Least squares fit of the non-H atoms involved in the co-ordination sphere of the selected DFT (green) and X-ray (yellow) structures studied in this work. RMSD values (Å) are indicated in the diagram.....193

Figure 6.4.2: Unconventional hydrogen bonding interactions responsible for the large RMSD (0.199 Å) value between the experimental and calculated structures of [Au(L7)Cl](PF ₆).....	194
Figure 6.4.3: Partially labelled diagram for calculated structures [Au(L10)Cl] ⁺ , [Au(L14)Cl] ⁺ and [Au(L16)Cl].....	197
Figure 6.4.4: Overlay of calculated and experimental frequency data for the gold(III) chelate [Au(HL3)Cl ₂].....	198
Figure 6.4.5: Plot of experimental versus calculated amide carbonyl stretching vibrations for all compounds discussed in the work except [Au(L8)Cl](PF ₆) (removed as an outlier). The correlation coefficient of the fit is 0.854.....	199
Figure 6.4.6: Overlay of experimental and calculated UV-vis spectra for compounds [Au(HL3)Cl ₂], [Au(L7)Cl](PF ₆), [Au(L13)Cl](PF ₆) and [Au(L15)Cl]. Extinction coefficient scaling factors of 0.2 and 0.75 were applied to the calculated data for compounds [Au(L13)Cl](PF ₆) and [Au(L15)Cl] respectively. Bandwidth of 2600 cm ⁻¹ was used to generate the calculated spectra	201
Figure 6.4.7: Energy level diagram for complex cations (from left to right) of compounds [Au(HL3)Cl ₂], [Au(L7)Cl](PF ₆), [Au(L13)Cl](PF ₆) and [Au(L15)Cl], depicting the HOMO(H)→LUMO(L) electronic transition as well as the frontier orbital plots for each complex.....	202
Figure 6.4.8: Plot of experimental versus calculated α-(left) and α'-(right) ¹ H chemical shifts for compounds discussed in the work. Chemical shifts for compounds [Au(L5)Cl](PF ₆) and [Au(L13)Cl](PF ₆) have been removed as outliers. The correlation coefficients of the respective fits are 0.876 and 0.800. Compounds [Au(HL1)Cl ₂]-[Au(L4)Cl ₂] do not contain an α'-proton and hence were not included in the respective plot.	205
Figure 6.4.9: Plot of experimental versus calculated α-(left) and α'-(right) ¹³ C chemical shifts for compounds discussed in the work. Chemical shifts for compounds [Au(L15)Cl] and [Au(L16)Cl] have been left out as the corresponding experimental values could not be determined. The correlation coefficient of the respective fits are 0.868 and 0.046 respectively.....	207
Figure 7.3.1.1: One-dose screening results for compound [Au(L12)Cl](PF ₆) over 60 human cancer cell lines. The bars have been coloured according to the cell line panel.....	220

Figure 7.3.1.2: Mean growth percent for all compounds submitted for one-dose testing against the NCI-60 cell lines. The blue bars represent compounds that failed the one-dose screen, green bars represent compounds that were accepted to 5-dose screening and the red bar indicates the compound that was accepted through to the *in vivo* phase of testing.....221

Figure 7.3.1.3: Dose-response data for the commercial anti-cancer drugs, cisplatin and daunorubicin as well as the gold(III) compounds [Au(L6)Cl](PF₆), [Au(L10)Cl](PF₆) and [Au(L12)Cl](PF₆) synthesised in this work. The data measures the response of the Colon cancer cell line HCT-116 to varying concentrations of the compounds mentioned above. The data for the commercial drugs, cisplatin and daunorubicin, were obtained from the DTP drug repository database.....224

Figure 7.3.1.4: Comparison of the $-\log GI_{50}$ values for complexes [Au(HL3)Cl₂], [Au(L6)Cl](PF₆), [Au(L10)Cl](PF₆), [Au(L12)Cl](PF₆) and [Au(L15)Cl] against some commercially available anti-cancer drugs for some specific cancer cell lines.....225

Figure 7.3.1.5: Plot of $-\log GI_{50}$ values for [Au(L12)Cl](PF₆) versus the same data for cisplatin for all common cell lines in the NCI-60 screen.....226

Figure 7.3.3.1: Statistical comparison between the $-\log GI_{50}$ values of 25 commercially available chemotherapeutic drugs with known mechanisms of action and the gold(III) amide compounds, [Au(HL3)Cl₂] (light blue) and [Au(L12)Cl](PF₆) (purple), synthesised in this work.....231

Figure 7.3.3.2: Non-EB gel showing the ineffective poisoning or inhibition of topoisomerase IB by compound [Au(HL3)Cl₂] through all concentrations tested.....233

Figure 7.3.3.3: Non-EB gel showing the effective poisoning or inhibition of topoisomerase IB by compound [Au(L12)Cl](PF₆) between metal compound concentrations of 1 and 10 μ M.....234

Figure 7.3.3.4: EB gel showing CPT acting as an interfacial poison through its generation of linear DNA. There is a slight increase in linear DNA in presence of compound [Au(L12)Cl](PF₆) from 0-5 μ M, after which, a decrease in linear DNA is observed.236

Figure 7.3.3.5: EB gel showing a wide range topoisomerase II α kDNA decatenation assay for compound [Au(HL3)Cl₂]. At low concentrations (50 nM) [Au(HL3)Cl₂] acts as a poison

while at higher concentrations $[\text{Au}(\text{HL}3)\text{Cl}_2]$ acts as a catalytic inhibitor.....237

Figure 7.3.3.6: EB gel showing a topoisomerase II α kDNA decatenation assay for $[\text{Au}(\text{HL}3)\text{Cl}_2]$ and the absence and presence of linear DNA before and after treatment with PK, respectively.....238

Figure 7.3.3.7: EB gel showing a wide range topoisomerase II α decatenation assay for compound $[\text{Au}(\text{L}12)\text{Cl}](\text{PF}_6)$. The compound shows no inhibitory/poisoning activity through the concentration range tested.....239

Figure 7.3.4.1: EMSA gel for EB (top left), $[\text{Au}(\text{HL}3)\text{Cl}_2]$ (top middle) and mAMSA (top right) at various indicated drug concentrations. Two dimensional peak deconvolution for EB (bottom left), $[\text{Au}(\text{HL}3)\text{Cl}_2]$ (bottom middle) and mAMSA (bottom right). DNA band identities: I, supercoiled DNA; II, nicked open-circular DNA.....241

Figure 7.3.4.2: EMSA gel for EB, Hoechst-33258 and $[\text{Au}(\text{L}12)\text{Cl}](\text{PF}_6)$ using relaxed DNA as the substrate. The gel shows no evidence for DNA intercalation by compound $[\text{Au}(\text{L}12)\text{Cl}](\text{PF}_6)$242

Figure 7.3.4.3: EMSA gel for $[\text{Au}(\text{L}13)\text{Cl}](\text{PF}_6)$ (top) at various indicated drug concentrations. The two dimensional peak deconvolution for $[\text{Au}(\text{L}13)\text{Cl}](\text{PF}_6)$ is shown below. DNA band identities: I, supercoiled DNA; II, nicked open-circular DNA.....243

Figure 7.3.4.4: Schematic representation of the hypothetical electrostatic interaction between $[\text{Au}(\text{L}12)\text{Cl}](\text{PF}_6)$ and a DNA molecule. The diagram shows the displacement of EB and sodium ions from helical DNA structure by $[\text{Au}(\text{L}12)\text{Cl}](\text{PF}_6)$244

List of tables

Table 1.2.1: Summary of the common oxidation states and stereochemistry of gold (table adapted from “Advanced Inorganic Chemistry”).....	4
Table 1.4.2.1: Summary of some different classes of chemotherapeutic agents.....	14
Table 4.1.3.1: Experimental IR data for all free ligands and metal compounds studied.....	101
Table 4.2.2.1: Table comparing α - and α' -proton shifts between ligands and metal compounds.....	111
Table 4.3.2.1: Summary of the two major λ_{\max} values in the π - π^* and LMCT regions of the metal complexes reported in this work.....	119
Table 4.5.3.1: Summary of the average $\log P_{o/w}$ values for the indicated gold(III) compounds synthesised in this work.....	133
Table 4.6.3.1: Summary of binding affinities, binding site size, hypochromism and bathochromic shift for stable gold(III) compounds from this work as well as some literature metallointercalators determined by UV/Visible DNA titrations.....	141
Table 4.6.3.2: Summary of ctDNA binding affinities, binding site size and hypochromism for the selected metal compounds, determined by ethidium bromide displacement titrations.....	146
Table 5.1.1: Co-ordination sphere bond lengths and bond angles for CSD-reported gold(III) structures.....	151
Table 5.1.2: Co-ordination sphere bond lengths and bond angles for CSD-reported gold(III) structures.....	152
Table 5.4.1: Selected Crystallographic Bond Distances and Bond Angles for [Au(HL1)Cl ₂]-[Au(L4)Cl ₂].....	155
Table 5.4.2: Hydrogen bond distances and angles for compounds [Au(HL1)Cl ₂]-[Au(L4)Cl ₂].....	161
Table 5.4.3: Crystal Structure, X-ray Data, and Structure Model Refinement Parameters for and [Au(HL1)Cl ₂]-[Au(L4)Cl ₂].....	162

Table 5.4.4: Selected Crystallographic Bond Distances and Bond Angles for [Au(L5)Cl](PF ₆)-[Au(L6)Cl](PF ₆).....	164
Table 5.4.5: Hydrogen bond distances and angles for compounds [Au(L5)Cl](PF ₆)-[Au(L7)Cl](PF ₆).....	169
Table 5.4.6: Crystal Structure, X-ray Data, and Structure Model Refinement Parameters for and [Au(L5)Cl](PF ₆)-[Au(L7)Cl](PF ₆).....	170
Table 5.4.7: Selected Crystallographic Bond Distances and Bond Angles for [Au(L8)Cl](PF ₆), [Au(L9)Cl]AuCl ₂ , [Au(L11)Cl](PF ₆)-[Au(L13)Cl](PF ₆) and [Au(L15)Cl].....	173
Table 5.4.8: Hydrogen bond distances and angles for compounds [Au(L8)Cl](PF ₆), [Au(L9)Cl](AuCl ₂), [Au(L11)Cl](PF ₆)-[Au(L13)Cl](PF ₆) and [Au(L15)Cl].....	182
Table 5.4.9: Crystal Structure, X-ray Data, and Structure Model Refinement Parameters for and [Au(L8)Cl](PF ₆), [Au(L9)Cl](AuCl ₂), [Au(L11)Cl](PF ₆)-[Au(L13)Cl](PF ₆) and [Au(L15)Cl].....	184
Table 6.4.1: Comparisons of the mean bond lengths and angles of the calculated and experimental structures of the gold(III) compounds: [Au(HL1)Cl ₂]-[Au(L9)Cl](PF ₆), [Au(L11)Cl](PF ₆)-[Au(L13)Cl](PF ₆) and [Au(L15)Cl].....	195
Table 6.4.2: Summary of calculated bond lengths and angles for complexes [Au(L10)Cl] ⁺ , [Au(L14)Cl] ⁺ and [Au(L16)Cl].....	197
Table 6.4.3: Summary of experimental and calculated frequencies for the amide C=O stretch for all gold(III) compounds studied in this work.....	200
Table 6.4.4: Summary of calculated and experimental transitions for the major peaks of the representative gold(III) compounds [Au(HL3)Cl ₂], [Au(L7)Cl](PF ₆), [Au(L13)Cl](PF ₆) and [Au(L15)Cl].	204
Table 6.4.5: Comparison of experimental and calculated ¹ H NMR data for the gold(III) compounds studied in this work.....	206
Table 6.4.6: Comparison of experimental and calculated ¹³ C NMR data for the gold(III) compounds studied in this work.....	208
Table 7.3.1.1: Summary of the average cytotoxicity data over the 60 human cancer cell lines for each of the nine compounds: [Au(HL3)Cl ₂], [Au(L6)Cl](PF ₆)-[Au(L8)Cl](PF ₆),	

[Au(L10)Cl](PF₆)-[Au(L13)Cl](PF₆) and [Au(L15)Cl] as well as some commercially available chemotherapeutic agents for comparison.....223

List of schemes

- Scheme 3.1.1:** Mechanistic scheme depicting the formation of a 3-substituted pyridine carboxylic acid via a Friedal crafts acylation reaction.....87
- Scheme 3.2.1:** Mechanistic scheme depicting the formation of an amide bond through a triphenylphosphite mediated pathway.....88
- Scheme 3.2.2:** Mechanistic scheme depicting the formation of an amide bond through an acyl chloride mediated pathway.....89
- Scheme 3.2.3:** Mechanistic scheme depicting the formation of an amide bond through a carbodiimide mediated pathway.....90
- Scheme 3.1.1.1:** Reaction scheme depicting the favored route to neutral monochelates of Au(III) as opposed to cationic trischelates of the metal.....92
- Scheme 4.1.3.1:** Illustration of bond resonance involving the metal-bound amide group of [Au(HL₃)Cl₂]. Lone pairs of electrons are shown for the amide group to aid visualisation of the two resonance forms.....100
- Scheme 8.2.1:** Synthetic method that may be employed for the generation of second generation gold(III) amide-based chelates with improved redox stability.....256
- Scheme 8.2.2:** Proposed synthetic route for the sugar-derivatised gold(III) amide-based second generation chelate.....257

Abstract

Since the discovery of cisplatin as an anti-cancer agent, there has been a broad and multidisciplinary interest over four decades in the development of metal complexes as metallotherapeutic drugs. The principal objective of this thesis was to develop and characterize a novel library of gold(III) complexes of aromatic and non-aromatic quinoline- and pyridine-amido ligands and to test their efficacy as cytotoxic agents against multiple human cancer cell lines. To this end, fifteen novel (16 in total) gold(III) complexes have been prepared and studied by multiple methods including FTIR, NMR, MS, and UV-visible spectroscopy, and in numerous cases, single crystal X-ray diffraction.

Ligands H₂L1–HL14 were prepared via the reaction of the relevant pyridine or quinoline carboxylic acid in the presence of triphenylphosphite and either picolylamine or 8-aminoquinoline in pyridine, in moderate to good yields. Ligands HL15 and HL16 were prepared via the reaction between benzoyl or 1-naphthoyl chloride and 8-aminoquinoline in good yields. The synthesis of complexes [Au(HL1)Cl₂]–[Au(L4)Cl₂] were prepared by the reaction between the respective ligand, K[AuCl₄] and NaOAc in 1:1 MeOH:DCM. Metal complexes [Au(L5)Cl](PF₆)–[Au(L14)Cl](PF₆) were synthesised by encouraging the formation of a AuCl₄⁻ counter ion in acetic acid and 3-fold excess of NaHCO₃. Subsequent metathesis afforded the desired PF₆⁻ anion. Complexes [Au(L15)Cl] and [Au(L16)Cl] were synthesised by the reaction of H[AuCl₄] and respective ligand in acetic acid and a 3-fold excess of NaHCO₃.

The solubility of all complexes was assessed, with complexes [Au(L8)Cl](PF₆)–[Au(L14)Cl](PF₆) proving to be the most stable in biologically relevant media (TBS 50 mM, NaCl 10mM, pH 7.34, 37°C). Complex [Au(L12)Cl](PF₆) was further evaluated for its stability in the presence of glutathione and imidazole and found to be sensitive to reduction by thiols, but substitution-inert to N-donor heterocycles such as imidazole. The DNA binding constants of [Au(L8)Cl](PF₆)–[Au(L11)Cl](PF₆) were subsequently evaluated by UV-vis spectroscopy and found to be in the range of 2.7(5) × 10⁵ to 4.7(6) × 10⁵ M⁻¹. Complexes [Au(L12)Cl](PF₆)–[Au(L14)Cl](PF₆) were similarly assessed using ethidium bromide displacement fluorescence assays, however their ability to bind DNA could not be conclusively proven. The log P_{o/w} values of complexes

[Au(L12)Cl](PF₆)-[Au(L14)Cl](PF₆) were measured and spanned the range -0.8 to -2.16, consistent with significant hydrophilic character.

The solid state structures of all complexes, with the exception of [Au(L10)Cl](PF₆), [Au(L14)Cl](PF₆) and [Au(L16)Cl](PF₆), were determined by X-ray crystallography with the gold(III) ion coordinated to the ligand in a square planar geometry. The co-ordination mode in complexes [Au(HL1)Cl₂]-[Au(HL3)Cl₂] was unexpected with the metal centre only co-ordinating to half the tetradentate ligand with a pair of *cis*-dichloro ions completing the square planar geometry. The average Au-N_{py/qu} distance is 2.02(2) Å while the average Au-N_{amide} distance is 1.97(4) Å. In all complexes the *trans* labilising effect of the anionic amide nitrogen was observed through a structural elongation of the respective Au-Cl bond length. Almost all complexes studied exhibited π -stacking interactions, with compound [Au(L12)Cl](PF₆) exhibiting a mean plane separation between rings of 3.307 Å. This is a result of the extended aromatic rings present in all compounds

DFT geometry optimizations, frequency, NMR, and energy calculations were carried out on all the gold(III) complexes at the HSEH1PBE/6-311G(d,p)/LanL2DZ level of theory. The 6-311G(d,p) basis set was used for all atoms with the exception of the gold atom for which the LanL2DZ basis set was used. In general, the chosen level of theory satisfactorily correlates with the experimental data for all complexes and was instrumental in deconvoluting the UV-vis spectra of all complexes. The lowest energy transitions (300–500 nm) were assigned to a LMCT while the higher energy transitions were assigned to π - π^* transitions.

The cytotoxicity profiles of all compounds, with the exception of [Au(HL1)Cl₂] and [Au(L16)Cl], were evaluated through one-dose screens against the 60 human cancer cell lines at the NCI, where [Au(HL3)Cl₂], [Au(L6)Cl](PF₆)-[Au(L8)Cl](PF₆), [Au(L10)Cl](PF₆)-[Au(L13)Cl](PF₆) and [Au(L15)Cl](PF₆) were deemed sufficiently cytotoxic to proceed further to five-dose screening. The cytotoxicity results for compound [Au(L12)Cl](PF₆) were most encouraging with GI₅₀, TGI and LC₅₀ values of 0.11(0.1), 0.70(0.7) and 26.5(1.5) μ M, respectively, against the breast cancer cell line MDA-MB-468.

Statistical analysis of the GI_{50} values for complexes $[Au(HL3)Cl_2]$ and $[Au(L12)Cl](PF_6)$ revealed they may exert their cytotoxicity through the inhibition/poisoning of topoisomerase II and I enzymes, respectively. Both compounds were assessed for this through a topoisomerase IB DNA unwinding assay and a topoisomerase II α decatenation assay. $[Au(HL3)Cl_2]$ was found to be a dual catalytic inhibitor and poison of topoisomerase II α between concentrations of 500 nM and 50 μ M while $[Au(L12)Cl](PF_6)$ was found to be a dual catalytic inhibitor and poison of topoisomerase IB between concentrations of 1 and 100 μ M.

Electrophoretic mobility shift assays were performed on both complexes, with $[Au(HL3)Cl_2]$ indicating DNA binding at a concentration of 50 μ M, while $[Au(L12)Cl](PF_6)$ displayed no evidence for DNA binding despite an unexpected increase in mobility shift of the substrate DNA. This is indicative of an alternative mechanism of DNA interaction such as electrostatic binding.

In summary, we present in this thesis, the discovery, synthesis and application of a novel series of gold(III) amide-based metal complexes as anti-cancer agents with the mechanism of action by which the complexes exert their cytotoxic activity being elucidated. The compounds show immense potential in the metallo-drug discovery field of research, and with further development, a leading class of metallotherapeutic drugs may be developed from this research.

Contents

Declaration – Plagiarism	ii
Acknowledgements	iii
Research outputs	iv
List of abbreviations	v
List of figures	ix
List of tables	xxiii
List of schemes	xxvi
Abstract	xxvii
Chapter One: Introduction	1
1.1 Preface	1
1.2 Gold: The Royal Metal	2
1.3 Gold(III) complexes and their general applications	7
1.4 Cancer and its Treatment	11
1.4.1 Background and History	11
1.4.2 Chemotherapy and its Use in the Treatment of Cancer	14
1.5 Drug-DNA Interactions	22
1.5.1 DNA Intercalation and insertion	22
1.5.2 DNA Groove binding	24
1.5.3 DNA three-way junction binders	25
1.5.4 DNA cross-linkers	26
1.6 Gold complexes and their applications in medicine	27
1.6.1 Gold(I) complexes in medicine	27
1.6.2 Gold(III) complexes in medicine	28
1.7 Bis(amide) and Mono(amide) Ligands and Metal Complexes	38
1.8 Objectives	43
1.9 References	45
Chapter Two: Experimental	51
2.1 General methods and instrumentation	51
2.2 Synthesis of 3-Aroyl-2-pyridinecarboxylic acid precursors, APC1, APC2, APC3	52
2.3 Synthesis of Gold(III) metal precursors	53

2.2.1 Synthesis of tetrabutylammonium tetrachloroaurate(III), [Bu ₄ N][AuCl ₄]	53
2.2.2 Synthesis of potassium tetrachloroaurate(III), K[AuCl ₄]	53
2.4 Synthesis of amide ligands	54
2.4.1 General procedure for synthesis of bis(amide) ligands	54
2.4.1.1 <i>N,N'</i> -ethane-1,2-diyl dipyridine-2-carboxamide, H ₂ L1	54
2.4.1.2 <i>N,N'</i> -propane-1,3-diyl dipyridine-2-carboxamide, H ₂ L2	54
2.4.1.3 <i>N,N'</i> -benzene-1,2-diyl diisoquinoline-3-carboxamide, H ₂ L3	55
2.4.2 General procedure for synthesis of mono(amide) N-donor ligands	57
2.4.2.1 <i>N</i> -(4-methoxyphenyl)pyridine-2-carboxamide, HL4	57
2.4.2.2 <i>N</i> -(pyridin-2-ylmethyl)pyridine-2-carboxamide, HL5	57
2.4.2.3 <i>N</i> -(pyridin-2-ylmethyl)isoquinoline-1-carboxamide, HL6	58
2.4.2.4 <i>N</i> -(pyridin-2-ylmethyl)quinoline-3-carboxamide, HL7	59
2.4.2.5 <i>N</i> -(quinolin-8-yl)pyridine-2-carboxamide, HL8	59
2.4.2.6 5-butyl- <i>N</i> -(quinolin-8-yl)pyridine-2-carboxamide, HL9	60
2.4.2.7 <i>N</i> -(quinolin-8-yl)isoquinoline-1-carboxamide, HL10	61
2.4.2.8 <i>N</i> -(quinolin-8-yl)isoquinoline-3-carboxamide, HL11	62
2.4.2.9 3-benzoyl- <i>N</i> -(quinolin-8-yl)pyridine-2-carboxamide, HL12	63
2.4.2.10 3-(4-fluorobenzoyl)- <i>N</i> -(quinolin-8-yl)pyridine-2-carboxamide, HL13	64
2.4.2.11 3-(4-methoxybenzoyl)- <i>N</i> -(quinolin-8-yl)pyridine-2-carboxamide, HL14	66
2.4.3 General procedure for synthesis of mono(amide) C, N-donor ligands	67
2.4.3.1 <i>N</i> -(quinolin-8-yl)benzamide, H ₂ L15	67
2.4.3.2 <i>N</i> -(quinolin-8-yl)naphthamide, H ₂ L16	67
2.5 Synthesis of gold(III) metal complexes	68
2.5.1 General synthesis of <i>cis</i> -dichloro gold(III) chelates	68
2.5.1.1 ((Pyridine-2-ylcarbonyl){2-[(pyridine-2-ylcarbonyl)amino]ethyl}azanido) dichlorogold(III), [Au(HL1)Cl ₂]	68
2.5.1.2 ((pyridine-2-ylcarbonyl){3-[pyridine-2-ylcarbonyl]amino}propyl}azanido) dichlorogold(III), [Au(HL2)Cl ₂]	69
2.5.1.3 ((Isoquinoline-3-ylcarbonyl){2-[isoquinoline-3-ylcarbonyl]amino}ethyl}azanido) dichlorogold(III), [Au(HL3)Cl ₂]	70
2.5.1.4 {(4-Methoxyphenyl)(pyridine-2-ylcarbonyl)azanido}dichlorogold(III), [Au(L4)Cl ₂]	71
2.5.2 General synthesis of <i>N</i> -donor aminomethyl-based tridentate gold(III) chelates	72
2.5.2.1 (Pyridin-2-ylcarbonyl)(pyridin-2-ylmethyl)azanidogold(III) hexafluorophosphate(V), [Au(L5)Cl](PF ₆)	73
2.5.2.2 (Isoquinolin-1-ylcarbonyl)(pyridin-2-ylmethyl)azanidogold(III) hexafluorophosphate(V), [Au(L6)Cl](PF ₆)	74
2.5.2.3 (Isoquinolin-3-ylcarbonyl)(pyridin-2-ylmethyl)azanidogold(III) hexafluorophosphate(V), [Au(L7)Cl](PF ₆)	75

2.5.3 General synthesis of <i>N</i> -donor 8-aminoquinoline-based tridentate gold(III) chelates	76
2.5.3.1 (Pyridin-2-ylcarbonyl)(quinolin-8-yl)azanidogold(III) hexafluorophosphate(V), [Au(L8)Cl](PF ₆)	77
2.5.3.2 [(5-Butylpyridin-2-yl)carbonyl](quinolin-8-yl)azanidogold(III) dichloroaurate, [Au(L9)Cl](AuCl ₂)	78
2.5.3.3 [(5-Butylpyridin-2-yl)carbonyl](quinolin-8-yl)azanidogold(III) hexafluorophosphate(V), [Au(L9)Cl](PF ₆)	78
2.5.3.4 (Isoqionolin-1-ylcarbonyl)(quinolin-8-yl)azanidogold(III) hexafluorophosphate(V), [Au(L10)Cl](PF ₆)	79
2.5.3.5 (Isoqionolin-3-ylcarbonyl)(quinolin-8-yl)azanidogold(III) hexafluorophosphate(V), [Au(L11)Cl](PF ₆)	80
2.5.3.6 [3-(Benzoylpyridin-2-yl)carbonyl](quinolin-8-yl)azanidogold(III) hexafluorophosphate(V), [Au(L12)Cl](PF ₆)	81
2.5.3.7 {[3-(4-Fluorobenzoyl)pyridin-2-yl]carbonyl}(quinolin-8-yl)azanidogold(III) hexafluorophosphate(V), [Au(L13)Cl](PF ₆)	82
2.5.3.8 {[3-(4-Methoxybenzoyl)pyridin-2-yl]carbonyl}(quinolin-8-yl)azanidogold(III) hexafluorophosphate(V), [Au(L14)Cl](PF ₆)	83
2.5.4 General synthesis of <i>C</i> , <i>N</i> -donor 8-aminoquinoline-based tridentate gold(III) chelates.	84
2.5.4.1 Benzoyl(quinolin-8-yl)azanidogold(III), [Au(L15)Cl]	84
2.5.4.2 (Naphthalen-1-ylcarbonyl)(quinolin-8-yl)azanidogold(III), [Au(L16)Cl]	85
2.6 References	86
Chapter Three: Synthesis	87
3.1 Synthesis of aroyl pyridine carboxylic acids	87
3.2 Synthesis of ligands	88
3.3 Synthesis of metal complexes	91
3.3.1 Synthesis of <i>cis</i> -dichloro gold(III) chelates	91
3.3.2 Synthesis of tridentate gold(III) chelates	93
3.4 References	97
Chapter Four: Spectroscopy	98
4.1 Infrared spectroscopy	98
4.1.2 Objectives	100
4.1.3 Results and discussion	100
4.2 NMR spectroscopy	104
4.2.1 Objectives	106
4.2.2 Results and discussion	106
4.3 UV-vis spectroscopy	116
4.3.1 Objectives	118

4.3.2 Results and discussion	118
4.4 Stability and reactivity	121
4.4.1 Objectives	122
4.4.2 Experimental	122
4.4.3 Results and discussion	123
4.5 Octanol/Water partition coefficients	130
4.5.1 Objectives	131
4.5.2 Experimental	131
4.5.3 Results and discussion	132
4.6 DNA binding studies	136
4.6.1 Objectives	138
4.6.2 Experimental	138
4.6.3 Results and discussion	140
4.7 References	147
Chapter five: X-ray crystallography	149
5.1 Introduction	149
5.2 Objectives	152
5.3 Experimental	153
5.4 Results and discussion	154
5.5 References	185
Chapter Six: Computational chemistry	187
6.1 Introduction	187
6.2 Objectives	190
6.3 Experimental	191
6.4 Results and discussion	191
6.5 References	209
Chapter Seven: Biological studies	211
7.1 Introduction	211
7.2 Experimental	213
7.2.1 <i>In Vitro</i> Cell Screening	213
7.2.2 <i>In vivo</i> testing	215
7.2.3 Mechanism of action elucidation	217
7.2.4 Gel electrophoresis experiments	217
7.3 Results and discussion	220
7.3.1 NCI-60 <i>in vitro</i> cytotoxicity screens	220
7.3.2 NCI <i>in vivo</i> testing	227
7.3.3 Mechanism of action	229
7.3.4 Electrophoretic gel mobility shift assays	240

7.3.5 Summary and conclusions	245
7.4 References	246
Chapter Eight: Summary, conclusions and future work	248
8.1 Summary and conclusions	248
8.2 Future work	254
8.3 References	258
Appendix A: NMR fid files	DVD
Appendix B: Crystallographic data	DVD
Appendix C: Computational files	DVD
Appendix D: Biological data	DVD

1. Introduction

1.1 Preface

In the fight against cancer there have been many successful drugs that have made a substantial impact, none more than cisplatin. Since the discovery of cisplatin in the 1940's there has been a steadily increasing research focus into the use of metal complexes as chemotherapeutics. The use of gold complexes as medicinal drugs is not a new idea as in 1890 it was discovered that gold(I) dicyanide was able to exhibit anti-tubercular activity.¹ This complex was not pursued further due to its toxic side effects. Nevertheless this was encouraging and further research into gold(I) anti-tubercular complexes led to the discovery of gold(I) thiolate complexes.¹ These complexes were used extensively in the early twentieth century in the treatment of tuberculosis. Following this discovery it was also found that another gold(I) complex, auranofin, was effective in the treatment of rheumatoid arthritis. Despite these encouraging finds, there are inherent problems with gold-based drugs, specifically, gold(III)-based drugs. The gold(III) ion is fairly redox unstable and is particularly susceptible to reduction.^{1, 2} This particular trait becomes problematic when placed in the reducing environment of living cells. Gold(III) complexes can undergo reduction to gold(I) species as well as to colloidal gold through several reducing agents present in living cells, e.g. glutathione.^{1, 2} These problems are inherent and are carried through to the laboratory where redox and hydrolysis reactions take place readily. Another problem encountered when trying to synthesise cationic gold(III) complexes is the tendency for the formation of $[\text{AuCl}_4]^-$ and $[\text{AuCl}_2]^-$ counterions. In some cases the formation of these counterions can be circumvented through specific reaction conditions but in others, like the work presented here, alternative methods have to be employed to arrive at the desired product. There is one report in literature by Yang and co-workers that presents a similar class of amide based gold(III) chelates.³ The work presented herein contains fifteen novel metal chelates of gold(III) with one previously reported. Their basic structure has shown to interact with DNA and therefore we envisage them as being effective chemotherapeutic agents.

Introduction

1.2 Gold: The royal metal

Pure metallic gold was probably one of the first metals known to early civilizations. The symbol derives from the Latin word *aurum*, which is related to the goddess of dawn, Aurora. Early civilizations equated gold with gods and power, possibly due to its alluring physical nature. This is evident in Egyptian culture where pharaohs were surrounded by gold. Some of the oldest pieces of gold jewellery were discovered in the tombs of Queen Zer of Egypt dating back to the third millennium BC,⁴ however the oldest known golden treasure was found in the *Varna Necropolis*,⁴ a burial site in the western industrial zone of Varna, Bulgaria. Archaeological findings suggest that gold was first used in the Middle East and Europe where the first civilizations developed.⁴ Pieces of natural gold have also been found in Spanish caves of Palaeolithic Man (40 000 BC).⁴ A 27% Silver: 63% Gold mixture, stamped out into lumps, called 'electrum' was first used as money by Lydian merchants (700 BC), hence it is one of the so called 'coinage metals', along with silver.⁴ Geographically, gold is found worldwide in its natural state in rivers and streams and through its discovery as such has led to the development of some of the largest cities in the world. The California Gold Rush of 1848 led to the substantial growth of San Francisco from a small settlement of 200 residents, to 36 000 by 1852. The establishment of Johannesburg, aptly named the city of gold or 'Isidingo', was also due the discovery of gold and consequently the Witwatersrand Gold Rush.

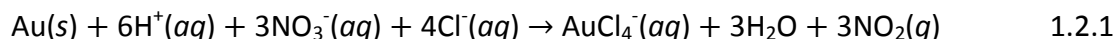


Figure 1.2.1: Gold nuggets.⁵

Gold (Figure 1.2.1) is a shiny, malleable and ductile 5d metal with an atomic number of 79. It is chemically unreactive and does not tarnish, hence its use in coinage and jewellery. One of the only liquids able to dissolve gold is aqua regia (3 : 1 mixture of HCl and HNO₃). Aqua regia is Latin for "king's water" and named so for its ability to dissolve the so-called noble

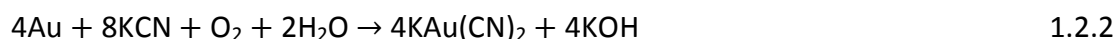
Introduction

metals, gold and platinum. It is able to dissolve gold because once the metal has been oxidised by the nitric acid, the chloride anions from the HCl bind to the Au^{III} metal centre forming a co-ordination complex that is stable (Equation 1.2.1).⁶



Gold metal melts at a temperature of 1337.58 K and boils at a temperature of 3080 K. It has an electronic configuration of [Xe] 4f¹⁴ 5d¹⁰ 6s¹ and like copper and silver (group congeners), has a single *s* electron outside of a completed *d* shell.⁷ In spite of the similar electronic structures there are few chemical resemblances between copper, silver and gold.⁷ There are no simple explanations for this, but gold's uniqueness may be traced back to the relativistic effects of the 6s electrons. Gold metal's density is 19.3 g/cm³ compared to the densest of all metals, osmium, which has a density of 22.6 g/cm³. Gold metal also has the lowest electrochemical potential of any metal as well as being the most electronegative metal. This means that in its cationic form it is able to accept electrons from almost any reducing agent to form metallic gold.⁴

Gold is usually associated with metal sulphide ores or quartz conglomerates. These ores can be accompanied by other metals such as iron, copper, silver and zinc. The main global sources of gold are China and Australia.⁸ There are several industrial methods used for the processing mined gold ores. The Miller process involves a stream of chlorine gas that is blown over and through a crucible containing molten impure gold. This technique works on the principle that nearly all other elements will form chlorides before gold does. These chlorides are insoluble in molten metal and are removed leaving gold of 99.95% purity. Another is froth flotation followed by leaching with cyanide and consequent precipitation using zinc (Equation 1.2.2 and 1.2.3).^{7,9}



In order to obtain even higher purity gold (99.9999 %), the Wohlwill process is employed. This is an electrochemical process where the anode is a gold bar of 95%+ purity (any lower

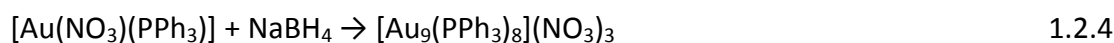
Introduction

purity will interfere with the reaction) and the cathode is a small sheet of 24 carat gold.⁹ The electrolyte in the system is chloroauric acid. When a current is applied to the system the impure gold is dissolved at the anode and is plated on the cathode through ion transfer of the chloroauric acid.⁹

Table 1.2.1: Summary of the common oxidation states and stereochemistry of gold (table adapted from “Advanced Inorganic Chemistry”).⁷

Oxidation State	Electronic Configuration	Co-ordination Number	Geometry
+1	d^{10}	2	Linear
		3	Trigonal
		4	Tetrahedral
+2	d^9	4	Square planar
+3	d^8	4	Square planar
		5	Trigonal bipyramidal
		6	Octahedral
+5	d^6	6	Octahedral

The chemistry of gold is extremely diverse with the metal being able to adopt several different oxidation states. These oxidation states vary from -1 to $+5$, although $+1$ and $+3$ dominate its chemistry.^{4, 6, 10} The common oxidation states and co-ordination geometries are summarised in Table 1.2.1. Gold(-I)-containing compounds are called aurides and due to the high electronegativity of gold, the auride anion is relatively stable.^{4, 7} Examples of binary alkali metal aurides (RbAu and CsAu) have been known for a number of years,^{11, 12} but the ternary auride oxides M_3AuO ($M = K, Rb, Cs$) and the auridaurates Rb_5Au_3O and M_7Au_5O ($M = Rh$ or Cs) have only been more recently discovered.¹³⁻¹⁶ The first non-metal auride, $NMe_4^+Au^-$, was synthesised through ion exchange of CsAu.¹⁷ Intermediate charge (between 0 and $+1$) gold compounds exist primarily as clusters containing other metals as well as phosphorus donor ligands. They are available through the reaction of gold(I) precursors such as $[AuX(PR_3)]$ ($X = \text{halide}, SCN, NO_3$) with reducing agents such as $NaBH_4$ or CO (Equation 1.2.4).¹⁸



Introduction

Gold(II) compounds are very scarce but occur formally in dithiophene compounds and in the dicarbollyl anion $[\text{Au}(\text{B}_9\text{C}_2\text{H}_{11})_2]^{2-}$.⁷ Another legitimate gold(II) complex is that of $[\text{AuXe}_4][\text{Sb}_2\text{F}_{11}]_2$ which contains the noble gas Xenon as a ligand (although very unstable).¹⁹ Crystals of this complex had to be grown at $-78\text{ }^\circ\text{C}$.¹⁹ The highest verified oxidation state of gold is (+5), which is present in the compounds AuF_5 and AuF_6^- .⁷



The gold(I) oxidation state is by far the most developed and therefore most prominent in literature. It can accommodate numerous geometries with many different types of ligands. Gold(I) is soft (according to hard soft acid base theory (HSAB)) and therefore has an affinity towards soft donor ligands (e.g. P- and S-donor ligands) and to this end the chemistry is well developed. It is also well known that gold(I) complexes can disproportionate to Au(0) and Au(III) (Equation 1.2.5).⁶ There is a relatively small energy difference between the filled d orbitals and the unfilled s valence shell orbital of gold(I).⁷ This permits the extensive hybridisation of the d_{z^2} and s orbitals (Figure 1.2.2).⁷

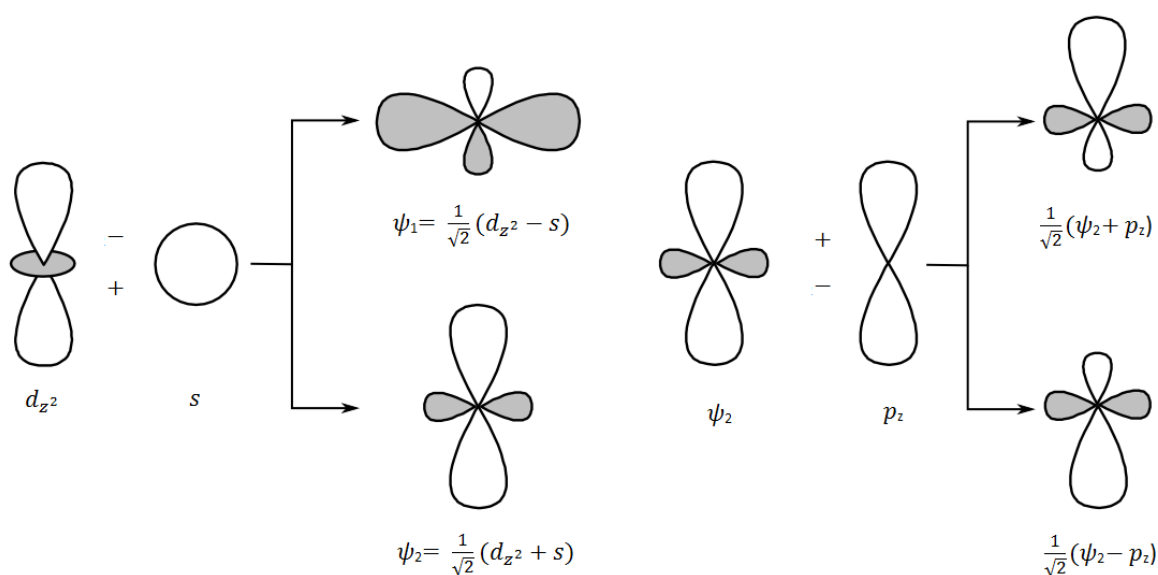


Figure 1.2.2: Hybrid orbitals formed from mixing d_{z^2} and an s orbital ψ_1 and ψ_2 and the hybrid orbitals formed from mixing ψ_2 and an p_z orbital.⁷

The electron pair initially in the d_{z^2} orbital occupies ψ_1 , giving a circular region of relatively high electron density from which ligands are somewhat repelled, and regions above and

Introduction

below the ring in which the electron density is relatively low.⁷ The ligands are attracted to the regions of lesser electron density. Two hybrid orbitals, suitable for the formation of linear covalent bonds can be formed by the further mixing of ψ_2 with the p_z orbital, hence the predominant linear geometry of gold(I) complexes.⁷

The gold(III) ion has a [Xe] $4f^{14} 5d^8$ electronic configuration and therefore adopts a square planar co-ordination geometry similar to other d^8 metals such as Pt(II), Pd(II), Rh(I) and Ir(I).²⁰ Valence Shell electron pair repulsion (VSEPR) theory tells us that the d_{z^2} orbital occupies the two axial co-ordination sites in the VSEPR view and therefore the four ligands accommodate the equatorial plane (Figure 1.2.3).²⁰ Due to the removal of ligands in the z direction, orbitals containing a z component are lowered in energy, specifically d_{z^2} , while the energies of the $d_{x^2-y^2}$ and d_{xy} orbitals are raised. Almost all square planar d^8 metals are diamagnetic since the highest energy orbital ($d_{x^2-y^2}$) is greatly destabilised and spin pairing in the d_{xy} orbital is more favourable than placing an unpaired spin in the ($d_{x^2-y^2}$) orbital.²⁰

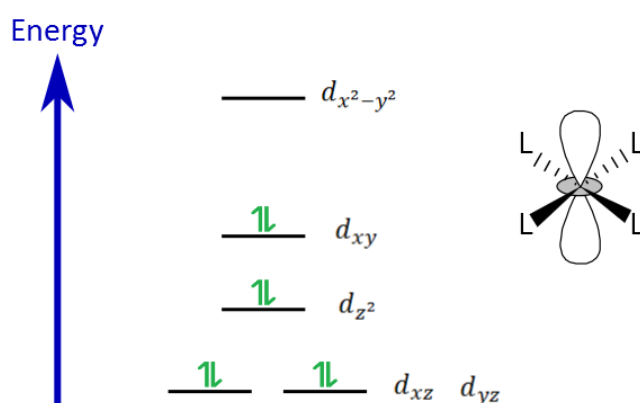


Figure 1.2.3: VSEPR view of d^8 square planar metal complexes showing the expected low spin configuration.

The above stated low spin square planar d^8 configuration is the ideal geometry when designing potential metallo-drugs to target DNA as the complex is flat and hence can intercalate DNA efficiently. There are, however some rare examples of gold(III) complexes that do not adhere to the predicted geometry (Figure 1.2.4).^{21, 22}

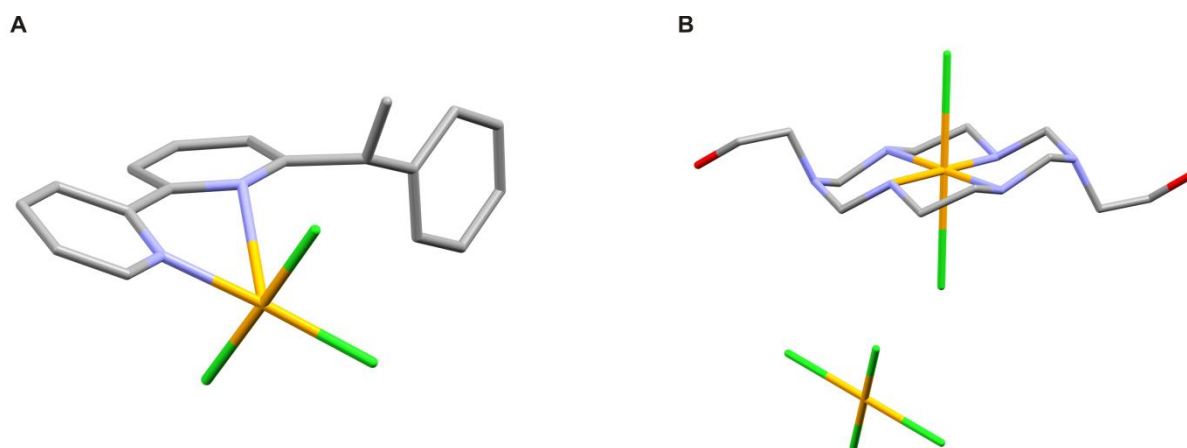
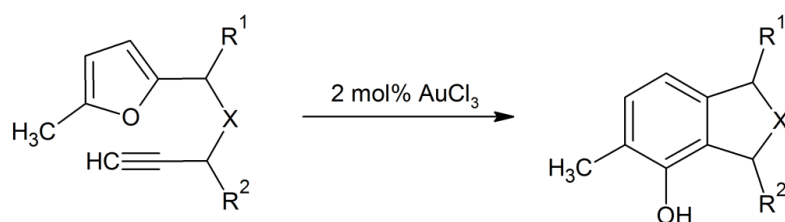


Figure 1.2.4: Molecular structures of a five co-ordinate gold(III) complex, $[\text{Au}\{\text{N}_2\text{C}_{10}\text{H}_7(\text{CHMePh})\text{-6}\}\text{C1}_3]$, (A) and a six co-ordinate gold(III) complex, $[\text{Au}(\text{L})\text{Cl}_2]\text{AuCl}_4$ (where $\text{L} = 1,8\text{-bis}(\text{hydroxyethyl})\text{-}1,3,6,8,10,13\text{-hexaazacyclotetradecane}$) (B). The compounds are redrawn from the CSD co-ordinates RADLAJ and TEMMED respectively and rendered as sticks.^{21,22}

1.3 Gold(III) complexes and their general applications

The focus of this project is gold(III) complexes and their biological activity. That said, there are other applications of gold(III) chelates with two key focus areas, specifically that of catalysis and luminescence. The amount of literature on gold(III) and catalysis is quite sparse in relation to other metals and still has some wide scope in terms of its development.^{23,24} It is not the focus of this research and therefore we will choose some selected examples to discuss.



	X	R ¹	R ²	Yield (%)
a	CH ₂	H	H	65
b	O	H	H	69
g	C(CO ₂ Me ₂) ₂	H	H	88
h	N(Ts)CH ₂	H	H	81 ^a

^a 6 mol% AuCl₃

Figure 1.3.1: Reaction scheme and percentage yields for some Au³⁺-catalysed cyclizations. Redrawn from reference 24.²⁵

Introduction

The most common gold catalysts are the simple gold(III) compounds AuCl_3 ²⁵⁻²⁷ and $\text{H}[\text{AuCl}_4]$ ²⁸, although there have been reports on some gold(III) complexes and their catalytic activity towards the 'synthesis of propargylamines via a three-component coupling reaction of aldehydes, amines and alkynes'²³ and the 'synthesis of azepines by a gold-catalyzed intermolecular [4 + 3]-annulation'.²⁸ An example of AuCl_3 being used as a catalyst was reported by Hashmi *et al.* in 2000, where the use of AuCl_3 as a catalyst in the synthesis of arenes was described (Figure 1.3.1).²⁵ From Figure 1.3.1 it can be seen that for the derivatives tested, the percentage yields were very good, most in the 80-90% range. The only pitfall of this reaction is that the catalyst eventually suffers deactivation.²⁵ They therefore suggest that modification of the catalyst from a simple gold salt to a complex may prevent this as well as enhance the catalytic activity.²⁵ An example where this has been put to good use is in a previously mentioned paper by Lo *et al.* in 2009. They attempted the synthesis of propargylamines using four documented gold(III) complexes $\text{Au}[\text{TPP}]^+$, $[\text{Au}(\text{C}^{\wedge}\text{N}^{\wedge}\text{C})\text{Cl}]$, $[\text{Au}(\text{sal}_2\text{pn})]\text{Cl}$ and $[\text{Au}(\text{C}^{\wedge}\text{N})\text{Cl}_2]$ (Figure 1.3.2).²³

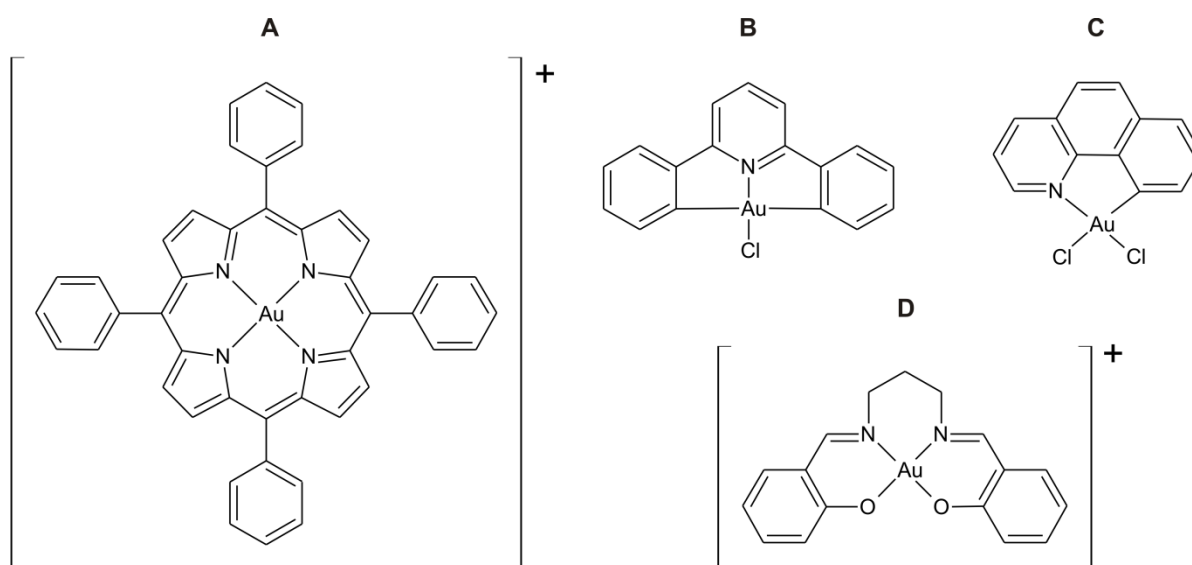


Figure 1.3.2: Chemical structures of $\text{Au}[\text{TPP}]^+$ (A), $[\text{Au}(\text{C}^{\wedge}\text{N}^{\wedge}\text{C})\text{Cl}]$ (B), $[\text{Au}(\text{sal}_2\text{pn})]\text{Cl}$ (C) and $[\text{Au}(\text{C}^{\wedge}\text{N})\text{Cl}_2]$ (D) used in the catalytic synthesis of propargylamines.²³

All four catalysts were tested for their catalytic activity according to the reaction scheme in Figure 1.3.3. Both $[\text{Au}(\text{sal}_2\text{pn})]\text{Cl}$ and $[\text{Au}(\text{C}^{\wedge}\text{N})\text{Cl}_2]$ showed good catalytic activity with yields of 94 and 82%, respectively. Compounds $\text{Au}[\text{TPP}]^+$ and $[\text{Au}(\text{C}^{\wedge}\text{N}^{\wedge}\text{C})\text{Cl}]$ however did not prove fruitful in their catalytic activity with yields in both cases not detectable.²³ The paper

Introduction

goes on to use $[\text{Au}(\text{C}^{\wedge}\text{N})\text{Cl}_2]$ in a variety of experiments using different starting materials in the synthesis of propargylamines in good yields of up to 99 % by NMR.²³

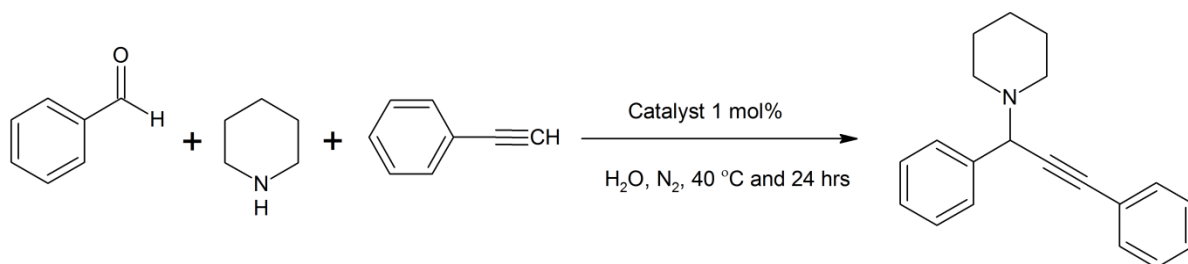


Figure 1.3.3: Reaction scheme used in the synthesis of propargylamines. Redrawn from ref 22.²³

The traditional field of phosphorescence and luminescence of gold complexes is dominated by gold(I).²⁹ Only recently has there been an interest gold(III) complexes and their phosphorescence and luminescence.³⁰⁻³³ In 2005, Wong *et al.* published a communication and soon after a patent regarding a series of gold(III) alkynyl-based organic light-emitting devices (Figure 1.3.4).^{32, 33} They found that their novel class of luminescent cyclometalated gold(III) alkynyl complexes was shown to possess electro-luminescent (EL) properties and was employed in the roles of electrophosphorescent emitters or dopants of organic light emitting diodes (OLEDs) with high brightness and efficiency. They showed that the colour of the EL was capable of being tuned from orange to blue by varying the DC voltage applied or varying the dopant concentration.³²

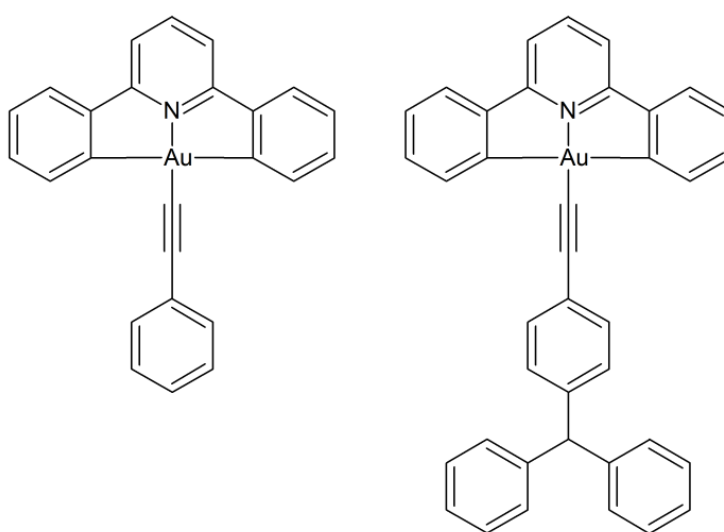


Figure 1.3.4: Chemical structures of gold(III) alkynyl-based organic light-emitting devices.³²

Introduction

Che and co-workers have recently reported an organogold(III) complex (Figure 1.3.5 (B)) and its diverse use.³⁴ In his communication it is reported that the complex exhibits a long-lived emission lifetime of 506 μs .³⁴ The emission was however seen to be oxygen sensitive and was tested as an oxygen sensor for living cells. When cell media was flushed with nitrogen and incubated with the organogold(III) complex, the cells became yellowish green upon illumination under a fluorescent microscope.³⁴ Due to the complex's high emission quantum yields and long lived excited states, the compound was deemed a good candidate for testing as a catalyst in photochemical reactions.³⁴ It was tested with two oxidation type reactions that have important application in organic synthesis: the α -substitution of tertiary amines and the oxidation of secondary amines to imines (Figure 1.3.5 D and E).³⁴ The complex performed extremely well in both cases with near 100% conversion rates and high yields.³⁴ The complex was then finally successfully tested as a catalyst in the generation of hydrogen from water (Figure 1.3.5 C). This paper therefore identifies the richness and diversity of organogold(III) chemistry.³⁴

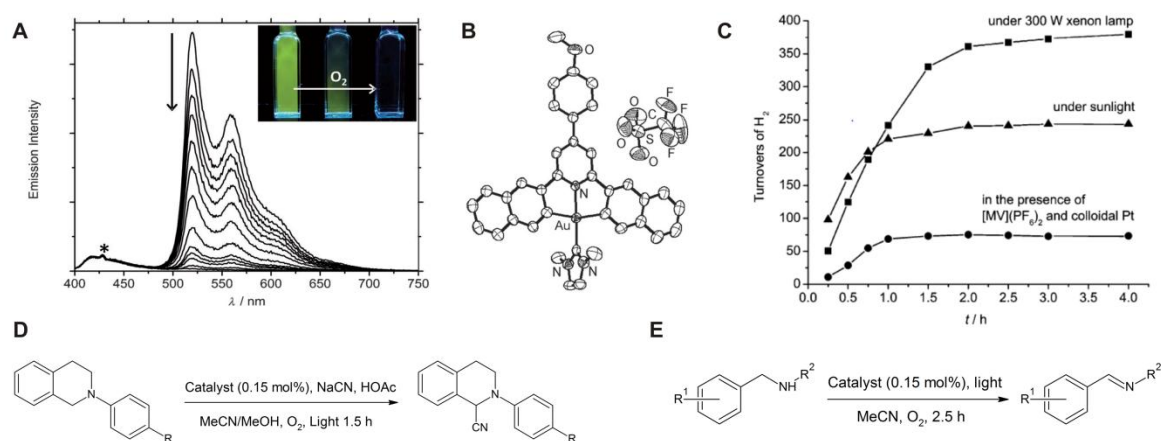


Figure 1.3.5: Oxygen sensitive Emission of Che's organogold(III) complex (A). Ortep view of the complex in question (B). Hydrogen production properties of the complex under different reaction conditions (C). Reaction scheme showing the oxidative cyanation of tertiary amines (D). Reaction scheme showing the oxidation of secondary amines by the complex (E). Adapted from reference 33.³⁴

Introduction

1.4 Cancer and its treatment

1.4.1 Background and history

The human body contains roughly 10 trillion cells (10^{13}).³⁵ These cells are subdivided into groups and classes to form the various tissues and organs that are programmed to perform various functions within the body.³⁵ Some cells, such as nerve cells, are believed to be incapable of further division once they have been formed during the development of the embryo or in infancy.³⁵ Other cells such as liver cells seldom divide during our lifetime but are able to do so if required.³⁵ Furthermore, cells constituting the gut, skin or bone marrow, for example, are constantly dividing to replace those that are destroyed.³⁵ Obviously, in tissues where cells multiply constantly, the total amount of cells must remain constant i.e. cell production must be equal to cell death.^{35, 36} Programmed cell production and cell death must therefore be under strict control.³⁶

In such a system where the throughput of cells is so large, it is expected that there may be Darwinian Selection and that the occasional cell may exhibit increased fitness in so far as it may be able to multiply faster than normal cells or can displace their neighbours whenever space is limited.³⁵ This is the basis of 'cancer'. When cells divide without the usual cellular restraints, but keep to their normal territory and do not invade surrounding tissues they form tumours that are labelled 'benign'.³⁵⁻³⁷ If these rapidly dividing cells acquire the ability to spread to surrounding tissue the tumour is then labelled 'malignant'.^{35, 36} Cancer can therefore be described as the uncontrolled division of a single group of abnormal cells which leads to the accumulation of a solid mass of cells, known as a tumour or neoplasm.³⁶

The initial tumour that develops generally only becomes life-threatening if it obstructs vessels or organs and impairs their function and/or irreversibly damages them.³⁵ The primary cause of death in most cancer patients is due to secondary tumours.³⁵⁻³⁷ These secondary tumours arise from a process called metastasis.^{35, 36} Metastasis is the process whereby cancerous cells from the primary tumour spread to other parts of the body, namely vital organs, giving rise to secondary tumours.^{35, 36} The most common ways in which cancerous cells are able to metastasise are through the penetration of lymphatic vessel walls as well as through blood vessels, since capillary walls are very thin.³⁶ Once cancerous cells have metastasised into the lymph and capillary networks it is very dangerous for the

Introduction

patient as these networks are extensively distributed throughout the body and allow the formation of secondary tumours in areas far removed from the primary tumour.³⁶ Once a primary tumour has metastasised (typically 50% of cancer patients) the use of curative surgery or radiotherapy is forgone and chemotherapy is usually proposed.³⁶

Tumorigenesis is the multistep process associated with the genetic transformation of healthy cells to cancerous cells. It is suggested that there are six modifications to cells which may lead to malignancy:³⁶

- Self-sufficiency in growth signals
- Insensitivity to growth-inhibitory signals
- Evasion of programmed cell death (apoptosis)
- Limitless replicative potential
- Sustained angiogenesis
- Tissue invasion and metastasis

It has been proposed that the need for a cell to acquire all of these traits prior to completing transformation is the reason why tumour cell formation is relatively rare during the average human lifespan.³⁶

It is generally accepted that cancer in general is a genetic disease resulting from changes to DNA sequence information in one or more genes, or from more profound structural changes.^{36, 38} These changes can arise from numerous processes, such as internal, external and hereditary.³⁶ Internal factors include genetic mutations, addition or loss of genetic material, epigenetic changes and modified gene expression.^{36, 38, 39} Genetic mutations arise in the form of point and translocation mutations.^{36, 38, 39} In a point mutation, only one nucleotide base is altered, and the resulting new codon can lead to the insertion of an incorrect amino acid at the corresponding position of the protein.^{36, 38, 39} If this protein is a regulatory protein i.e. a tumour suppressor protein, then tumorigenesis may occur. In a translocation mutation, an entire segment of DNA is moved from one part of the gene or chromosome to another.^{36, 38, 39} In this case, loss of the protein associated with the original DNA sequence or the production of a new protein may lead to tumorigenesis. The original genes involved in this process are called pro-oncogenes, meaning genes that do not cause cancer themselves unless suitably activated to form what is called an oncogene.^{36, 38, 39} This

Introduction

concept has been validated in certain types of cancer such as Burkitt's lymphoma, in which the precise sequences involved in the translocation have been identified.³⁶

External factors include viruses, bacterial infections, chemicals, radioactivity and electromagnetic radiation.³⁶ Certain chemicals in the environment, encountered through diet, lifestyle and occupation can lead to tumorigenesis.³⁶ For example the link between lung cancer and cigarette smoke is well established as too is the link between alcohol and head and neck cancer.³⁷ The production of polycyclic aromatic hydrocarbons, formed when frying or barbequing red meat, have also been associated with colon tumours.³⁶ Potent carcinogens known as aflatoxins (Figure 1.4.1.1), found in low concentrations in peanut butter, are formed as secondary metabolites by a fungus that can infect peanuts during growth.³⁶

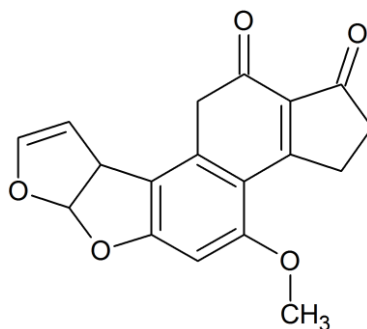


Figure 1.4.1.1 Chemical structure of Aflatoxin.

There are numerous chemicals that workers can be exposed to through occupation that have been directly linked with cancer. One of the most infamous examples of such a chemical is asbestos. Asbestos was commonly used, post-World War 2, in the construction industry. The continuous inhalation of asbestos over time causes physical damage to the pleura in the lungs which, in turn, can cause the development of mesothelioma.³⁶

The third type of alteration is a hereditary one where the inheritance of certain genes can predispose one to certain types of cancer.^{36, 38} An example is the inheritance of two genes (BRCA1 and BRCA2), which have been identified and sequenced in being associated with breast cancer.^{36, 38}

There are several ways in which cancer can be treated, namely surgery, radiotherapy, photodynamic therapy, biological response modifying agents and chemotherapy. The

Introduction

former methods can generally only be used when the tumour is small and/or reasonably well defined and, in the case of photodynamic therapy, close to the tissue surface. Surgery is also a very invasive technique that is very traumatic for the patient and in some cases can cause the 'seeding' of secondary tumours due to suppressed bodily function. In almost all cases chemotherapy is used as the exclusive treatment or in conjunction with the other mentioned treatments.

1.4.2 Chemotherapy and its use in the treatment of cancer

Cancer is one of the most serious health problems of the western world; however there has been significant progress and development of novel drugs and drug targets since the accidental discovery of the nitrogen mustards and cisplatin.^{36, 40, 41} There are certain forms of cancer that have a high success rate in being cured if detected early. Overall chemotherapy is the most diverse and widely used form of cancer treatment (Table 1.4.2.1).^{36, 37} One advantage of chemotherapy is that the low molecular weight drugs are administered intravenously and are able to distribute throughout most tissues in the body and therefore are able to kill tumour cells in protected areas such as the brain.³⁶ The problem however, is in the non-specificity of most chemotherapeutic agents and acquired resistance. Because of this, chemotherapy also targets healthy living cells that are rapidly dividing such as bone marrow, hair and nails, leading to the five common side effects of nausea, hair loss, gastric tract lesions and marrow suppression.³⁶ These side effects are usually temporary and only last up to a couple of weeks after treatment has been discontinued. There are several different classes of chemotherapeutic agents, some of which are described in the table below.

Table 1.4.2.1: Summary of some different classes of chemotherapeutic agents

Drug Type	Example	Mode of action
Anti-metabolites	5-Fluoro Uracil	Inhibit pyrimidine synthesis
DNA-Interactive Agents	Topotecan	Topoisomerase I inhibitor
Anti-tubulin Agents	Vinblastine	Inhibits tubulin formation
Molecularly Targeted Agents	Erlotinib	EGFR inhibitor
Hormonal Therapies	Tamoxifen	Non-steroidal oestrogen antagonist

Introduction

TOPOISOMERASE ENZYMES: THEIR FUNCTION AND INHIBITION/POISONING BY CHEMOTHERAPEUTICS:

The gold(III) amide complexes in this work have been synthesised and designed to effect their cytotoxicity through DNA intercalation. This is because they contain planar regions of extended aromaticity that are able to intercalate between base pairs of double stranded DNA. Since the biological target of the complexes is DNA it seems logical that the complexes may exhibit their cytotoxicity by inhibiting enzymes that maintain the structure and function of DNA. One such class of enzymes are the topoisomerases which have two distinct forms. The first is topoisomerase I, which relaxes supercoiled DNA, and the second is topoisomerase II, which is a decatenase.⁴²

Nuclear DNA is an extremely long polymer. A single mammalian genome corresponds to approximately 2 metres of linearised DNA, which is squeezed into a cell nuclear volume of approximately 10^{-17} m^3 .⁴³ Cellular DNA must therefore be highly compacted, which creates many curved DNA domains (loops) and points of contact between these DNA domains.⁴³ Moreover, DNA metabolism requires the two strands of the duplex to be separated for them to serve as templates for transcription, replication, recombination and repair.⁴³ DNA tends to be overwound (positively supercoiled) upstream of replication or transcription forks and underwound (negatively supercoiled) downstream of these forks.⁴³ Removing positive supercoils is required for replication and transcription progression. Otherwise, their accumulation in advance of replication and transcription complexes hinders the melting of the DNA duplex (by helicases) and consequently polymerase translocation along the DNA template.⁴⁴ The function of the topoisomerase's is therefore to maintain DNA integrity by relieving the strain caused by winding and unwinding during the replication process.^{42, 44-46} The two main Eukaryotic topoisomerases are topoisomerase IB (topo IB) and topoisomerase II α (topo II α).^{42, 45}

TOPOISOMERASE I:

topo IB performs its function by first forming a 'clamp' around the DNA.⁴⁶ The active site tyrosine then performs a nucleophilic attack on a DNA phosphodiester bond.^{44, 46} The bond is cleaved and the enzyme forms a transient DNA-(3'-phosphotyrosyl)-enzyme 'covalent complex' and a free 5'-OH DNA end.^{43, 44, 46} It is interesting to note that only topo I enzymes

Introduction

form a covalent cleavage complex with the 3'-end of the broken DNA.⁴⁴ The remaining topoisomerase forms a bond to the 5'-end (Figure 1.4.2.1).⁴⁴ This specific characteristic classifies the eukaryotic topoisomerase I enzymes into the broader family of site-specific tyrosine recombinases of prokaryotes and yeast.⁴⁴

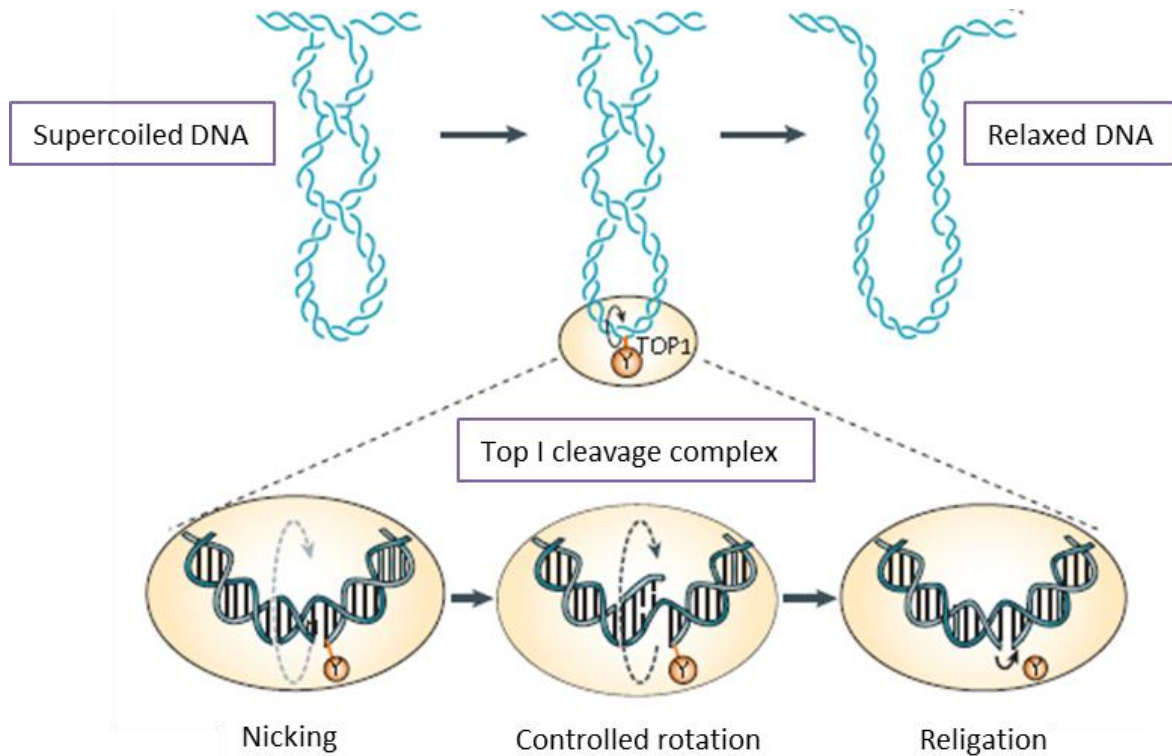


Figure 1.4.2.1: Diagram showing the relaxation of the DNA supercoiled structure by topoisomerase I and the trapping of the cleavage complex by a drug. Adapted from reference 42.⁴³

Once the DNA–(3'-phosphotyrosyl)-enzyme 'covalent complex' is formed it allows the torsional energy within the DNA supercoil to be released by rotation of the free 5'-OH end.^{43,44,46} Following the removal of a number of random supercoils the free 5'-OH end is then religated to the backbone of the DNA and the enzyme is free to repeat the process.⁴⁶ This process does not require ATP or divalent metal binding (e.g. Mg^{2+}), which is the case for topoisomerase II.⁴⁴ The remarkable efficiency of the nicking-closing activity of Topoisomerase I enables the enzyme to relax both negatively and positively supercoiled DNA (even at 0 °C) with similar efficiency.⁴⁴ This is in contrast to topoisomerase II α , which more efficiently relaxes positive supercoiling.⁴⁴ This process can, however, be disrupted when the 5'-OH end, generated by the nicking reaction, becomes misaligned.⁴⁴ In such a case the cleavage complex becomes without an effective religation partner.⁴⁴ These covalent complexes are known as "suicide

Introduction

complexes".⁴⁴ Nevertheless, topo I can relegate an illegitimate 5'-OH end, effectively acting as a recombinase.⁴⁴

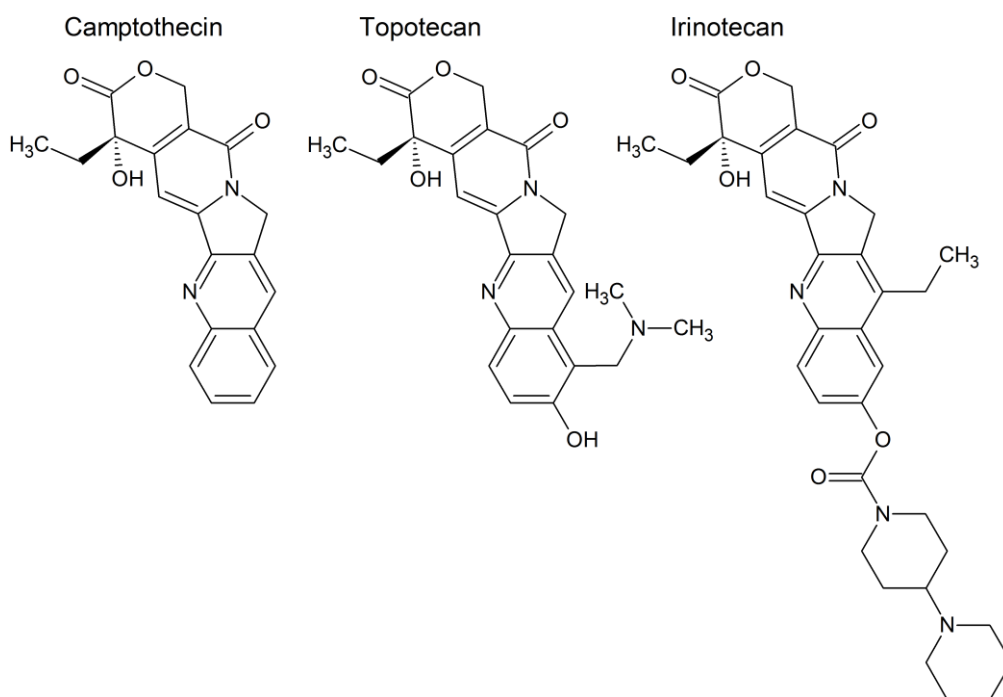


Figure 1.4.2.2: Chemical structures of quinolone alkaloid based topo I poisons.

By inhibiting the function of this enzyme the integrity of the DNA structure and function may be compromised as the cell would not be able to replicate and hence cease to exist. topo I is therefore a validated target for chemotherapy and there is a significant amount of research in the discovery of topo I inhibitors and their mechanisms of action.⁴²⁻⁵⁰ Currently in clinical use there are several drugs based on the natural product camptothecin (Figure 1.4.2.2), which is a quinolone-based alkaloid that is extracted from the bark of the Chinese *camptotheca* tree.³⁶ The drug, topotecan, is effective against metastatic ovarian cancer³⁶ and effects its inhibition of topo I by intercalating into the nick generated by topo IB on the DNA, forming a ternary topo IB-DNA-drug complex that traps the enzyme on the DNA.⁵⁰ This irreversible ternary complex is converted into cytotoxic DNA lesions that cause cell death.^{46, 50} This binding mode has been studied by X-ray crystallography through the structure of a 70-kDa form of topo I (topo 70) covalently bound to DNA in the presence of topotecan (Figure 1.4.2.3).⁵⁰ The ternary structure shows the drug intercalated at the site of the DNA cleavage and its stabilisation via stacking interactions with base-pairs above and below itself.⁵⁰ The planar ring system of topotecan mimics a DNA base-pair and occupies the same

Introduction

area that the base-pair above it would without the drug bound.⁵⁰ The intercalation binding site is created by conformational changes of the phosphodiester bond between the base pairs above and below the uncleaved strand, which effectively “opens” the DNA duplex.⁵⁰ Positioning of the phosphodiester in the ternary complex is stabilised through hydrogen bond contacts to the main chain nitrogens of residues Arg-362 and Gly-363.⁵⁰

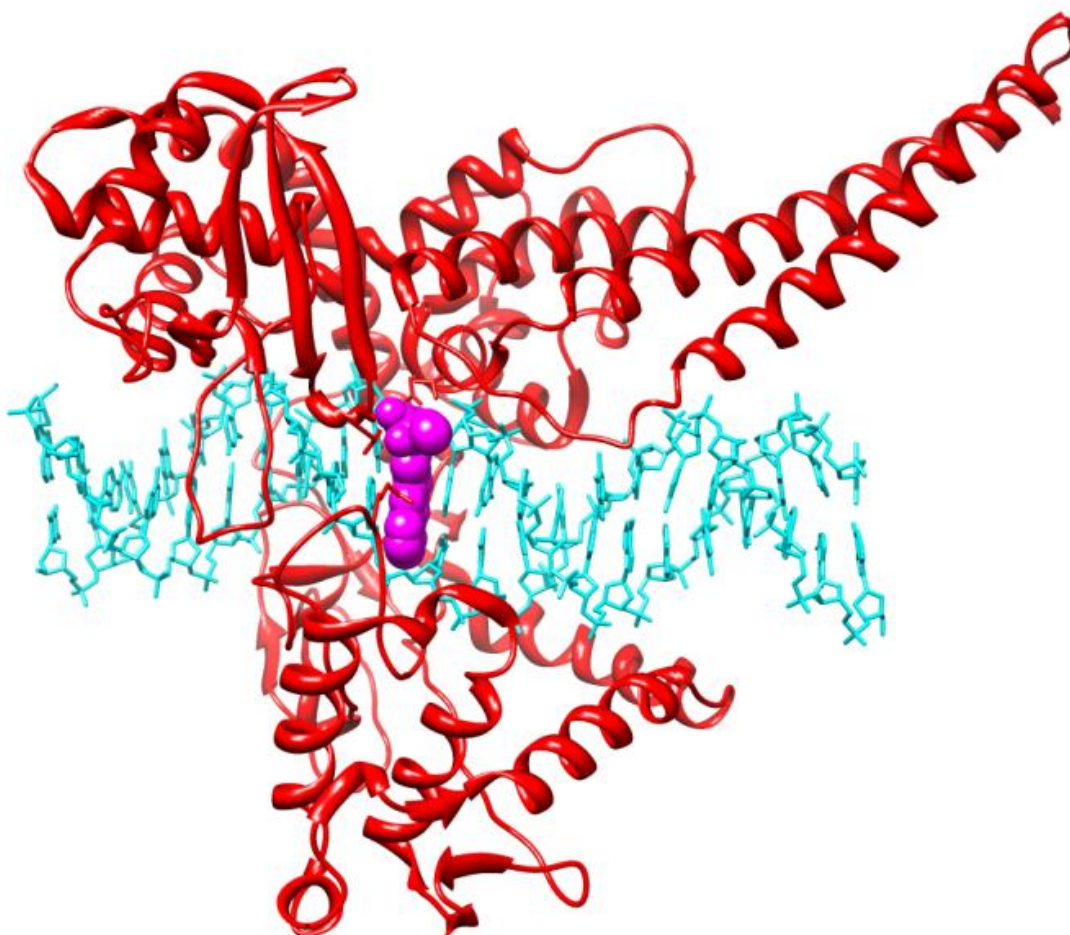


Figure 1.4.2.3: Crystal structure of topo I-DNA-drug complex redrawn from the coordinates in PDB1T8I. The topo I enzyme has been coloured in red, the DNA in blue and the drug, topotecan, has been rendered as pink spheres.⁵⁰ Molecular graphics generated with the UCSF Chimera package.⁵¹

TOPOISOMERASE II:

The mechanism for topo II is much more complicated than for topo I (Figure 1.4.2.4). It requires the use of divalent metal ions as well as ATP to perform its function. The reaction cycle for type IIA topoisomerases is believed to use a ‘two-gate’ mechanism for strand passage.⁵²⁻⁵⁴ The enzyme introduces a double strand break in one DNA strand, termed the G

Introduction

or gate segment, and will pass a second strand termed the T segment through the break.⁵⁵ In the presence of Mg^{2+} , the enzyme can cleave the DNA, forming a phosphotyrosine linkage between each single strand and a tyrosine in each subunit.⁵⁵ ATP binding causes the enzyme to form a closed clamp. The closed clamp may also capture another strand (the T strand) that will pass through the break made in the G strand.⁵⁵ After passing through the break in the G strand, the T strand exits the enzyme through the carboxy end.⁵⁵ ATP hydrolysis occurs at two steps in the reaction cycle. The first ATP hydrolysed may assist in strand passage.⁵⁵

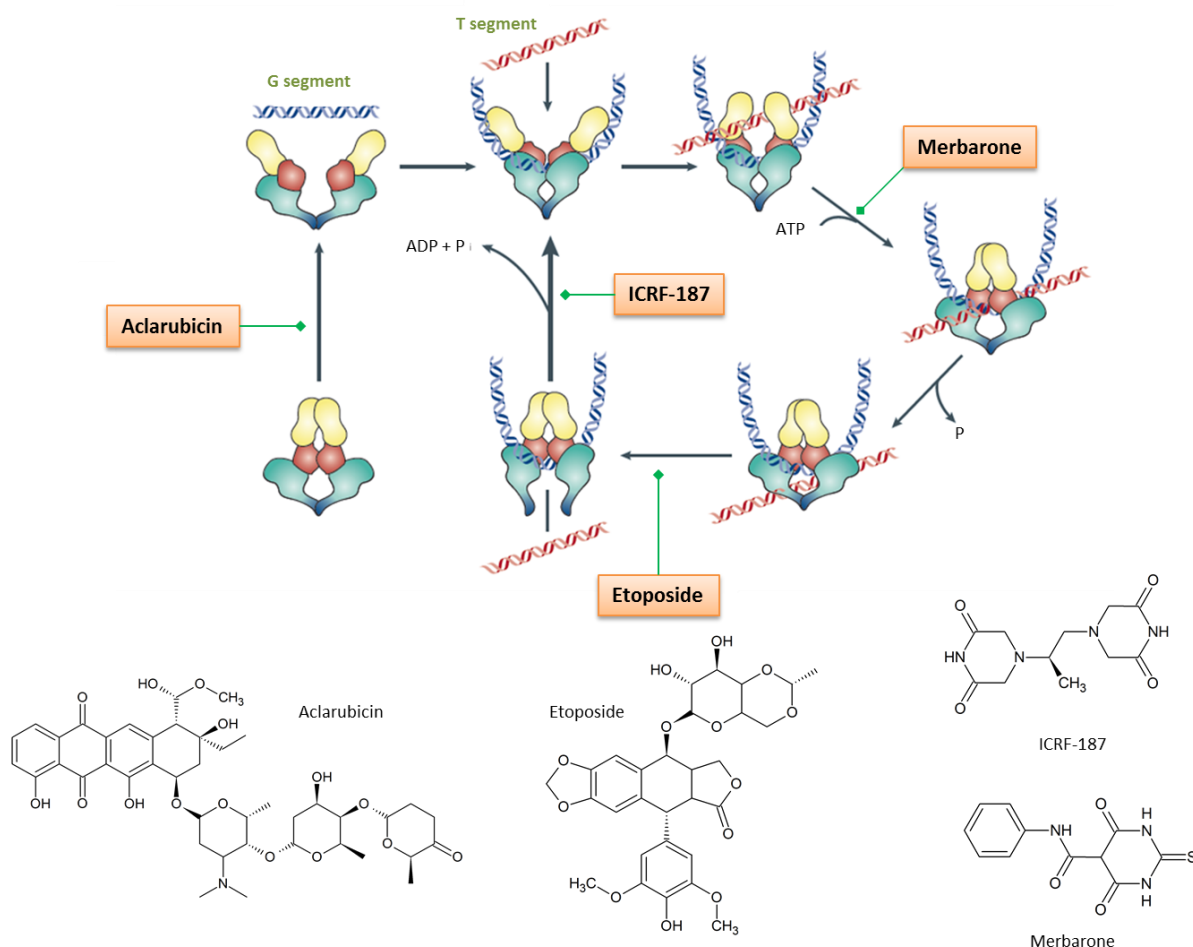


Figure 1.4.2.4: Schematic diagram showing the mechanism through which topoisomerase II exhibits its function and the critical points in its function where inhibitors with well-studied mechanisms of action arrest or inhibit the catalytic cycle. Etoposide is a poison; ICRF-187, merbarone, and aclarubicin are catalytic inhibitors that operate in mechanistically distinct ways. Adapted from reference's 53 and 54.^{54,55}

The second hydrolysis step (along with release of ADP and inorganic phosphate (P)) allows the clamp to reopen, and allows release of the G segment.⁵⁵ Alternately, the enzyme may

Introduction

initiate another catalytic cycle without dissociating from the G strand.⁵⁵ Since the structure and the function of the enzyme is more complicated than for topo I, it is intuitive that there may be several points in the enzyme's catalytic cycle that can be used to inhibit or poison the enzyme from performing its function, and so is the case. One simple mode of inhibition is to inhibit a step early in the enzyme reaction cycle.⁵⁴ For example, competitive inhibitors of ATP binding prevent strand passage and do not generate enzyme-mediated DNA damage.⁵⁴ Similar effects would occur with inhibitors that prevent the binding of topo II to DNA such as aclarubicin.⁵⁴ Agents that prevent DNA cleavage by topo II such as merbarone would also be expected to act as simple catalytic inhibitors.⁵⁴ Although merbarone clearly prevents DNA cleavage by topo II, merbarone affects other targets besides topo II.⁵⁴ A second mode of inhibition is blocking the catalytic cycle after DNA is cleaved but before DNA re-ligation.⁵⁴ This mode of inhibition occurs for most currently used topo II targeting agents, including anthracyclines and epipodophyllotoxins, as well as for agents that target prokaryotic type II topoisomerases.⁵⁴ These agents prevent enzyme turnover and are therefore poisons of catalytic activity. The most obvious effect of topo II poisons is the generation of high levels of topo II–DNA covalent complexes.⁵⁴ Therefore, poisons generate DNA damage and interfere with many DNA metabolic events such as transcription and replication.⁵⁴ Topo II can be inhibited after strand passage is completed but before ATP hydrolysis and dissociation of amino-terminal dimerization.⁵⁴ Bisdioxopiperazines such as dexrazoxane (ICRF-187) inhibit both ATP hydrolysis and maintain the topo II structure as a closed clamp.⁵⁴ As is the case with topo II poisons, bisdioxopiperazines inhibit topo II catalytic activity mainly by blocking enzyme turnover.⁵⁴ Although these agents are frequently termed catalytic inhibitors, they leave topo II trapped on DNA and might interfere with DNA metabolism in a manner that may be analogous to topo II poisons.⁵⁴ Wu and co-workers have recently reported a high-resolution DNA-topo-etoposide complex that gives significant insight into how the drug performs its function. It is conclusive proof that the drug blocks the catalytic cycle after DNA is cleaved but before re-ligation. The etoposide molecules in the resolved structure were bound between base pairs, immediately flanking the two cleaved scissile phosphates, with the drug's polycyclic aglycone core (rings A to D) sitting between base pairs, and the glycosidic group and the E ring protruding toward the DNA major and minor grooves, respectively.⁵⁶ The insertion of etoposide removes the stacking interaction between base pairs.⁵⁶ The 3'-OH of the neighbouring nucleotide is held

Introduction

~8 Å away from the enzyme-linked scissile phosphate, which effectively blocks relegation of the cleaved phosphodiester bond.⁵⁶ Due to structurally mitigating factors beyond the scope of this work, it suffices to say that two etoposide molecules are needed to stabilise a double-stranded DNA break (Figure 1.4.2.5).⁵⁶

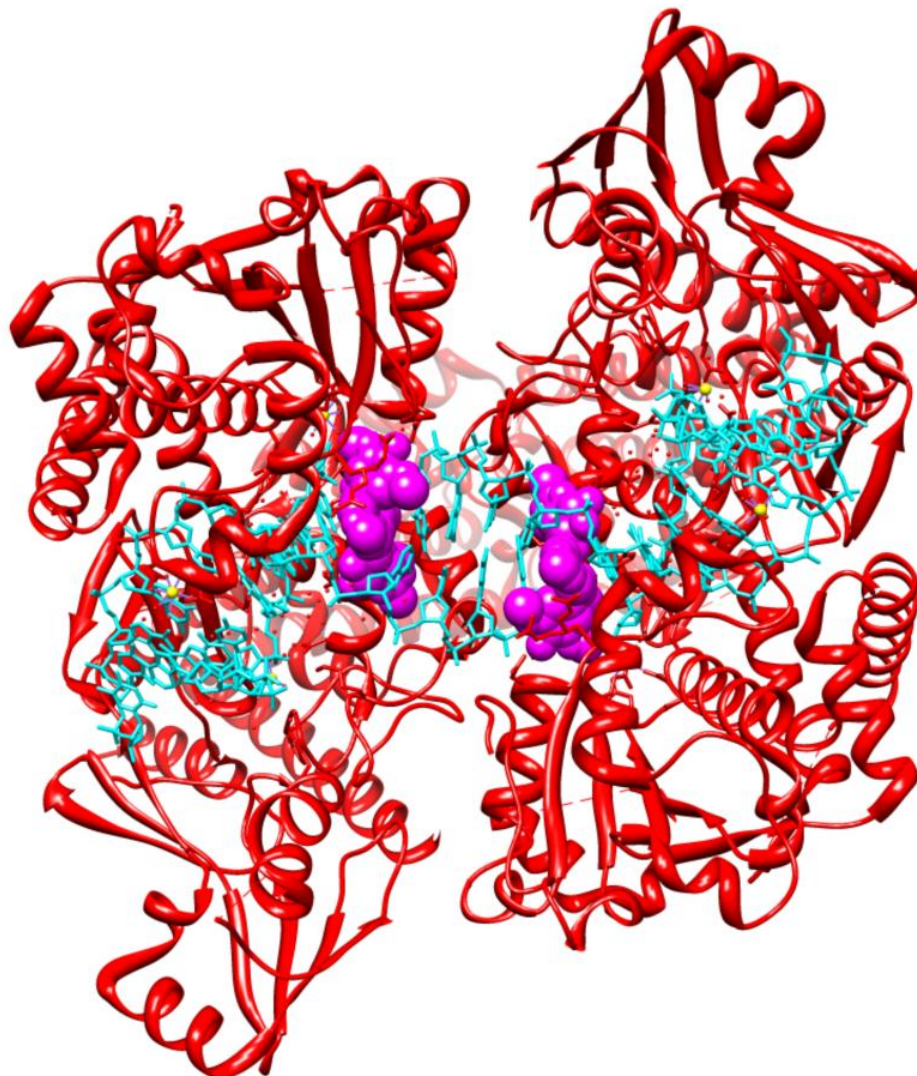


Figure 1.4.2.5: Crystal structure of topo II-DNA-drug complex redrawn from the coordinates in PDB 3QX3. The topo II enzyme has been coloured in red, the DNA in blue and the drug, topotecan, has been rendered as pink spheres. Reproduced from reference 54.⁵⁶ Molecular graphics generated with the UCSF Chimera package.⁵¹

1.5 Drug-DNA interactions

Since the elucidation of the three dimensional structure of DNA there has been a concerted effort in synthesis of small molecules that recognise and interact with it. Initially the field was dominated by the synthesis of organic small molecules. More recently, there has been significant interest in and development of, the synthesis of transition metal complexes that can recognise/target DNA. Since DNA is the blueprint for life, it stands to reason that by designing small molecules that interact with it, we may be able to gain access to and control the way it behaves. Once a small molecule binds to DNA it invariably leads to distortion of the double helix structure and the inhibition of cell replication through many different established mechanisms. Hence, these small molecules are used in the fight against cancer, where they prevent cell division in tumours. The ternary structure of DNA is quite complex with multiple localised regions that small molecules may interact with. There are also several other more complex DNA structures that arise during certain cell cycles, lending themselves as possible targets for DNA-drug interactions. The four main DNA-drug interactions that will be discussed further are:

- DNA intercalation and insertion
- DNA groove binding
- DNA three-way junction binders
- DNA cross linkers

1.5.1 DNA intercalation and insertion

Some of the most successful chemotherapeutics on the market today effect their action through DNA intercalation. Some examples of such drugs are the anthracyclines and quinolone alkaloids.^{49, 57, 58} In context with the work in this thesis, the focus will be centred on metal complexes. The most common form of DNA is the anti-parallel, right-handed double helix termed B-DNA. The structure is essentially two complementary linear fragments of DNA that assemble via hydrogen-bonding between nucleobases, A with T and C with G, to form a double helical structure. There is a 3.4 Å rise per base while there are ten base pairs per helical turn. The base pairs collectively form a central, hydrogen-bonded π -stack that runs parallel to the helical axis between the two strands of the sugar-phosphate backbone. Within the 3D helical structure of DNA there are two distinct grooves, a wide

Introduction

major groove and a narrow minor groove. All of these structural characteristics can and have been exploited for molecular recognition. The target of intercalator-based small molecules and metal complexes is the vacant space between base pairs of DNA where they partially unwind DNA in order to insert between them (Figure 1.5.1.1 left). A major characteristic required for a DNA binding metal complex is, with few exceptions, that they must be kinetically inert, a requisite trait due to the paramount importance of stability.⁵⁹ Most of the complexes are d^6 octahedral or d^8 square-planar. In addition, most exhibit a rigid or mostly rigid three-dimensional structure and most contain planar aromatic fused ring systems able to π -stack with the DNA base pairs.⁵⁹

Another type of metal complex-DNA interaction is insertion (Figure 1.5.1.1 right). There are very few examples of these types of complexes in literature. The way in which these complexes interact with DNA is remarkably specific. They recognise DNA mismatch pairs such as CC and AC that are destabilised due to imperfect hydrogen bonding and insert their

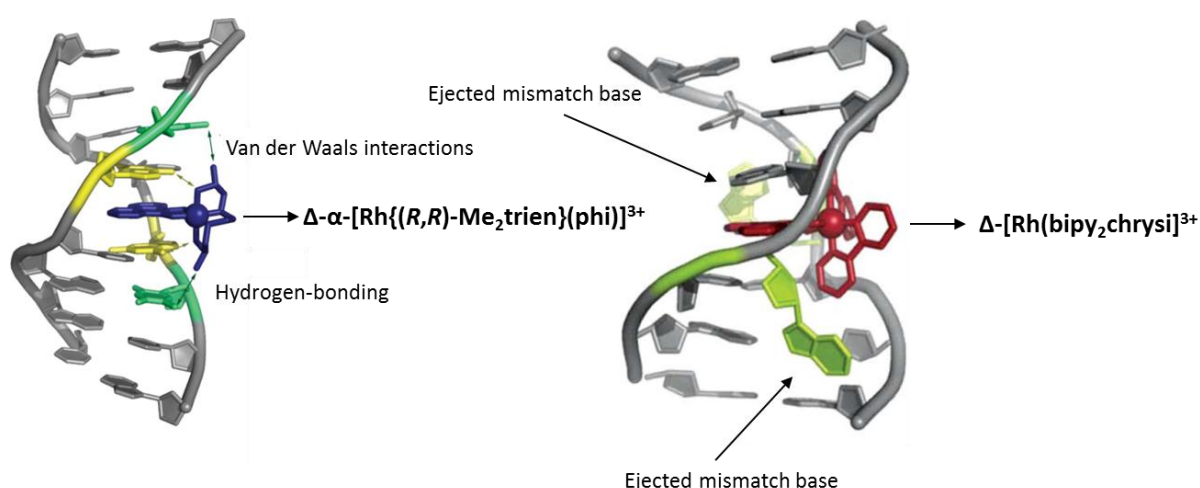


Figure 1.5.1.1: Crystal structures showing a rhodium intercalator, $\Delta\text{-}\alpha\text{-}[\text{Rh}\{(R,R)\text{-Me}_2\text{trien}\}(\text{phi})]^{3+}$ (where $(R,R)\text{-Me}_2\text{trien}$ = $2R,9R$ -diamino-4,7-diazadecane and phi = 9,10-Diaminophenanthrene), left, and a rhodium inserter $\Delta\text{-}[\text{Rh}(\text{bipy}_2\text{chrysi})]^{3+}$ (where bipy = 2,2'-bipyridine and chrysi = 5,6-chryseno quinone diimine), right, bound to DNA. Adapted from reference 58.⁵⁹

planar ligand between two intact base-pairs, ejecting the bases of a single base-pair, with their planar ligand acting as a π -stacking replacement in the DNA base stack.⁵⁹ This remarkable specificity was achieved by simply replacing the DNA-interacting ligand with ligand that is slightly wider and too bulky to intercalate in the traditional manner.⁵⁹

Introduction

1.5.2 DNA groove binding

As mentioned previously, DNA contains two structural motifs called the major and minor grooves. These motifs are the targets of a class of compounds labelled 'groove binders'. They are generally longer single-chain molecules that are flexible and contain a sickle shape. Groove binding can occur via either the major groove or the minor groove. Most DNA proteins interact via the major groove, while small molecules (<1000 Da) generally interact with the minor groove.⁶⁰ The minor groove is therefore recognised as a vulnerable site of attack for drugs since it is generally unoccupied.⁶⁰ The advantage of groove binders is that they are able to recognise and bind to sequence-specific regions of DNA depending on their structural characteristics.⁶⁰⁻⁶² The literature on groove binders is far more prevalent with organic molecules compared to that of metal complexes. Two well-known organic groove binders, Hoechst 33258 and Netropsin, are able to recognise and bind AT-rich sequences of DNA and can even compete with synthetic zinc-chelating peptides for binding sites on DNA.⁶⁰⁻⁶² An example of a metal complex groove binder is Cu(phen)₂ (where phen = phenanthroline).⁵⁹ Groove binders have been known to inhibit topo I and II as their mechanism of action in effecting cell death.^{60, 61, 63} The crystal structure of Hoechst 33342 bound to DNA via the minor groove was elucidated by Sriram and co-workers in 1992 and confirms that Hoechst 33342 binds DNA at the AATT region, as expected, and covers six base pairs (Figure 1.5.2.1).⁶³

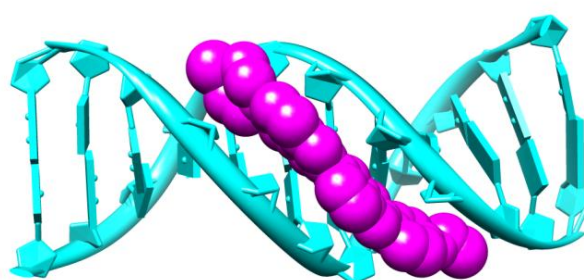


Figure 1.5.2.1: Crystal structure of Hoechst 33342 bound to DNA via the minor groove redrawn from the co-ordinates in PDB 129D. DNA is coloured blue and Hoechst 33342 is rendered as spheres and coloured pink.⁶³ Molecular graphics generated with the UCSF Chimera package.⁵¹

1.5.3 DNA three-way junction binders

DNA junctions are unique branched structures that consist of several double strands of DNA that converge at a single point. Three-way junctions occur within DNA and RNA. In DNA they are formed transiently during replication and in RNA they are involved in biological functions such as splicing and translation. Metallo-supramolecular cylinders are a class of compounds that have the remarkable ability to recognise these three-way junctions. They generally comprise a chiral assembly of three ditopic bidentate ligands around two metal centres.⁶⁴⁻⁶⁶ Initially these metallo-supramolecular cylinders were synthesised in order to mimic zinc finger proteins that recognise DNA via the major groove, and indeed they were able to bind non-covalently to the major groove of DNA.⁶⁶ It was then discovered that these metallo-supramolecular cylinders were also able to bind to the three-way junctions associated with cell replication (replication fork).⁶⁴⁻⁶⁷ Further development has shown them to have cytotoxic and anti-bacterial properties.⁶⁴⁻⁶⁷ Hannon and co-workers have been most active in this field and have reported the synthesis of iron and ruthenium supramolecular complexes that are highly cytotoxic three-way-junction binders and in particular have reported the crystal structure of an iron metallo-supramolecular cylinder bound to DNA three way junctions (Figure 1.5.3.1).⁶⁴

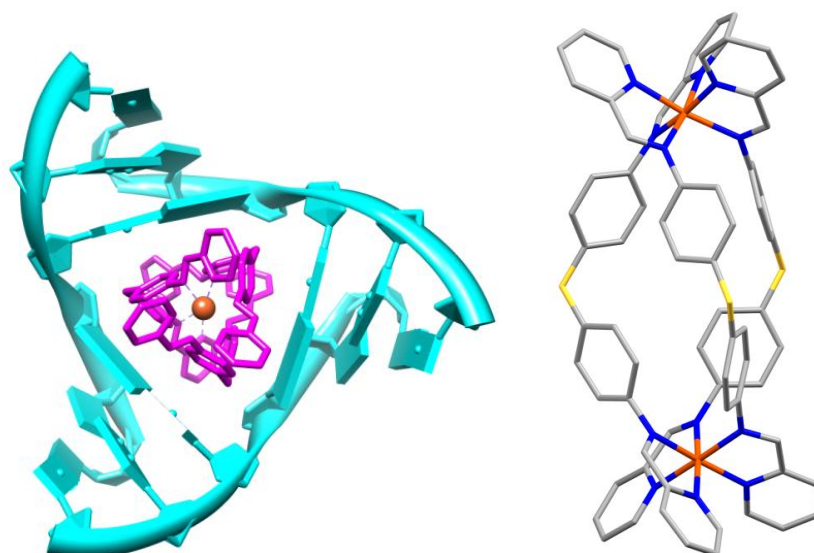


Figure 1.5.3.1: Crystal structure of an iron metallo-supramolecular cylinder (pink) non-covalently bound to a DNA three-way junction (blue), left, redrawn from the coordinates in PDB 3FX8.⁶⁴ Molecular structure of the iron metallo-supramolecular cylinder, right. Molecular graphics generated with the UCSF Chimera package.⁵¹

Introduction

1.5.4 DNA cross-linkers

The nitrogen mustards and the cisplatin group of complexes belong to this class of compounds, both of which were discovered serendipitously. There are numerous types of organic DNA cross linkers, but the focus will be on cisplatin and its analogues. Cisplatin and its ability to inhibit cell growth was discovered by Rosenberg and co-workers while passing an alternating electric current through platinum electrodes in an electric cell containing *Escherichia coli*. They observed that the cells were not multiplying but rather growing into long spindle-like shapes. This prompted the development of cisplatin into one of the most successful anti-cancer drugs still being used today. The way in which cisplatin effects its anti-cancer ability is through the formation of inter- and intrastrand crosslinks within the DNA helix. The majority of adducts formed are guanine(N7)-guanine(N7) and guanine(N7)-adenine(N7) intrastrand crosslinks. In 1996 Lippard and co-workers elucidated a high resolution crystal structure of cisplatin bound to DNA (Figure 1.5.4.1). These intrastrand crosslinks distort the three dimensional structure of the DNA and prevent replication from occurring. There is, however, acquired resistance to cisplatin treatment in some cases and it is thought that DNA repair surveillance enzymes learn to recognise the distorted DNA structure and are able to co-ordinate the repair by excising the platinum-DNA adduct.

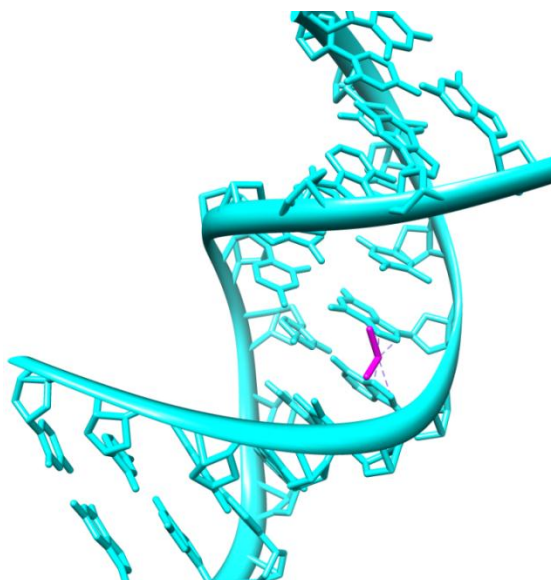


Figure 1.5.4.1: Crystal structure of a cisplatin (pink) intrastrand crosslink within a DNA helix (blue) redrawn from the co-ordinates in PDB 1AIO.⁶⁸ Molecular graphics generated with the UCSF Chimera package.⁵¹

1.6 Gold complexes and their applications in medicine

1.6.1 Gold(I) complexes in medicine

Traditionally gold(I) has been the choice oxidation state when working with gold since it is the most stable oxidation state. The most common use of gold(I) compounds is for the treatment of rheumatoid arthritis and skin diseases that have similar autoimmune responses to that of rheumatoid arthritis.⁶⁹ Three of these compounds are aurothiomalate, aurothioglucose and auranofin (Figure 1.6.1.1).

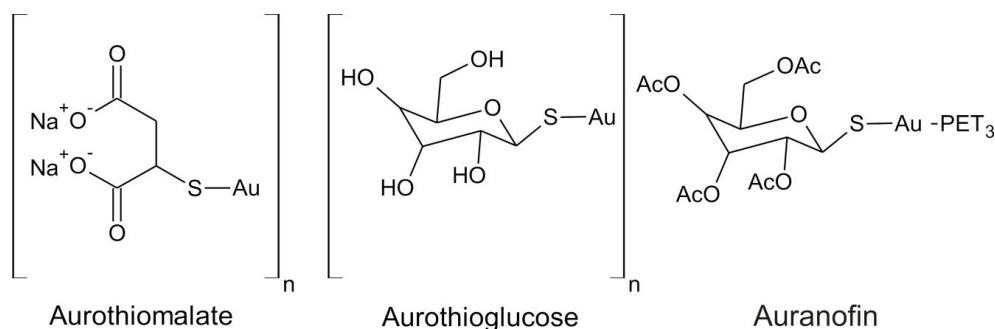


Figure 1.6.1.1: Chemical structures of gold(I) compounds for treatment of rheumatoid arthritis.

Gold(I) complexes show potential anti-cancer, anti-parasitic and anti-viral properties.⁶⁹⁻⁷² One of the most recent and promising finds was that of Rackham *et al.*, who describes a gold(I) phosphine complex that is selective towards breast cancer cells (Figure 1.6.1.2).⁷³ Some of the most promising attributes of gold complexes are the ability to administer them orally in daily doses, compared to similar acting drugs that have to be administered intravenously or intramuscularly. They are also active against cisplatin resistant cell lines.^{1, 69, 74} The mechanism of action for gold complexes is, however, not very well understood. It is thought that gold(I) complexes localise in the mitochondria and therefore their apoptotic pathway is associated with that.^{73, 75} The general problem with gold(I) phosphine complexes is that they can be fairly toxic. Generally these side effects occur after bioaccumulation in the body. Gold(I) phosphines are known to affect skin, blood, kidneys as well as other organs. Other major side effects include proteinuria, thrombocytopenia or nephropathy.⁷⁵

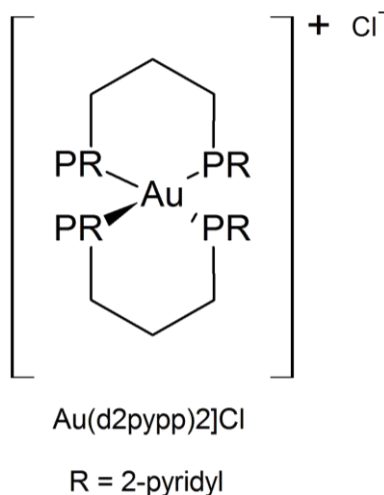


Figure 1.6.1.2: Chemical structure of $\text{Au}(\text{d}2\text{pypp})_2]\text{Cl}$.

1.6.2 Gold(III) complexes in medicine

Gold(III) is highly reactive and generally unstable to the reductive physiological environment.⁷⁶ It is readily reduced to gold(I) or colloidal gold; hence the metallotherapeutic use of gold(III) compounds was overlooked in earlier years. Recently, there has been renewed interest in gold(III) because new ligands have been designed that are able to further stabilise the gold(III) centre. These ligands can be bi-, tri- or tetradentate, generally containing strong sigma donors such as nitrogen, oxygen or carbon atoms.⁷⁵ Because gold(III) is isoelectronic and isosteric with platinum(II), but less toxic, by using gold(III) compounds instead of platinum(II) compounds it is hoped that there will be fewer side effects associated with gold complexes than with the platinum complexes. There are numerous gold(III) complexes that have been described in the literature, many with potentially useful anti-cancer properties.^{1, 69, 70, 75, 77-79} The most common gold(III) complexes include chelates with polyamines, cyclams, terpyridines, phenanthrolines and DAMP (*N*-benzyl-*N,N*-dimethylamine), dithiocarbamates and porphyrins.⁷⁸

GOLD(III)-DITHIOCARBAMATE COMPLEXES:

The first gold(III) dithiocarbamate complexes were reported in 1964 by Blaauw *et al.*, who reported the synthesis and properties of some simple dialkylgold(III) *N,N*-dialkyldithiocarbamates (Fig 1.6.2.1 A).⁸⁰ Recently Ronconi *et al.* have reported some new gold(III)-dithiocarbamate complexes (Fig 1.6.2.1 B).

Introduction

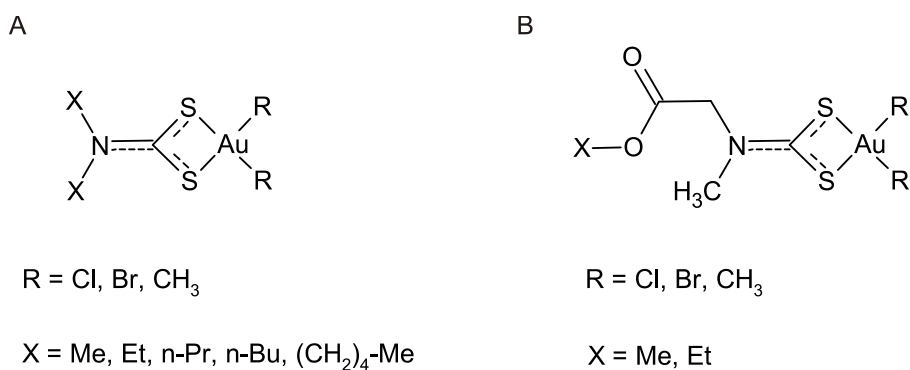


Figure 1.6.2.1: Chemical structures of gold(III) dithiocarbamate complexes.

The first paper relating gold(III) dithiocarbamates to medicine was in 1982, when Calis *et al.* reported a 'Mossbauer study of gold(I) and gold(III) dithiolate complexes related to anti-arthritic drugs',⁸¹ but it wasn't until 2005 that Giovagnini *et al.* reported on the cytotoxic properties of these compounds.⁷⁶ Since then, there have been several papers and two patents published highlighting the effectiveness of these compounds as anti-cancer compounds.^{82, 83}

The choice of the dithiocarbamate ligands was not random; they were chosen to observe their effectiveness, or lack thereof, to inhibit nephrotoxicity without decreasing its anti-cancer activity.⁷⁸ The complexes were tested *in vivo* for their cytotoxic activity towards a range of human cancer cell lines. It was shown that complexes A (Figure 1.6.2.1, where X = Me and R = Cl or Br) and complexes B (Figure 1.6.2.1, where X = Me and R = Cl or Br) were 1-4 times more cytotoxic than cisplatin and were able to a large extent to overcome both intrinsic and acquired resistance to cisplatin.⁷⁸ Since there are two *cis*-chloride atoms bound to the gold center that may undergo hydrolysis, it was thought that these complexes may act in a similar way to that of cisplatin. The tests showed, however, that the gold(III) dithiocarbamate complexes may have different molecular targets to that of cisplatin, but were not enlightening of what these targets might be. Through a series of tests and assays against various strains of cancerous and non-cancerous human breast cells, Milacic *et al.* showed that the most likely mode of action of these gold(III) dithiocarbamate complexes is, as previously suggested, different to that of cisplatin.⁸⁴ They suggest, with strong evidence, that the molecular target of these gold(III) dithiocarbamate complexes is the proteasome.⁸⁴ They further suggest that the complexes may affect the production of reactive oxygen species (ROS) which, in turn, delivers oxidative damage to the proteasome.⁸⁴ This work

Introduction

further indicated that the complexes modify mitochondrial functions as well, which leads to both apoptotic and non-apoptotic mechanisms.⁸⁵ Of relative importance in this study was the identification that the oxidation state of the metal center was central to the success of the complexes.^{76, 84} The analogous gold(I) complexes (which happen to be binuclear as a result of their co-ordination geometry) were tested and found to be ineffective when compared to the gold(III) complexes.^{76, 84} These compounds still need to undergo pre-clinical *in vivo* tests and ultimately clinical trials, but the results are encouraging.

GOLD(III)-DMAMP COMPLEXES:

Gold(III) dmamp-type complexes and their biological activities are well studied and are prominent in the literature.⁸⁶⁻¹⁰⁹ The first report of them was in 1984 when Vicente *et al.* described a series of these compounds in '2-[(Dimethylamino)methyl]phenylgold(III) complexes'.¹⁰⁶ Again it wasn't until later in the 90's that their biological behaviour was investigated. Parish *et al.* synthesised two gold(III)-dmamp complexes (Figure 1.6.2.2) and tested for their anti-bacterial and anti-tumour activity as well as their reactivity towards some biomolecules.⁸⁸

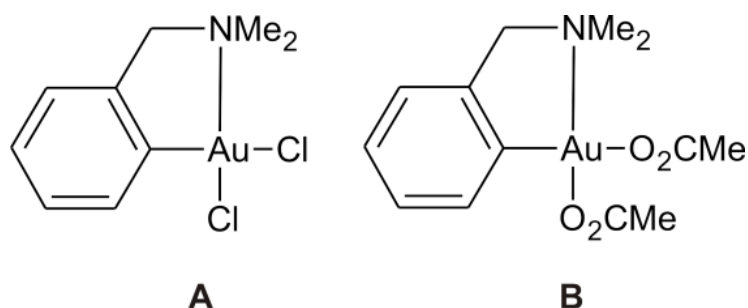


Figure 1.6.2.2: Chemical structures of [AuCl(dmamp)], (A) and [Au(O₂CMe)(dmamp)], (B).

[AuCl(dmamp)] showed similar anti-tumor activity to that of cisplatin, but its anti-bacterial activity was not high.¹⁰¹ The lack of anti-bacterial activity was attributed to its insolubility in water, hence the synthesis of [Au(O₂CMe)(dmamp)], which showed a marked improvement in solubility as well as its anti-tumour and anti-bacterial activity.¹⁰¹ Parish *et al.* reported that [Au(O₂CMe)(dmamp)] demonstrated promising selectivity towards gram-positive bacteria and cancerous Chinese hamster ovary cells.¹⁰¹ Evidence was also found for an inherent binding preference of such complexes to sulfur-containing biomolecules, such as cysteine and glutathione.¹⁰¹ A similar, but more in-depth, study was published by Buckley *et*

Introduction

al. also in 1996 that tested the anti-tumour activity of compounds [AuCl(dmamp)] and [Au(O₂CMe)(dmamp)] as well as three other derivatives, where the chloride ions were replaced with thiocyanate [Au(SCN)(dmamp)], oxalate [Au(Ox)(dmamp)] and malanato [Au(Mal)(dmamp)] ions.⁸⁸ All the compounds were tested *in vivo* as well as *in vitro* against a number of human tumour xenograft models.⁸⁸ [Au(O₂CMe)(dmamp)] and [Au(Mal)(dmamp)] showed similar, if not better, activity than cisplatin. It was also observed that in some cases they were active against cisplatin resistant cell lines.⁸⁸ Flow cytometry results indicated that, unlike cisplatin, [Au(SCN)(dmamp)] was not cell cycle specific, and plasmid mobility results showed that [Au(SCN)(dmamp)] and [Au(Mal)(dmamp)] interact with DNA (Figure 1.6.2.3), but significantly less than that of cisplatin.⁸⁸ Both of these results indicate that the gold(III) complexes behave mechanistically different to that of cisplatin.

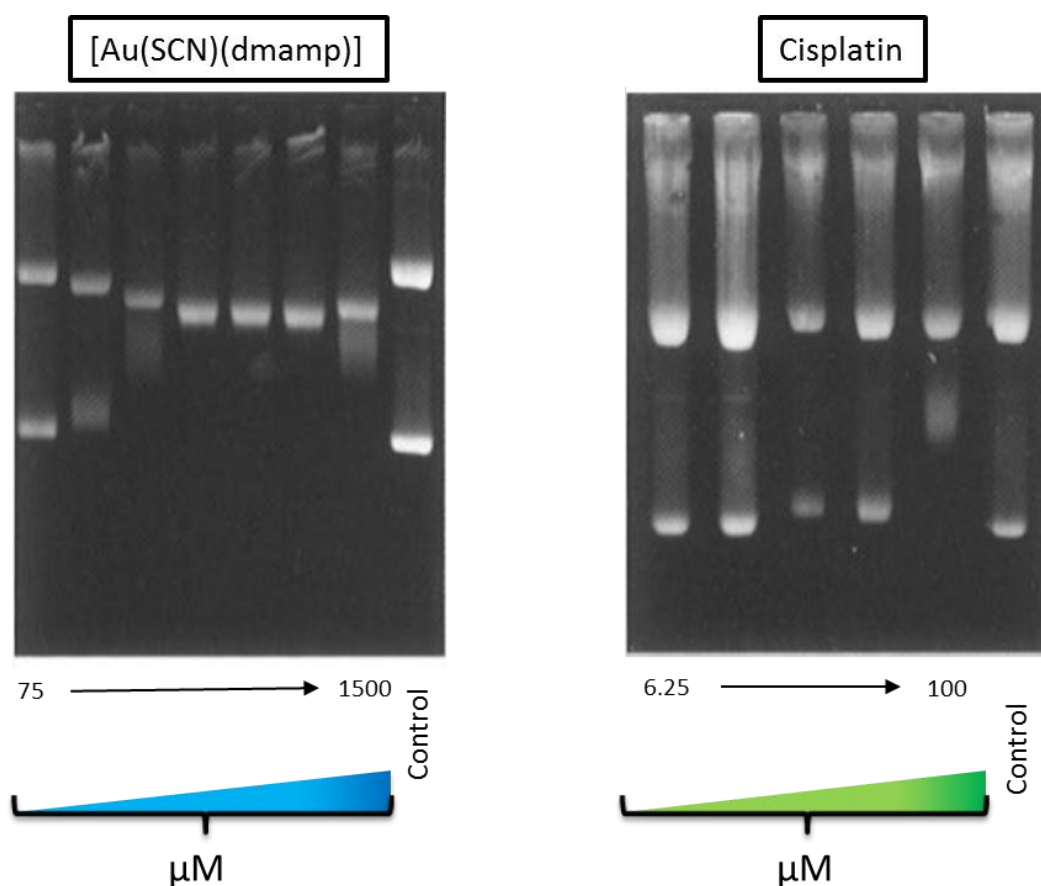


Figure 1.6.2.3: Photographs of electrophoresis gels showing the changes in mobility of the RF I (upperband) and RF II (lowerband) forms of the Col E1 plasmid after treatment with [Au(SCN)(dmamp)] (left) and cisplatin (right). Left (from left to right): [Au(SCN)(dmamp)] at 75, 150, 300, 600, and 1500 μM and plasmid control. Right (from left to right): cisplatin at 6.25, 9.4, 18.8, 37.5, 50, 75, and 100 μM and plasmid control. Adapted from ref 87.⁸⁸

Introduction

Since then there have been a series of papers describing various derivatives of the gold(III) dmamp system and their biological activities.^{89, 92, 93, 96, 97, 110} Some of the most promising results were obtained by Dinger *et al.* who describes a series of thiosalicylate and salicylate complexes (Figure 1.6.2.4), which all exhibit IC₅₀ values in the ng mL⁻¹ range. Of particular interest was the methoxy-derivatised thiosalicylate complex, which exhibited an IC₅₀ value of 301 ng mL⁻¹.⁹¹

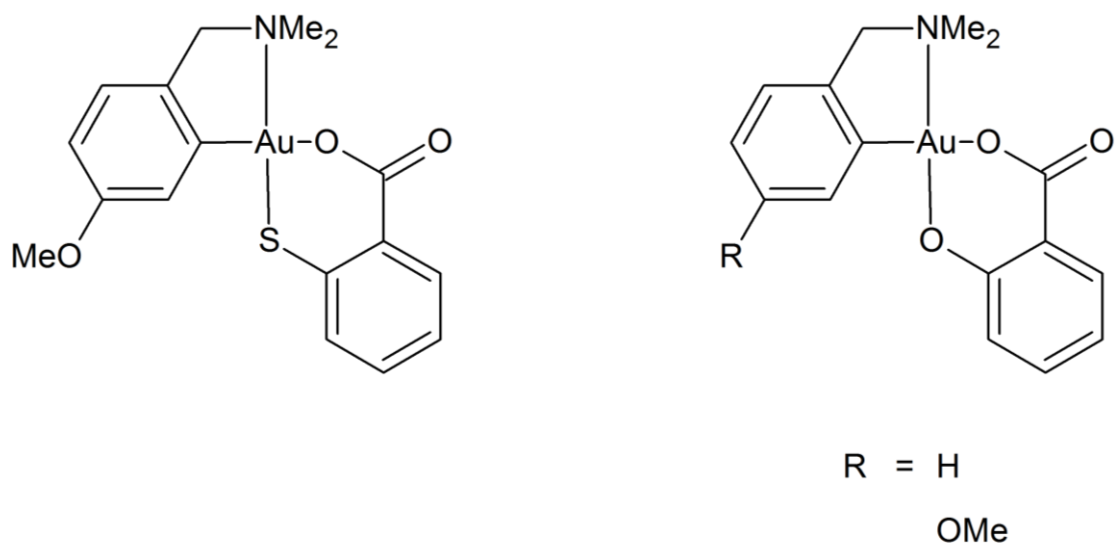


Figure 1.6.2.4: Chemical structures of thiosalicylate and salicylate gold(III) derivatives synthesised by Dinger *et al.*⁹¹

The class of gold(III) dmamp compounds, in general, seems to show anti-cancer activities close to, if not better, than that of cisplatin as well as in some cases anti-microbial activity. The activity of these compounds appears to be related to their solubility with the more soluble complexes being more active than the less soluble ones in general.

GOLD(III) PORPHYRIN COMPLEXES:

Porphyrins date back to the earliest of civilizations and were generally used as a purple pigment in fabric dyes. They were extracted from sea molluscs and used to dye the robes of royalty and priests. Gold(III) porphyrins are well documented in the literature.^{2, 111-117} In 1983 Kessel *et al.* reported on the phenomena that porphyrins seem to localise in cancer cells,¹¹⁸ but it was not until 2003 that Che *et al.* reported on the possibility that gold(III) porphyrins could potentially be used as anti-cancer agents.² Che's group has since reported several articles on gold porphyrins and their anti-cancer effects.¹¹⁹ The most common type

Introduction

of porphyrin used to chelate the gold(III) centre is based on meso-tetraphenylporphyrin (Figure 1.6.2.5). The stability of gold(III) porphyrins in typical organic solvents as well as in the presence of some typical biological reducing agents has been well studied, particularly for the original gold(III) meso-tetraphenylporphyrin [Au(TPP)+] where TPP = 5,10,15,20-tetraphenylporphyrin dianion.^{2, 119}

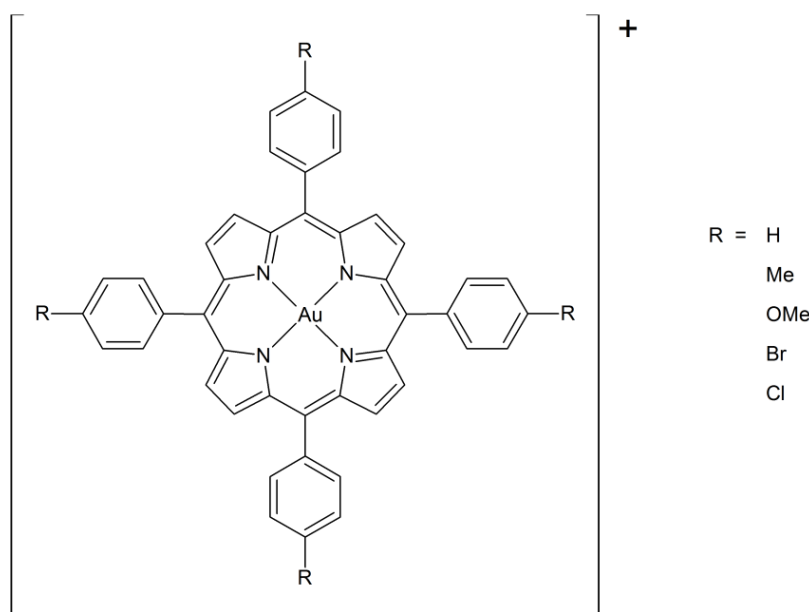


Figure 1.6.2.5: Chemical structures of cytotoxic gold(III) porphyrin complexes reported by Che *et al.*²

Che *et al.* have shown that [Au(TPP)+] is stable in phosphate-buffered saline (PBS) and Tris-buffered saline (TBS) containing 5% DMSO. Using UV-vis spectroscopy there was less than 5% change in absorbance in each of the solutions over a period of 48 hrs.² [Au(TPP)+] was also tested against reduction to gold(I) or colloidal gold by glutathione by NMR and UV-vis spectroscopy, both of which indicated no such action.² The stability of gold(III) complexes in solution seems to be related to their biological activity, therefore understanding their solution stability, or lack thereof, will facilitate decoding their mechanism(s) of action. [Au(TPP)+] was tested *in vitro*, by means of MTT assay, against a panel of human cancer cell lines. The results showed that it was active against most of the cell lines it was screened against, with IC₅₀ values ranging between 0.11 and 0.73 μM .^{2, 120, 121} Most importantly, it was shown that [Au(TPP)+] was equally toxic towards cisplatin-resistant cell lines, having IC₅₀ values in the 0.15 μM range. This corresponds to a 200-1600 times greater efficacy than that of cisplatin.^{2, 120, 121} Che *et al.* also did a comparative test on the cytotoxic effects of

Introduction

[Au(TPP)+] against healthy human cells and cancerous human cells. The tests showed that it was 10-fold more cytotoxic towards cancerous cells than towards healthy cells.¹²⁰

The presence of the gold(III) ion was proven to be critical to the *in vitro* anti-cancer activity of [Au(TPP)+], as the analogous zinc complex was 110 times less cytotoxic and the free gold salts $K[AuCl_4]$ and $[nBu_4N][AuCl_4]$ were 30-90 times less cytotoxic.¹²⁰ It was therefore proposed that '[Au(TPP)+] acts as a stable lipophilic planar cation for binding to biomolecular target(s) through non-covalent interactions', the exact targets are however unknown.^{79, 120} In the presence of serum proteins several studies have shown that certain metal-based drug's exhibit diminished activity, including that of cisplatin.^{122, 123} [Au(TPP)+] was tested for its cytotoxicity in the presence of fetal bovine serum and was shown to be unaffected, whereas cisplatin's cytotoxic activity was significantly reduced.¹²⁴ The *in vivo* anti-cancer properties of [Au(TPP)+] were also established against various nasopharyngeal carcinoma cells.¹²⁵ [Au(TPP)+] effectively suppressed tumor growth after treatment of 3 mg/kg week.^{79, 120} No significant side effects or weight loss were observed in the treated animals (Figure 1.6.2.6).

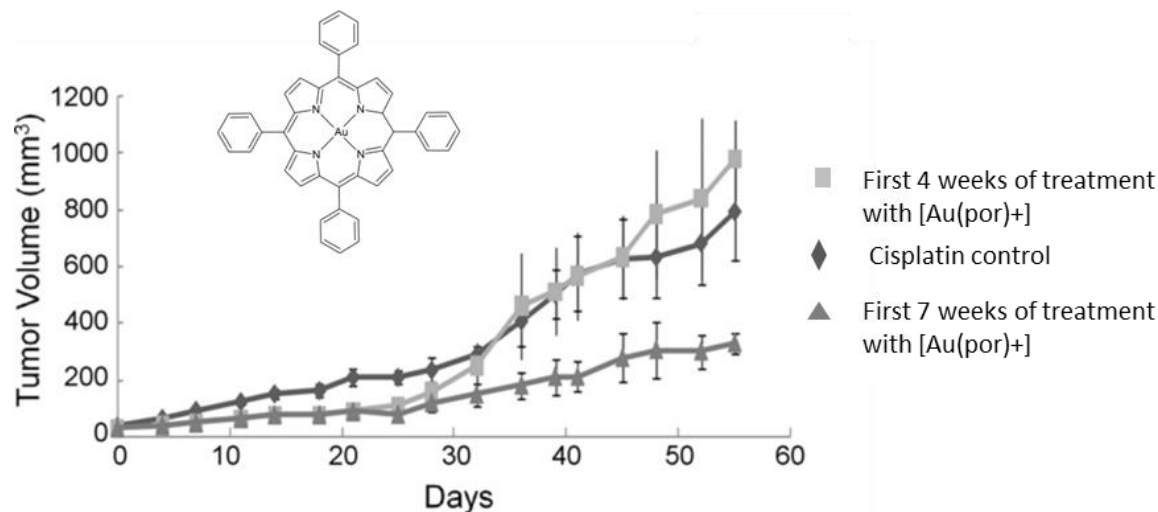


Figure 1.6.2.6: *In vivo* anti-cancer activity of [Au(TPP)+] toward nasopharyngeal carcinoma cells. Adapted from reference 78.⁷⁹

It was also proven by confocal microscopy that gold(III) porphyrin complexes induce apoptosis in cancerous cells and not necrosis (Figure 1.6.2.7). This is very important as necrosis triggers inflammatory tissue reactions, and could be detrimental to the treated

Introduction

patient's health. Overall Che *et al.* have shown the possibility that gold(III) porphyrin derivatives could be developed into successful anti-cancer drugs.

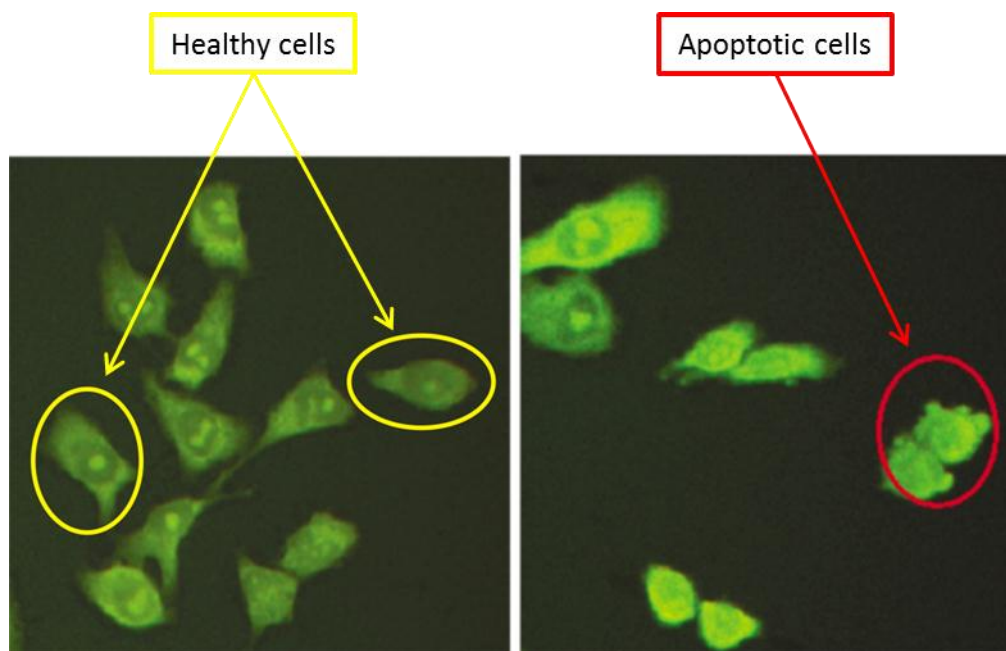


Figure 1.6.2.7: Laser confocal micrographs of the HeLa cells treated with $[\text{Au}(\text{TPP})^+]$ ($0.5 \mu\text{M}$) at time intervals of (a) 0 h and (b) 15 h. Healthy cells are marked by a yellow circle and apoptotic cells are marked by a red circle. Reproduced from ref 2.²

GOLD(III) PHEN, BIPY, TERPY, AND VARIABLE CYCLOMETALLATED COMPLEXES:

There have been several reports in the literature on the cytotoxicity of the above mentioned gold(III) complexes and their derivatives.¹²⁶⁻¹²⁹ Some selected examples of these compounds are shown below (Figure 1.6.2.8). The complexes $[\text{Au}(\text{bipy})\text{Cl}_2]\text{Cl}$ and $[\text{Au}(\text{bipy}^c\text{-H}(\text{OH}))(\text{PF}_6)]$ were tested for their cytotoxicity by Marcon *et al.* in 2002. Their activity towards various cisplatin-resistant and non-resistant, cancerous cell lines was investigated. Their results showed that $[\text{Au}(\text{bipy}^c\text{-H}(\text{OH}))(\text{PF}_6)]$ was the most cytotoxic of the two, but with both compounds having IC_{50} values in the low μM range.¹²⁸ Both compounds were more active than cisplatin. Their interaction with DNA was also investigated by electronic spectroscopy and circular dichroism (CD) spectroscopy; some evidence for the compounds interacting in some way with DNA was obtained.¹²⁸

Introduction

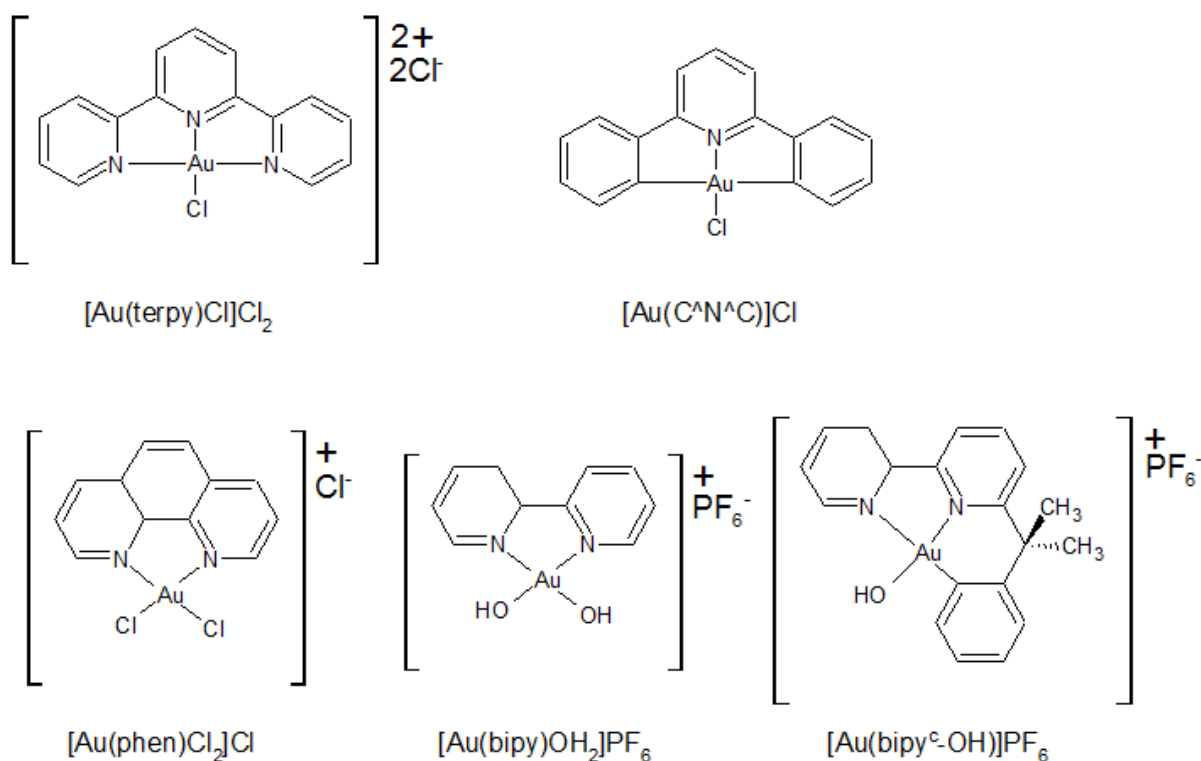


Figure 1.6.2.8: Chemical structures of various gold(III) complexes.

The gold(III) complexes of traditional metalointercalator ligands phen and terpy were also assessed for their biological activity by Messori *et al.* in 2000.¹²⁹ They were tested against the A2780 ovarian human cancer cell line either sensitive (A2780/S) or resistant (A2780/R) to cisplatin. The results showed that both [Au(phen)Cl₂]Cl and [Au(terpy)Cl]Cl₂ were cytotoxic with [Au(terpy)Cl]Cl₂ being the most cytotoxic (IC₅₀ = 0.2 μM) and both showing activity towards the cisplatin-resistant cell line.¹²⁹ The free ligands were then also assessed for their cytotoxicity and, interestingly, it was found that they possessed close to, if not equal, cytotoxicity to that of the metal complex.¹²⁹ Therefore the cytotoxicity of the complex cannot be solely attributed to the metal and more detailed investigations need to be completed in order for these systems to be completely understood. The complex [Au(C^N^C)]Cl, first synthesised by Che *et al.* in 1998, and was tested for its cytotoxic properties in 2006, again by Che *et al.*^{127, 130} It was tested against four cell lines, namely HeLa, HepG2, SUNE1 and CNE1 with IC₅₀ values of 3.4, 17, 4.0, 3.1 μM respectively. Again the activity of [Au(C^N^C)]Cl was comparable to that of cisplatin.^{127, 130} Overall the compounds in Figure 1.6.2.8 are mostly cytotoxic with [Au(bipy^c-H(OH))(PF₆)] being the most active.

Introduction

GOLD(III) AMINE AND IMINE COMPLEXES:

Gold(III) amine complexes include complexation with alkyl amines such as en and dien as well as some macrocyclic polyamines.¹³¹⁻¹³³ There have been three biological studies that have involved the basic complexes $[\text{Au}(\text{cyclam})](\text{ClO}_4)_2\text{Cl}$, $[\text{Au}(\text{en})_2]\text{Cl}_3$, $[\text{Au}(\text{dien})\text{Cl}]\text{Cl}_2$, (Figure 1.6.2.9).^{126, 129, 134}

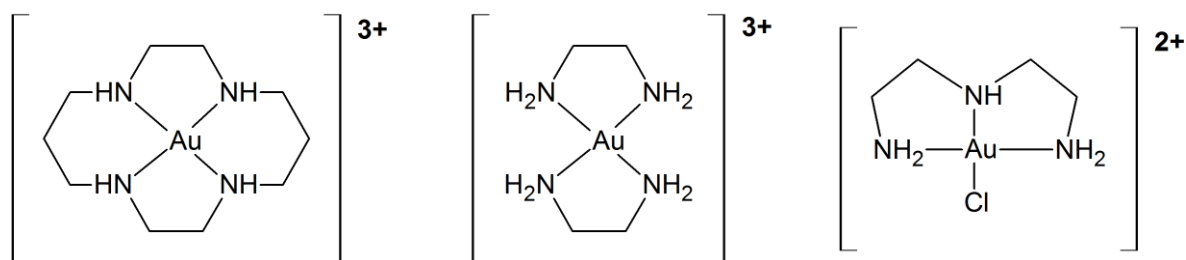


Figure 1.6.2.9: Chemical structures of $[\text{Au}(\text{cyclam})](\text{ClO}_4)_2\text{Cl}$ (left), $[\text{Au}(\text{en})_2]\text{Cl}_3$ (middle) and $[\text{Au}(\text{dien})\text{Cl}]\text{Cl}_2$ (right).

All three studies tested these three compounds against the A2780 ovarian human cell line either sensitive (A2780/S) or resistant (A2780/R) to cisplatin. The first study completed by Carotti *et al.* in 1998 showed that $[\text{Au}(\text{en})_2]\text{Cl}_3$ and $[\text{Au}(\text{dien})\text{Cl}]\text{Cl}_2$ were active against both A2780/S ($[\text{Au}(\text{en})_2]\text{Cl}_3$ $\text{IC}_{50} = 8.4 \mu\text{M}$, $[\text{Au}(\text{dien})\text{Cl}]\text{Cl}_2$ $\text{IC}_{50} = 8.2 \mu\text{M}$) and A2780/R ($[\text{Au}(\text{en})_2]\text{Cl}_3$ $\text{IC}_{50} = 17 \mu\text{M}$, $[\text{Au}(\text{dien})\text{Cl}]\text{Cl}_2$ $\text{IC}_{50} = 18.7 \mu\text{M}$) cell lines.¹³⁴ $[\text{Au}(\text{cyclam})](\text{ClO}_4)_2\text{Cl}$ was found to be essentially non-cytotoxic towards these cell lines.¹³⁴ These results were confirmed in 2000 by Messori *et al.* who further investigated these compounds.¹²⁹ These workers tested the free ligands of the complexes $[\text{Au}(\text{cyclam})](\text{ClO}_4)_2\text{Cl}$, $[\text{Au}(\text{en})_2]\text{Cl}_3$ and $[\text{Au}(\text{dien})\text{Cl}]\text{Cl}_2$ against the same cell lines. The free ligands were ineffective in their cytotoxic properties, hence the cytotoxic action of $[\text{Au}(\text{en})_2]\text{Cl}_3$ and $[\text{Au}(\text{dien})\text{Cl}]\text{Cl}_2$ can be directly attributed to the presence of the gold(III) centre.¹²⁹

There have only been two gold(III) salen complexes reported in the literature by Barnholtz *et al.* in 2001 (Figure 1.6.2.10). They reported the structures of $[\text{Au}(\text{sal}_2\text{en})](\text{PF}_6)$ and $[\text{Au}(\text{sal}_2\text{pn})]\text{Cl}\cdot 2.5\text{H}_2\text{O}$.¹³⁵

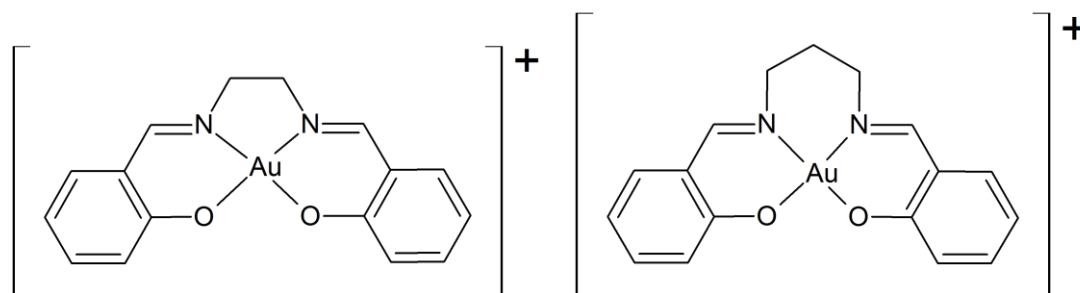


Figure 1.6.2.10: Chemical structures of [Au(sal₂en)](PF₆) (left) and [Au(sal₂pn)]Cl·2.5H₂O (right).

Only recently in a review has there been mention of these gold(III) salen complexes and their biological activity. Che *et al.* reported that these complexes, like the bis(amides), below, have limited stability in solution, with an approximately 10% reduction in absorbance over a short period of 4 hours compared to [Au(TPP)]⁺ which showed a less than 5% reduction in absorbance over 48 hours.¹³⁵ These complexes also showed instability towards the reducing agent glutathione, with almost instant changes in the electronic absorption spectrum upon the addition of glutathione.¹³⁵ Notwithstanding this redox instability, the complexes still had appreciable cytotoxicities (IC₅₀ values in the 10-30 μM range).¹³⁵

1.7 Bis(amide) and mono(amide) ligands and metal complexes

The goal of this work was to synthesise a range of known as well as novel *N,N'*-bis(amide) and *N*-mono(amide) ligands and chelate them to gold(III) (Figure 1.7.1). Ligands of this nature are known in the literature and have been used for a variety of diverse functions. The general structure of the *N,N'*-bis(amide) ligand comprises a set of heteroaromatic (pyridine or quinoline) rings which are joined through a di(amide) linkage, which too can be varied. The *N*-mono(amide) ligands consist of two heteroaromatic or non-heteroaromatic substituents linked via an amide bond to form bidentate or tridentate ligands.

Introduction

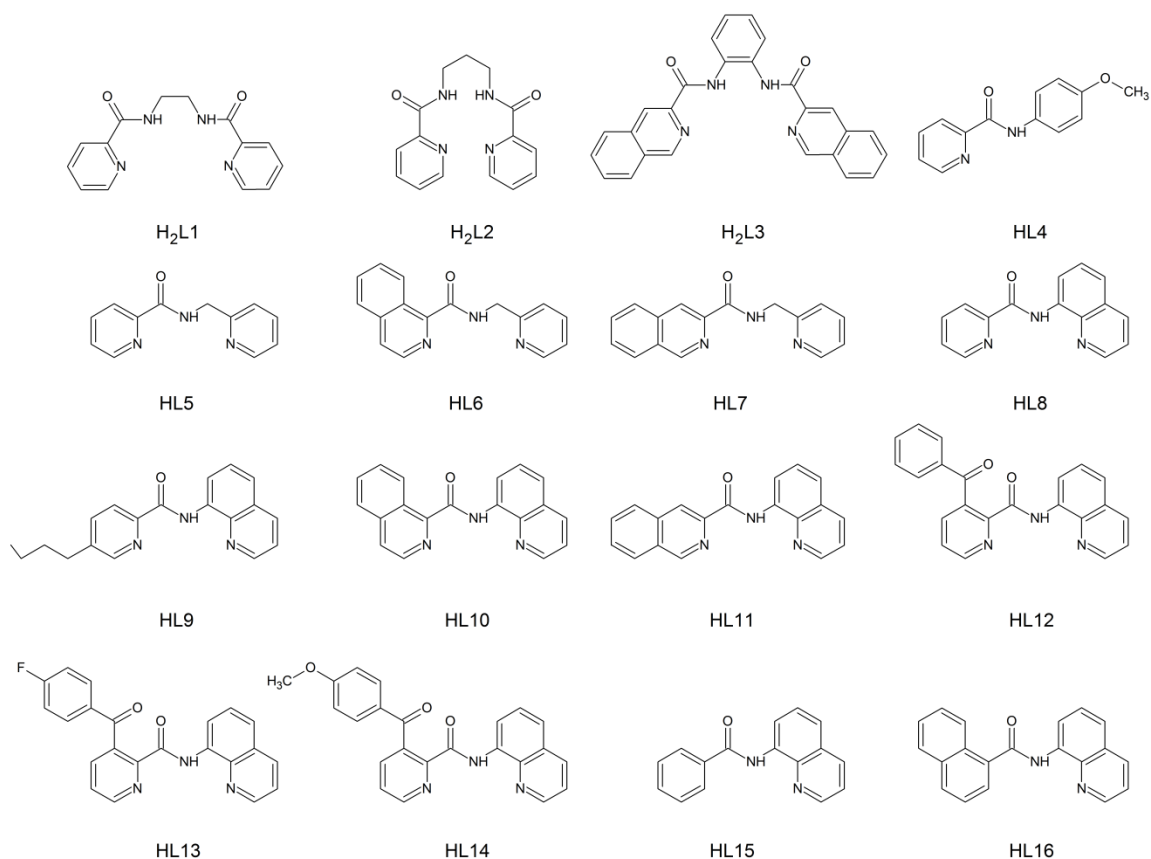


Figure 1.7.1: Chemical structures and naming scheme of the ligands used in this work.

In general, co-ordination of this class of compounds to a metal centre is accompanied by deprotonation of the amide N–H, so in the case of the *N,N'*-bis(amide) ligand, it becomes a tetradentate dianionic ligand, while the *N*-mono(amide) ligands become monoanionic bidentate or tridentate ligands. Since the amide is able to form a hybrid resonance structure (Figure 1.7.2), the deprotonation of the amide N–H is not always concomitant upon chelation to a metal centre and a suitable base is sometimes required during metallation.

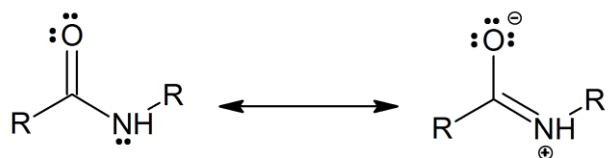


Figure 1.7.2: Resonance hybrid structure of a general amide bond.

Metal chelates of both the *N,N'*-bis(amide) and *N*-mono(amide) ligands are present in the literature and have been used to investigate interesting molecular structures and their physical properties due to their ability to form dinuclear species¹³⁶⁻¹³⁹. They have also been used in the biological field as therapeutics and as imaging agents.^{140, 141} Specifically, gold(III)

Introduction

amide chelates are not very prominent in the literature with only a few examples having been published. Yang *et al.* synthesised the first and only reported gold(III) mono-amide complex in 2003 and tested its reactivity towards 5'-GMP.¹⁴² They found by electrospray mass spectrometry (ESMS) that their compound was able to form bis-GMP adducts.¹⁴² Che *et al.* have synthesised a number of bis(amide) complexes.^{2, 79, 143} They have reported the synthesis of a gold(III) amide complex: $[\text{Au}(\text{HL})\text{Cl}_2]$ ($\text{H}_2\text{L} = 2,2'$ -bis(2-pyridylcarboxamide)-1,1'-binaphthyl) (Figure 1.7.3). In this complex the gold centre has only chelated to the one half of the tetradentate ligand along with two chloride ions to complete the square planar geometry, thus leaving a free amide moiety that is non-bound (Figure 1.7.3).¹⁴³

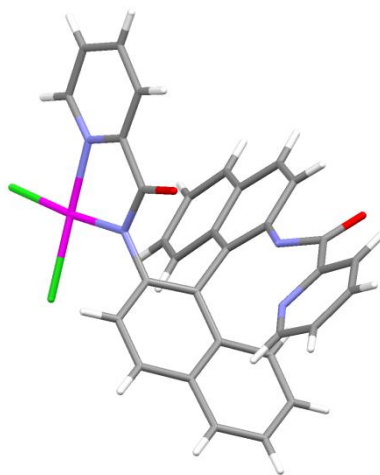


Figure 1.7.3: Diagram of $[\text{Au}(\text{HL})\text{Cl}_2]$ ($\text{H}_2\text{L} = 2,2'$ -bis(2-pyridylcarboxamide)-1,1'-binaphthyl).

It was assumed that because of the steric hindrance between H-atoms of the binaphthyl bridge, the ligand was not able to support the square planar geometry required by the gold(III) centre, and hence the structure above is favoured. It will be shown in this work that this may partly be the case, in conjunction with intrinsic properties of bis(amide) ligands that evidently detract from co-ordination of two pyridyl-amide moieties to gold(III). A recent review by Che reported some tetradentate chelates of the bis(amide) ligand system, including a discussion of their biological activities (Figure 1.7.4). From the four compounds shown, only two of them have appreciable cytotoxicities (A and B). Complex B showed similar cytotoxicity to the following literature compounds: $[\text{Au}(\text{en})_2]$ [IC_{50} (human ovarian carcinoma A2780, 48 h) = 8.4 μM];⁶⁶ $[\text{Au}(\text{esal})\text{Cl}_2]$ [IC_{50} (human ovarian carcinoma A2780, 72 h) = 2.1 μM];⁷⁴ $[\text{AuCl}_2(\text{dmamp})]$ [IC_{50} (human colon carcinoma SW620, 72 h) = 50 μM],²⁶ and

Introduction

$\text{Na}[\text{AuCl}_4]$ [IC_{50} (human ovarian carcinoma A2780, 72 h) = 11 μM],¹²⁹ while complex A showed cytotoxicity towards SUNE1 cells (IC_{50} = 21.1 μM). The compounds have only been tested against a small range of cells and further studies are warranted.⁷⁹ Complex B is again fairly unstable to reduction by common biological reducing agents such as glutathione; a 10% reduction in absorbance was noted over a period of 4 hours compared to $[\text{Au}(\text{TPP})^+]$, which showed a less than 5% reduction in absorbance over 48 hours.⁷⁹

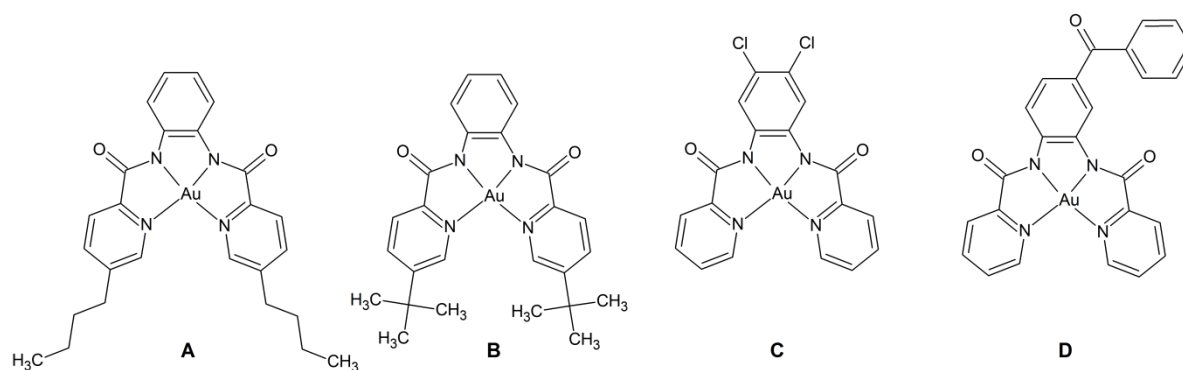


Figure 1.7.4: Chemical structures of bis(amide) gold(III) complexes.

In 2003 there were two reports published on the chelation of gold(III) with picolinamide to form the complex $[\text{Au}(\text{pla})\text{Cl}_2]$, where pla = picolinamide.^{144, 145} The first was by Fan *et al.*¹⁴⁴ who reported “Chemical and biological studies of gold(III) complexes with uninegative bidentate N–N ligands”. In this study, the cytotoxic properties of the complex against MOLT-4 (human leukemia) and C2C12 (mouse tumour) cell lines were determined as, 3.1 and 8.0 μM , respectively.¹⁴⁴ In a study published not more than a week later, Hill and co-workers reported a gold-197 Mossbauer study on the same complex. More recently Cinellu and co-workers reported on the synthesis and reactivity of chiral pyridinyl–oxazoline ligands coordinated to gold(III).¹⁴⁶ This prompted a study by Maiore *et al.*, published in 2012, focusing on the biological properties of these complexes. They investigated their solution stability, interaction with horse cytochrome c and their anti-proliferative profiles against human ovarian cancer cell lines A2780R (cisplatin resistant) and A2780S (cisplatin susceptible). They found that the complexes were stable at least for a few hours, were able to form adducts with horse cytochrome c and in general were active against the cell lines tested.¹⁴⁷

In 2003, Yang and co-workers published an article on three 8-aminoquinoline based gold(III) amide complexes (Figure 1.7.5). They reported that these compounds were highly cytotoxic

Introduction

against the cell lines B16-BL6, P388, HL-60, A-549 and BEL-7402 and tentatively suggested they may be able to intercalate DNA.³ The data from this paper are, however, compromised by the lack of experimental DNA binding constants or IC₅₀ values.

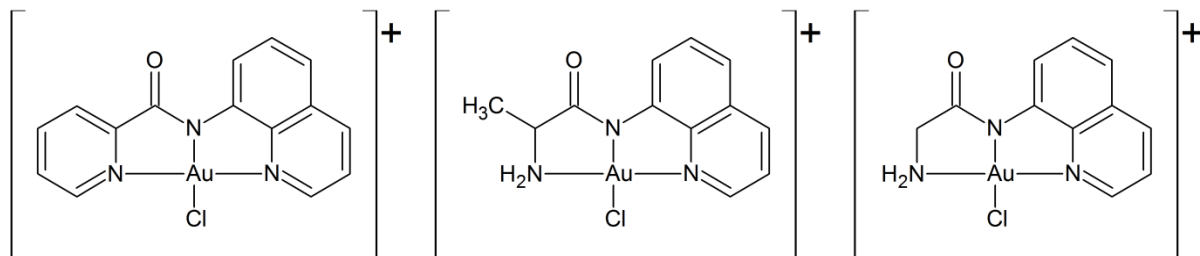


Figure 1.7.5: Chemical structures of the complexes synthesised by Yang *et al.*³

The cytotoxic gold(III) complexes in Yang *et al.*'s report underpin our interest in this class of tridentate complexes and we hypothesised that by derivitising this class of compounds through functional group changes, extending or removing aromaticity, and/or including hydrogen bonding groups we might be able to develop a wider group of cationic gold(III) complexes with enhanced cytotoxicity towards human cancer cell lines. A full and more complete investigation into this class of compounds has been undertaken in this thesis.

In December 2011, after the synthesis and characterisation work of this project was complete, a patent was published by Wang *et al.* directly pertaining to a class of gold(III) compounds to be presented in this thesis (Figure 1.7.6).¹⁴⁸ Since the intention of this thesis is not to seek a patent on the 8-aminoquinolylamide gold(III) chelates, for which prior art exists, but to investigate structure-activity relationships and the physical and biological properties of numerous compounds falling into this promising group of compounds, the patent by Wang and co-workers corroborates the general importance of the compounds studied in this work. Moreover, we have been able to structurally characterise the patented gold(III) complexes and have thereby obtained heretofore unprecedented data crucial to outlining any structure-based mechanism of action for these and related compounds.

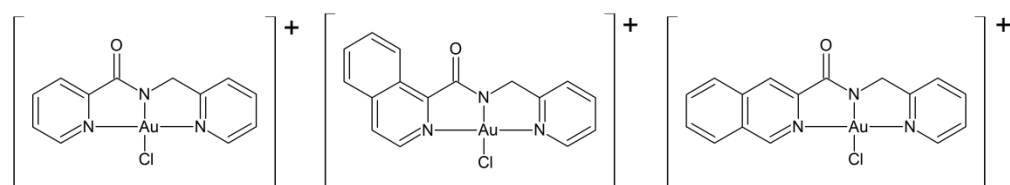


Figure 1.7.6: Chemical structures of the compounds relating to the recent patent.

Introduction

with appropriate experimental data in order to determine the precision of the calculations.

- 6) To determine, by spectroscopy, a series of biologically relevant parameters such as: octanol/water partition coefficients, DNA binding properties, stability in a physiologically representative medium such as a buffer as well as stability towards biomolecules such as glutathione and imidazole.
- 7) To submit the complexes for cytotoxicity screening at the National Cancer Institute (NCI) in the USA and to analyse the cytotoxicity profiles of complexes proceeding to 5-dose screens for cell-line specificity.
- 8) To determine the possible mechanism of action of metal chelates proceeding to 5-dose NCI cytotoxicity screens by statistical cluster analysis methods. To confirm the biological targets of lead drug candidates by standard enzyme-inhibition or other suitable biochemical assays.

1.9 References

1. P. J. Sadler and R. E. Sue, *Met.-Based Drugs*, 1994, **1**, 107-144.
2. C.-M. Che, R. W.-Y. Sun, W.-Y. Yu, C.-B. Ko, N. Zhu and H. Sun, *Chem. Commun. (Cambridge, U. K.)*, 2003, 1718-1719.
3. T. Yang, C. Tu, J. Zhang, L. Lin, X. Zhang, Q. Liu, J. Ding, Q. Xu and Z. Guo, *Dalton Trans.*, 2003, 3419-3424.
4. A. Laguna, *Modern Supramolecular Gold Chemistry: Gold-Metal Interactions and Applications*, Wiley and Sons, 2008.
5. <http://en.wikipedia.org/wiki/Gold>, 2012.
6. J. E. Brady, *General Chemistry: Principles and Structure*, 5th Edition edn., Wiley and Sons, 1990.
7. F. A. Cotton and G. Wilkinson, *Advanced Inorganic Chemistry*, 5th Edition edn., Wiley and Sons, 1988.
8. M. Kolesnikova, Bloomberg, 2012.
9. D. Pletcher and F. Walsh, *Industrial Electrochemistry*, Springer, 1990.
10. E. d. B. Baenett and C. L. Wilson, *Inorganic Chemistry*, 2nd Edition edn., Longmans, Green and Co. Ltd., 1958.
11. A. Sommer, *Nature* 1943, **152**, 215.
12. W. Biltz, F. Weibke, H. J. Ehrhorn and R. Wedemeyer, *Z. Anorg. Allg. Chem.*, 1938, **236**, 12-23.
13. C. Feldmann and M. Jansen, *Angew. Chem., Int. Ed.*, 1993, **105**, 1107-1108 (See also *Angew. Chem., Int. Ed. Engl.*, 1993, 1132(1107), 1049-1150).
14. A.-V. Mudring and M. Jansen, *Angew. Chem., Int. Ed.*, 2000, **39**, 3066-3067.
15. C. Feldmann and M. Jansen, *Z. Anorg. Allg. Chem.*, 1995, **621**, 1907-1912.
16. A.-V. Mudring, J. Nuss, U. Wedig and M. Jansen, *J. Solid State Chem.*, 2000, **155**, 29-36.
17. P. D. C. Dietzel and M. Jansen, *Chem. Commun. (Cambridge, U. K.)*, 2001, 2208-2209.
18. P. L. Bellon, F. Cariati, M. Manassero, L. Naldini and M. Sansoni, *J. Chem. Soc. D.*, 1971, 1423-1424.
19. S. Seidel and K. Seppelt, *Science*, 2000, **290**, 117-118.
20. D. F. Shriver and P. W. Atkins, *Inorganic Chemistry*, 4th Edition edn., Oxford University Press, 2006.
21. M. A. Cinellu, A. Zucca, S. Stoccoro, G. Minghetti, M. Manassero and M. Sansoni, *J. Chem. Soc., Dalton Trans.*, 1996, 4217-4225.
22. M. P. Suh, I. S. Kim, B. Y. Shim, D. Hong and T.-S. Yoon, *Inorg. Chem.*, 1996, **35**, 3595-3598.
23. V. K.-Y. Lo, K. K.-Y. Kung, M.-K. Wong and C.-M. Che, *J. Organomet. Chem.*, 2009, **694**, 583-591.
24. Y.-P. Xiao, X.-Y. Liu and C.-M. Che, *J. Organomet. Chem.*, 2009, **694**, 494-501.
25. A. S. K. Hashmi, T. M. Frost and J. W. Bats, *J. Am. Chem. Soc.*, 2000, **122**, 11553-11554.
26. Y. Zhang, J. P. Donahue and C.-J. Li, *Org. Lett.*, 2007, **9**, 627-630.
27. Y. Fukuda and K. Utimoto, *J. Org. Chem.*, 1991, **56**, 3729-3731.
28. N. D. Shapiro and F. D. Toste, *J. Am. Chem. Soc.*, 2008, **130**, 9244-9245.
29. E. R. T. Tiekink and J.-G. Kang, *Coord. Chem. Rev.*, 2009, **253**, 1627-1648.

Introduction

30. V. K.-M. Au, K. M.-C. Wong, N. Zhu and V. W.-W. Yam, *J. Am. Chem. Soc.*, 2009, **131**, 9076-9085.
31. V. W.-W. Yam, K. M.-C. Wong, L.-L. Hung and N. Zhu, *Angew. Chem., Int. Ed.*, 2005, **44**, 3107-3110.
32. K. M.-C. Wong, X. Zhu, L.-L. Hung, N. Zhu, V. W.-W. Yam and H.-S. Kwok, *Chem. Commun. (Cambridge, U. K.)*, 2005, 2906-2908.
33. V. W.-W. Yam, M.-C. Wong, H.-S. Kwok and X. Zhu, *US7572912B2*, 2009.
34. W.-P. To, G. S.-M. Tong, W. Lu, C. Ma, J. Liu, A. L.-F. Chow and C.-M. Che, *Angew. Chem., Int. Ed.*, 2012, **51**, 2654-2657, S2654/2651-S2654/2630.
35. J. Cairns, *Cancer: Science and Society*, W. H. Freeman and Company, 1978.
36. D. E. Thurston, *Chemistry and Pharmacology of Anticancer Drugs*, Taylor and Francis Group, 2007.
37. S. Missailidis, *The Cancer Clock*, Wiley and Sons, 2007.
38. P. Turnpenny and S. Ellard, *Emery's Elements of Medical Genetics*, 12th edn., Elsevier, 2005.
39. D. P. Snustad and M. J. Simmons, *Principles of Genetics*, 4th Edition edn., Wiley and Sons, 2006.
40. J. C. Dabrowaik, *Metals in Medicine*, Wiley and Sons, 2009.
41. W. B. Pratt, R. W. Ruddon, W. D. Ensminger and J. Maybaum, *The Anticancer Drugs*, 2nd Edition edn., Oxford University Press, 1994.
42. J. J. Champoux, *Annu. Rev. Biochem.*, 2001, **70**, 369-413.
43. Y. Pommier, *Nat. Rev. Cancer*, 2006, **6**, 789-802.
44. Y. Pommier, *Chem. Rev.*, 2009, **109**, 2894-2902.
45. K. D. Corbett and J. M. Berger, *Annu. Rev. Biophys. Biomol. Struct.*, 2004, **33**, 95-118, 116 plates.
46. D. A. Koster, K. Palle, E. S. M. Bot, M.-A. Bjornsti and N. H. Dekker, *Nature* 2007, **448**, 213-217.
47. A. Ioanoviciu, S. Antony, Y. Pommier, B. L. Staker, L. Stewart and M. Cushman, *J. Med. Chem.*, 2005, **48**, 4803-4814.
48. Y. Pommier, E. Leo, H.-L. Zhang and C. Marchand, *Chem. Biol. (Cambridge, MA, U. S.)*, 2010, **17**, 421-433.
49. B. L. Staker, M. D. Feese, M. Cushman, Y. Pommier, D. Zembower, L. Stewart and A. B. Burgin, *J. Med. Chem.*, 2005, **48**, 2336-2345.
50. B. L. Staker, K. Hjerrild, M. D. Feese, C. A. Behnke, A. B. Burgin, Jr. and L. Stewart, *Proc. Natl. Acad. Sci.*, 2002, **99**, 15387-15392.
51. <http://www.cgl.ucsf.edu/chimera>, 2012.
52. J. M. Berger, S. J. Gamblin, S. C. Harrison and J. C. Wang, *Nature* 1996, **379**, 225-232.
53. K. C. Dong and J. M. Berger, *Nature* 2007, **450**, 1201-1205.
54. J. L. Nitiss, *Nat. Rev. Cancer*, 2009, **9**, 338-350.
55. J. L. Nitiss, *Nat. Rev. Cancer*, 2009, **9**, 327-337.
56. C.-C. Wu, T.-K. Li, L. Farh, L.-Y. Lin, T.-S. Lin, Y.-J. Yu, T.-J. Yen, C.-W. Chiang and N.-L. Chan, *Science* 2011, **333**, 459-462.
57. C. A. Frederick, L. D. Williams, G. Ughetto, d. M. G. A. Van, B. J. H. Van, A. Rich and A. H. J. Wang, *Biochemistry*, 1990, **29**, 2538-2549.
58. G. A. Leonard, T. Brown and W. N. Hunter, *Eur. J. Biochem.*, 1992, **204**, 69-74.
59. B. M. Zeglis, V. C. Pierre and J. K. Barton, *Chem. Commun. (Cambridge, U. K.)*, 2007, 4565-4579.

Introduction

60. B. S. P. Reddy, S. M. Sondhi and J. W. Lown, *Pharmacology & Therapeutics*, 1999, **84**, 1-111.
61. T. Yamori, A. Matsunaga, S. Sato, K. Yamazaki, A. Komi, K. Ishizu, I. Mita, H. Edatsugi, Y. Matsuba, K. Takezawa, O. Nakanishi, H. Kohno, Y. Nakajima, H. Komatsu, T. Andoh and T. Tsuruo, *Cancer Res.*, 1999, **59**, 4042-4049.
62. G. M. Sriram, A. v. d. Marel, H. L.P.F. Roelen, J. H. v. Boom and A. H.-J. Wang, *The EMBO Journal*, 1992, **11**, 225-232.
63. M. Sriram, d. M. G. A. Van, H. L. P. F. Roelen, B. J. H. Van and A. H. J. Wang, *EMBO J.*, 1992, **11**, 225-232.
64. D. R. Boer, J. M. C. A. Kerckhoffs, Y. Parajo, M. Pascu, I. Uson, P. Lincoln, M. J. Hannon and M. Coll, *Angew. Chem., Int. Ed.*, 2010, **49**, 2336-2339, S2336/2331-S2336/2313.
65. C. Ducani, A. Leczkowska, N. J. Hodges and M. J. Hannon, *Angew. Chem., Int. Ed.*, 2010, **49**, 8942-8945, S8942/8941-S8942/8945.
66. G. I. Pascu, A. C. G. Hotze, C. Sanchez-Cano, B. M. Kariuki and M. J. Hannon, *Angew. Chem., Int. Ed.*, 2007, **46**, 4374-4378.
67. S. E. Howson, A. Bolhuis, V. Brabec, G. J. Clarkson, J. Malina, A. Rodger and P. Scott, *Nat. Chem.*, 2012, **4**, 31-36.
68. P. M. Takahara, C. A. Frederick and S. J. Lippard, *J. Am. Chem. Soc.*, 1996, **118**, 12309-12321.
69. H. E. Abdou, A. A. Mohamed, J. P. Fackler, A. Burini, R. Galassi, J. M. Lopez-de-Luzuriaga and M. E. Olmos, *Coord. Chem. Rev.*, 2009, **253**, 1661-1669.
70. M. Navarro, *Coord. Chem. Rev.*, 2009, **253**, 1619-1626.
71. T. Okada, B. K. Patterson, S. Q. Ye and M. E. Gurney, *Virology*, 1993, **192**, 631-642.
72. K. Yamaguchi, H. Ushijima, M. Hisano, Y. Inoue, T. Shimamura, T. Hirano and W. E. G. Muller, *Microbiol. Immunol.*, 2001, **45**, 549-555.
73. O. Rackham, S. J. Nichols, P. J. Leedman, S. J. Berners-Price and A. Filipovska, *Biochem. Pharmacol.*, 2007, **74**, 992-1002.
74. M. M. Jellicoe, S. J. Nichols, B. A. Callus, M. V. Baker, P. J. Barnard, S. J. Berners-Price, J. Whelan, G. C. Yeoh and A. Filipovska, *Carcinogenesis*, 2008, **29**, 1124-1133.
75. I. Ott, *Coord. Chem. Rev.*, 2009, **253**, 1670-1681.
76. L. Ronconi, L. Giovagnini, C. Marzano, F. Bettio, R. Graziani, G. Pilloni and D. Fregona, *Inorg. Chem.*, 2005, **44**, 1867-1881.
77. P. J. Barnard and S. J. Berners-Price, *Coord. Chem. Rev.*, 2007, **251**, 1889-1902.
78. V. Milacic and Q. P. Dou, *Coord. Chem. Rev.*, 2009, **253**, 1649-1660.
79. R. W.-Y. Sun and C.-M. Che, *Coord. Chem. Rev.*, 2009, **253**, 1682-1691.
80. H. J. A. Blaauw, R. J. F. Nivard and d. K. G. J. M. van, *J. Organomet. Chem.*, 1964, **2**, 236-244.
81. G. H. M. Calis, J. M. Trooster, M. T. Razi and P. J. Sadler, *J. Inorg. Biochem.*, 1982, **17**, 139-145.
82. T. P. Kennedy, *US20010016600A1*, 2001.
83. D. White, R. R. Whittle, G. W. Stowell, L. B. Whittall and T. Kennedy, *US20050096304A1*, 2005.
84. V. Milacic, D. Chen, L. Ronconi, K. R. Landis-Piwowar, D. Fregona and Q. P. Dou, *Cancer Res.*, 2006, **66**, 10478-10486.

Introduction

85. D. Saggioro, M. P. Rigobello, L. Paloschi, A. Folda, S. A. Moggach, S. Parsons, L. Ronconi, D. Fregona and A. Bindoli, *Chem. Biol. (Cambridge, MA, U. S.)*, 2007, **14**, 1128-1139.
86. U. Abram, J. Mack, K. Ortner and M. Muller, *J. Chem. Soc., Dalton Trans.*, 1998, 1011-1020.
87. U. Abram, K. Ortner, R. Gust and K. Sommer, *Dalton Trans.*, 2000, 735-744.
88. R. G. Buckley, A. M. Elsome, S. P. Fricker, G. R. Henderson, B. R. C. Theobald, R. V. Parish, B. P. Howe and L. R. Kelland, *J. Med. Chem.*, 1996, **39**, 5208-5214.
89. J. S. Casas, M. V. Castano, M. C. Cifuentes, J. C. Garcia-Monteaugudo, A. Sanchez, J. Sordo and U. Abram, *J. Inorg. Biochem.*, 2004, **98**, 1009-1016.
90. A. Castineiras, S. Dehnen, A. Fuchs, I. Garcia-Santos and P. Sevillano, *Dalton Trans.*, 2009, 2731-2739.
91. M. B. Dinger and W. Henderson, *J. Organomet. Chem.*, 1998, **560**, 233-243.
92. L. Engman, M. McNaughton, M. Gajewska, S. Kumar, A. Birmingham and G. Powis, *Anti-Cancer Drugs*, 2006, **17**, 539-544.
93. S. P. Fricker, R. M. Mosi, B. R. Cameron, I. Baird, Y. Zhu, V. Anastassov, J. Cox, P. S. Doyle, E. Hansell, G. Lau, J. Langille, M. Olsen, L. Qin, R. Skerlj, R. S. Y. Wong, Z. Santucci and J. H. McKerrow, *J. Inorg. Biochem.*, 2008, **102**, 1839-1845.
94. S. I. Garcia, A. Hagenbach and U. Abram, *Dalton Trans.*, 2004, 677-682.
95. C. H. A. Goss, W. Henderson, A. L. Wilkins and C. Evans, *J. Organomet. Chem.*, 2003, **679**, 194-201.
96. K. J. Kilpin, W. Henderson and B. K. Nicholson, *Polyhedron*, 2007, **26**, 434-447.
97. K. J. Kilpin, W. Henderson and B. K. Nicholson, *Polyhedron*, 2007, **26**, 204-213.
98. J. Mack, K. Ortner, U. Abram and R. V. Parish, *Z. Anorg. Allg. Chem.*, 1997, **623**, 873-879.
99. K. Ortner and U. Abram, *Inorg. Chem. Commun.*, 1998, **1**, 251-253.
100. K. Ortner and U. Abram, *Polyhedron*, 1999, **18**, 749-754.
101. R. V. Parish, J. Mack, L. Hargreaves, J. P. Wright, R. G. Buckley, A. M. Elsome, S. P. Fricker and B. R. C. Theobald, *J. Chem. Soc., Dalton Trans.*, 1996, 69-74.
102. J. Vicente, M. D. Bermudez, M. T. Chicote and M. J. Sanchez-Santano, *J. Organomet. Chem.*, 1989, **371**, 129-135.
103. J. Vicente, M. D. Bermudez, M. T. Chicote and M. J. Sanchez-Santano, *J. Organomet. Chem.*, 1990, **381**, 285-292.
104. J. Vicente, M. D. Bermudez, M. T. Chicote and M. J. Sanchez-Santano, *J. Chem. Soc., Dalton Trans.*, 1990, 1945-1950.
105. J. Vicente, M. D. Bermudez, M. J. Sanchez-Santano and J. Paya, *Inorg. Chim. Acta*, 1990, **174**, 53-56.
106. J. Vicente, M. T. Chicote and M. D. Bermudez, *J. Organomet. Chem.*, 1984, **268**, 191-195.
107. J. Vicente, M. T. Chicote, M. D. Bermudez, M. J. Sanchez-Santano and P. G. Jones, *J. Organomet. Chem.*, 1988, **354**, 381-390.
108. J. Vicente, M. T. Chicote, M. D. Bermudez, M. J. Sanchez-Santano, P. G. Jones, C. Fittschen and G. M. Sheldrick, *J. Organomet. Chem.*, 1986, **310**, 401-409.
109. J. Vicente, C. M. Teresa, R. Guerrero, U. Herber and D. Bautista, *Inorg. Chem.*, 2002, **41**, 1870-1875.
110. L. Messori, G. Marcon and P. Orioli, *Bioinorg. Chem. Appl.*, 2003, 177-187.

Introduction

111. Z. Abou-Gamra, A. Harriman and P. Neta, *J. Chem. Soc., Faraday Trans. 2*, 1986, **82**, 2337-2350.
112. A. Antipas, D. Dolphin, M. Gouterman and E. C. Johnson, *J. Am. Chem. Soc.*, 1978, **100**, 7705-7709.
113. E. B. Fleischer and A. Laszlo, *Inorg. Nucl. Chem. Lett.*, 1969, **5**, 373-376.
114. M. E. Jamin and R. T. Iwamoto, *Inorg. Chim. Acta*, 1978, **27**, 135-143.
115. K. M. Kadish, W. E. Z. Ou, J. Shao, P. J. Sentic, K. Ohkubo, S. Fukuzumi and M. J. Crossley, *Chem. Commun. (Cambridge, U. K.)*, 2002, 356-357.
116. Z. Ou, K. M. Kadish, E. Wenbo, J. Shao, P. J. Sentic, K. Ohkubo, S. Fukuzumi and M. J. Crossley, *Inorg. Chem.*, 2004, **43**, 2078-2086.
117. R. Timkovich and A. Tulinsky, *Inorg. Chem.*, 1977, **16**, 962-963.
118. D. Kessel and T. H. Chou, *Adv. Exp. Med. Biol.*, 1983, **160**, 115-127.
119. R. W.-Y. Sun, C. K.-L. Li, D.-L. Ma, J. J. Yan, C.-N. Lok, C.-H. Leung, N. Zhu and C.-M. Che, *Chem.--Eur. J.*, 2010, **16**, 3097-3113, S3097/3091-S3097/3030.
120. Y. F. To, R. W.-Y. Sun, Y. Chen, V. S.-F. Chan, W.-Y. Yu, P. K.-H. Tam, C.-M. Che and C.-L. S. Lin, *Int. J. Cancer.*, 2009, **124**, 1971-1979.
121. Y. Wang, Q.-Y. He, R. W.-Y. Sun, C.-M. Che and J.-F. Chiu, *Cancer Res.*, 2005, **65**, 11553-11564.
122. A.-F. Aubry, N. Markoglou, M. H. Adams, J. Longstreth and I. W. Wainer, *J. Pharm. Pharmacol.*, 1995, **47**, 937-944.
123. C. L. Litterst and V. G. Schweitzer, *Res. Commun. Chem. Pathol. Pharmacol.*, 1988, **61**, 35-48.
124. Y. Wang, Q.-Y. He, R. W.-Y. Sun, C.-M. Che and J.-F. Chiu, *Eur. J. Pharmacol.*, 2007, **554**, 113-122.
125. Y. F. To, R. W.-Y. Sun, Y. Chen, V. S.-F. Chan, W.-Y. Yu, P. K.-H. Tam, C.-M. Che and C.-L. S. Lin, *Int. J. Cancer*, 2009, **124**, 1971-1979.
126. A. Casini, C. Hartinger, C. Gabbiani, E. Mini, P. J. Dyson, B. K. Keppler and L. Messori, *J. Inorg. Biochem.*, 2008, **102**, 564-575.
127. C. K.-L. Li, R. W.-Y. Sun, S. C.-F. Kui, N. Zhu and C.-M. Che, *Chem.--Eur. J.*, 2006, **12**, 5253-5266.
128. G. Marcon, S. Carotti, M. Coronello, L. Messori, E. Mini, P. Orioli, T. Mazzei, M. A. Cinellu and G. Minghetti, *J. Med. Chem.*, 2002, **45**, 1672-1677.
129. L. Messori, F. Abbate, G. Marcon, P. Orioli, M. Fontani, E. Mini, T. Mazzei, S. Carotti, T. O'Connell and P. Zanello, *J. Med. Chem.*, 2000, **43**, 3541-3548.
130. K.-H. Wong, K.-K. Cheung, M. C.-W. Chan and C.-M. Che, *Organometallics*, 1998, **17**, 3505-3511.
131. W. H. Baddley, F. Basolo, H. B. Gray, C. Nolting and A. J. Poe, *Inorg. Chem.*, 1963, **2**, 921-928.
132. B. P. Block and J. C. Bailar, Jr., *J. Am. Chem. Soc.*, 1951, **73**, 4722-4725.
133. E. Kimura, Y. Kurogi and T. Takahashi, *Inorg. Chem.*, 1991, **30**, 4117-4121.
134. S. Carotti, A. Guerri, T. Mazzei, L. Messori, E. Mini and P. Orioli, *Inorg. Chim. Acta*, 1998, **281**, 90-94.
135. S. L. Barnholtz, J. D. Lydon, G. Huang, M. Venkatesh, C. L. Barnes, A. R. Ketrings and S. S. Jurisson, *Inorg. Chem.*, 2001, **40**, 972-976.
136. G. Gupta, S. Gloria, S. L. Nongbri, B. Therrien and K. M. Rao, *J. Organomet. Chem.*, 2011, **696**, 2014-2022.

Introduction

137. M. S. Saraiva, S. Quintal, F. C. M. Portugal, T. A. Lopes, V. Felix, J. M. F. Nogueira, M. Meireles, M. G. B. Drew and M. J. Calhorda, *J. Organomet. Chem.*, 2008, **693**, 3411-3418.
138. Z.-H. Ni, H.-Z. Kou, L.-F. Zhang, W.-W. Ni, Y.-B. Jiang, A.-L. Cui, J. Ribas and O. Sato, *Inorg. Chem.*, 2005, **44**, 9631-9633.
139. I. Y. Yoo, D. W. Ryu, J. H. Yoon, A. R. Sohn, K. S. Lim, B. K. Cho, E. K. Koh and C. S. Hong, *Dalton Trans.*, 2012, **41**, 1776-1785.
140. C. Che, *WO2004024146A1*, 2004.
141. P. Mascharak, *J. Am. Chem. Soc.*, 2008, **130**, 2880-2882.
142. T. Yang, J.-Y. Zhang, C. Tu, J. Lin, Q. Liu and Z.-J. Guo, *Wuji Huaxue Xuebao*, 2003, **19**, 45-48.
143. T.-C. Cheung, T.-F. Lai and C.-M. Che, *Polyhedron*, 1994, **13**, 2073-2077.
144. D. Fan, C.-T. Yang, J. D. Ranford and J. J. Vittal, *Dalton Trans.*, 2003, 4749-4753.
145. D. T. Hill, K. Burns, D. D. Titus, G. R. Girard, W. M. Reiff and L. M. Mascavage, *Inorg. Chim. Acta*, 2003, **346**, 1-6.
146. M. A. Cinellu, L. Maiore, G. Minghetti, F. Cocco, S. Stoccoro, A. Zucca, M. Manassero and C. Manassero, *Organometallics*, 2009, **28**, 7015-7024.
147. L. Maiore, M. A. Cinellu, S. Nobili, I. Landini, E. Mini, C. Gabbiani and L. Messori, *J. Inorg. Biochem.*, 2012, **108**, 123-127.
148. S. Wang, J. Zhang, S. Li, X. Qin, C. Song and W. Shao, *CN102268027A*, 2011.
149. C. G. Hartinger, S. Zorbas-Seifried, M. A. Jakupec, B. Kynast, H. Zorbas and B. K. Keppler, *J. Inorg. Biochem.*, 2006, **100**, 891-904.

2. Experimental

2.1 General methods and instrumentation

All reactions were carried out open to the atmosphere unless otherwise stated. All solvents used were either dry or of high purity. Pyridine, methanol and nitromethane were Chromosolve® HPLC grade solvents, used as received from Aldrich. THF and DCM were distilled over calcium hydride. All reagents were used as received from Aldrich unless otherwise stated. Gold pellets were received as a loan from Mintek as part of project AuTEK Biomed.

Electronic spectra were recorded with a Shimadzu UV-1800 (fixed slit width = 1 nm) spectrophotometer using varying solvents in 1.0 cm pathlength quartz cuvettes. IR spectra were obtained on a Bruker Alpha spectrometer (36 scans, spectral resolution = 1.0 cm^{-1}) with an ATR platinum Diamond 1 reflectance accessory for analysis of microcrystalline samples. ^1H and ^{13}C NMR spectra were recorded using saturated solutions in DMSO- d_6 , CD_3CN or CDCl_3 using either a 500 MHz Bruker Avance III spectrometer equipped with a 11.7 T magnet and 5 mm BBO probe, or a 400 MHz Bruker Avance III spectrometer equipped with a 9.4 T magnet and 5 mm BBOF probe. The solvent signal was used as the reference. All spectra were recorded at 303.15 K unless otherwise stated. The proton and carbon NMR spectra were assigned using 2D COSY data, with the help of HSQC and HMBC data where needed. High resolution masses were recorded by direct injection into a Waters Acquity-LCT Premier mass spectrometer using electrospray ionisation in either positive or negative mode. Emission spectra were recorded on a Photon Technologies Int. (PTI) fluorescence spectrometer controlled by PTI's Felix32© Version 1.1 software. Steady state emission spectra were recorded using PTI's Xenoflash™ 300 Hz pulsed light source. Detection was by means of PTI's Model 814 Analog/Photon-Counting Photomultiplier Detector.

Experimental

2.2 Synthesis of 3-Aroyl-2-pyridinecarboxylic acid precursors, APC1, APC2, APC3.

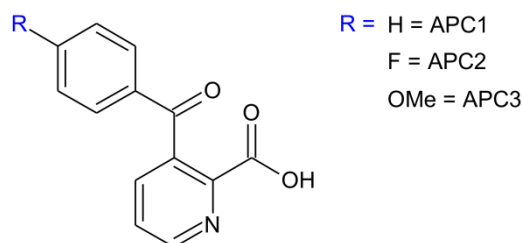


Figure 2.2.1: labelling scheme used for aroyl-2-pyridinecarboxylic acids.

A modified procedure of Youssef¹ and co-worker's procedure was used, whereby; anhydrous aluminium chloride (4.00 g, 30.0 x 10⁻³ mol) was added to a stirred mixture of dry aromatic substrate (10 mL) and quinolinic anhydride (1.00 g, 6.70 x 10⁻³ mol). The reaction mixture was then heated to 80 °C for 4-5 h after which the formed complex was decomposed with conc. HCl to form a clear solution. The solution was then placed on ice while 10 mL of ice-water was added and the mixture stirred vigorously until a cream/white coloured precipitate had formed. The precipitate was collected by vacuum filtration and allowed to air dry before characterisation. **APC1:** ¹H NMR (400 MHz, CDCl₃, 303 K) [δ, ppm]: 8.83 (d, 1H); 7.99 (d, 1H); 7.74 (m, 3H), 7.65 (m, 3H); 7.52 (m, 2H); 4.32 (s, 1H). **APC2:** ¹H NMR (400 MHz, CDCl₃, 303 K) [δ, ppm]: 8.83 (d, 1H); 7.99 (d, 1H); 7.75 (m, 3H), 7.34 (m, 2H); 4.48 (s, 1H). **APC3:** ¹H NMR (400 MHz, CDCl₃, 303 K) [δ, ppm]: 8.80 (d, 1H); 7.94 (d, 1H); 7.73 (m, 1H), 7.63 (m, 2H); 7.04 (m, 2H); 4.77 (s, 1H); 3.83 (s, 3H). All other characterisation data were in agreement with the relevant data in the literature.¹

Experimental

2.3 Synthesis of gold(III) metal precursors

2.3.1 Synthesis of tetrabutylammonium tetrachloroaurate(III), [Bu₄N][AuCl₄], gold precursor

Elemental gold (500 mg, 2.54×10^{-3} mol) was added to aqua regia (3 mL) and allowed to dissolve overnight. The solution was then stirred and heated to boiling while a further 2 mL of HCl (33%) was added. Heating was continued and the solution was allowed to evaporate to about 5% of the original volume before ultra-pure water (3 mL) was added. The solution was again allowed to boil and evaporate to about 5% of the original volume; this process was repeated until the vapours released were no longer acidic. The viscous aurochloric acid was then dissolved in ultra-pure water (100 mL), to which tetrabutylammonium hydrogen sulphate (0.82 g, 2.54×10^{-3} mol) was added to form a yellow precipitate. The solid was extracted repeatedly with DCM. The DCM extract was then dried over anhydrous MgSO₄ and then evaporated to dryness to afford [Bu₄N][AuCl₄] as a yellow solid.

2.3.2 Synthesis of potassium tetrachloroaurate(III), KAuCl₄, gold precursor

Hydrogen tetrachloroaurate(III) was prepared from gold pellets as described above. The viscous aurochloric acid was then dissolved in ultra-pure water/EtOH (2:8, 100 mL), to which KCl (0.189 g, 2.54×10^{-3} mol) was added. The solution was then stirred for 6 h after which the solvent was removed under vacuum to afford K[AuCl₄] as a yellow powder.

Experimental

2.4 Synthesis of amide ligands

2.4.1 General procedure for synthesis of bis(amide) ligands

To a solution of pyridine- or isoquinoline-3-carboxylic acid (1.624×10^{-2} mol) in dry pyridine (15 mL) was added diamine (8.122×10^{-3} mol) in pyridine (5 mL). The mixture was stirred for 5 minutes during which a white precipitate formed. The mixture was then heated to 110 °C and triphenylphosphite (5.041 g, 1.624×10^{-2} mol) was added drop-wise and the mixture stirred at 110 °C for 4 h.

2.4.1.1 *N,N'*-ethane-1,2-diyl dipyridine-2-carboxamide, H₂L1

The solution was then allowed to cool and stand overnight, after which the product crystallised out of solution. The product was isolated by filtration and washed with diethylether (2 x 25 mL) and distilled water (2 x 25 mL) to obtain colourless clear crystals of H₂L1. X-ray quality crystals were obtained by slow evaporation of a saturated solution of H₂PyEt in DMSO. ¹H NMR (400 MHz, CDCl₃, 303 K) [δ, ppm]: 8.56 (d, 2H, *J* = 4.41 Hz); 8.40 (s, 2H); 8.21 (d, 2H, *J* = 7.76 Hz); 7.84 (t, 2H, *J* = 7.71 Hz); 7.43 (m, 2H); 3.77 (m, 4H). All further characterization data were in agreement with the relevant data in the literature.²

2.4.1.2 *N,N'*-propane-1,3-diyl dipyridine-2-carboxamide, H₂L2

The solution was then allowed to cool and 15 mL of chloroform added. This solution was then washed with distilled water (3 x 25 mL), followed by a saturated solution of sodium hydrogen carbonate (4 x 25 mL) and then again with distilled water (3 x 25 mL). The solution was then dried over anhydrous MgSO₄, filtered and the solvent removed to leave a brown oil. The oil was taken up in a minimal amount of chloroform and added drop-wise to vigorously stirred ice-cold diethylether. The solution was then filtered and washed with diethylether (2 x 25 mL) and distilled water (2 x 25 mL) to obtain a cream solid. A solution of H₂L2 in chloroform/diethylether (1 : 6) was allowed to slowly evaporate from a test tube to afford X-ray quality crystals. ¹H NMR (400 MHz, CDCl₃, 303 K) [δ, ppm]: 8.55 (d, 2H, *J* = 4.80 Hz); 8.41 (s, 2H); 8.21 (d, 2H, *J* = 7.79 Hz); 7.84 (t, 2H, *J* = 7.71 Hz); 7.41 (m, 2H); 3.60 (m, 4H); 1.96 (m, 2H). All further characterisation data were in agreement with the relevant data in the literature.²

Experimental

2.4.1.3 *N,N'*-benzene-1,2-diyldiisoquinoline-3-carboxamide, H₂L3

The solution was then allowed to cool and stand overnight, after which the product precipitated out of solution. The product was then filtered and washed with diethylether (2 x 25 mL) and distilled water (2 x 25 mL) to obtain a white powder. X-ray quality crystals were obtained by diffusion of diethyl ether into a saturated solution of H₂QuPh in DCM.

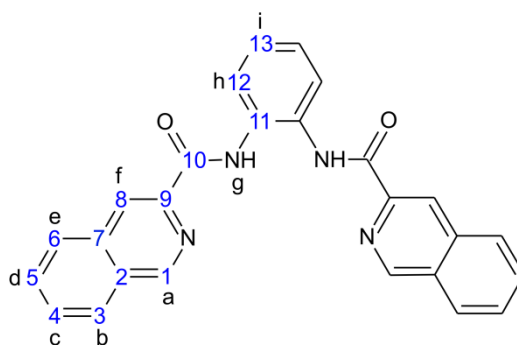


Figure 2.4.1.1: Numbering scheme employed for NMR characterisation of H₂L3, black letters correspond to ¹H NMR signals and blue numbers correspond to ¹³C NMR signals.

Yield, 65% (colourless crystals). TOF MS ES: *m/z* 419.1507 (calc, 419.1508), M⁺. IR (powder, cm⁻¹): 3337 (s, ν(N-H), R-NH-COR); 1689 (s, ν(CO), RNH-CO-R). ¹H NMR (500 MHz, DMSO-*d*₆, 303.15 K) [δ, ppm]: 10.90 (s, 2H, *g*); 9.36 (s, 2H, *a*); 8.73 (s, 2H, *f*); 8.25 (d, 4H, *J* = 9.0 Hz, *e,b*); 7.90 (ddd, 2H, *J*₁ = 9.4 Hz, *J*₂ = 4.3 Hz, *J*₃ = 1.2 Hz, *d*); 7.87 (dd, 2H, *J*₁ = 5.9 Hz, *J*₂ = 3.6 Hz, *h*); 7.82 (ddd, 2H, *J*₁ = 9.3 Hz, *J*₂ = 4.3 Hz, *J*₃ = 1.1 Hz *c*); 7.33 (dd, 2H, *J*₁ = 6.0 Hz, *J*₂ = 3.6 Hz, *i*). ¹³C NMR (123 MHz, DMSO-*d*₆, 303.15 K) [δ, ppm]: 163.62 (C-10); 152.13 (C-1); 143.76 (C-9); 135.91 (C-11); 132.01 (C-5); 131.67 (C-7); 129.92 (C-4); 129.89 (C-2); 128.59 (C-3); 128.37 (C-6); 126.07 (C-12); 125.68 (C-13); 121.04 (C-8).

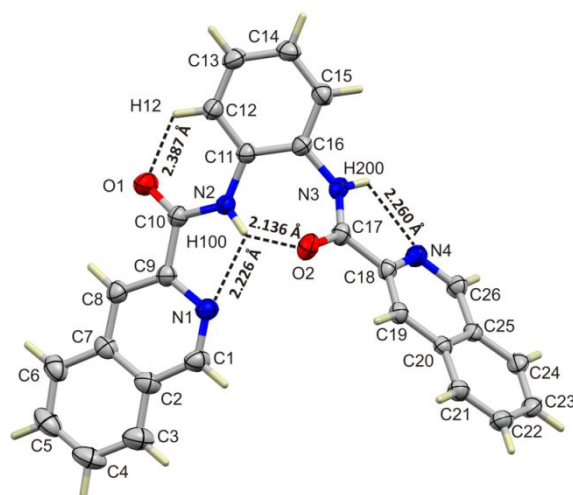


Figure 2.4.1.2: Fully labelled thermal ellipsoid view (50% probability surfaces) of the molecular structure of H₂L3. All hydrogen atoms are shown as sticks. The four intramolecular hydrogen bonds present are rendered as a broken black line (N1...H100, 2.23 Å; N1...N2, 2.681(2) Å; N1...H100–N2, 113(1)°; O2...H100, 2.14 Å; O2...N2, 2.830(2) Å; O2...H100–N2, 137(2)°; O1...H12, 2.39 Å; O1...C12, 2.882(2) Å; O2...H100–N2, 113(1)°; N4...H200, 2.26 Å; N4...N3, 2.684(2) Å; N4...H200–N3, 111(2)°).

Chemical formula, C₂₆H₁₈N₄O₂; Mr, 418.44; crystal system, monoclinic; space group, *P*2₁/*n* temperature (K), 296 (2); *a*, *b*, *c* (Å): 5.7773 (2), 13.3867 (5), 26.7245 (9); α , β , γ (°): 90, 93.836 (3), 90; *V* (Å³), 2062.22 (13); *Z*, 4; radiation type, Mo K α ; μ (mm⁻¹), 0.09; crystal size (mm), 0.60 × 0.20 × 0.10; *N_m* (number of measured reflections), *N_i* (number of independent reflections), *N_o* (number of observed reflections with *I* > 2 σ (*I*)): 21333, 4036, 3035; *R_{int}*, 0.038; *R₁*, 0.049; *wR*(*F*²), 0.138; *S*, 1.06; *N_p* (number of parameters), 297; *N_{res}* (number of restraints), 0; $\Delta\rho_{max}$, $\Delta\rho_{min}$ (e Å⁻³): 0.23, -0.28.

Experimental

2.4.2 General procedure for synthesis of mono(amide) N-donor ligands

To a solution of pyridine-, isoquinoline-3- or isoquinoline-1-carboxylic acid (1.624×10^{-2} mol) in dry pyridine (15 mL) was added the relevant aryl or alkyl amine (1.624×10^{-2} mol) in pyridine (5 mL). The mixture was stirred for 5 minutes after which it was heated to 110 °C and triphenylphosphite (5.041 g, 1.624×10^{-2} mol) was added drop-wise and the mixture stirred at 110 °C for 4 h.

2.4.2.1 *N*-(4-methoxyphenyl)pyridine-2-carboxamide, HL4

The solution was then allowed to cool and stand overnight, after which the product crystallised out of solution. The product was then filtered and washed with diethylether (2 x 5 mL) and distilled water (2 x 25 mL) to obtain colourless clear crystals of HL4. ^1H NMR (400MHz, CDCl_3 , 303 K) [δ , ppm]: 9.92 (s, 1H); 8.62 (d, 1H, $J = 4.79$ Hz); 8.31 (d, 1H, U, $J = 7.80$ Hz); 7.91 (t, 1H, $J = 7.76$ Hz); 7.71 (d, 2H, $J = 9.02$ Hz); 7.48 (m, 1H); 6.94 (d, 2H, $J = 9.04$ Hz) 3.84 (s, 3H). All further characterisation data were in agreement with the relevant data in the literature.³

2.4.2.2 *N*-(pyridin-2-ylmethyl)pyridine-2-carboxamide, HL5

The solution was then allowed to cool and 15 mL of chloroform added. This solution was then washed with distilled water (3 x 25 mL), then with a saturated solution of sodium hydrogen carbonate (4 x 25 mL) and then again with distilled water (3 x 25 mL). The solution was then dried over anhydrous MgSO_4 , filtered and the solvent removed to leave a brown oil. ^1H NMR (400 MHz, CDCl_3 , 303 K) [δ , ppm]: 8.94 (s, 1H); 8.58 (m, 2H); 8.21 (d, 1H, $J = 7.83$ Hz); 7.83 (t, 1H, $J = 7.73$ Hz); 7.66 (t, 1H, $J = 7.74$ Hz); 7.42 (m, 1H);); 7.35 (d, 1H, $J = 7.83$ Hz); 7.20 (t, 1H, $J = 5.01$ Hz). All further characterisation data were in agreement with the relevant data in the literature.⁴

Experimental

2.4.2.3 *N*-(pyridin-2-ylmethyl)isoquinoline-1-carboxamide, HL6

To the solution was added 20 mL of EtOH and 10 mL of H₂O and the flask stoppered and placed in the freezer overnight, after-which a microcrystalline product was isolated via vacuum filtration.

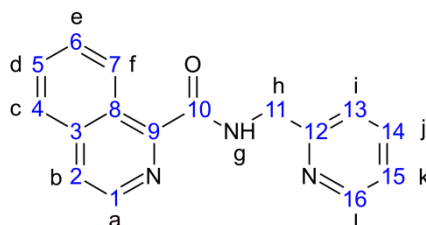


Figure 2.4.2.1: Numbering scheme employed for NMR characterisation of HL6, black letters correspond to ¹H NMR signals and blue numbers correspond to ¹³C NMR signals.

Yield, 62% (colourless crystals). TOF MS ES: *m/z* 286.0959 (calc, 286.0956), M⁺. IR (powder, cm⁻¹): 3298 (s, ν(N-H), R-NH-COR); 1646 (s, ν(CO), RNH-CO-R). ¹H NMR (400 MHz, CDCl₃, 303.15 K) [δ, ppm]: 9.58 (d, 1H, *J* = 8.30 Hz, *f*); 9.06 (s, 1H, *g*); 8.60 (d, 1H, *J* = 4.24 Hz, *l*); 8.50 (d, 1H, *J* = 5.52 Hz, *a*); 7.84 (m, 1H, *c*); 7.79 (d, 1H, *J* = 5.48 Hz, *b*); 7.71 (m, 1H, *e*); 7.69 (m, 2H, *d, k*); 7.41 (d, 1H, *J* = 7.80 Hz, *i*); 7.21 (m, 1H, *j*); 4.87 (d, 2H, *J* = 5.7 Hz, *h*). ¹³C NMR (100 MHz, CDCl₃, 303.15 K) [δ, ppm]: 166.26 (C-10); 157.15 (C-12); 149.21 (C-16); 148.27 (C-9); 140.41 (C-1); 137.39 (C-8); 136.90 (C-15); 130.43 (C-6); 128.59 (C-5); 127.78 (C-7); 127.06 (C-3); 126.76 (C-4); 124.31 (C-2); 122.34 (C-14); 44.81 (C-11).

Experimental

2.4.2.4 *N*-(pyridin-2-ylmethyl)quinoline-3-carboxamide, HL7

To the solution was added 20 mL of EtOH and 10 mL of H₂O and the flask stoppered and placed in the freezer overnight, after-which, a microcrystalline product was isolated via vacuum filtration.

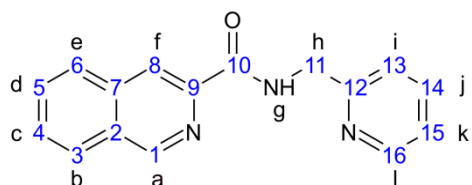


Figure 2.4.2.2: Numbering scheme employed for NMR characterisation of HL7, black letters correspond to ¹H NMR signals and blue numbers correspond to ¹³C NMR signals.

Yield, 58% (colourless crystals). TOF MS ES: *m/z* 286.0960 (calc, 286.0956), M⁺. IR (powder, cm⁻¹): 3349 (s, ν(N-H), R-NH-COR); 1652 (s, ν(CO), RNH-CO-R). ¹H NMR (400 MHz, CDCl₃, 303.15 K) [δ, ppm]: 9.19 (s, 1H, *a*); 9.11 (s, 1H, *g*); 8.63 (s, 1H, *f*); 8.60 (d, 1H, *J* = 4.28 Hz, *l*); 8.02 (d, 1H, *J* = 7.72 Hz, *e*); 8.98 (d, 1H, *J* = 8.12 Hz, *b*); 7.75 (m, 1H, *c*); 7.68 (m, 2H, *d*, *j*); 7.38 (d, 1H, *J* = 7.80 Hz, *i*); 7.20 (m, 1H, *k*); 4.86 (d, 2H, *J* = 5.72 Hz, *h*); ¹³C NMR (100 MHz, CDCl₃, 303.15 K) [δ, ppm]: 165.07 (C-10); 157.13 (C-12); 151.2 (C-1); 149.23 (C-16); 143.58 (C-9); 136.85 (C-14); 135.97 (C-7); 130.98 (C-4); 129.73 (C-2); 128.81 (C-5); 128.11 (C-3); 127.63 (C-6); 122.32 (C-15); 122.01 (C-13); 120.42 (C-8); 44.83 (C-11).

2.4.2.5 *N*-(quinolin-8-yl)pyridine-2-carboxamide, HL8

To the solution was added 20 mL of H₂O which afforded a light brown/cream coloured precipitate which was isolated by vacuum filtration and recrystallized from EtOH to afford pure HL8. ¹H NMR (400 MHz, CDCl₃, 303 K) [δ, ppm]: 10.65 (s, 1H); 9.00 (m, 1H); 8.67 (m, 1H); 8.52 (m, 1H); 7.79 (m, 1H); 7.70 (m, 2H);); 7.61 (m, 1H); 7.54 (m, 2H); 7.24 (m, 1H). All further characterisation data were in agreement with the relevant data in the literature.⁵

Experimental

2.4.2.6 5-butyl-*N*-(quinolin-8-yl)pyridine-2-carboxamide, HL9

To the solution was added 20 mL of H₂O which afforded a light brown/cream coloured precipitate which was isolated by vacuum filtration and recrystallised from EtOH to afford pure HL9.

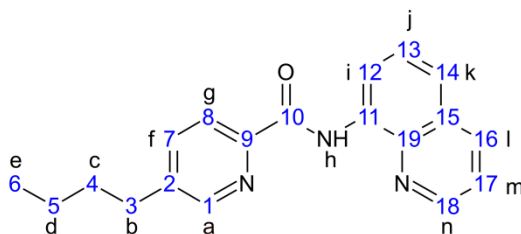


Figure 2.4.2.3: Numbering scheme employed for NMR characterisation of HL9, black letters correspond to ¹H NMR signals and blue numbers correspond to ¹³C NMR signals.

Yield, 73% (colourless crystals). TOF MS ES: *m/z* 328.1427 (calc, 328.1426), M⁺. IR (powder, cm⁻¹): 3303 (s, ν(N-H), R-NH-COR); 2958, 2926, 2857 (s, ν(C-H), butyl chain); 1676 (s, ν(CO), RNH-CO-R). ¹H NMR (400 MHz, CDCl₃, 303.15 K) [δ, ppm]: 12.22 (s, 1H, *h*); 9.00 (d, 1H, *J* = 8.32 Hz, *n*); 8.96 (m, 1H, *i*); 8.61 (s, 1H, *a*); 8.26 (d, 1H, *J* = 7.96 Hz, *g*); 8.18 (d, 1H, *J* = 8.24 Hz, *k*); 7.71 (m, 1H, *f*); 7.58 (m, 2H, *l, m*); 7.47 (m, 1H, *j*); 2.73 (t, 2H, *J* = 8.24 Hz, *b*); 1.67 (m, 2H, *c*); 1.39 (m, 2H, *d*); 0.96 (t, 3H, *J* = 7.32 Hz, *e*). ¹³C NMR (100 MHz, CDCl₃, 303.15 K) [δ, ppm]: 162.98 (C-10); 148.75 (C-1); 148.62 (C-18); 148.31 (C-11); 141.31 (C-9); 139.31 (C-19); 137.14 (C-7); 136.32 (C-14); 134.58 (C-15); 128.19 (C-2); 127.37 (C-17); 122.18 (C-8); 121.87 (C-16); 121.55 (C-13); 116.93 (C-12); 33.02 (C-6); 32.76 (C-5); 22.17 (C-4); 13.80 (C-3).

Experimental

2.4.2.7 *N*-(quinolin-8-yl)isoquinoline-1-carboxamide, HL10

To the solution was added 20 mL of H₂O which afforded a light brown/cream coloured precipitate which was isolated by vacuum filtration and recrystallised from EtOH to afford pure HL10.

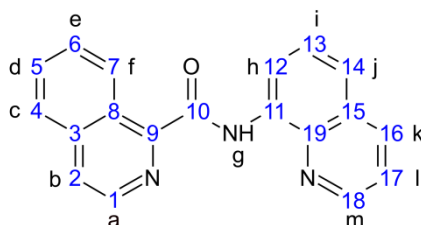


Figure 2.4.2.4: Numbering scheme employed for NMR characterisation of HL10, black letters correspond to ¹H NMR signals and blue numbers correspond to ¹³C NMR signals.

Yield, 80% (colourless crystals). TOF MS ES: *m/z* 322.0955 (calc, 322.0956), M⁺. IR (powder, cm⁻¹): 3272 (s, ν(N–H), R–NH–COR); 1671 (s, ν(CO), RNH–CO–R). ¹H NMR (500 MHz, CDCl₃, 303.15 K) [δ, ppm]: 12.42 (s, 1H, *g*); 9.69 (m, 1H, *f*); 9.07 (dd, 1H, *J*₁ = 7.57 Hz, *J*₂ = 1.32 Hz, *h*); 8.97 (dd, 1H, *J*₁ = 4.22 Hz, *J*₂ = 1.67 Hz, *m*); 8.71 (d, 1H, *J* = 5.50 Hz, *a*); 8.23 (dd, 1H, *J*₁ = 8.22 Hz, *J*₂ = 1.52 Hz, *j*); 7.91 (m, 1H, *c*); 7.89 (m, 1H, *b*); 7.75 (m, 2H, *d*, *e*); 7.65 (m, 1H, *l*); 7.59 (m, 1H, *k*); 7.51 (m, 1H, *i*). ¹³C NMR (123 MHz, CDCl₃, 303.15 K) [δ, ppm]: 164.32 (C-10); 148.53 (C-11); 148.40 (C-18); 140.42 (C-1); 139.08 (C-19); 137.66 (C-9); 136.79 (C-14); 134.58 (C-15); 130.64 (C-5 or 6); 128.82 (C-5 or 6); 128.30 (C-8); 127.77 (C-7); 127.52 (C-17); 127.25 (C-3); 127.00 (C-2); 124.61 (C-4); 122.11 (C-16); 121.57 (C-13); 117.37 (C-12).

Experimental

2.4.2.8 *N*-(quinolin-8-yl)isoquinoline-3-carboxamide, HL11

To the solution was added 20 mL of H₂O which afforded a light brown/cream coloured precipitate which was isolated by vacuum filtration and recrystallised from EtOH to afford pure HL11.

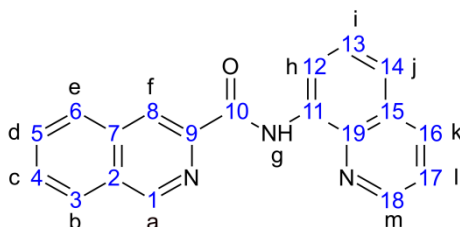


Figure 2.4.2.5: Numbering scheme employed for NMR characterisation of HL11, black letters correspond to ¹H NMR signals and blue numbers correspond to ¹³C NMR signals.

Yield, 85% (colourless crystals). TOF MS ES: *m/z* 322.0958 (calc, 322.0956), M⁺. IR (powder, cm⁻¹): 3301 (s, v(N-H), R-NH-COR); 1677 (s, v(CO), RNH-CO-R). ¹H NMR (400 MHz, CDCl₃, 303.15 K) [δ, ppm]: 12.46 (s, 1H, *g*); 9.39 (s, 1H, *a*); 9.09 (d, 1H, *J*₁ = 8.14 Hz, *h*); 9.01 (d, 1H, *J*₁ = 4.20 Hz, *m*); 8.78 (s, 1H, *f*); 8.20 (d, 1H, *J*₁ = 8.26 Hz, *j*); 8.09 (d, 1H, *J* = 7.84 Hz, *e*); 8.04 (d, 1H, *J* = 8.08 Hz, *b*); 7.78 (m, 1H, *c*); 7.73 (m, 1H, *d*); 7.64 (m, 1H, *l*); 7.57 (m, 1H, *k*); 7.50 (dd, 1H, *J*₁ = 8.24 Hz, *J*₂ = 4.20 Hz, *i*). ¹³C NMR (100 MHz, CDCl₃, 303.15 K) [δ, ppm]: 163.28 (C-10); 151.58 (C-1); 148.73 (C-18); 144.36 (C-9); 139.42 (C-19); 136.25 (C-14); 136.11 (C-7); 134.71 (C-15); 131.07 (C-4); 129.82 (C-2); 128.96 (C-5); 128.20 (C-3); 127.79 (C-6); 127.37 (C-17); 121.96 (C-16); 121.59 (C-13); 120.77 (C-8); 121.04 (C-12); C11 not observed.

2.4.2.9 3-benzoyl-*N*-(quinolin-8-yl)pyridine-2-carboxamide, HL12

To the solution was added 20 mL of H₂O which afforded a light brown/cream coloured precipitate which was isolated by vacuum filtration and recrystallised from EtOH to afford pure HL12.

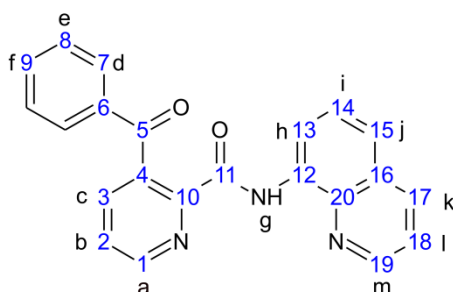


Figure 2.4.2.6: Numbering scheme employed for NMR characterisation of HL12, black letters correspond to ¹H NMR signals and blue numbers correspond to ¹³C NMR signals.

Yield, 69% (colourless crystals). TOF MS ES: *m/z* 376.1054 (calc, 376.1062), M⁺. IR (powder, cm⁻¹): 3289 (s, ν(N-H), R-NH-COR); 1664 (s, ν(CO), R-CO-R), 1579 (s, ν(CO), RNH-CO-R). ¹H NMR (400 MHz, CDCl₃, 303.15 K) [δ, ppm]: 12.17 (s, 1H, *g*); 8.97 (d, 1H, *J* = 4.24 Hz, *m*); 8.93 (d, 1H, *J* = 4.72 Hz, *a*); 8.76 (d, 1H, *J* = 7.52 Hz, *h*); 8.18 (d, 1H, *J* = 8.26 Hz, *k*); 7.84 (m, 2H, *d*); 7.80 (d, 1H, *J* = 7.70 Hz, *c*); 7.63 (dd, 1H, *J*₁ = 7.66 Hz *J*₂ = 4.74 Hz, *b*); 7.43-7.58 (m, 6H, *e, f, i, j, l*). ¹³C NMR (100 MHz, CDCl₃, 303.15 K) [δ, ppm]: 195.16 (C-5); 161.50 (C-11); 149.09 (C-1); 148.66 (C-19); 147.93 (C-10); 139.14 (C-20); 137.09 (C-4); 136.39 (C-17); 136.29 (C-3); 133.84 (C-6); 133.15 (C-8, 9, 14, 15 or 18); 129.33 (C-7); 128.58 (C-8, 9, 14, 15 or 18); 128.09 (C-16); 127.23 (C-8, 9, 14, 15 or 18); 125.88 (C-2); 122.29 (C-8, 9, 14, 15 or 18); 121.61 (C-8, 9, 14, 15 or 18); 117.45 (C-13); C-12 not observed.

Experimental

2.4.2.10 3-(4-fluorobenzoyl)-*N*-(quinolin-8-yl)pyridine-2-carboxamide, HL13

To the solution was added 20 mL of H₂O which afforded a light brown/cream coloured precipitate which was isolated by vacuum filtration and recrystallised from EtOH to afford pure HL9.

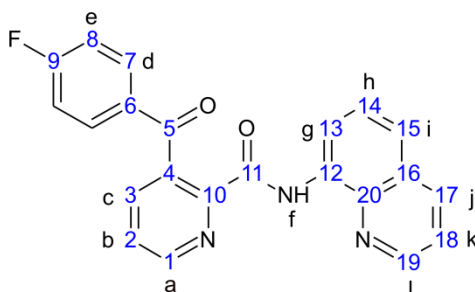


Figure 2.4.2.7: Numbering scheme employed for NMR characterisation of HL13, black letters correspond to ¹H NMR signals and blue numbers correspond to ¹³C NMR signals.

Yield, 60% (colourless crystals). TOF MS ES: *m/z* 394.0969 (calc, 394.0968), [(M+Na)⁺]. IR (powder, cm⁻¹): 3290 (s, ν(N-H), R-NH-COR); 1672 (s, ν(CO), R-CO-R), 1597 (s, ν(CO), RNH-CO-R). ¹H NMR (400 MHz, CDCl₃, 303.15 K) [δ, ppm]: 12.19 (s, 1H, *f*); 8.97 (d, 1H, *J* = 4.18 Hz, *l*); 8.93 (d, 1H, *J* = 4.68 Hz, *a*); 8.74 (d, 1H, *J* = 7.52 Hz, *g*); 8.18 (d, 1H, *J* = 8.24 Hz, *j*); 7.86 (m, 2H, *d*); 7.80 (d, 1H, *c*); 7.64 (m, 1H, *b*); 7.46-7.55 (m, 3H, *h, i* or *k*); 7.12 (m, 2H, *e*). ¹³C NMR (100 MHz, CDCl₃, 303.15 K) [δ, ppm]: 193.64 (C-5); 165.73 (C-9, *J* = 254.71 Hz); 161.42 (C-11); 149.22 (C-1); 148.75 (C-19); 147.88 (C-10); 139.25 (C-20); 136.77 (C-12); 136.27 (C-17); 136.23 (C-3); 133.85 (C-4); 133.66 (C-5, *J* = 3.09 Hz); 131.85 (C-7, *J* = 9.50 Hz); 128.09 (C-16); 127.19 (C-14, 15 or 18); 125.93 (C-2); 122.34 (C-14, 15 or 18); 121.64 (C-14, 15 or 18); 117.28 (C-13); 115.77 (C-8, *J* = 22.01 Hz). ¹⁹F NMR (376 MHz, CDCl₃, 303.15 K) [δ, ppm]: -105.07 (m, 1F).

Experimental

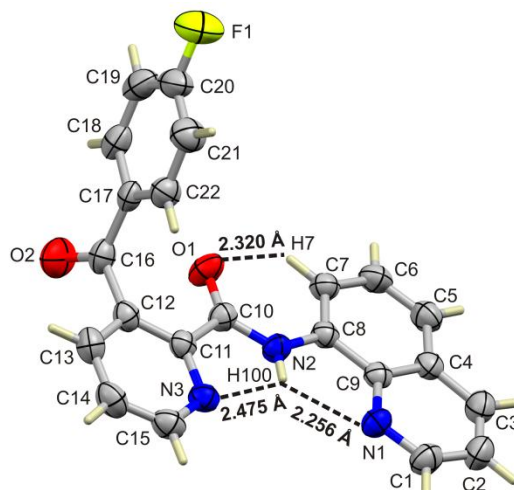


Figure 2.4.2.8: Fully labelled thermal ellipsoid view (50% probability surfaces) of the molecular structure of HL13. All hydrogen atoms are shown as sticks. The three intramolecular hydrogen bonds present are rendered as broken black lines (N1...H100, 2.26 Å; N1...N2, 2.655(1) Å; N1...H100-N2, 109(1)°; N3...H100, 2.48 Å; N3...N2, 2.640(1) Å; N3...H100-N2, 114(1)°; O1...H7, 2.32 Å; O1...C7, 2.918(1) Å; O1...H7-C7, 121(1)°).

Chemical formula, $C_{22}H_{14}N_3O_2F$; Mr, 371.36; crystal system, monoclinic; space group, $P2_1/c$ temperature (K), 298 (2); a , b , c (Å): 11.4112 (6), 7.6790 (5), 20.2481 (12); α , β , γ (°): 90, 91.217 (5), 90; V (Å³), 1773.87 (18); Z , 4; radiation type, Mo $K\alpha$; μ (mm⁻¹), 0.09; crystal size (mm), 0.40 × 0.20 × 0.40; Abs. correction, Multi-scan; T_{min} , T_{max} : 0.962, 0.981; N_m (number of measured reflections), N_i (number of independent reflections), N_o (number of observed reflections with $I > 2\sigma(I)$): 18426, 5690, 1968; R_{int} , 0.052; R_1 , 0.044; $wR(F^2)$, 0.109; S , 0.723; N_p (number of parameters) 257; N_{res} (number of restraints), 0; $\Delta\rho_{max}$, $\Delta\rho_{min}$ (e Å⁻³): 0.11, -0.22.

Experimental

2.4.2.9 3-(4-methoxybenzoyl)-*N*-(quinolin-8-yl)pyridine-2-carboxamide, HL14

To the solution was added 20 mL of H₂O which afforded a light brown/cream coloured precipitate which was isolated by vacuum filtration and recrystallised from EtOH to afford pure HPy8AmQ.

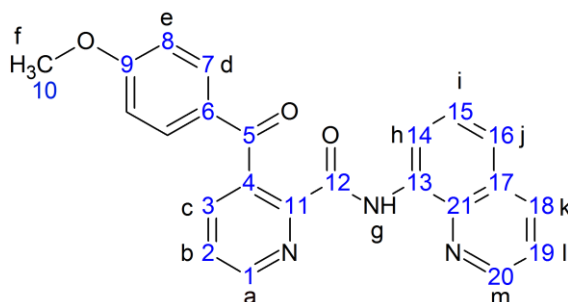


Figure 2.4.2.9: Numbering scheme employed for NMR characterisation of HL14, black letters correspond to ¹H NMR signals and blue numbers correspond to ¹³C NMR signals.

Yield, 71% (colourless crystals). TOF MS ES: *m/z* 406.1164 (calc, 406.1168), [(M+Na)⁺]. IR (powder, cm⁻¹): 3289 (s, ν(N-H), R-NH-COR); 1664 (s, ν(CO), R-CO-R), 1579 (s, ν(CO), RNH-CO-R). ¹H NMR (400 MHz, CDCl₃, 303.15 K) [δ, ppm]: 12.09 (s, 1H, *g*); 9.02 (d, 1H, *J* = 4.24 Hz, *m*); 8.99 (d, 1H, *J* = 4.72 Hz, *a*); 8.59 (d, 1H, *J* = 7.70 Hz, *h*); 8.43 (d, 1H, *J* = 8.30 Hz, *k*); 8.01 (d, 1H, *J* = 7.70 Hz, *c*); 7.86 (d, 2H, *J* = 7.74 Hz, *b*); 7.66-7.71 (m, 4H, *d, j, l*); 7.54 (m, 2H, *e*); 3.81 (s, 3H, *f*). ¹³C NMR (100 MHz, CDCl₃, 303.15 K) [δ, ppm]: 193.36 (C-5); 163.67 (C-9); 161.56 (C-12); 149.87 (C-1); 149.82 (C-19); 146.65 (C-11); 138.62 (C-13); 137.37 (C-4); 137.34 (C-3); 137.20 (C-18); 133.76 (C-21); 131.70 (C-7, 15 or 18); 130.32 (C-6); 128.34 (C-17); 127.57 (C-2); 127.45 (C-14); 123.11 (C-7, 15 or 18); 122.89 (C-7, 15 or 18); 116.46 (C-13); 114.48 (C-8); 56.02 (C-10).

Experimental

2.4.3 General procedure for synthesis of mono(amide) C, N-donor ligands

To a solution of acid chloride dissolved in dry THF was added a solution of 8-aminoquinoline in dry THF via cannula transfer under nitrogen atmosphere. The solution turned orange immediately and a precipitate started to form. The solution was stirred at room temperature overnight, after which it was washed with a saturated aqueous bicarbonate solution and extracted with 3 x 100 mL of chloroform. The organic phase was then isolated, dried over anhydrous magnesium sulphate, and its volume reduced to dryness in *vacuo* to afford the respective amide as a white solid. ***N*-(quinolin-8-yl)benzamide, H₂L15**: ¹H NMR (400 MHz, CDCl₃, 303 K) [δ, ppm]: 10.76 (s, 1H); 8.96 (d, 1H); 8.87 (d, 1H), 8.20 (d, 1H); 8.11 (d, 2H); 7.55-7.62 (m, 5H); 7.49 (dd, 1H). All other characterisation were in agreement with literature.⁶ ***N*-(quinolin-8-yl)naphthamide, H₂L16**: ¹H NMR (400 MHz, CDCl₃, 303 K) [δ, ppm]: 10.45 (s, 1H); 9.09 (d, 1H); 8.76 (d, 1H), 8.57 (m, 1H); 8.20 (d, 1H); 8.02 (d, 1H); 7.94 (m, 2H); 7.55-7.69 (m, 5H); 7.46 (dd, 1H). All other characterisation were in agreement with literature.⁷

Experimental

2.5 Synthesis of gold(III) metal complexes

2.5.1 General synthesis of *cis*-dichloro gold(III) chelates

A solution of the relevant ligand (5.29×10^{-4} mol) in DCM (15 mL) was added to a solution of $K[AuCl_4]$ (5.29×10^{-4} mol) in methanol (10 mL). This solution was then stirred while sodium acetate (6.00×10^{-4} mol) in methanol (10 mL) was added drop-wise, after which the reaction mixture was brought to reflux for 2 hours. The reaction mixture was then cooled to room temperature and allowed to stir overnight to afford an orange/red precipitate that was filtered off and washed with methanol (2 x 10 mL).

2.5.1.1 ((Pyridine-2-ylcarbonyl){2-[(pyridine-2-ylcarbonyl)amino]ethyl}azanido) dichlorogold(III), $[Au(HL1)Cl_2]$

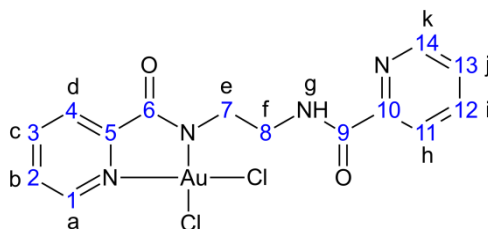


Figure 2.5.1.1: Numbering scheme employed for NMR characterisation of $[Au(HL1)Cl_2]$, black letters correspond to 1H NMR signals and blue numbers correspond to ^{13}C NMR signals.

Yield, 72% (orange powder). TOF MS (ES): m/z 558.9976 (calc, 558.9979), $[(M+Na)^+]$. UV-vis (CH_2Cl_2) [λ_{max} , nm (ϵ , $M^{-1} cm^{-1}$)]: 312 (5.1×10^3), 453 (1.6×10^2). IR (powder, cm^{-1}): 3360 (s, $\nu(N-H)$, R-NH-COR); 1645 (s, $\nu(CO)$, RNH-CO-R); 1602 (s, $\nu(CO)$, RN-CO-R). 1H NMR (400 MHz, $DMSO-d_6$, 303.15 K) [δ , ppm]: 9.32 (d, 1H, $J = 3.04$ Hz, a); 8.88 (t, 1H, $J = 5.93$ Hz, g); 8.56 (d, 1H, $J = 2.04$ Hz, k); 8.48 (t, 1H, $J = 7.64$ Hz, c); 8.03 (t, 1H, $J = 6.82$ Hz, b); 7.92 (m, 3H, d,h,i); 7.54 (m, 1H, j); 3.72 (t, 2H, $J = 5.42$ Hz, e); 3.57 (m, 2H, f). ^{13}C NMR (100 MHz, $DMSO-d_6$, 303.15 K) [δ , ppm]: 171.66 (C-6); 164.73 (C-9); 150.60 (C-11); 149.40 (C-10); 148.70 (C-5); 145.51 (C-1); 145.31 (C-3); 138.06 (C-2); 130.33 (C-4); 128.65 (C-14); 126.73 (C-13); 122.19 (C-12); 46.35 (C-7); 40.23 (C-8).

2.5.1.2 ((pyridine-2-ylcarbonyl){3-[pyridine-2-ylcarbonyl]amino}propyl)azanido dichlorogold(III), [Au(HL2)Cl₂]

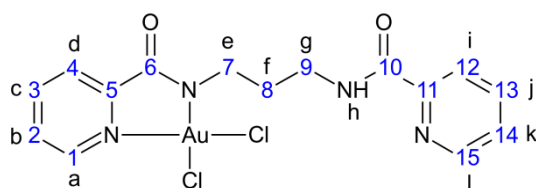


Figure 2.5.1.2: Numbering scheme employed for NMR characterisation of [Au(HL2)Cl₂], black letters correspond to ¹H NMR signals and blue numbers correspond to ¹³C NMR signals.

Yield, 78% (orange powder). TOF MS (ES): *m/z* 573.0134 (calc, 573.0135), [(M+Na)⁺]. UV-vis (CH₂Cl₂) [λ_{\max} , nm (ϵ , M⁻¹ cm⁻¹): 310 (3.9 x 10³), 449 (1.2 x 10²). IR (powder, cm⁻¹): 3392 (s, ν (N-H), R-NH-COR); 1666 (s, ν (CO), RNHCO- R); 1643 (s, ν (CO), RN-CO-R). ¹H NMR (400 MHz, DMSO-*d*₆, 303.15 K) [δ , ppm]: 9.29 (d, 1H, *J* = 2.85 Hz, a); 8.81 (t, 1H, *J* = 6.13 Hz, h); 8.61 (m, 1H, i); 8.50 (t, 1H, *J* = 7.72 Hz, b); 8.00 (m, 4H, c, d, k, l); 7.58 (m, 1H, j); 3.56 (m, 2H, e); 3.36 (m, 2H, g); 1.86 (m, 2H, f). ¹³C NMR (100 MHz, DMSO-*d*₆, 303.15 K) [δ , ppm]: 170.96 (C-6); 163.55 (C-10); 149.95 (C-15); 148.82 (C-11); 148.28 (C-5); 145.03 (C-1); 144.91 (C-3); 137.77 (C-13); 129.82 (C-2); 128.18 (C-4); 126.34 (C-14); 121.72 (C-12); 44.49 (C-7); 36.31 (C-9); 29.94 (C-8).

Experimental

2.5.1.3 ((Isoquinoline-3-ylcarbonyl){2-[isoquinoline-3-ylcarbonyl]amino}ethyl)azanido) dichlorogold(III), [Au(HL3)Cl₂]

The same procedure as the rest of the complexes was adopted except instead of the product being isolated by filtration, the solution was allowed to evaporate to dryness from a beaker to afford AuL3 as well as by product. The mixture was then dissolved in DCM and the byproduct filtered off. The solution was layered in test tubes with diethylether to afford clean AuL3 as a dark red powder. X-ray quality crystals were obtained by slow diffusion of diethylether into a saturated solution of AuL3 in nitromethane.

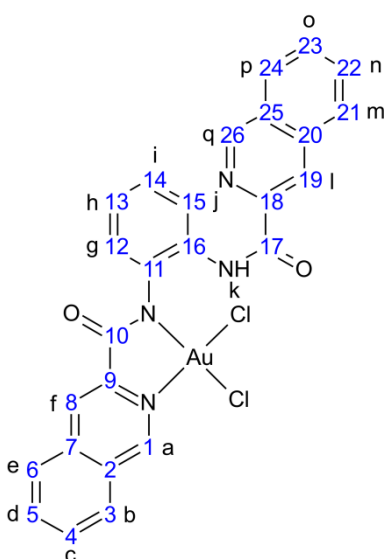


Figure 2.5.1.3: Numbering scheme employed for NMR characterisation of [Au(HL3)Cl₂], black letters correspond to ¹H NMR signals and blue numbers correspond to ¹³C NMR signals.

Yield, 30% (dark red powder). TOF MS (ES): *m/z* 685.0463 (calc, 685.0472), M⁺. IR (powder, cm⁻¹): 3324 (s, v(N-H), R-NH-COR); 1697 (s, v(CO), RNH-CO-R); 1622 (s, v(CO), RN-CO-R). UV-vis (CH₂Cl₂) [λ_{max} , nm (ϵ , M⁻¹ cm⁻¹): 240 (1.2 x 10⁵), 247 (1.0 x 10⁵), 297 (3.0 x 10⁴), 326 (2.2 x 10⁴), 468 (2.9 x 10³). ¹H NMR (400 MHz, DMSO-*d*₆, 303.15 K) [δ , ppm]: 10.85 (s, 1H, *k*); 10.33 (s, 1H, *a*); 9.10 (s, 1H, *q*); 8.84 (m, 2H, *e, f*); 8.69 (s, 1H, *l*); 8.53 (d, 1H, *J* = 8.14 Hz, *b*); 8.48 (d, 1H, *J* = 8.14 Hz, *j*); 8.29 (t, 1H, *J* = 7.75 Hz, *c*); 8.22 (s, 1H, *J* = 4.00 Hz, *p*); 8.13 (m, 2H, *m, d*); 7.88 (t, 1H, *J* = 7.51 Hz, *o*); 7.78 (t, 1H, *J* = 7.63 Hz, *n*); 7.47 (m, 2H, *h, g*); 7.22 (t, 1H, *J* = 7.54 Hz, *i*). ¹³C NMR (100 MHz, DMSO-*d*₆, 303.15 K) [δ , ppm]: 169.95 (C-10); 161.62 (C-17); 151.76 (C-26); 150.37 (C-1); 142.89 (C-18); 138.93 (C-5); 136.90 (C-9); 136.25 (C-16); 135.40 (C-11); 134.90 (C-4); 133.80 (C-14); 131.98 (C-3); 131.65 (C-22); 131.27 (C-7); 129.93 (C-12); 129.59

Experimental

(C-8); 129.51 (C-20); 129.27 (C-23); 128.64 (C-6); 128.60 (C-24), 128.11 (C-21); 127.88 (C-2); 127.86 (C-25); 123.64 (C-13); 120.25 (C-19); 119.30 (C-15).

2.5.1.4 {(4-Methoxyphenyl)(pyridine-2-ylcarbonyl)azanido}dichlorogold(III), [Au(L4)Cl₂]

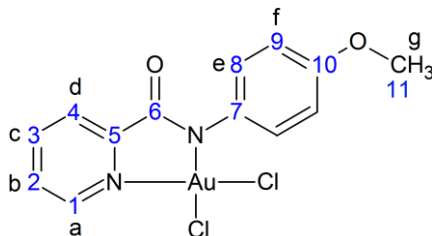


Figure 2.5.1.4: Numbering scheme employed for NMR characterisation of [Au(L4)Cl₂], black letters correspond to ¹H NMR signals and blue numbers correspond to ¹³C NMR signals.

Yield, 69% (dark red powder). TOF MS (ES): *m/z* 494.9947 (calc, 494.9941), M⁺. IR (powder, cm⁻¹): 2947, 3063, 3105 (s, v(CH); OCH₃) 1593 (s, v(CO), RN-CO-R). UV-vis (CH₂Cl₂) [λ_{max}, nm (ε, M⁻¹ cm⁻¹)]: 269 (1.8 × 10⁴), 377 (9.7 × 10³), 404 (6.5 × 10³), 477 (6.3 × 10³). ¹H NMR (400 MHz, DMSO-*d*₆, 303.15 K) [δ, ppm]: 9.36 (d, 1H, *J* = 2.86 Hz, *a*); 8.55 (t, 1H, *J* = 7.73 Hz, *c*); 8.09 (t, 1H, *b*); 8.08 (d, 1H, *d*); 7.20 (m, 2H, *e*); 6.91 (m, 2H, *f*); 3.78 (s, 3H, *g*). ¹³C NMR (100 MHz, DMSO-*d*₆, 303.15 K) [δ, ppm]: 169.83 (C-6); 158.26 (C-10); 148.26 (C-5); 144.98 (C-1); 144.98 (C-3); 137.14 (C-7); 130.04 (C-8); 130.01 (C-2) 128.44 (C-4); 113.36 (C-9); 55.24 (C-11).

Experimental

2.5.2 General synthesis of *N*-donor aminomethyl-based tridentate gold(III) chelates

K[AuCl₄] (2.943×10^{-4} mol) and the relevant ligand (2.943×10^{-4} mol) were dissolved in 25 mL ethanol and placed in a 50 mL round bottom flask and stirred. To this was added sodium acetate (2.943×10^{-4} mol) in 5 mL methanol and the solution brought to reflux for 4 h, after which a yellow precipitate was isolated by centrifugation and washed with 2 x 5 mL aliquots of methanol. The yellow precipitate was then added to a round bottom flask containing tetrabutylammonium chloride (3.100×10^{-4} mol) dissolved in DCM and the resulting suspension stirred for 3 h. The yellow precipitate was again collected by centrifugation and washed with 2 x 5 mL aliquots of DCM. The solid was then added to a test tube containing potassium hexafluorophosphate (3.100×10^{-4} mol) dissolved in acetonitrile and the solution heated until clear and then placed in a freezer at -20 °C for 15 minutes. The solution was then filtered to remove potassium chloride and precipitation was induced by addition of diethylether. The product was then isolated by centrifugation and washed with 2 x 5 mL portions of diethylether to afford the respective hexafluorophosphate salt of each complex. X-ray quality crystals were grown by vapour diffusion of diethylether into a saturated solution of complex in acetonitrile.

Experimental

2.5.2.1 (Pyridin-2-ylcarbonyl)(pyridin-2-ylmethyl)azanidogold(III) hexafluorophosphate(V), [Au(L5)Cl](PF₆)

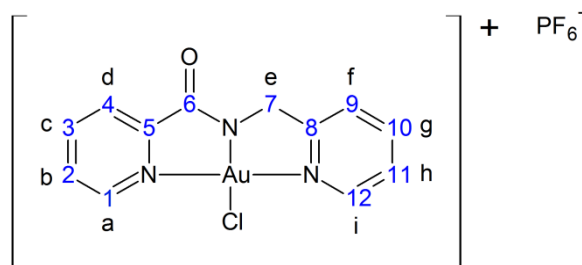


Figure 2.5.2.1: Numbering scheme employed for NMR characterisation of [Au(L5)Cl](PF₆), black letters correspond to ¹H NMR signals and blue numbers correspond to ¹³C NMR signals.

Yield, 60% (yellow powder, based on gold). TOF MS (ES): *m/z* 444.0182 (calc, 444.0178), M⁺. IR (powder, cm⁻¹): 1676 (s, v(CO), RN-CO-R). UV-vis (MeCN) [λ_{max} , nm (ϵ , M⁻¹ cm⁻¹): 224 (3.2 x 10⁴), 256 (5.5 x 10³), 317 (4.0 x 10³). ¹H NMR (400 MHz, CD₃CN, 303.15 K) [δ , ppm]: 9.12 (d, 1H, *J* = 5.36 Hz, *a*); 9.08 (d, 1H, *J* = 5.72 Hz, *i*); 8.54 (m, 1H, *c*); 8.38 (m, 1H, *g*); 8.03 (d, 1H, *J* = 8.11 Hz, *d*); 8.00 (m, 1H, *b*); 7.89 (d, 1H, *J* = 8.00 Hz, *f*); 7.78 (m, 1H, *h*); 5.36 (s, 2H, *e*). ¹³C NMR (100 MHz, CD₃CN, 303.15 K) [δ , ppm]: 170.69 (C-8); 166.15 (C-6); 152.53 (C-5); 148.91 (C-1); 148.58 (C-12); 146.21 (C-3); 144.47 (C-10); 131.03 (C-2); 129.35 (C-4); 126.39 (C-11); 125.06 (C-9); 56.52 (C-7). ¹⁹F NMR (376 MHz, CD₃CN, 303.15 K) [δ , ppm]: -70.17 (d, 6F). ³¹P NMR (162 MHz, CD₃CN, 303.15 K) [δ , ppm]: -144.20 (m, 1P).

Experimental

2.5.2.2 (Isoquinolin-1-ylcarbonyl)(pyridin-2-ylmethyl)azanidogold(III) hexafluorophosphate(V), [Au(L6)Cl](PF₆)

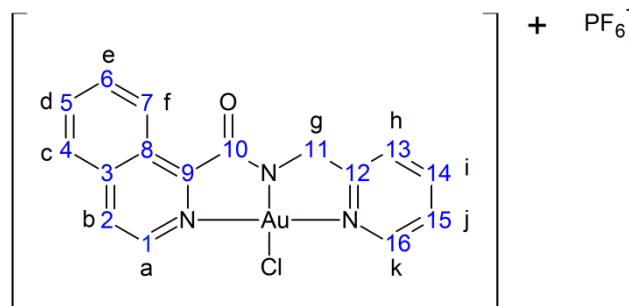


Figure 2.5.2.2: Numbering scheme employed for NMR characterisation of [Au(L6)Cl](PF₆), black letters correspond to ¹H NMR signals and blue numbers correspond to ¹³C NMR signals.

Yield, 58% (yellow powder, based on gold). TOF MS (ES): *m/z* 494.0337 (calc, 494.0334), *M*⁺. IR (powder, cm⁻¹): 1672 (s, v(CO), RN-CO-R). UV-vis (MeCN) [*λ*_{max}, nm (ε, M⁻¹ cm⁻¹): 226 (4.5 × 10⁴), 247 (5.1 × 10⁴), 301 (8.2 × 10³). ¹H NMR (500 MHz, CD₃CN, 303.15 K) [δ, ppm]: 9.85 (d, 1H, *J* = 8.90 Hz, *f*); 9.13 (t, 1H, *J* = 5.53 Hz, *k*); 9.07 (t, 1H, *J* = 6.55 Hz, *a*); 8.42 (d, 1H, *J* = 6.55 Hz, *b*); 8.40 (m, 1H, *i*); 8.29 (d, 1H, *J* = 6.55 Hz, *c*); 8.19 (m, 1H, *d*); 8.11 (m, 1H, *e*); 7.93 (d, 1H, *J* = 8.15 Hz, *h*); 7.80 (m, 1H, *j*); 5.42 (s, 2H, *g*). ¹³C NMR (123 MHz, CD₃CN, 303.15 K) [δ, ppm]: 170.15 (C-12); 168.00 (C-10); 148.63 (C-16); 144.48 (C-14); 140.17 (C-9); 138.99 (C-1); 137.64 (C-8); 135.99 (C-5); 131.96 (C-6); 128.83 (C-3); 128.59 (C-2); 127.87 (C-4); 126.38 (C-15); 125.03 (C-13); 124.87 (C-7); 56.69 (C-11). ¹⁹F NMR (376 MHz, CD₃CN, 303.15 K) [δ, ppm]: -70.18 (d, 6F). ³¹P NMR (162 MHz, CD₃CN, 303.15 K) [δ, ppm]: -144.19 (m, 1P).

Experimental

2.5.3 General synthesis of *N*-donor 8-aminoquinoline-based tridentate gold(III) chelates.

Initial method:

To a stirred solution of $\text{K}[\text{AuCl}_4]$ (2.943×10^{-4} mol) in 15 mL MeOH was added the relevant ligand (2.943×10^{-4} mol) dissolved in 15 mL DCM and heated. To the heated solution was added solid sodium acetate (2.943×10^{-4} mol) and the solution brought to reflux for 12 h, after which a brown precipitate was isolated by centrifugation and washed with 2 x 5 mL aliquots of water and dried in the oven.

Corrected method:

Chloride salt. $\text{K}[\text{AuCl}_4]$ (5.885×10^{-4} mol) and relevant ligand (2.943×10^{-4} mol) were dissolved in 25 mL acetic acid and placed in a 50 mL round bottom flask, stirred and heated. To the heated solution was added solid sodium bicarbonate (8.829×10^{-4} mol) and the solution brought to reflux for 12 h, after which a brown precipitate was isolated by centrifugation and washed with 2 x 5 mL aliquots of water. The brown precipitate was then added to a round bottom flask containing tetrabutylammonium chloride (3.100×10^{-4} mol) dissolved in DCM and the resulting suspension stirred for 12 h. The resulting orange/brown precipitate was again collected by centrifugation and washed with 2 x 5 mL aliquots of DCM.

Hexafluorophosphate salt. The chloride salt above was dissolved in boiling water prior to adding a saturated aqueous solution of potassium hexafluorophosphate. The resulting brown precipitate was then isolated by centrifugation and washed several times with water before drying in an oven at 100 °C. X-ray quality crystals were grown by slow diffusion of diethylether into a layered, saturated solution of complex in acetonitrile or nitromethane.

Experimental

2.5.3.1 (Pyridin-2-ylcarbonyl)(quinolin-8-yl)azanidogold(III) hexafluorophosphate(V), [Au(L8)Cl](PF₆)

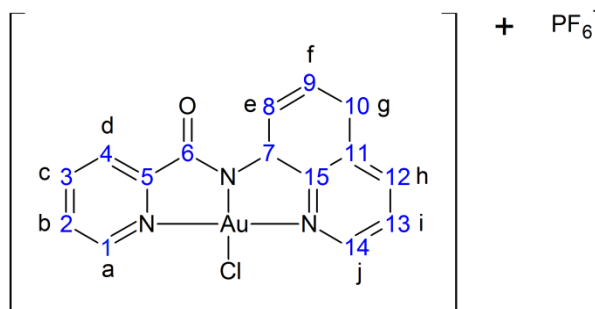


Figure 2.5.3.1: Numbering scheme employed for NMR characterisation of [Au(L8)Cl](PF₆), black letters correspond to ¹H NMR signals and blue numbers correspond to ¹³C NMR signals.

Yield, 86% (brown powder, based on gold). TOF MS (ES): *m/z* 480.0181 (calc, 480.0178), M⁺. IR (powder, cm⁻¹): 1655 (s, ν(CO), RN-CO-R). UV-vis (MeCN) [λ_{max} , nm (ϵ , M⁻¹ cm⁻¹): 256 (4.4 x 10⁴), 364 (1.2 x 10⁴). ¹H NMR (400 MHz, DMSO-*d*₆, 303.15 K) [δ , ppm]: 9.36 (d, 1H, *J* = 5.56 Hz, *j*); 9.21 (d, 1H, *J* = 5.74 Hz, *a*); 9.13 (d, 1H, *J* = 8.40 Hz, *j*); 8.69 (m, 1H, *c*); 8.65 (d, 1H, *J* = 8.40 Hz, *e*); 8.23 (d, 1H, *J* = 7.78 Hz, *d*); 8.16 (m, 1H, *b*); 8.08 (dd, 1H, *J*₁ = 8.36 Hz, *J*₂ = 5.56 Hz, *i*); 8.01 (d, 1H, *J* = 8.25 Hz, *g*); 7.91 (m, 1H, *f*). ¹³C NMR (100 MHz, DMSO-*d*₆, 303.15 K) [δ , ppm]: 164.68 (C-6); 153.73 (C-5); 151.44 (C-14); 149.25 (C-1); 146.87 (C-3); 146.20 (C-7); 145.50 (C-12); 141.73 (C-15); 132.26 (C-11); 132.07 (C-2); 131.58 (C-9); 130.42 (C-4); 125.70 (C-10); 124.92 (C-13); 122.21 (C-8). ¹⁹F NMR (376 MHz, DMSO-*d*₆, 303.15 K) [δ , ppm]: -70.18 (d, 6F). ³¹P NMR (162 MHz, DMSO-*d*₆, 303.15 K) [δ , ppm]: -144.21 (m, 1P).

Experimental

2.5.3.2 [(5-Butylpyridin-2-yl)carbonyl](quinolin-8-yl)azanidogold(III) dichloroaurate, [Au(L9)Cl](AuCl₂) using initial method.

Yield, 46% (brown powder, based on gold). TOF MS (ES): *m/z* 536.0808 (calc, 536.0804), M⁺. ¹H NMR shifts were found to be the same as the hexafluorophosphate salt. No further characterisation was undertaken.

2.5.3.2 [(5-Butylpyridin-2-yl)carbonyl](quinolin-8-yl)azanidogold(III) hexafluorophosphate(V), [Au(L9)Cl](PF₆)

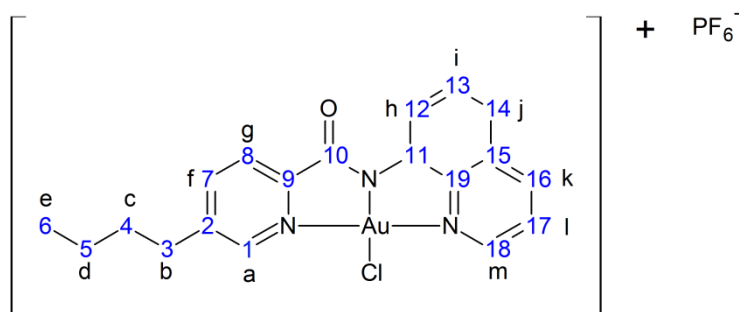


Figure 2.5.3.2: Numbering scheme employed for NMR characterisation of [Au(L9)Cl](PF₆), black letters correspond to ¹H NMR signals and blue numbers correspond to ¹³C NMR signals.

Yield, 64% (brown powder, based on gold). TOF MS (ES): *m/z* 536.0806 (calc, 536.0804), M⁺. IR (powder, cm⁻¹): 1663 (s, v(CO), RN-CO-R). UV-vis (MeCN) [λ_{max} , nm (ϵ , M⁻¹ cm⁻¹): 257 (6.4 x 10³), 362 (2.4 x 10⁴). ¹H NMR (400 MHz, DMSO-*d*₆, 303.15 K) [δ , ppm]: 9.36 (d, 1H, *J* = 5.54 Hz, *m*); 9.12 (d, 1H, *J* = 8.40 Hz, *k*); 8.99 (s, 1H, *a*); 8.64 (d, 1H, *J* = 7.74 Hz, *h*); 8.56 (d, 1H, *J* = 8.02 Hz, *f*); 8.15 (d, 1H, *J* = 8.00 Hz, *g*); 8.07 (dd, 1H, *J*₁ = 7.74 Hz, *J*₂ = 7.74 Hz, *l*); 8.00 (d, 2H, *J* = 8.31 Hz, *j*); 7.90 (m, 1H, *i*); 2.95 (t, 2H, *J* = 7.75 Hz, *b*); 1.65 (m, 2H, *c*); 1.37 (m, 2H, *d*); 0.94 (t, 3H, *J* = 7.34 Hz, *e*). ¹³C NMR (100 MHz, DMSO-*d*₆, 303.15 K) [δ , ppm]: 164.67 (C-10); 151.54 (C-9); 151.40 (C-18); 148.08 (C-1); 147.67 (C-2); 146.16 (C-7); 146.13 (C-11); 145.45 (C-16); 141.82 (C-19); 132.25 (C-15); 131.56 (C-13); 130.00 (C-8); 125.58 (C-14); 124.87 (C-17); 122.10 (C-12); 32.70 (C-4); 32.41 (C-3); 21.99 (C-5); 14.08 (C-6). ¹⁹F NMR (376 MHz, DMSO-*d*₆, 303.15 K) [δ , ppm]: -70.20 (d, 6F). ³¹P NMR (162 MHz, DMSO-*d*₆, 303.15 K) [δ , ppm]: -144.21 (m, 1P).

Experimental

2.5.3.3 (Isoquinolin-1-ylcarbonyl)(quinolin-8-yl)azanidogold(III) hexafluorophosphate(V), [Au(L10)Cl](PF₆)

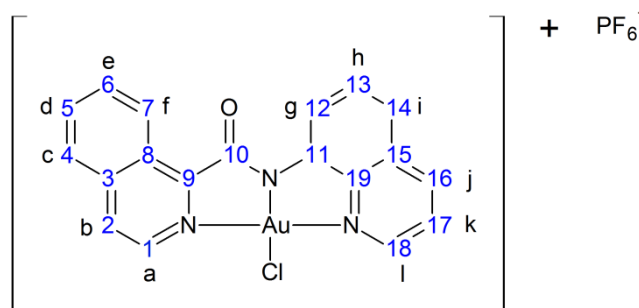


Figure 2.5.3.3: Numbering scheme employed for NMR characterisation of [Au(L10)Cl](PF₆), black letters correspond to ¹H NMR signals and blue numbers correspond to ¹³C NMR signals.

Yield, 89% (orange powder, based on gold). TOF MS (ES): *m/z* 530.0328 (calc, 530.0334), M⁺. IR (powder, cm⁻¹): 1662 (s, ν(CO), RN-CO-R). UV-vis (CH₂Cl₂) [*λ*_{max}, nm (ε, M⁻¹ cm⁻¹)]: 248 (6.7 × 10⁴), 304 (7.0 × 10³), 374 (9.0 × 10³). ¹H NMR (500 MHz, DMSO-*d*₆, 303.15 K) [δ, ppm]: 9.86 (d, 1H, *J* = 8.57 Hz, *f*); 9.41 (d, 1H, *J* = 5.55 Hz, *l*); 9.16 (d, 1H, *J* = 6.45 Hz, *a*); 9.14 (d, 1H, *J* = 5.55 Hz, *j*); 8.78 (d, 1H, *J* = 7.80 Hz, *g*); 8.68 (d, 1H, *J* = 6.50 Hz, *b*); 8.45 (d, 1H, *J* = 8.30 Hz, *c*); 8.27 (m, 1H, *d*); 8.21 (m, 1H, *e*); 8.10 (dd, 1H, *J*₁ = 8.37, *J*₂ = 5.52 Hz, *k*); 8.05 (d, 1H, *J* = 8.20 Hz, *i*); 7.94 (m, 1H, *h*). ¹³C NMR (123 MHz, DMSO-*d*₆, 303.15 K) [δ, ppm]: 166.31 (C-10); 151.38 (C-18); 151.05 (C-9); 146.31 (C-11); 145.44 (C-16); 141.88 (C-19); 140.02 (C-8); 139.54 (C-1); 136.25 (C-5); 132.75 (C-6); 132.26 (C-15); 131.58 (C-13); 129.61 (C-2); 128.99 (C-3); 128.82 (C-4); 125.96 (C-14); 124.92 (C-17); 124.84 (C-7); 122.73 (C-12). ¹⁹F NMR (376 MHz, DMSO-*d*₆, 303.15 K) [δ, ppm]: -70.10 (d, 6F). ³¹P NMR (162 MHz, DMSO-*d*₆, 303.15 K) [δ, ppm]: -144.19 (m, 1P).

Experimental

2.5.3.4 (Isoqionolin -3-ylcarbonyl)(quinolin-8-yl)azanidogold(III) hexafluorophosphate(V), [Au(L11)Cl](PF₆)

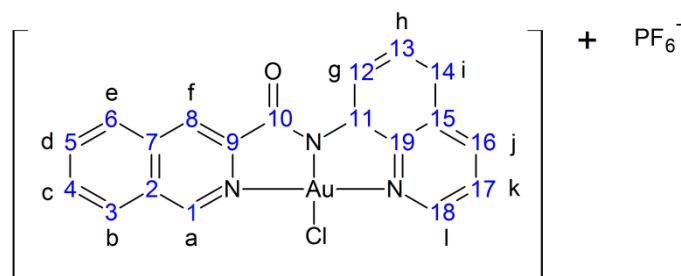


Figure 2.5.3.4: Numbering scheme employed for NMR characterisation of [Au(L11)Cl](PF₆), black letters correspond to ¹H NMR signals and blue numbers correspond to ¹³C NMR signals.

Yield, 87% (brown powder, based on gold). TOF MS (ES): *m/z* 530.0339 (calc, 530.0334), *M*⁺. IR (powder, cm⁻¹): 1666 (s, v(CO), RN-CO-R). UV-vis (MeCN) [λ_{max} , nm (ϵ , M⁻¹ cm⁻¹)]: 248 (9.3 x 10⁴), 304 (1.5 x 10⁴), 349 (1.2 x 10⁴). ¹H NMR (500 MHz, DMSO-*d*₆, 303.15 K) [δ , ppm]: 10.09 (s, 1H, *a*); 9.43 (d, 1H, *J* = 6.05 Hz, *l*); 9.14 (d, 1H, *J* = 6.05 Hz, *j*); 8.85 (s, 1H, *f*); 8.83 (d, 1H, *J* = 8.20 Hz, *e*); 8.74 (d, 1H, *J* = 7.86 Hz, *g*); 8.55 (d, 1H, *J* = 8.25 Hz, *b*); 8.31 (m, 1H, *c*); 8.17 (m, 1H, *d*); 8.10 (dd, 1H, *J*₁ = 8.20 Hz, *J*₂ = 8.20 Hz, *k*); 8.01 (m, 1H, *J* = 7.91 Hz, *i*); 7.92 (m, 1H, *h*). ¹³C NMR (123 MHz, DMSO-*d*₆, 303.15 K) [δ , ppm]: 164.49 (C-10); 153.89 (C-1); 150.90 (C-18); 145.44 (C-11); 144.93 (C-16); 144.66 (C-9); 141.62 (C-19); 136.90 (C-4); 136.62 (C-7); 132.50 (C-5); 131.68 (C-15); 131.37 (C-6); 131.05 (C-13); 129.60 (C-2); 129.23 (C-8); 128.87 (C-3); 124.93 (C-14); 124.30 (C-17); 121.74 (C-12). ¹⁹F NMR (376 MHz, DMSO-*d*₆, 303.15 K) [δ , ppm]: -70.21 (d, 6F). ³¹P NMR (162 MHz, DMSO-*d*₆, 303.15 K) [δ , ppm]: -144.21 (m, 1P).

Experimental

2.5.3.5 [3-(Benzoylpyridin-2-yl)carbonyl](quinolin-8-yl)azanidogold(III) hexafluorophosphate(V), [Au(L12)Cl](PF₆)

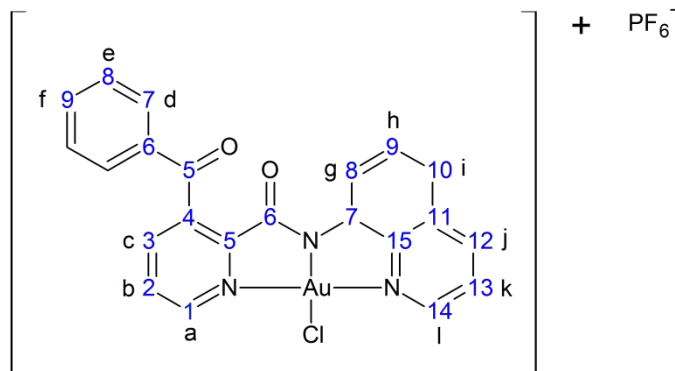


Figure 2.5.3.5: Numbering scheme employed for NMR characterisation of [Au(L12)Cl](PF₆), black letters correspond to ¹H NMR signals and blue numbers correspond to ¹³C NMR signals.

Yield, 82% (brown powder, based on gold). TOF MS (ES): *m/z* 584.0439 (calc, 584.0440), M⁺. IR (powder, cm⁻¹): 1658 (s, ν(CO), RN-CO-R), 1593 (s, ν(CO), R-CO-R). UV-vis (MeCN) [λ_{max}, nm (ε, M⁻¹ cm⁻¹): 253 (3.8 × 10⁴), 369 (7.7 × 10³). ¹H NMR (400 MHz, CDCl₃, 303.15 K) [δ, ppm]: 9.37 (m, 2H, *a*, *l*); 9.12 (d, 1H, *J* = 7.84 Hz, *j*); 8.77 (d, 1H, *J* = 7.90 Hz, *c*); 8.40 (d, 1H, *J* = 7.68 Hz, *h*); 8.28 (dd, 1H, *J*₁ = 7.88 Hz, *J*₂ = 5.76 Hz, *b*); 8.08 (dd, 1H, *J*₁ = 8.32 Hz, *J*₂ = 5.64 Hz, *k*); 7.98 (d, 1H, *i*); 7.86 (d, 2H, *J* = 8.45 Hz, *d*); 7.77 (m, 1H, *g*); 7.73 (m, 1H, *f*); 7.58 (m, 2H, *e*). ¹³C NMR (100 MHz, DMSO-*d*₆, 303.15 K) [δ, ppm]: 190.75 (C-5); 164.17 (C-11); 151.67 (C-19); 150.73 (C-10); 150.12 (C-1); 146.05 (C-12); 145.59 (C-17); 144.69 (C-3); 142.48 (C-4); 141.27 (C-20); 136.51 (C-6); 134.96 (C-9), 132.23 (C-16); 131.82 (C-2); 131.48 (C-14); 129.78 (C-7); 129.46 (C-8); 125.89 (C-15); 124.97 (C-18); 122.35 (C-13). ¹⁹F NMR (376 MHz, DMSO-*d*₆, 303.15 K) [δ, ppm]: -70.18 (d, 6F). ³¹P NMR (162 MHz, DMSO-*d*₆, 303.15 K) [δ, ppm]: -144.19 (m, 1P).

Experimental

2.5.3.6 {[3-(4-Fluorobenzoyl)pyridin-2-yl]carbonyl}(quinolin-8-yl)azanidogold(III) hexafluorophosphate(V), [Au(L13)Cl](PF₆)

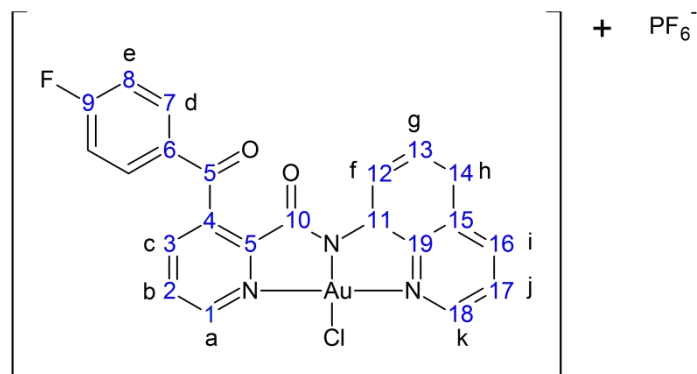


Figure 2.5.3.6: Numbering scheme employed for NMR characterisation of [Au(L13)Cl](PF₆), black letters correspond to ¹H NMR signals and blue numbers correspond to ¹³C NMR signals.

Yield, 75% (brown powder, based on gold). TOF MS (ES): *m/z* 602.0341 (calc, 602.0346), M⁺. IR (powder, cm⁻¹): 1672 (s, v(CO), RN-CO-R), 1591 (s, v(CO), R-CO-R). UV-vis (MeCN) [λ_{max} , nm (ϵ , M⁻¹ cm⁻¹): 255 (3.4 x 10⁴), 369 (7.3 x 10³). ¹H NMR (500 MHz, DMSO-*d*₆, 303.15 K) [δ , ppm]: 9.38 (m, 2H, *a*, *k*); 9.12 (d, 1H, *J* = 8.37 Hz, *i*); 8.77 (d, 1H, *J* = 7.90 Hz, *c*); 8.41 (d, 1H, *J* = 7.82 Hz, *f*); 8.29 (dd, 1H, *J*₁ = 7.90 Hz, *J*₂ = 5.75 Hz, *b*); 8.09 (dd, 1H, *J*₁ = 8.37 Hz, *J*₂ = 5.62 Hz, *j*); 7.97 (m, 3H, *h*, *d*); 7.79 (m, 1H, *g*); 7.43 (m, 2H, *e*). ¹³C NMR (123 MHz, DMSO-*d*₆, 303.15 K) [δ , ppm]: 188.86 (C-5); 166.68 (C-6); 164.66 (C-4); 163.67 (C-11); 151.18 (C-1); 149.68 (C-19); 145.55 (C-12); 145.10 (C-17); 144.21 (C-3); 141.66 (C-10); 140.73 (C-20); 132.94 (d, *J* = 2.55 Hz, C-9), 132.36 (d, *J* = 9.85 Hz, C-7); 131.73 (C-16); 131.36 (C-2); 130.98 (C-14); 125.41 (C-15); 124.46 (C-18); 121.86 (C-13); 116.65 (d, *J* = 22,31 Hz, C-8). ¹⁹F NMR (376 MHz, DMSO-*d*₆, 303.15 K) [δ , ppm]: -70.14 (d, 6F); -103.53 (m, 1F). ³¹P NMR (162 MHz, DMSO-*d*₆, 303.15 K) [δ , ppm]: -144.19 (m, 1P).

Experimental

2.5.3.7 {[3-(4-Methoxybenzoyl)pyridin-2-yl]carbonyl}(quinolin-8-yl)azanidogold(III) hexafluorophosphate(V), [Au(L14)Cl](PF₆)

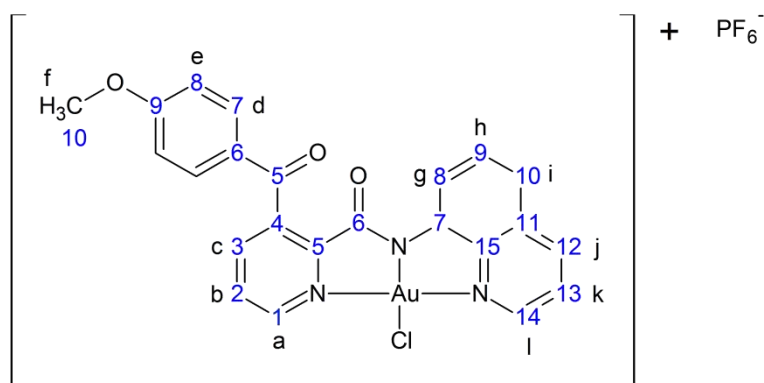


Figure 2.5.3.7: Numbering scheme employed for NMR characterisation of [Au(L14)Cl](PF₆), black letters correspond to ¹H NMR signals and blue numbers correspond to ¹³C NMR signals.

Yield, 86% (brown powder, based on gold). TOF MS (ES): *m/z* 614.0538 (calc, 614.0546), *M*⁺. IR (powder, cm⁻¹): 3070, 3084, 3109 (s, ν(CH); OCH₃) 1659 (s, ν(CO), RN-CO-R), 1594 (s, ν(CO), R-CO-R). UV-vis (MeCN) [*λ*_{max}, nm (ε, M⁻¹ cm⁻¹): 256 (3.2 × 10⁴), 286 (2.6 × 10⁴), 362 (9.0 × 10³). ¹H NMR (400 MHz, DMSO-*d*₆, 303.15 K) [δ, ppm]: 9.36 (m, 2H, *a*, *l*); 9.11 (d, 1H, *J* = 7.68 Hz, *j*); 8.70 (d, 1H, *J* = 7.86 Hz, *c*); 8.41 (d, 1H, *J* = 7.84 Hz, *g*); 8.26 (dd, 1H, *J*₁ = 7.90 Hz, *J*₂ = 5.74 Hz, *b*); 8.08 (dd, 1H, *J*₁ = 8.30 Hz, *J*₂ = 5.66 Hz, *k*); 7.98 (d, 1H, *J* = 8.00 Hz, *i*); 7.81 (m, 3H, *d*, *h*); 7.09 (m, 2H, *e*); 3.86 (s, 3H, *f*). ¹³C NMR (100 MHz, DMSO-*d*₆, 303.15 K) [δ, ppm]: 188.98 (C-5); 164.67 (C-9); 164.07 (C-12); 151.64 (C-1); 150.39 (C-11); 150.00 (C-20); 146.04 (C-13); 145.59 (C-18); 144.70 (C-3); 142.88 (C-4); 141.35 (C-21); 132.32 (C-8 or 15), 132.23 (C-16); 131.74 (C-2); 131.49 (C-8 or 15); 129.65 (C-6); 125.85 (C-16); 124.95 (C-19); 122.33 (C-14); 114.79 (C-7); 56.28 (C-10). ¹⁹F NMR (376 MHz, DMSO-*d*₆, 303.15 K) [δ, ppm]: -70.19 (d, 6F). ³¹P NMR (162 MHz, DMSO-*d*₆, 303.15 K) [δ, ppm]: -144.20 (m, 1P).

Experimental

2.5.4 General synthesis of C, N-donor 8-aminoquinoline-based tridentate gold(III) chelates.

KAuCl_4 (5.885×10^{-4} mol) and respective ligand (2.943×10^{-4} mol) were dissolved in 25 mL acetic acid and placed in a 50 mL round bottom flask, stirred and heated. To the heated solution was added solid bicarbonate (8.829×10^{-4} mol) and the solution brought to reflux for 12 h, after which a brown precipitate was isolated by centrifugation and washed with 2 x 5 mL aliquots of water. The solid was then dissolved in a minimum amount of boiling dimethylformamide and any insoluble impurities filtered off. The dimethylformamide solution was then placed in the fridge for 6 hours after which the resulting golden yellow microcrystalline solid was isolated by centrifugation and washed with 2 x 10 mL portions of diethylether.

2.5.4.1 Benzoyl(quinolin-8-yl) azanidogold(III), $[\text{Au}(\text{L15})\text{Cl}]$

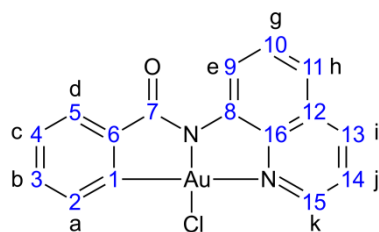


Figure 2.5.4.1: Numbering scheme employed for NMR characterisation of $[\text{Au}(\text{L15})\text{Cl}]$, black letters correspond to ^1H NMR signals and blue numbers correspond to ^{13}C NMR signals.

Yield, 85% (yellow crystals). TOF MS (ES): m/z 479.0241 (calc, 479.0226), M^+ . IR (powder, cm^{-1}): 1647 (s, $\nu(\text{CO})$, RN-CO-R). UV-vis (DMSO) [λ_{max} , nm (ϵ , $\text{M}^{-1} \text{cm}^{-1}$): 330 (5.4×10^3), 376 (6.3×10^3). ^1H NMR (400 MHz, $\text{DMSO-}d_6$, 303.15 K) [δ , ppm]: 9.08 (d, 1H, $J = 4.95$ Hz); 8.85 (m, 2H); 7.97 (dd, 1H, $J_1 = 8.37$ Hz, $J_2 = 4.97$ Hz); 7.75 (m, 2H); 7.70 (m, 1H); 7.39 (m, 3H). ^{13}C NMR (100 MHz, $\text{DMSO-}d_6$, 303.15 K) [δ , ppm]: Compound too insoluble to record spectrum.

2.5.4.2 (Naphthalen-1-ylcarbonyl)(quinolin-8-yl)azanidogold(III), [Au(L16)Cl]

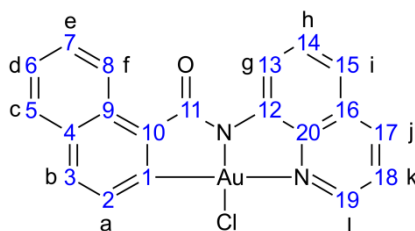


Figure 2.5.4.2: Numbering scheme employed for NMR characterisation of [Au(L16)Cl], black letters correspond to ^1H NMR signals and blue numbers correspond to ^{13}C NMR signals.

Yield, 78% (yellow powder). TOF MS (ES): m/z 528.0298 (calc, 528.0304), M^+ . IR (powder, cm^{-1}): 1644 (s, $\nu(\text{CO})$, RN-CO-R). UV-vis (DMSO) [λ_{max} , nm (ϵ , $\text{M}^{-1} \text{cm}^{-1}$): 333 (1.0×10^4), 379 (7.7×10^3). ^1H NMR (400 MHz, DMSO- d_6 , 303.15 K) [δ , ppm]: 9.53 (d, 1H, $J = 8.60$ Hz); 9.10 (m, 1H); 8.94 (m, 1H); 8.85 (m, 1H); 7.97 (m, 4H); 7.75 (m, 2H); 7.69 (m, 1H); 7.58 (m, 1H). ^{13}C NMR (100 MHz, DMSO- d_6 , 303.15 K) [δ , ppm]: Compound too insoluble to record spectrum.

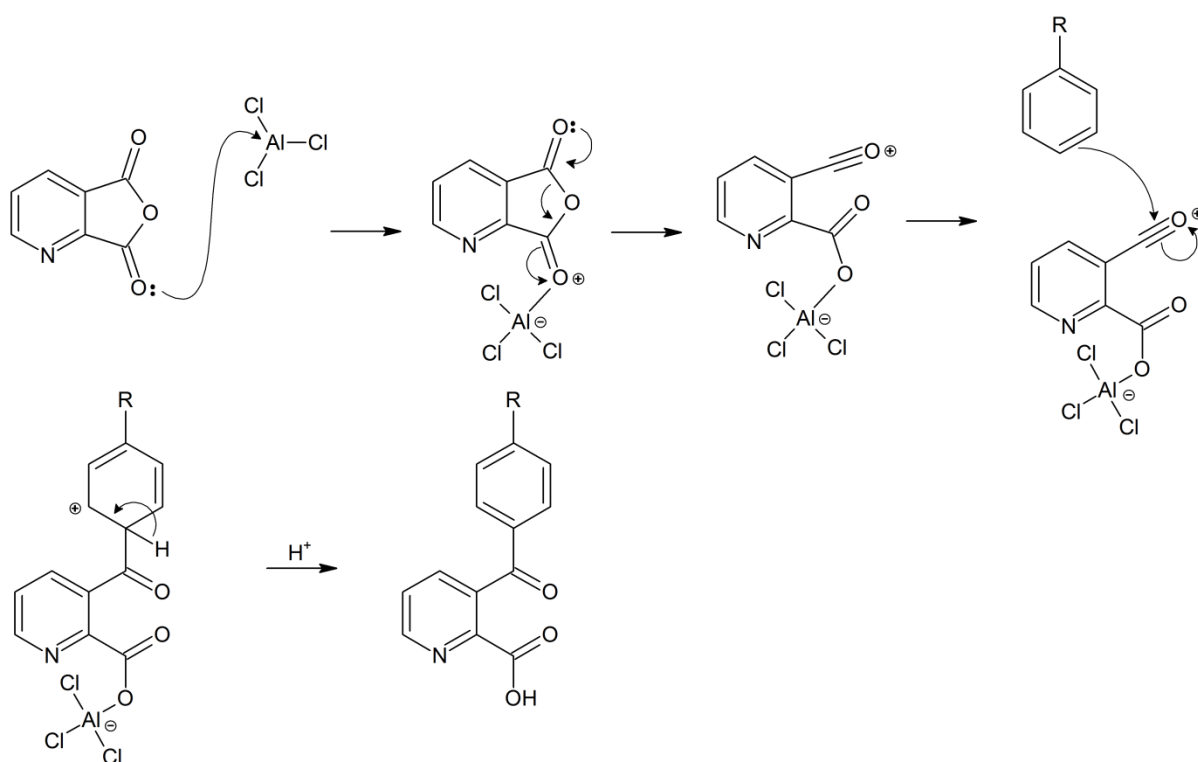
2.6 References

1. M. S. K. Youssef, A. F. Fahmy, M. S. A. Halim, M. A. Hassan and J. Sauer, *Organic Preparations and Procedures International*, 2005, **37**, 247-256.
2. D. J. Barnes, R. L. Chapman, R. S. Vagg and E. C. Watton, *Journal of Chemical and Engineering Data*, 1978, **23**, 349-350.
3. S. Dutta, S. Pal and P. K. Bhattacharya, *Polyhedron*, 1999, **18**, 2157-2162.
4. J. M. Rowland, M. M. Olmstead and P. K. Mascharak, *Inorganic Chemistry*, 2002, **41**, 2754-2760.
5. T. Yang, C. Tu, J. Zhang, L. Lin, X. Zhang, Q. Liu, J. Ding, Q. Xu and Z. Guo, *Dalton Transactions*, 2003, 3419-3424.
6. M. A. Altmeyer, A. Marschner, R. Schiffmann and C. D. Klein, *Bioorganic & Medicinal Chemistry Letters*, 2010, **20**, 4038-4044.
7. Y. Ano, M. Tobisu and N. Chatani, *Organic Letters*, 2012, **14**, 354-357.

3. Synthesis

3.1 Synthesis of aroyl pyridine carboxylic acids

The synthesis of aroyl pyridine carboxylic acids from quinolic anhydride is well documented in literature.¹⁻³ The aroyl pyridine carboxylic acid is generated as a key intermediate *en route* to the synthesis of anthracenediones as well as anthrapyrazoles.¹⁻³ These molecules are used as DNA intercalators in the fight against cancer.¹⁻³ The procedure is relatively straight forward, employing a Friedel crafts acylation reaction between the anhydride and an aromatic substrate.

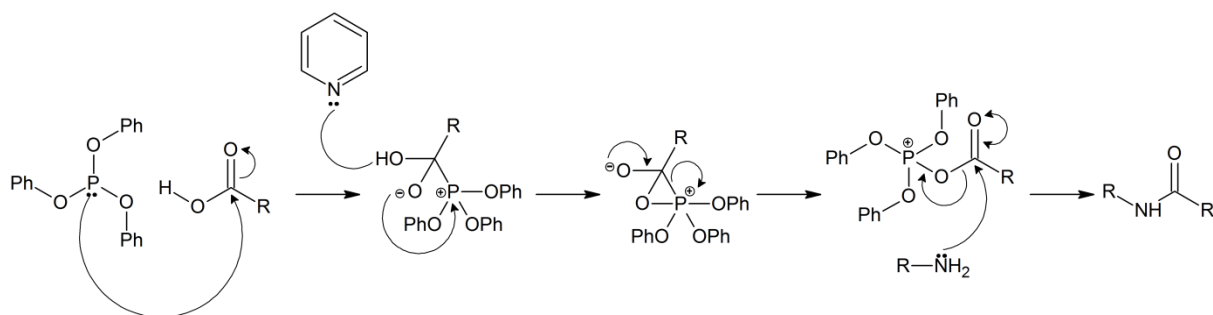


Scheme 3.1.1: Mechanistic scheme depicting the formation of a 3-substituted pyridine carboxylic acid via a Friedel-Crafts acylation reaction.

The lone pair from one of the carbonyl oxygen's of the anhydride attacks the aluminium trichloride and forms a co-ordination complex with it. This creates an electron deficient co-ordinated oxygen that facilitates the ring opening of the anhydride and the formation of an acylium ion. The acylium ion is susceptible to nucleophilic attack from the aromatic substrate to form the ketone which is aromatised through hydrogen elimination. Acid work up cleaves the complex and allows for the formation of the aroyl pyridine carboxylic acid. The reaction is clean and high yielding, requiring no chromatography.

3.2 Synthesis of ligands

The bis(amide) and amide ligand system was chosen because of its facile synthesis, solubility and ability to chelate metal ions.⁴⁻⁹ There are a number of synthetic methods that can be employed when considering the synthesis of bis(amide) and amide ligands. The most well-documented method for the synthesis of bis(amide) and amide ligands was reported by Vagg *et al.* in 1978 and involves the reaction between an amine and a triphenylphosphite-activated carboxylic acid in the presence of pyridine (acting as a base). Pyridine deprotonates the carboxylic acid and the lone pair from the phosphorus atom of the triphenylphosphite attacks the deprotonated carboxylic acid forming activated ester with the phosphorus atom being electron poor. The lone pair from the amine then attacks the carbonyl group and the triphenylphosphite leaves as triphenylphosphite oxide to afford the amide bond. The driving force of this reaction is the formation of the phosphorus-oxygen double bond. An example of the mechanistic scheme is shown below (Scheme 3.2.1). This method is the most common method employed in literature in the synthesis of both bis as well as mono(amide) ligands. The positives regarding this method are that the reaction is a one-pot synthetic route that is high yielding of a clean product, i.e. does not require column chromatography for work-up. The reaction can be performed open to the atmosphere without any special precautions to exclude oxygen or water. The negatives are the use of pyridine in the reaction, which, is harmful to males, and the work up can be lengthy, comprising multiple washings and extractions, if the product is aliphatic in nature.

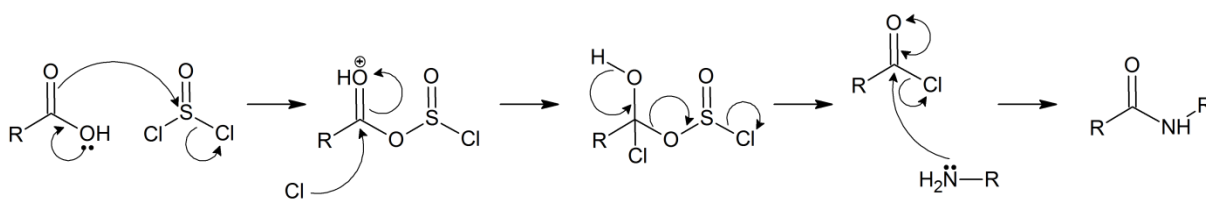


Scheme 3.2.1: Mechanistic scheme depicting the formation of an amide bond through a triphenylphosphite mediated pathway.

There have been other methods reported for the synthesis of amide ligands. One of these methods involves the conversion of a carboxylic acid to an acid chloride via the use of an acylating agent such as thionyl chloride, oxalyl chloride or phosphoryl chloride.^{10, 11} The

Synthesis

chloride of an acyl chloride functional group acts as a good leaving group facilitating attack by the amine to form the required amide bond.



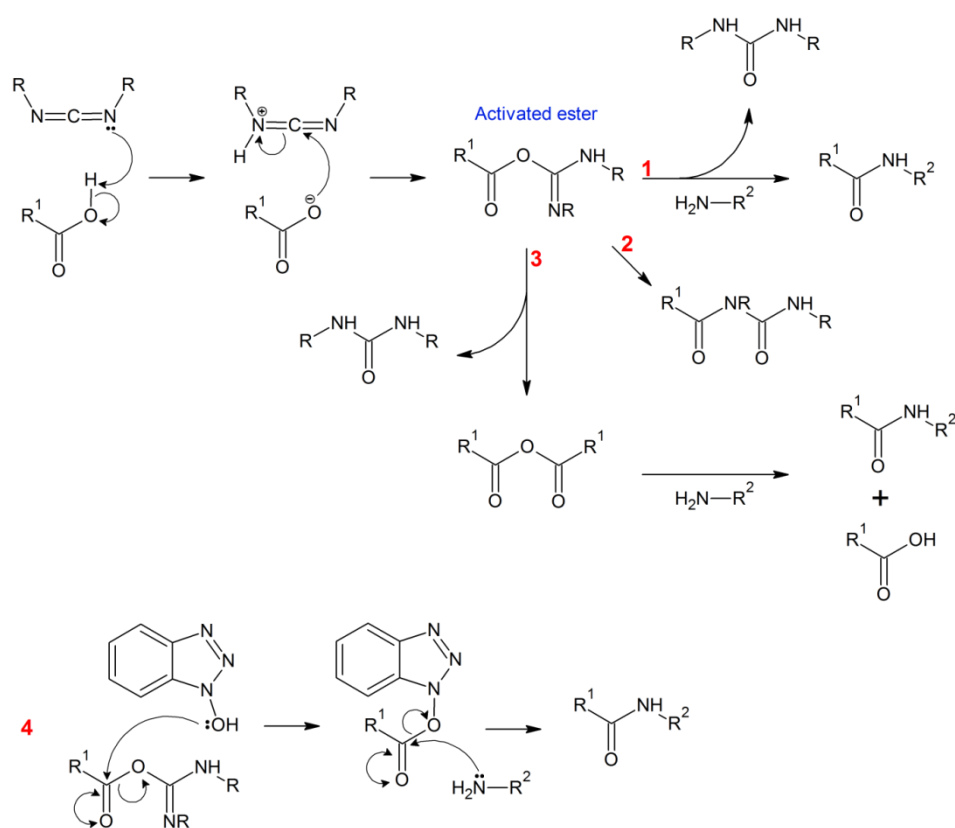
Scheme 3.2.2: Mechanistic scheme depicting the formation of an amide bond through an acyl chloride mediated pathway.

The electrons from the carbonyl double bond of the acid attack the sulfonyl group of thionyl chloride, causing a chloride ion to leave, and in the process forming an ester. The chloride anion then attacks the electron poor carbonyl of the ester, releasing HCl and SO₂, on the way to forming the acyl chloride. The acyl chloride is then attacked by the amine, forming the amide and releasing HCl in the process. An example of the synthetic scheme is shown above (Scheme 3.2.2). This method is also quite popular in literature. The problems with this method are that when forming the acid chloride from a heteroaromatic carboxylic acid there is a tendency to form the hydrochloride salt of the acid chloride as well as polymeric species.¹⁰ This is particularly evident in the preparation of the acid chloride of picolinic acid using thionyl chloride.¹⁰ Therefore the reactions are generally performed under an inert atmosphere using a mild acylating reagent such as oxalyl chloride to afford the correct product in good yield.¹⁰ The reaction is normally a two-step reaction where the acid chloride is generated and isolated first, followed by the amide bond formation. Acylating reagents are normally very corrosive and harmful towards humans and the environment. The positives are that the reaction can be very high yielding of a clean product.

The third method that can be employed is generally used in the biological synthesis of peptide bonds.¹² It involves the reaction of the carboxylic acid with a carbodiimide coupling agent, such as dicyclohexylcarbodiimide (DCCl), to form an activated ester which facilitates nucleophilic attack by an amine to form the intended amide bond. The reaction is driven by the expulsion of a very stable substituted urea molecule that is generally insoluble. The problem with this reaction is that the activated ester is susceptible to attack from numerous nucleophiles present in the reaction and hence the possibility of producing by-products. The first of these pathways is attack by the amine to form the intended amide (pathway 1), the

Synthesis

second is attack via another activated ester molecule (since it contains an amine functional group) to form a diamide species (pathway 2) and the third is attack from the original acid to form an intermediate ether species which, after coupling with the amine, results in the intended amide and an equivalent amount of acid (pathway 3). The presence of these side reactions led to the development of a strategy to avoid this which involves the addition of a coupling agent such as N-hydroxysuccinamide or 1-hydroxybenzotriazole (HOBt). The function of these coupling agents is to intercept the activated ester and speed up the reaction so that the event of side reactions is significantly reduced (pathway 4). The reaction can be conducted as a one- or two-step process depending on the cleanliness and efficiency of the reaction. The final product usually requires clean-up via column chromatography.



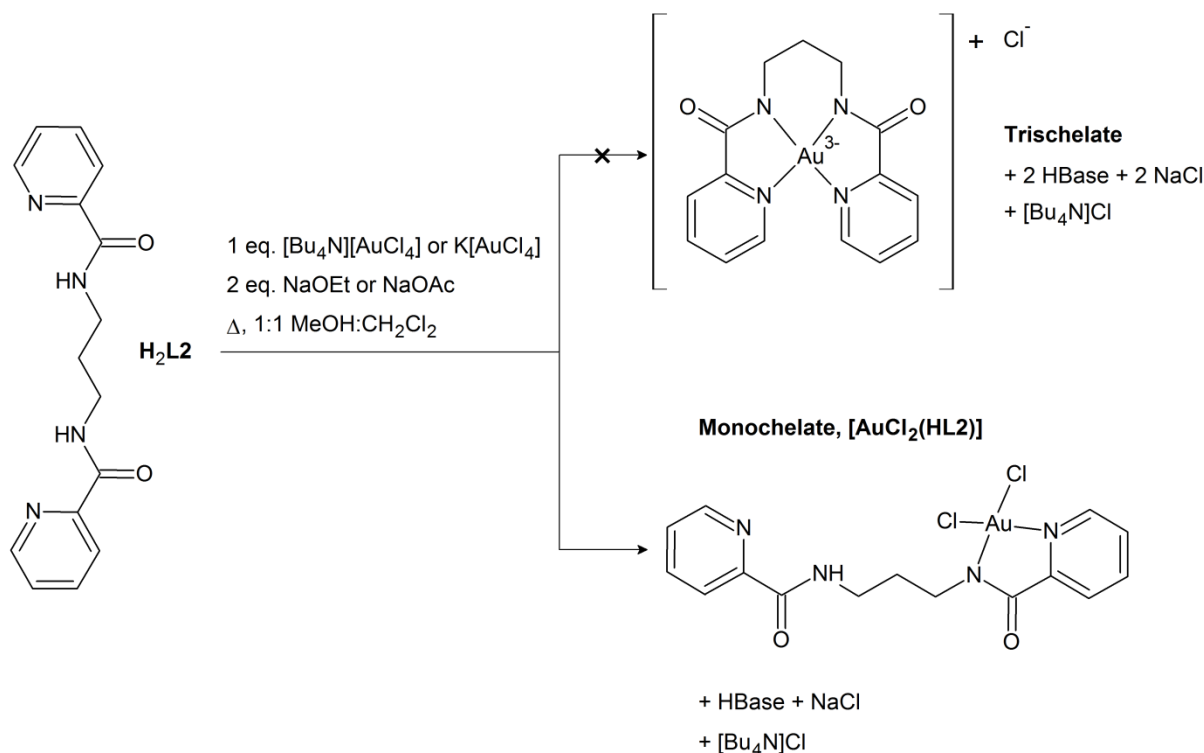
Scheme 3.2.3: Mechanistic scheme depicting the formation of an amide bond through a carbodiimide mediated pathway.

The method represented in scheme 3.2.1 was employed in the synthesis for all of the ligands as it is a one pot synthesis that gives a clean product in good yields.

3.3 Synthesis of metal complexes

3.3.1 Synthesis of *cis*-dichloro gold(III) complexes

The objective of our work was to synthesise structurally unique, predominantly planar cationic tetradentate bis(amido) Au(III) complexes that could potentially act as DNA intercalators and thus anti-cancer agents by virtue of their anticipated cytotoxicity—a goal based on similar traits exhibited by Au(III) porphyrins.¹³ Well-documented ligands H₂L1 and H₂L2 were considered first in order to optimise reaction conditions for the chelation of Au(III). Refluxing 1 eq. of H₂L2 with 1 eq. [Bu₄N][AuCl₄] in dichloromethane for 24 h was accompanied by no colour change and both starting materials were recovered. Clearly, a suitable base was needed to deprotonate the amide N–H group under thermodynamically driving conditions (higher boiling solvent) to facilitate chelation of an apparently substitution-inert Au(III) species, [AuCl₄][−]. We therefore attempted the reaction under reflux in 1:1 MeOH:DCM using [Bu₄N][AuCl₄] and two equivalents of sodium acetate as the base for 2 h (as recommended in a recent review), followed by stirring at ambient temperature overnight. An orange powder precipitated from the solution that, when recrystallised and analysed by single crystal X-ray diffraction, was the monochelate. The reaction was attempted again under the same conditions with 2 eq. of ethoxide ions (generated *in situ*) under the premise that a stronger base might yield the desired trischelate (Scheme 3.3.1.1). However, monochelate [Au(HL2)Cl₂] was isolated a second time, despite the use of the stronger base under the same reaction conditions. The use of K[AuCl₄] with either acetate or ethoxide as the base also led to the isolation of [Au(HL2)Cl₂] after work-up. It is noteworthy that the use of more than two equivalents of either base resulted in the formation of a black precipitate after a few minutes of reflux, which is typical of the reduction of Au(III) to colloidal gold. The behaviour of Au(III) with H₂L2 contrasts starkly with that of Pd(II) since the isoelectronic (but neutral) square-planar Pd(II) analogue of the trischelate (Scheme 3.1.1.1) has been synthesised and structurally characterised.



Scheme 3.3.1.1: Reaction scheme depicting the favored route to neutral monochelates of Au(III) as opposed to cationic trischelates of the metal.

Based on these observations, we conclude that the rather covalent and substitution-inert Au–Cl bonds in this system (especially the bond *trans* to the pyridine nitrogen) militate against formation of the desired mononuclear trischelates. It is also possible that steric repulsion between the α -C–H groups of the two closely positioned *cis*-pyridyl rings in the trischelate introduces significant steric strain in the product complex—enough to limit the prevalence of this species in solution under the given reaction conditions. Interestingly, if we reacted ligand H₂L₂ and either [Bu₄N][AuCl₄] or K[AuCl₄] in metal to ligand ratio of 1:1 or 1:2, the same mononuclear dichloro species [Au(HL₂)Cl₂] was always obtained, despite the former reaction stoichiometry potentially favouring the formation of a coordination polymer. Due to the interesting bidentate chelating modes of the ligands in complexes [Au(HL₁)Cl₂], [Au(HL₂)Cl₂], and [Au(L₄)Cl₂], which unintentionally provide an additional substituent with H-bond donor and acceptor sites and π -stacking bases in each case, no further attempts were made to generate tetradentate AuN₂N'₂ trischelates in favour of exploring the structural, electronic, and biological chemistry of the four new Au(III) complexes.

3.3.2 Synthesis of tridentate gold(III) complexes

After synthesis of the *cis*-dichloro monochelates mentioned above we focussed our attention on the synthesis of a series of tridentate gold(III) chelates. A series of three aminomethyl-based ligands (ligands HL5-HL7, Figure 1.7.1) were synthesised. Knowing the shortcomings encountered during the synthetic trials mentioned above, the initial metallation of the tridentate ligands involved the reaction of gold(III), $K[AuCl_4]$ or $H[AuCl_4]$, in the presence of equimolar amounts of ligand, NaOAc and potassium hexafluorophosphate in ethanol to afford a yellow solid. The reaction proceeded smoothly with ^{31}P and ^{19}F NMR indicating the correct counterion being present. This was later confirmed via single crystal X-ray crystallographic analysis. After discovery of the synthetic difficulties associated with the 8-aminoquinoline-based complexes (discussed below) a metathesis step was performed as a precaution to ensure the isolation of the desired hexafluorophosphate salt. The aminomethyl-based gold(III) chelates were abandoned upon realisation that they are particularly unstable. This was discovered when submitting samples for 1H and ^{13}C NMR. The samples were dissolved in $DMSO-d_6$ and a spectrum recorded. After satisfactory assignment of the proton signals the samples were submitted for ^{13}C and 2-D NMR experiments. Due to the low concentration of the samples the spectra had to be run overnight with multiple scans. On returning the next morning, data analysis revealed multiple 'new' peaks. Since these complexes are being synthesised with their intended application as chemotherapeutics, it is imperative they display solution stability, at least, in traditional NMR solvents. The spectroscopic experiments used to determine the stability of these chelates are discussed thoroughly in Chapter 4.

It was thought that substituting the aminomethyl group with 8-aminoquinoline we could render the ligand fully aromatic via the delocalisation of electrons through the amide bond and hence increase the σ -donor ability of the ligands and effect a more stable gold(III) chelate. A literature method for the synthesis of such chelates exists and was reported by Yang *et al.*¹⁴ The exact ligand 'Quinpy' was synthesised and the metallation method followed in which we refluxed equimolar amounts of ligand and $H[AuCl_4]$ in MeOH. This resulted in a dark brown precipitate which was filtered and analysed by TOF MS as well as 1H NMR. Initial investigations showed the correct complex, $[Au(Quinpy)Cl]Cl$ or $[Au(L8)Cl_2]PF_6$, had been synthesised. The 'correct' NMR shifts and solubility were observed.

Synthesis

The complex was soluble in DMSO, nitromethane and sparingly soluble in acetonitrile. Through ^1H NMR spectroscopy the complex was deemed stable in DMSO and so a series of associated but structurally different ligands were synthesised. Attempts to grow single crystals of $[\text{Au}(\text{L8})\text{Cl}_2]_x$ were futile due to the lack of solubility of the complex. A further three chelates were synthesised ($[\text{Au}(\text{L9})\text{Cl}_2]_x$, $[\text{Au}(\text{L10})\text{Cl}_2]_x$ and $[\text{Au}(\text{L11})\text{Cl}_2]_x$) using a slightly modified procedure. The solvent system was modified to contain 50% DCM to facilitate the dissolution of ligands HL9, HL10 and HL11 due to their lack of solubility in pure MeOH as well as the presence of NH_4PF_6 to encourage formation of the PF_6^- salt of the complexes. Evidence for the formation of the PF_6^- salt of the complexes was displayed via ^{19}F and ^{31}P NMR, however, both complexes, $[\text{Au}(\text{L10})\text{Cl}_2]_x$ and $[\text{Au}(\text{L11})\text{Cl}_2]_x$, displayed limited solubility akin to $[\text{Au}(\text{L8})\text{Cl}_2]_x$ while $[\text{Au}(\text{L9})\text{Cl}_2]_x$ exhibited improved solubility, presumably, due to the presence of the aliphatic butyl chain. Single crystals of $[\text{Au}(\text{L9})\text{Cl}_2]\text{AuCl}_2^-$ were grown by addition of a small amount of H_2O to a saturated solution of $[\text{Au}(\text{L9})\text{Cl}_2]\text{AuCl}_2^-$ in THF. Upon standing overnight pale orange crystals had grown and single crystal X-ray analysis revealed the correct chelate cation with the incorrect linear $[\text{AuCl}_2]^-$ anion. This was quite surprising as ^{19}F and ^{31}P NMR had suggested the correct, PF_6^- , ion pair was present. This was probably due to the presence of NH_4PF_6 impurities in the isolated product. This is possible as, both ^{19}F and ^{31}P NMR, are highly sensitive and the presence of even a small amount is capable of registering strong signals for both nuclei. In retrospect this result was understandable and explained the lack of solubility the complexes exhibited. The metallation reactions for $[\text{Au}(\text{L8})\text{Cl}_2]_x$, $[\text{Au}(\text{L9})\text{Cl}_2]_x$, $[\text{Au}(\text{L10})\text{Cl}_2]_x$ and $[\text{Au}(\text{L11})\text{Cl}_2]_x$ were then repeated using the literature as well as the modified technique and the products analysed by negative ionisation TOF MS. This was done to ascertain whether the presence of DCM in the reaction mixture facilitated the formation of the $[\text{AuCl}_2]^-$ anion. The mass spectral data revealed the presence of both $[\text{AuCl}_2]^-$ and $[\text{AuCl}_4]^-$ anions irrespective of the metallation method (Figure 3.3.2.1). The presence of gold counterions in the synthesis of cationic gold(III) chelates in literature is not uncommon. This is due to the aforementioned (Chapter 1) redox instability of gold in its +3 oxidation state as well as the tendency for the gold salts to be highly insoluble, driving their formation. Numerous strategies are employed in the synthesis of gold(III) chelates to avoid the formation of gold counterions, namely the inclusion of a PF_6^- salt and the ligand in excess to encourage chelation to occur rapidly. Metallation reactions were conducted under a significant variety of conditions through varying the solvent (EtOH

Synthesis

and mixtures with DCM, MeOH and mixtures with DCM) or base (EtO^- , MeO^- , NaOAc and NaHCO_3) as well as the source of gold(III) ions ($\text{H}[\text{AuCl}_4]$, $\text{K}[\text{AuCl}_4]$ and $[\text{Bu}_4\text{N}][\text{AuCl}_4]$). The reaction times were varied from 2 hrs to 48 hrs both under reflux and at ambient temperature.

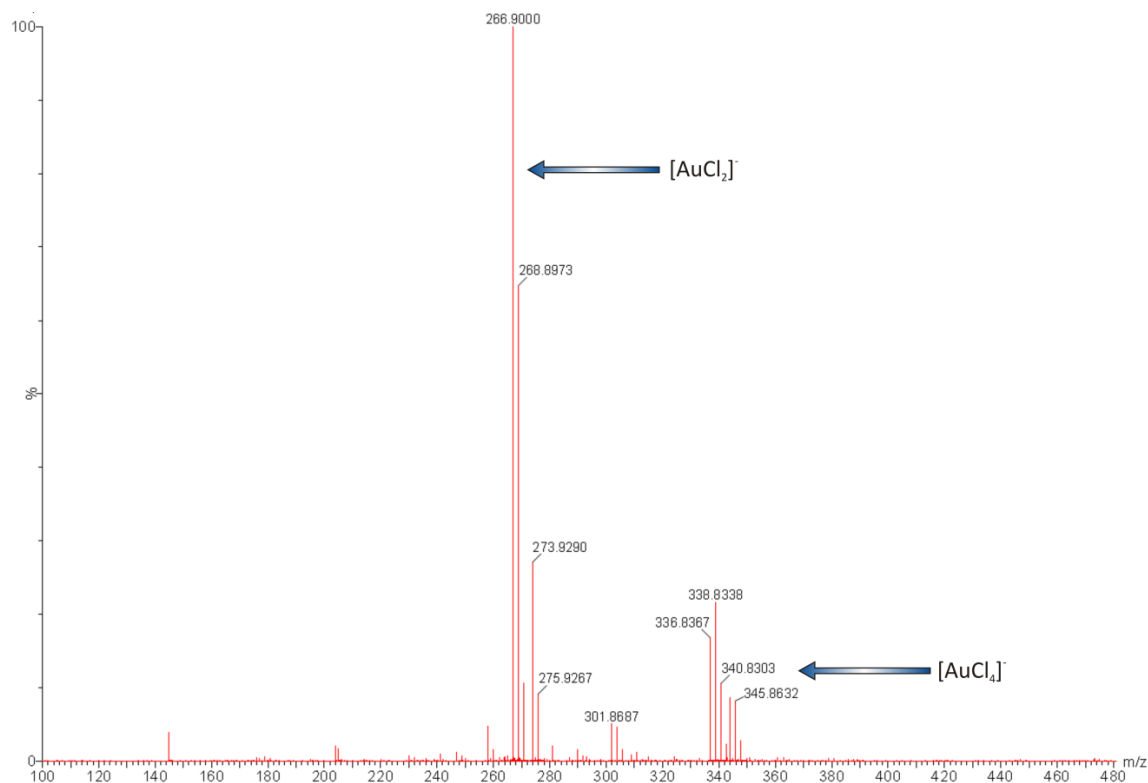


Figure 3.3.2.1: Negative ionisation mass spectral data of $[\text{Au}(\text{L10})\text{Cl}_2]\text{AuCl}_2^-$ showing the presence of both $[\text{AuCl}_2]^-$ and $[\text{AuCl}_4]^-$ as counterions.

No matter the conditions, base, or source of gold(III) ions, the same mixed-counterion, product was always obtained. Eventually a strategy was discovered that focussed on the formation of the $[\text{AuCl}_4]^-$ counterion by virtue of performing the metallation reaction with two equivalents of gold(III) salt ($\text{H}[\text{AuCl}_4]$, $\text{K}[\text{AuCl}_4]$ or $[\text{Bu}_4\text{N}][\text{AuCl}_4]$).¹⁵ The reaction was performed in acetic acid with 3 equivalents of NaHCO_3 affording a dark brown precipitate that when analysed by TOF MS revealed the intended complex as its tetrachloroaurate salt. This salt was then suspended in DCM in a round bottomed flask and stirred after the addition of excess $[\text{Bu}_4\text{N}][\text{Cl}]$. After stirring overnight, the precipitate was isolated and characterised as the chloride salt of the respective complex. The metathesis is successful since the formation of $[\text{Bu}_4\text{N}][\text{AuCl}_4]$ is driven forward by its solubility in DCM while the charged chloride salt of the complex is particularly insoluble in DCM. The chloride salts of all

Synthesis

the complexes were soluble in H₂O and therefore metathesis with KPF₆ afforded the hexafluorophosphate salt of each complex with ease. The solubility of the hexafluorophosphate salts of the complexes was markedly different to that of the gold-based counterion salts. The PF₆⁻ salts of all complexes were readily soluble in MeCN, MeNO₂, MeOH and EtOH, whereas the gold-based counterion salts of the complexes were sparingly soluble in MeCN and not at all soluble in the alcohols.

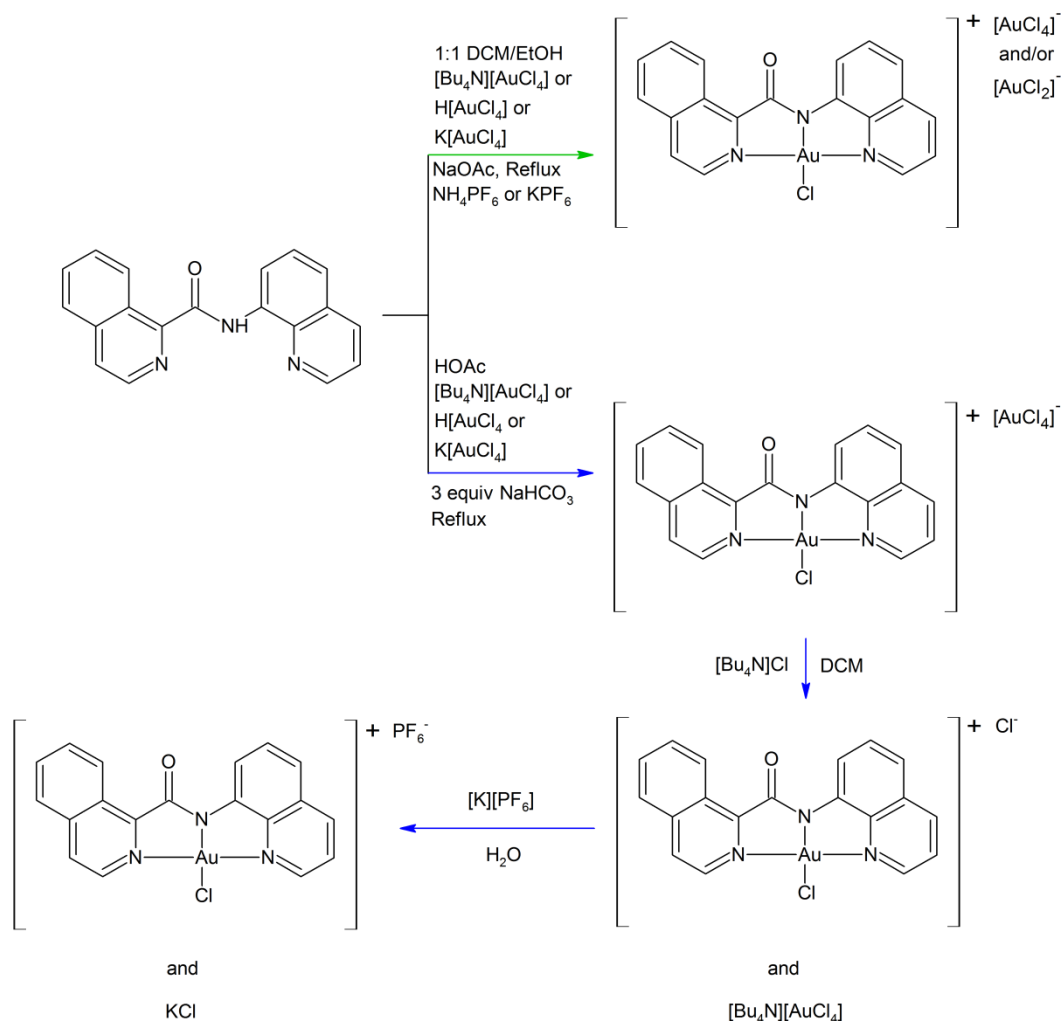


Figure 3.3.2.2: Schematic diagram depicting the different methods of synthesis used to generate the gold(III) chelates represented in this work. The green arrow shows the synthetic route employed for the synthesis of gold(III) chelates with mixed gold(I) and gold(III) counterions while the blue arrows show the synthetic scheme used in the successful synthesis of the PF₆⁻ salt of the gold(III) complexes. Ligand HL10 is used as an example in the scheme.

3.4 References

1. A. P. Krapcho, E. Menta, A. Oliva, D. R. Di, L. Fiocchi, M. E. Maresch, C. E. Gallagher, M. P. Hacker, G. Beggiolin, F. C. Giuliani, G. Pezzoni and S. Spinelli, *J. Med. Chem.*, 1998, **41**, 5429-5444.
2. A. P. Krapcho, M. E. Petry, Z. Getahun, J. J. Landi, Jr., J. Stallman, J. F. Polsenberg, C. E. Gallagher, M. J. Maresch, M. P. Hacker and a. et, *J. Med. Chem.*, 1994, **37**, 828-837.
3. O. C. Mansour, B. J. Evison, B. E. Sleebbs, K. G. Watson, A. Nudelman, A. Rephaeli, D. P. Buck, J. G. Collins, R. A. Bilardi, D. R. Phillips and S. M. Cutts, *J. Med. Chem.*, 2010, **53**, 6851-6866.
4. S. Dutta, S. Pal and P. K. Bhattacharya, *Polyhedron*, 1999, **18**, 2157-2162.
5. S. Nag, R. J. Butcher and S. Bhattacharya, *Eur. J. Inorg. Chem.*, 2007, 1251-1260.
6. A. K. Patra, M. J. Rose, K. A. Murphy, M. M. Olmstead and P. K. Mascharak, *Inorg. Chem.*, 2004, **43**, 4487-4495.
7. A. T. Vlahos, E. I. Tolis, C. P. Raptopoulou, A. Tsohos, M. P. Sigalas, A. Terzis and T. A. Kabanos, *Inorg. Chem.*, 2000, **39**, 2977-2985.
8. T. Yang, J.-Y. Zhang, C. Tu, J. Lin, Q. Liu and Z.-J. Guo, *Wuji Huaxue Xuebao*, 2003, **19**, 45-48.
9. R. W.-Y. Sun and C.-M. Che, *Coord. Chem. Rev.*, 2009, **253**, 1682-1691.
10. K. I. Naettinen and K. Rissanen, *Cryst. Growth Des.*, 2003, **3**, 339-353.
11. B. Rieger, A. S. Abu-Surrah, R. Fawzi and M. Steiman, *J. Organomet. Chem.*, 1995, **497**, 73-79.
12. K. Susumu, H. T. Uyeda, I. L. Medintz, T. Pons, J. B. Delehanty and H. Mattoussi, *J. Am. Chem. Soc.*, 2007, **129**, 13987-13996.
13. C.-M. Che, R. W.-Y. Sun, W.-Y. Yu, C.-B. Ko, N. Zhu and H. Sun, *Chem. Commun. (Cambridge, U. K.)*, 2003, 1718-1719.
14. T. Yang, C. Tu, J. Zhang, L. Lin, X. Zhang, Q. Liu, J. Ding, Q. Xu and Z. Guo, *Dalton Trans.*, 2003, 3419-3424.
15. S. Stoccoro, G. Alesso, M. A. Cinellu, G. Minghetti, A. Zucca, M. Manassero and C. Manassero, *Dalton Trans.*, 2009, 3467-3477.

4. Spectroscopy

4.1 Infrared spectroscopy

Infrared spectroscopy is based on the principle that almost all molecules that contain covalent bonds are able to absorb electromagnetic radiation in the IR region, with the exception of a few homonuclear molecules such as O₂, N₂ and Cl₂.¹ For chemical purposes and general application the characteristic window is normally observed between the wavenumber range of 400 and 4000 cm⁻¹.¹⁻⁴ The absorption of infrared radiation is a quantized process with specific functional groups within a molecule absorbing certain IR frequencies.⁴ The internal molecular energy of a molecule can be separated into three different components: (1) the vibration of each atom in the molecule, (2) the rotation of the molecule, and (3) movement of electrons in the molecule.⁴

$$E_{\text{total}} = E_{\text{vib}} + E_{\text{rot}} + E_{\text{el}} \quad 4.1.1$$

Only vibrational transitions occur within the IR spectral range and so it is only these transitions that are observed in the IR spectrum.^{3, 4} IR spectra are the result of photons being absorbed by transitions between two vibrational energy levels of the molecule in the ground state. The vibrations of a molecule when induced by the absorption of IR energy are generally of two forms: (1) stretching and (2) bending. A stretch is a vibration occurring along the line of the bond that changes the bond length and a bend is a vibration that does not occur along the line of the bond but changes the bond angle. In molecules containing three or more atoms these vibrations can become even more complicated. One can have asymmetric as well as symmetric stretches and bends. Since every type of bond has a different natural frequency of vibration and two of the same types of bond in different molecules are in different environments, all molecules exhibit a unique IR absorption pattern.¹⁻⁴ In general IR spectroscopy is less accurate as a qualitative tool compared to other spectroscopic techniques such as UV-visible spectroscopy.² This is because of its lower sensitivity and frequent deviation from Beer's law.² IR measurements are also considerably less precise than other spectroscopic methods.² IR spectroscopy is, therefore, primarily used as a fingerprinting tool in qualitative analysis. All functional groups have a characteristic, narrow region in the IR spectrum that they absorb.^{1, 2} These individual absorption bands add up to collectively create a fingerprint spectrum for individual molecules. Figure 4.4.1

Spectroscopy

summarises the characteristic absorption bands for some common functional groups present in organic molecules.

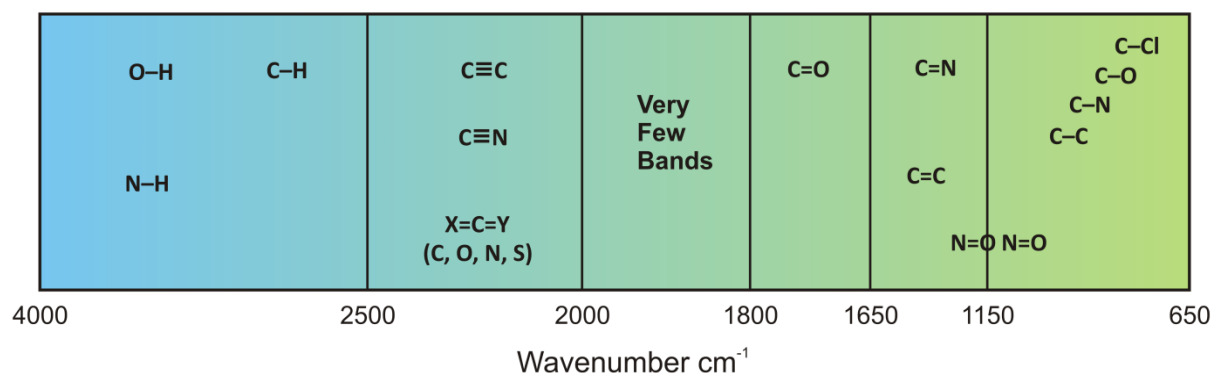


Figure 4.1.1: Approximate absorption regions of some common functional groups. Diagram adapted and modified from 'Introduction to Spectroscopy' 4th Edition.⁴

The ligands presented in this work contain functional groups that exhibit characteristic absorption bands. The most prevalent and characteristic is the amide functional group. It contains both $\nu(\text{C}=\text{O})$ and $\nu(\text{N}-\text{H})$ bands, of which, the $\nu(\text{N}-\text{H})$ disappears upon chelation to the gold(III) ion. The $\nu(\text{C}=\text{O})$ band remains present, but, shifts to lower wavenumbers. The characteristic wavenumber for the $\nu(\text{C}=\text{O})$ stretch is approximately 1650 cm^{-1} , while for the $\nu(\text{N}-\text{H})$ stretch it is approximately $3200\text{-}3500\text{ cm}^{-1}$. The methyl groups associated with the butyl chain of ligand HL9 and methoxy group of ligands HL4 and HL14 also show characteristic CH_3 stretches in the $2700\text{-}3300\text{ cm}^{-1}$ region. Ligands HL12-HL14 also contain a ketone functional group, this displays a characteristic stretch also in the 1650 cm^{-1} region.

There are relatively very few examples of gold(III) amide compounds in the literature. Of the few reports present the characterisation data on them is sparse at best, with only CHN data available for the compound, $[\text{Au}(\text{HL})\text{Cl}_2]$ ($\text{H}_2\text{L} = 2,2'$ -bis(2-pyridylcarboxyamide)-1,1'-binaphthyl), reported by Che and co-workers in 1994. Yang *et. al* reported three gold(III) amide compounds in 2003, namely $[\text{Au}(\text{Quinpy})\text{Cl}]\text{Cl}$, $[\text{Au}(\text{Quingly})\text{Cl}]\text{Cl}$ and $[\text{Au}(\text{Quinala})\text{Cl}]\text{Cl}$, with all three compounds exhibiting characteristic $\nu(\text{C}=\text{O})$ stretches at 1679 , 1658 and 1664 cm^{-1} respectively.⁵ The metal compound stretches could not be compared to their respective free ligand $\nu(\text{C}=\text{O})$ stretches as this data is not reported in the literature, however, the boc-protected $\nu(\text{C}=\text{O})$ stretches are available for the ligands QuinglyBoc and QuinalaBoc (1713 and 1700 cm^{-1} respectively).^{6,7} Chelation of the ligand to gold(III) is seen to therefore induce a shift in $\nu(\text{C}=\text{O})$ stretch to lower frequencies. In 2009

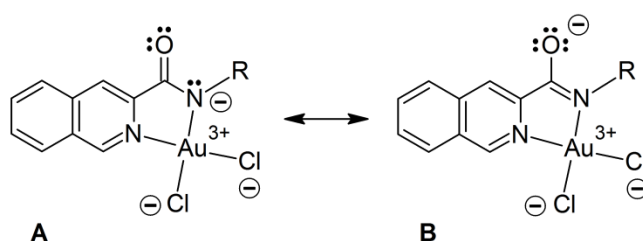
Cinellu and co-workers reported the formation of two chiral tridentate gold(III) amide compounds, *S*-5 and *R*-6 of the deprotonated ligands *N*-(1-hydroxy-3-*R*-2-yl)pyridine-2-carboxamide (*R*=*i*Pr, Ph), which were acquired via the ring opening of a chiral pyridinyl-oxazoline ligand.⁸ The $\nu(\text{C}=\text{O})$ stretches for these compounds were both reported to be 1649 cm^{-1} .

4.1.2 Objectives

The main objective of infrared spectroscopy is a secondary analytical tool. It is used to determine the presence of certain functional groups (*vide supra*) and to compare their absorption bands in the free ligand to the metal complex. The characteristic absorption bands will also be compared to the calculated values from the DFT simulations and used to determine the accuracy of the computational method used.

4.1.3 Results and discussion

The two most prominent absorption bands present in the IR spectrum of all ligands presented are the $\nu(\text{C}=\text{O})$ and $\nu(\text{N}-\text{H})$ stretching bands. The $\nu(\text{C}=\text{O})$ stretching bands range between 1579-1689 cm^{-1} while the $\nu(\text{N}-\text{H})$ stretching bands range between 3272-3349 cm^{-1} (Table 4.1.3.1). The $\nu(\text{C}=\text{O})$ stretching frequency for the metal compound is shifted to a lower frequency relative to that of the free ligand for all complexes except $[\text{Au}(\text{L5})\text{Cl}](\text{PF}_6)$ – $[\text{Au}(\text{L7})\text{Cl}](\text{PF}_6)$ (Table 4.1.3.1).



Scheme 4.1.3.1: Illustration of bond resonance involving the metal-bound amide group of $[\text{Au}(\text{HL3})\text{Cl}_2]$. Lone pairs of electrons are shown for the amide group to aid visualisation of the two resonance forms.

This characteristic is expected and well documented in literature.^{5, 9, 10} The simplest explanation for the shift to lower wavenumber for the metal-bound amide band, $\nu(\text{C}=\text{O})$, relative to the free amide band is that the resonance hybrid structure for the compound lies somewhere between the two resonance forms A ($-\text{N}=\text{C}=\text{O}$) and B ($\text{N}=\text{C}-\text{O}^-$) illustrated in

Spectroscopy

Scheme 4.1.3.1. Because a decrease in the C–O bond order is expected to reduce the frequency of the normal mode of vibration for the carbonyl group, the experimental data suggest that the resonance hybrid structures of the metal compounds lie slightly closer to resonance form B than form A, consistent with the behaviour previously deduced by Rosenberg for several peptide compounds of Cu(II).¹⁰ Compounds [Au(L5)Cl](PF₆)–[Au(L7)Cl](PF₆) however display the opposite trend, suggesting their resonance hybrid structures of the metal compounds lie closer to resonance form A than form B compared to that of the free ligand.

Table 4.1.3.1: Experimental IR data for all free ligands and metal compounds studied.^a

	$\nu(\text{N-H})/\text{cm}^{-1c}$	$\nu_1(\text{C=O})/\text{cm}^{-1}$	$\nu_2(\text{C=O})/\text{cm}^{-1}$	$\nu_{\Delta 1,2}(\text{C=O})/\text{cm}^{-1}$
[Au(HL1)Cl ₂]	3326	1654	1647	+7
[Au(HL2)Cl ₂]	3299	1650	1645	+5
[Au(HL3)Cl ₂]	3335 and 3300	1685	1652	+33
[Au(L4)Cl ₂]	3337	1689	1643	+46
[Au(L5)Cl](PF ₆)	3359	1664	1676	-12
[Au(L6)Cl](PF ₆)	3298	1646	1672	-24
[Au(L7)Cl](PF ₆)	3349	1652	1664	-12
[Au(L8)Cl](PF ₆)	3287	1684	1655	+29
[Au(L9)Cl](PF ₆)	3303	1676	1663	+13
[Au(L10)Cl](PF ₆)	3272	1671	1662	+9
[Au(L11)Cl](PF ₆)	3301	1677	1666	+10
[Au(L12)Cl](PF ₆)	3289	1664	1658	+6
[Au(L13)Cl](PF ₆)	3290	1672	1672	0
[Au(L14)Cl](PF ₆)	3289	1664	1659	+5
[Au(L15)Cl](PF ₆)	3349	1669	1647	+22
[Au(L16)Cl](PF ₆)	3353	1667	1644	+23
[Au(Quinpy)Cl]Cl ⁵	N/A	1687	1679	+8
[Au(Quingly)Cl]Cl ⁵	N/A	1713 ^{b,6,7}	1658	+55
[Au(Quinala)Cl]Cl ⁵	N/A	1700 ^{b,6,7}	1664	+36
S-5 ⁸	N/A	N/A	1649	N/A
R-6 ⁸	N/A	N/A	1649	N/A

^aAbbreviations: $\nu_1(\text{C=O})$ and $\nu_2(\text{C=O})$ are the stretching frequencies for the free ligand and metal compounds respectively; $\nu_{\Delta 1,2}(\text{C=O})$ is the difference between ν_1 and ν_2 .^bTabulated stretches are for boc protected analogues used. ^c $\nu(\text{N-H})$ refers to the stretching frequency of the respective free ligand.

Spectroscopy

For complexes $[\text{Au}(\text{HL1})\text{Cl}_2]$ – $[\text{Au}(\text{HL3})\text{Cl}_2]$ it is interesting to note that the gold(III) ion only binds to half the donor atoms present in the ligand. One would therefore expect these metal compounds to have several distinct stretching modes present in their spectra and indeed there are. There are separate stretching modes for the metal bound amide $\nu(\text{C}=\text{O})$ and the free amide $\nu(\text{C}=\text{O})$ (*vide supra*) as can be expected. There is also the presence of a $\nu(\text{N}-\text{H})$ stretch due to the unbound amide group. In the overlay (Figure 4.1.3.1) below the black trace depicts the IR spectrum of the free ligand while the green trace portrays the IR spectrum of the metal compound. Interestingly the black arrow in the $\nu(\text{N}-\text{H})$ region indicates the presence of two sharp peaks at 3300 and 3335 cm^{-1} , indicating the presence of two individual or chemically distinct $\nu(\text{N}-\text{H})$ stretches. This is unexpected considering ligand $\text{H}_2\text{L3}$ contains C_2 symmetry, at least in solution, evident by NMR (see Chapter 4.2) and therefore the individual $\nu(\text{N}-\text{H})$ stretches should be chemically equivalent and display one unique signal. The case in the solid state, however, is markedly different (see Chapter 2). One of the amide $\nu(\text{N}-\text{H})$ groups is intramolecularly hydrogen bonded to the neighbouring amide carbonyl oxygen as well as the pyridine nitrogen. These hydrogen bonds elongate the $\nu(\text{N}-\text{H})$ bond slightly so that less energy is required to induce a stretch compared to the other $\nu(\text{N}-\text{H})$ bond in the same molecule. The black arrow in the $\nu(\text{C}=\text{O})$ region indicates the ligand $\text{H}_2\text{L3}$ amide carbonyl stretch at 1685 cm^{-1} . Hydrogen bonding does not affect the individual $\nu(\text{C}=\text{O})$ moieties and one stretch is observed. The green arrow in the $\nu(\text{N}-\text{H})$ region at 3322 cm^{-1} corresponds to the single amide $\nu(\text{N}-\text{H})$ stretch present in the metal complex while the two green arrows in the $\nu(\text{C}=\text{O})$ region at 1649 and 1622 cm^{-1} , respectively, correspond to the free and bound amide $\nu(\text{C}=\text{O})$ stretches. The rest of the ligands and their complexes displayed a characteristic and expected disappearance of the $\text{N}-\text{H}$ stretch upon chelation of the gold(III) ion to the ligand. Ligands HL12 - HL14 and their metal compounds contain a ketone carbonyl group in addition to their amide carbonyl group. These two carbonyl groups would be expected to display distinct $\nu(\text{C}=\text{O})$ stretching modes in both the free ligand and metal compound IR spectrums. This is because the ketone has a higher bond order since it is a traditional $\text{C}=\text{O}$ double bond, while the amide carbonyl $\text{C}=\text{O}$ has a lower bond order due to the delocalisation of electrons through the $\text{N}-\text{C}-\text{O}$ amide functionality (*vide supra*). This means that more energy is required to induce the ketone stretch than the amide carbonyl stretch. In reality the individual stretching modes are close in energy and practically indistinguishable.

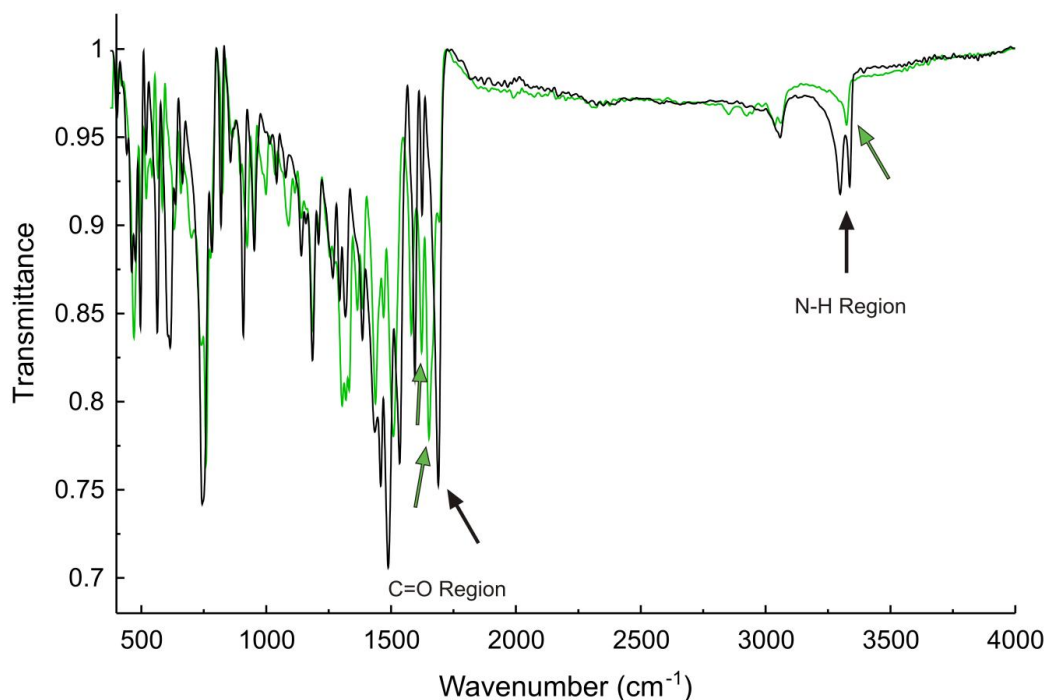


Figure 4.1.3.1: IR spectra overlay of H₂L3 (black) and [Au(HL3)Cl₂] (green).

For ligand HL12 and its respective complex there is no evidence for individual stretches, while for ligands HL13-HL14 and their complexes there is slight evidence as the second band is part of the other as a shoulder. Ligands HL4, HL9 and HL14 and their respective metal compounds also display sharp stretches in the 3000-3300 cm⁻¹ range which are attributed to the CH₃ stretches of the methoxy groups of HL4, HL14, [Au(L4)Cl₂] and [Au(L14)Cl](PF₆), while the butyl chain for HL9 and [Au(L9)Cl](PF₆) contribute the same distinct stretches. Overall the $\nu(\text{C}=\text{O})$ stretches for the compounds in this work follow the trend in the literature, shifting to a lower wavenumber when chelated to a gold(III) ion. The $\nu(\text{C}=\text{O})$ stretch for the previously reported free ligand and compound, Quinpy (1687 cm⁻¹) and [Au(Quinpy)Cl]Cl (1679 cm⁻¹) compare well with the values obtained for the analogous compounds synthesised in this work, HL8 (1684 cm⁻¹) and [Au(L8)Cl](PF₆) (1655 cm⁻¹).

4.2 NMR spectroscopy

NMR spectroscopy was developed in the 1940s to study the properties of atomic nuclei but in 1951, chemists realised that NMR could also be used to determine the structures of molecules.² Electrons are charged spinning particles with either one of two allowed spin states: $+\frac{1}{2}$ or $-\frac{1}{2}$. Certain nuclei also have allowed spins states of $+\frac{1}{2}$ or $-\frac{1}{2}$ and this is the property that allows them to be studied by NMR.^{2, 11} Examples of such nuclei are ^1H , ^{13}C , ^{15}N , ^{19}F and ^{31}P . Spinning charged nuclei generate a magnetic field, similar to that of a bar magnet. In the absence of an applied magnetic field the nuclei are randomly orientated according to their spin; however, when a magnetic field is applied the nuclei orientate themselves with or against the field (Figure 4.2.1).^{2, 11} More energy is required to align them against the magnetic field than with it, hence there are more nuclei aligned with the magnetic field than against it.² In the case of ^1H NMR, protons that are aligned with the magnetic field are in the lower spin-energy α -spin state and the protons that are aligned against the applied magnetic field are in the higher spin-energy β -spin state.² The difference in populations of the two spin states is small, but enough to form the basis of NMR.²

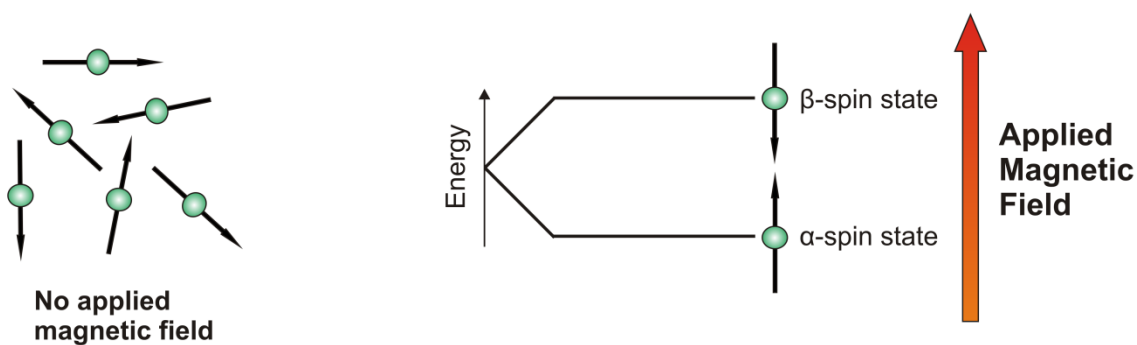


Figure 4.2.1: The spins of nuclei in the absence (left) and in the presence (right) of a magnetic field. Diagram adapted and modified from 'Organic Chemistry' 4th Edition.²

The energy difference (ΔE) between the α - and β -spin states depends on the strength of the applied magnetic field (B_0).² The bigger the applied magnetic field, the bigger the energy difference between the two states. When a sample is subjected to a pulse of energy that corresponds with the energy difference between the α - and β -spin states, the nuclei in the α -spin state are promoted to the β -spin state.² This transition is called spin 'flipping'.² The radiation required to induce spin 'flipping' is generally in the radiofrequency (rf) region of

Spectroscopy

the electromagnetic spectrum.² When the nuclei undergo relaxation from the β -spin state back to the α -spin state, they emit electromagnetic signals, which are detected and displayed as an NMR spectrum. Planck's constant, h , is the proportionality constant relating to the energy difference (ΔE) to the frequency (ν).² The equation below shows that the energy difference between spin states (ΔE) depends on the operating frequency of the spectrometer, which in turn depends on the strength of the magnetic field (B_0), and the gyromagnetic ratio (γ).² The gyromagnetic ratio (γ) is a constant that depends on the magnetic moment of the particular nucleus.

$$\Delta E = h\nu = h \frac{\gamma}{2\pi} B_0 \quad 4.2.1$$

Cancelling Planck's constant on both side of the equation gives

$$\nu = \frac{\gamma}{2\pi} B_0 \quad 4.2.2$$

This equation can be used to show the magnetic field (B_0) is proportional to the operating frequency (MHz), so a spectrometer with a more powerful magnet must have a higher operating frequency. In general, the stronger the magnet, the higher the resolution of the acquired spectrum.

Although gold(III) is diamagnetic, ^{197}Au NMR is not possible since the nucleus is quadrupolar ($I = \frac{3}{2}$) with a large quadrupolar moment and gyromagnetic ratio. The resonance frequency is therefore out of the range of most NMR spectrometers. Only the most symmetrical gold(III) complexes would display a ^{197}Au signal sharp enough to observe, but even then the sample would have to be highly concentrated and the experiment conducted on a specialised spectrometer.

Upon chelation of a gold(III) ion to the ligands presented in this work, we expect to observe a general downfield shift in proton signals of the respective compounds compared to those of the respective ligands. This is due to the deshielding environment introduced by the gold(III) ion. In general this shift is most prominent with the α -protons since they are the closest in proximity to the metal ion. This effect is observed for the previously mentioned literature gold(III) amide compounds, $[\text{Au}(\text{Quinpy})\text{Cl}]\text{Cl}$, $[\text{Au}(\text{Quinpy})\text{Cl}]\text{Cl}$, $[\text{Au}(\text{Quinpy})\text{Cl}]\text{Cl}$,

S-5 and S-6, which all contain metal compound α -protons with a chemical shift > 8.95 ppm.^{5, 8}

4.2.1 Objectives

The main objective of NMR is a primary identification tool. Once a new ligand or complex is synthesised, NMR is the initial technique used to determine if the reaction was a success. It can also be used to determine the stability of compounds and the experimental shifts can be compared to calculated shifts in order to determine the accuracy of the computational method used.

4.2.2 Results and discussion

The ^1H and ^{13}C NMR spectra for all ligands and complexes are fully assigned in the experimental section. Ligands $\text{H}_2\text{L1}$ – $\text{H}_2\text{L3}$ all contain C_2 symmetry and therefore protons and carbons on both sides of the ligands are in equivalent chemical environments. The consequence of this is that only one signal is present for both atoms on each side of the molecule. This symmetry is however removed upon chelation to the gold(III) ion due to the unusual co-ordination of the ligand to the metal ion. The result is that each individual proton and carbon atom in the ^1H and ^{13}C NMR spectra of the respective complexes displays a unique signal. This is similarly observed for a cis-dichloro amide gold(III) complex synthesised by Che and co-workers.⁹ Effectively there is a double up in signals from the ligand to the metal complex with the only exception being the signal from one, as opposed to two, amide NH protons (deprotonation of the metal-bound amide group accounting for loss of the second amide proton). The rest of the ligands and complexes are asymmetrical in nature and therefore display individual signals for each proton and carbon atom. A more detailed discussion on the ^1H spectra of ligands $\text{H}_2\text{L3}$, HL12 and their respective complexes is presented below. The reason for this is that both complexes $[\text{Au}(\text{HL3})\text{Cl}_2]$ and $[\text{Au}(\text{L12})\text{Cl}](\text{PF}_6)$ form the focus of this research and consequently have been studied in detail with regards to their biological and structural aspects. The ^{13}C spectra for all ligands and complexes display similar trends to that of the proton spectra and hence will not be discussed in detail in the view of keeping the discussion concise. Only specific details of interesting trends or properties in ^{13}C pertaining to certain ligands and/or complexes will be discussed.

The ^1H NMR spectrum for the free ligand $\text{H}_2\text{L3}$ exhibits an “all-aromatic” proton spectrum with signals spanning the 7–11 ppm range (Figure 4.2.2.1). The chemically and magnetically equivalent amide NH protons of the free ligand resonate farthest downfield (10.90 ppm). The relatively narrow line width (2.33 Hz) of the amide N–H signal indicates negligible dynamic proton exchange in solution at ambient temperature. Analysis of the intramolecular hydrogen bonds of $\text{H}_2\text{L3}$ (see Chapter 2) shows that the amide N–H atom H100 is involved in a 3-center (bifurcated) hydrogen bond in which the adjacent isoquinoline nitrogen (N1) and carbonyl oxygen (O1) atoms act as H-bond acceptors for the N–H donor. The amide N–H atom H200 is hydrogen-bonded to the adjacent isoquinoline nitrogen atom N4. Even if some rotational exchange of the two isoquinoline-amide moieties occurs in solution, the NH protons of $\text{H}_2\text{L3}$ are expected to be rigorously H-bonded throughout such a process, consistent with an intrinsically narrow line width. From Figure 4.2.2.1 it is evident that the amide proton (*k*) in the gold(III) complex exhibits a minor (0.07 ppm) upfield shift relative to the free ligand. More marked, however, is the splitting and dramatic shifts of the isoquinoline α -CH proton resonances (i.e. those adjacent to the isoquinoline N atom, *a* and *q*) upon chelation of the metal ion. From the X-ray structure of $[\text{Au}(\text{HL3})\text{Cl}_2]$, CH proton *a* forms an intramolecular hydrogen bond to the closest chloride ligand (Cl1). The effect of this particular interaction is marked deshielding of the proton (labelled *a* in both spectral traces), which culminates in a 0.97-ppm downfield shift in the signal for $[\text{Au}(\text{HL3})\text{Cl}_2]$ relative to the chemical shift of the proton in the free ligand. The analogous proton on the metal-free isoquinoline group of $[\text{Au}(\text{HL3})\text{Cl}_2]$, proton *q*, is chemically and magnetically distinct from proton *a*. Because of the spatial location of proton *q* directly over the metal-bound isoquinoline ring containing N1 (at a fairly loose ring centroid-to-proton distance of 4.33 Å), proton *q* is shielded by the ring current of the ring system. The magnitude of the upfield shift is 0.26 ppm. Equivalent protons *f* in the free ligand split into two single-integral signals (*f* and *l*) in complex $[\text{Au}(\text{HL3})\text{Cl}_2]$. These protons are only marginally affected by metallation of the ligand, consistent with an essentially unchanged environment relative to the free ligand. The remaining isoquinoline ring protons of $[\text{Au}(\text{HL3})\text{Cl}_2]$ split into independent signals consistent with the fact that only one isoquinoline ring serves as a ligand to Au(III) and all symmetry is lost in the metal complex.

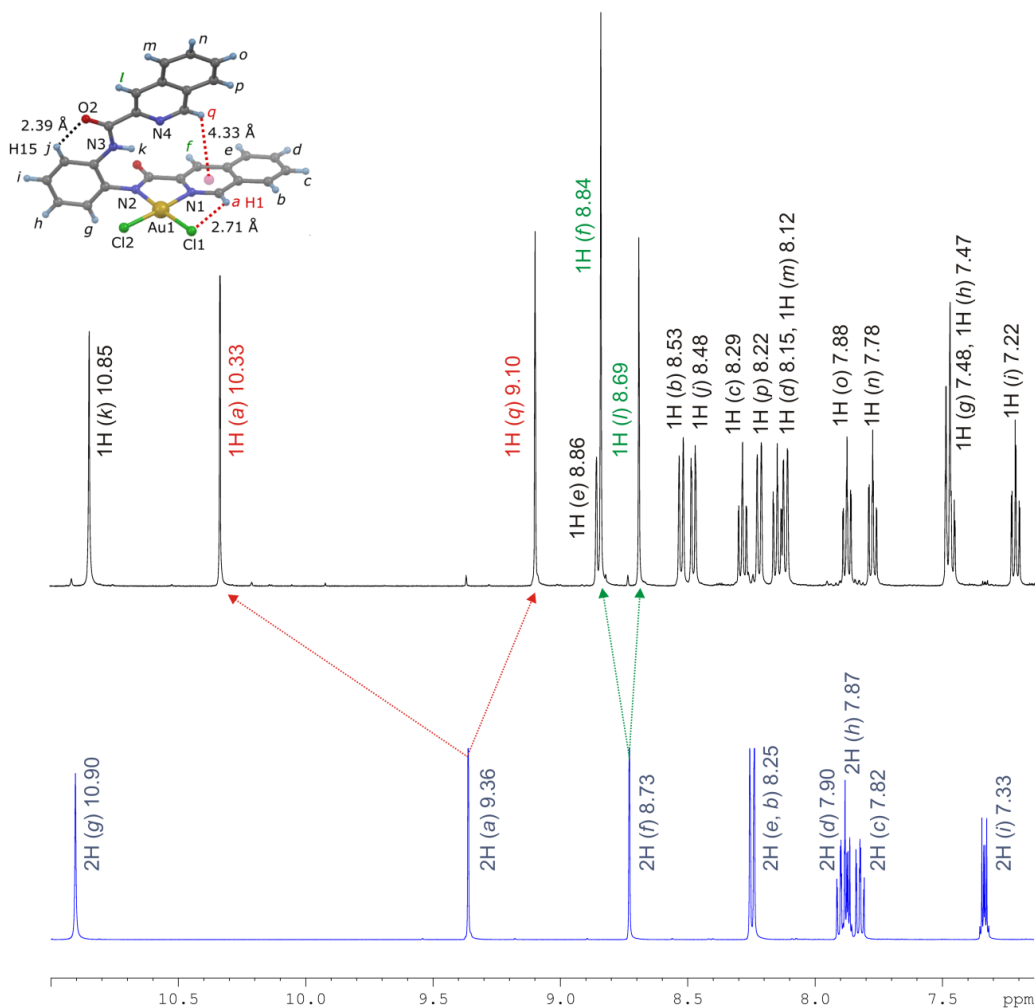


Figure 4.2.2.1: ^1H NMR spectra (500.01 MHz) of symmetric H_2L_3 (blue) and its asymmetric mono(amido) gold(III) complex (black), $[\text{Au}(\text{L}_3)\text{Cl}](\text{PF}_6)$ (inset structure) recorded in DMSO-d_6 . Signal integrals and peak assignments are based on the schemes for H_2L_3 and $[\text{Au}(\text{HL}_3)\text{Cl}_2]$ given in the Experimental Section. Arrows track the splittings and shifts for protons *a* and *f* that accompany chelation of gold(III) and the loss of symmetry in $[\text{Au}(\text{HL}_3)\text{Cl}_2]$ relative to the free ligand. Intramolecular hydrogen bonds and a mid-range $\text{C-H}\cdots\pi$ interaction are shown with dashed lines and interaction distances (structure inset).

For example, metallation splits the 4-fold degenerate doublet at 8.25 ppm of the free ligand (protons *b* and *e*) into four independent doublets (*b*, *e*, *m*, and *p*); protons *b* and *e* belonging to the metal-bound isoquinoline ring exhibit a ≥ 0.27 ppm downfield shift relative to the free ligand and reflect, in broad terms, the effect that polarization of the ring by the metal ion has on ^1H nuclear shielding in the present system. The ^1H NMR spectrum for the free ligand HL12 also exhibits an “all-aromatic” proton spectrum with signals spanning the 7–12.5 ppm range (Figure 4.2.2.2). Since the ligand is asymmetric in the first instance, compared to that

Spectroscopy

of H₂L3, all protons display individual signals. The amide N–H resonates particularly far downfield at 12.17 ppm, 1.27 ppm further than that for H₂L3. This may be because in the amide N–H (donor) is hydrogen bonded to both, pyridine and quinoline nitrogen atoms (acceptors), in a bifurcated hydrogen bonding system. This would create a greatly deshielded environment for the amide N–H, causing its far downfield resonance. This is however only speculation as a solid-state structure for this ligand has not been determined. The line width of the N–H signal is 5.2 Hz, which is slightly larger than that of H₂L3 but still fairly narrow in general terms, indicating minimal proton exchange at ambient temperature.

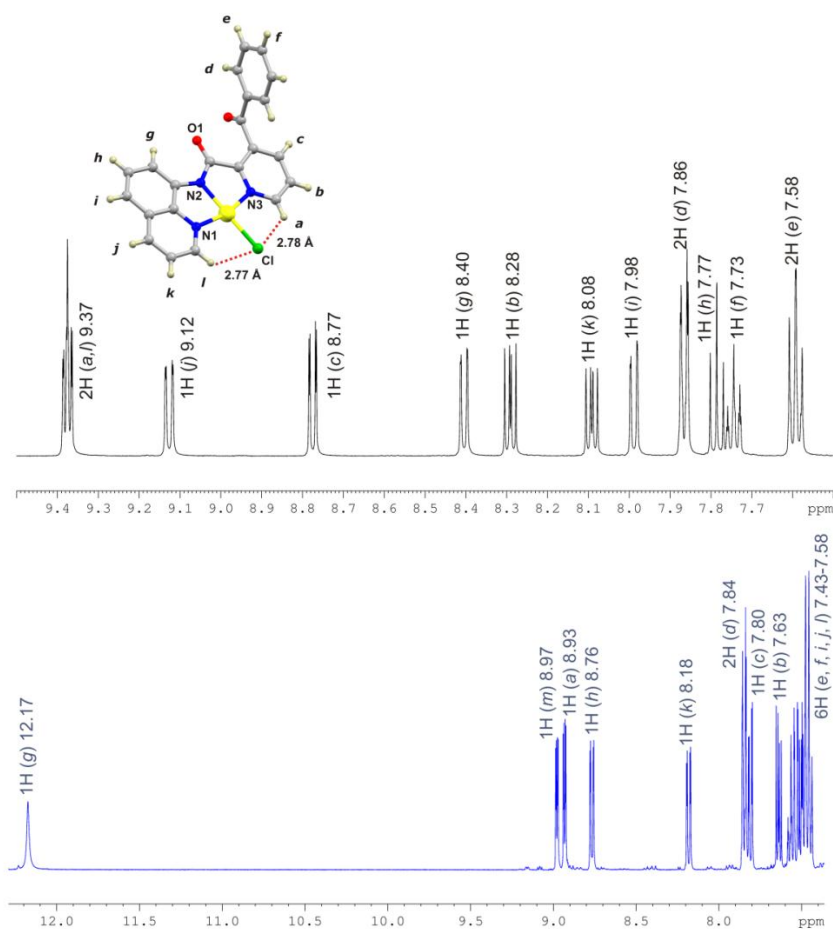


Figure 4.2.2.2: ¹H NMR spectra (400 MHz) of asymmetric ligand HL12 (blue) and its mono(amido) gold(III) complex (black), [Au(L12)Cl](PF₆) (inset structure) recorded in CDCl₃ and DMSO-*d*₆ respectively. Signal integrals and peak assignments are based on the schemes for HL12 and [Au(L12)Cl](PF₆) given in the Experimental Section.

Comparisons in shifts and line widths between ligands H₂L3 and HL12 are only estimates and cannot be taken as accurate since their spectra have been recorded in different solvents (DMSO-*d*₆ and CDCl₃, respectively). The proton signals for *e*, *f*, *i*, *j* and *l* are contained within

similar chemical environments so that their signals overlap in a region spanning 7.43-7.58 ppm. From Figure 4.2.2.2 it is evident that the spectral window is greatly decreased (7.58-9.40 ppm) on chelation of the gold(III) ion to the ligand. This is due to the loss of the amide N–H signal. Complexes $[\text{Au}(\text{L5})\text{Cl}](\text{PF}_6)$ - $[\text{Au}(\text{L16})\text{Cl}](\text{PF}_6)$ intrinsically contain two ' α ' protons since they are tridentate compounds. For simplistic reasons we have designated the proton on the amide side of the complex the α -proton and the proton on the opposite side of the complex, the α' -proton. A diagrammatic representation of the α -proton assignments is shown below for clarity.

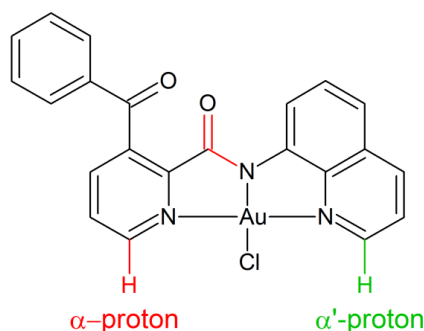


Figure 4.2.2.3: Diagrammatic representation of the α -proton designations for ligands HL5–HL16 and their gold(III) metal compounds. Metal compound $[\text{Au}(\text{L12})\text{Cl}](\text{PF}_6)$ is used as an example.

For the gold compound $[\text{Au}(\text{HL3})\text{Cl}_2]$, and in fact all compounds presented in this work (Table 4.2.2.1), the α - and α' -protons all exhibit a marked downfield shift when compared to their respective ligands. For all complexes, bar two (discussed below), the α -proton signals are the furthest downfield. For complex $[\text{Au}(\text{L12})\text{Cl}](\text{PF}_6)$ this effect is firstly due to two intramolecular hydrogen bonds between protons α and α' and the chloride ligand Cl1. Secondly, the presence of the gold(III) ion bound to the neighbouring pyridine and quinoline nitrogen atoms creates a significantly deshielded environment for these protons. For the complex $[\text{Au}(\text{L12})\text{Cl}](\text{PF}_6)$ protons α and α' resonate at the same frequency and appear as a multiplet at 9.37 ppm. Proton α exhibits a downfield shift of 0.44 ppm compared to the same proton present in the ligand while proton α' displays a downfield shift of 0.40 ppm compared to the same proton in the free ligand. Once again these measurements are only an estimate as the ligand and complex were recorded in different solvents (CDCl_3 and $\text{DMSO}-d_6$ respectively).

Spectroscopy

Table 4.2.2.1: Table comparing α - and α' -proton shifts between ligands and metal compounds.

Complex	Ligand	Difference	Complex	Ligand	Difference	
$\delta(^1\text{H}) \alpha /$ ppm	$\delta(^1\text{H}) \alpha /$ ppm	ppm	$\delta(^1\text{H}) \alpha' /$ ppm	$\delta(^1\text{H}) \alpha' /$ ppm	ppm	
[Au(HL1)Cl ₂]	9.32	8.56	0.76	N/A	N/A	N/A
[Au(HL2)Cl ₂]	9.29	8.55	0.74	N/A	N/A	N/A
[Au(HL3)Cl ₂]	10.33	9.36	0.97	N/A	N/A	N/A
[Au(L4)Cl ₂]	9.36	8.62	0.74	N/A	N/A	N/A
[Au(L5)Cl](PF ₆)	9.12	8.58	0.54	9.08	8.21	0.87
[Au(L6)Cl](PF ₆)	9.07	8.50	0.57	9.13	8.60	0.53
[Au(L7)Cl](PF ₆)	9.88	9.19	0.69	9.14	8.60	0.54
[Au(L8)Cl](PF ₆)	9.21	9.00	0.21	9.13	8.52	0.61
[Au(L9)Cl](PF ₆)	8.99	8.61	0.38	9.36	9.00	0.36
[Au(L10)Cl](PF ₆)	9.16	8.71	0.45	9.41	8.97	0.44
[Au(L11)Cl](PF ₆)	10.09	9.39	0.70	9.43	9.01	0.42
[Au(L12)Cl](PF ₆)	9.37	8.93	0.44	9.37	8.97	0.40
[Au(L13)Cl](PF ₆)	9.38	8.93	0.45	9.38	8.97	0.41
[Au(L14)Cl](PF ₆)	9.36	8.99	0.37	9.36	9.02	0.34
[Au(L15)Cl](PF ₆)	9.08	8.87	0.21	8.85	8.20	0.65
[Au(L16)Cl](PF ₆)	9.10	8.57	0.53	8.85	8.20	0.65
[Au(Quinpy)Cl]Cl ⁵	9.37	9.21	0.16	9.07	8.52	0.55
[Au(Quingly)Cl]Cl ⁵	9.19	8.88	0.31	N/A	N/A	N/A
[Au(Quinala)Cl]Cl ⁵	9.91	8.87	1.04	N/A	N/A	N/A
<i>S</i> -5 ⁸	8.95	N/A	N/A	N/A	N/A	N/A
<i>R</i> -6 ⁸	9.00	N/A	N/A	N/A	N/A	N/A

The signals *d* and *e* at 7.86 and 7.58 ppm, respectively, integrate for two protons. This is because there is free rotation around carbon C5-C6 bond allowing for the *ortho* and *meta* protons (*d* and *e*) of the ring to be chemically equivalent and hence their individual signals are averaged out as one. One other point to note is that the introduction of the gold(III) ion creates a significant enough change in environment so that almost all individual proton

signals are discernible from each other which starkly contrasts with the free ligand proton signals. As mentioned above for all complexes, bar two, the α -proton signals are the furthest downfield. The downfield shift in α -proton signal for compounds in this work correlate well with some literature gold(III) amide compounds, [Au(Quinpy)Cl]Cl (9.37 ppm), [Au(Quinpy)Cl]Cl (9.19 ppm), [Au(Quinpy)Cl]Cl (9.91 ppm), S-5 (8.95 ppm) and S-6 (9.00 ppm), which contain α -proton signals that are similarly downfield.^{5, 8} The two complexes that do not exhibit this trait are [Au(L6)Cl](PF₆) and [Au(L10)Cl](PF₆). Both these complexes contain a 1-isoquinoline moiety with proton *f* displaying the furthest downfield signal (9.85 and 9.86 ppm, respectively) in both cases (see Chapter 2). The reason for this is again presumed to be due to hydrogen bonding. Since the amide carbonyl oxygen contains two lone pairs of electrons, it is able to hydrogen bond with both protons *f* and *g* (Figure 4.2.2.4). These interactions create pseudo six-membered rings which add to the stability of the bonds. This would therefore create a greatly deshielded environment for these protons allowing them to resonate far downfield. As mentioned this is particularly evident for proton *f* in complexes [Au(L6)Cl](PF₆) and [Au(L10)Cl](PF₆). The effect is less pronounced for proton *g* but still evident. In general all ligands and complexes containing 1-isoquinoline and/or 8-aminoquinoline rings with protons that are equivalent to *f* and/or *g* displayed an increased downfield shift.

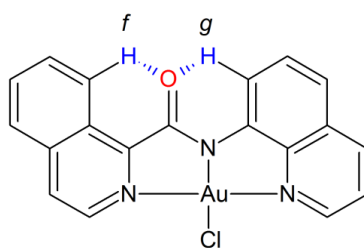


Figure 4.2.2.4: Intramolecular hydrogen bonding between protons *f* and *g* with the carbonyl oxygen of the amide bond for compound [Au(L10)Cl](PF₆).

Ligand HL13 and its respective complex [Au(L13)Cl](PF₆) contain a *para* substituted phenyl ketone ring. In the ring the hydrogen atom has been substituted with a fluorine atom. The presence of the fluorine atom adds an extra degree of intricacy to the ¹H and ¹³C spectra that are already complex. This is because the ¹⁹F nucleus is able to couple to and split both ¹H and ¹³C resonances. For both HL13 and [Au(L13)Cl](PF₆) this results in the splitting of what would normally be singlet carbon signals C7-C9 (see Chapter 2) into doublets while the

proton signals *e* and *d* (see Chapter 2) are split into triplets instead of doublets. This was unequivocally confirmed for the proton splitting pattern using acquisition parameters allowing for a ^{19}F decoupled proton spectrum where the coupling effect of the ^{19}F nucleus is removed (Figure 4.2.2.5). The black line represents the standard proton spectrum acquired for $[\text{Au}(\text{L13})\text{Cl}](\text{PF}_6)$ with the peaks at approximately 7.45 and 7.95 ppm displaying the characteristic triplet due to the protons coupling with each other as well as the fluorine nucleus. The peak at 7.95 ppm is less clear due to overlap with another proton signal. The blue line represents the ^{19}F decoupled proton spectrum. One can see the same proton peaks at 7.45 and 7.95 ppm are now represented as doublets instead of triplets.

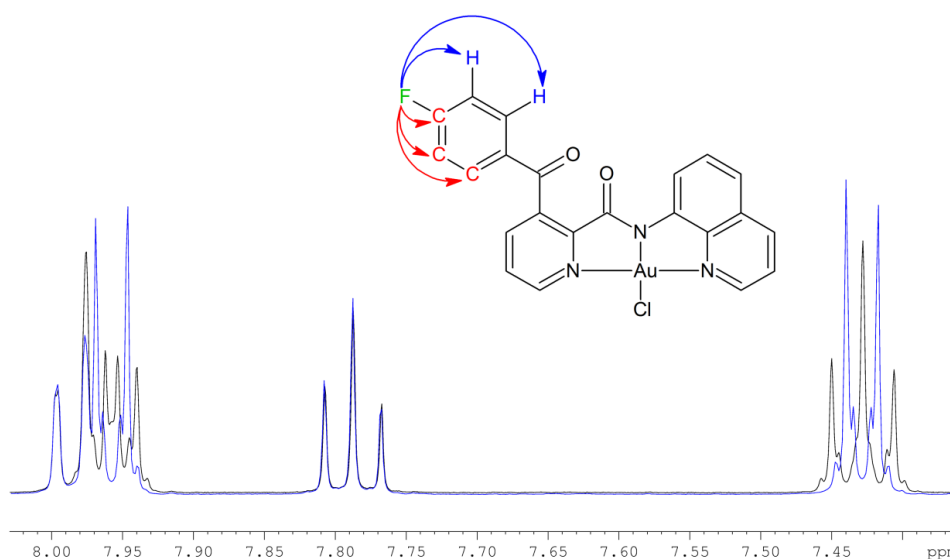


Figure 4.2.2.5: Diagram showing the ^{19}F coupled ^1H spectrum of AuL13 (black trace) and the ^{19}F decoupled proton spectrum (blue trace). The figure inset graphically shows the proton (blue) and carbon (red) atoms of the phenyl ketone ring that the fluorine atom couples with.

The series of three complexes, $[\text{Au}(\text{L5})\text{Cl}](\text{PF}_6)$ – $[\text{Au}(\text{L7})\text{Cl}](\text{PF}_6)$, containing the aminomethyl substituent were synthesised in the hope that they showed enhanced stability over the *cis*-dichloro compounds with the vision of being DNA intercalators. After their initial synthesis, the compounds were characterised by NMR spectroscopy. The compounds were dissolved in $\text{DMSO}-d_6$ and their proton spectra were recorded immediately. The spectra displayed clean proton signals correlating to the correct number of protons and hence the samples were queued overnight to record all required spectra (^1H , COSY, ^{13}C , DEPT135, HSQC and HMBC). Analysis of these spectra the next day revealed multiple ‘new’ peaks which is

indicative of some form of chemical transformation. It was immediately assumed to be some sort of decomposition process as gold(III) complexes are notorious for this.¹²⁻¹⁴ This was investigated by setting up an array experiment where individual spectra were recorded every thirteen minutes for 48 h. When analysing the data for $[\text{Au}(\text{L6})\text{Cl}](\text{PF}_6)$ (used as an example) (Figure 4.2.2.6) several characteristic features were observed which indeed confirmed that the complex was undergoing decomposition-specifically demetallation. The final spectra are complicated due to the presence of two species in solution; consequently multiple overlapping peaks are evident. Two particular regions have been excised from the full spectral window (9-9.75 ppm and 4.7-5.5 ppm) in order to clearly display the demetallation of complex $[\text{Au}(\text{L6})\text{Cl}](\text{PF}_6)$. In Figure 4.2.2.6, the region between 9-9.75 ppm shows the emergence of a triplet and the disappearance of two doublets. The emergence of the triplet corresponds to the amide N–H proton of the free ligand while the disappearance of the doublet signals correspond to protons *a* and *k* (see Chapter 2) of complex $[\text{Au}(\text{HL})\text{Cl}_2]$. It is interesting that the amide signal displays a 1:2:1 splitting pattern indicative of coupling to a neighbouring proton. This clearly is the case when observing the 4.7-5.5 ppm region of the spectrum. The methylene singlet from the aminomethyl moiety associated with $[\text{Au}(\text{L6})\text{Cl}](\text{PF}_6)$ slowly disappears while a doublet signal, slightly upfield, arises related to the free ligand. The singlet associated with the complex is characteristically further downfield than the signal related to the free ligand due to the deshielded environment accompanying the gold(III) ion. The emerging signal is split into a doublet, due to coupling with another proton. In this case it is due to coupling with the free ligand amide N–H proton mentioned above. The coupling of the amide N–H proton to the methylene protons is confirmed by a strong COSY correlation between the two signals. From this evidence and comparison of the spectral arrays to that of the free ligand in $\text{DMSO}-d_6$ it was concluded that the complexes were unstable, undergoing demetallation. It is assumed that the demetallation process is reductive as the solution becomes colourless with the concomitant formation of a dark brown/black precipitate, indicative of gold(III) reduction to colloidal gold.

Spectroscopy

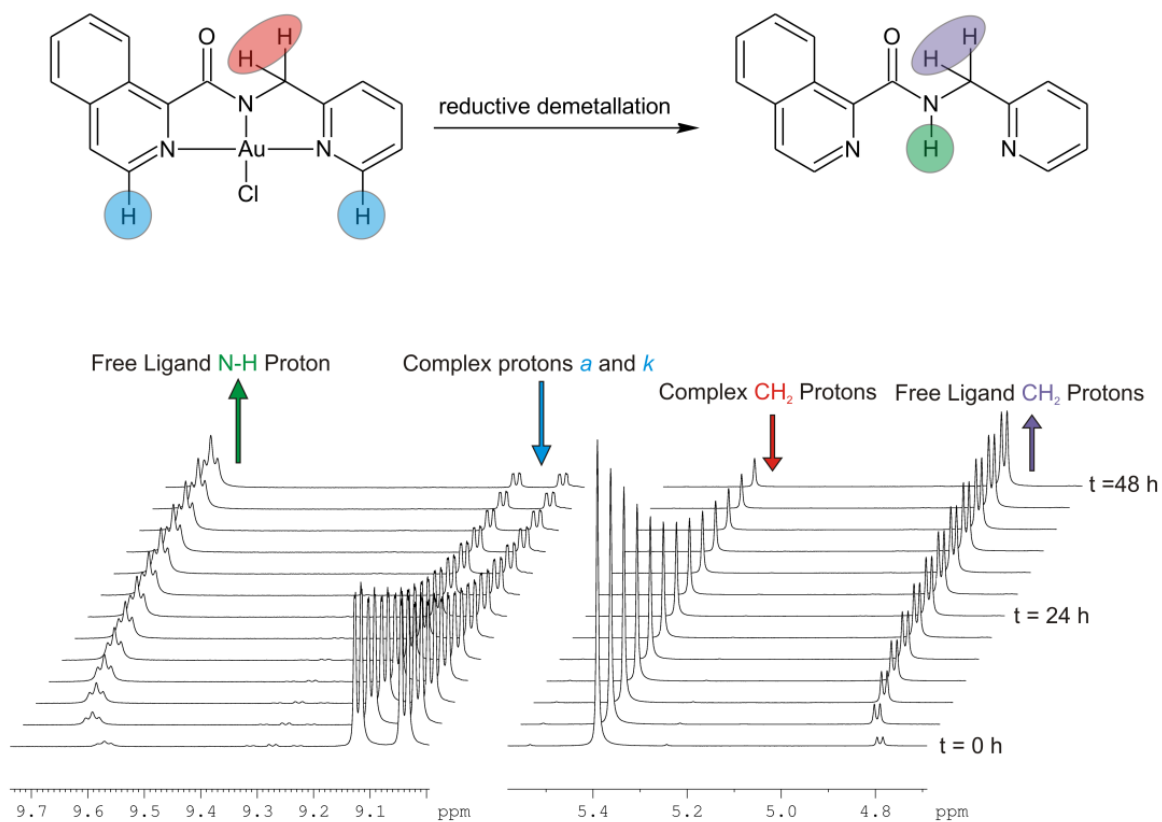


Figure 4.2.2.6: Selected regions of the spectral window showing the decomposition of $[\text{Au}(\text{L6})\text{Cl}](\text{PF}_6)$ in $\text{DMSO-}d_6$ over a 48 h period.

4.3 UV-visible spectroscopy

UV-vis spectroscopy provides information about compounds containing conjugated double bonds and/or metal ions.^{2, 4, 15} Ultraviolet and visible light have just the right energy to cause an electronic transition, which is the excitation of the system from the ground electronic state to another of higher energy. Depending on the energy required for the transition, the molecule will either absorb ultraviolet or visible light. Ultraviolet light is electromagnetic radiation with wavelengths ranging from 180-400 nm. Visible light has wavelengths from 400-780 nm. The normal electronic configuration of a molecule is known as its ground state and all the electrons are contained within the lowest energy molecular orbitals. When a molecule absorbs light of an appropriate wavelength and an electron is promoted to a higher energy orbital, the molecule is said to be in an excited state. The relative energies of the bonding, nonbonding and anti-bonding molecular orbitals are shown below (Figure 4.3.1).^{2, 4}

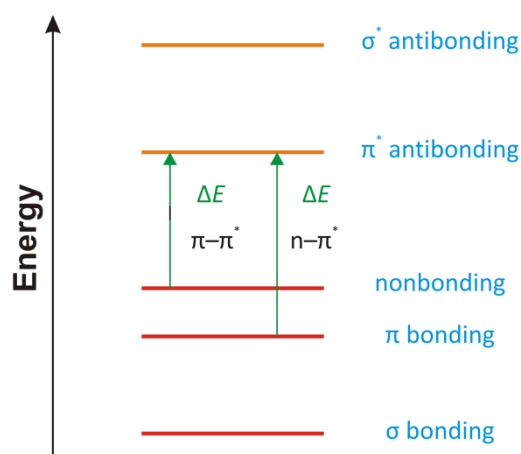


Figure 4.3.1: Electronic energy levels and the two of the possible transitions in organic molecules. Diagram adapted from 'Organic Chemistry, Fourth Edition'.²

Ultraviolet and visible light have sufficient energy to cause only the two electronic transitions in Figure 4.3.1. The electronic transition with the highest energy is the promotion of a non-bonding electron into a π^* anti-bonding molecular orbital.^{2, 4} This is called an $n \rightarrow \pi^*$ transition. The lower energy transition is the promotion of an electron from a π bonding molecular orbital to a π^* anti-bonding molecular orbital.^{2, 4} This transition is labelled a $\pi \rightarrow \pi^*$ transition. In the case of most aromatic molecules the LUMO orbitals are generally the π^*

Spectroscopy

orbitals while the HOMO orbitals usually contain full π -symmetry.^{2, 4} These transitions normally occur in the 200-320 nm region.^{2, 4}

Wilhelm Beer and John Lambert independently proposed that at a given wavelength, the absorbance of a sample depends on the amount of sample the light encounters as it passes through a solution of said sample.^{2, 4} This implied that absorbance depends on the concentration of sample as well as the length of the light path through the sample. This is known as the Beer-Lambert law, is given below:

$$A = \epsilon cl \quad 4.3.1$$

A = absorbance of the sample = $\log \frac{I_0}{I}$

I_0 = Intensity of radiation entering sample

I = Intensity of radiation emerging from sample

c = concentration of sample (mol dm^{-3})

l = length of the light path through sample (cm)

ϵ = molar absorptivity ($\text{litre mol}^{-1} \text{cm}^{-1}$)

The introduction of a metal ion to the system introduces the possibility of additional absorption bands in the 350-500 nm region.¹⁵ These absorption bands correspond to the d-d metal transitions and/or metal ligand charge transfer bands (ligand-to-metal-charge-transfer, LMCT, and metal-to-ligand-charge-transfer, MLCT). These transitions are usually visible for square planar metal complexes.¹⁵

For the complexes synthesised in this work the $\pi\text{-}\pi^*$ transitions associated with the ligand are expected to dominate the absorption spectrum in the 200-320 nm region. The low symmetry of the complexes allows the presence of d-d bands which may become more intense due to the mixing of metal d and ligand orbitals. The tridentate gold(III) amide compounds $[\text{Au}(\text{Quinpy})\text{Cl}]\text{Cl}$, $[\text{Au}(\text{Quinpy})\text{Cl}]\text{Cl}$, $[\text{Au}(\text{Quinpy})\text{Cl}]\text{Cl}$ and S-5, reported in the literature, all contain absorption bands between 300 and 400 nm. For the compounds $[\text{Au}(\text{Quinpy})\text{Cl}]\text{Cl}$, $[\text{Au}(\text{Quinpy})\text{Cl}]\text{Cl}$ and $[\text{Au}(\text{Quinpy})\text{Cl}]\text{Cl}$ these bands are assigned to LMCT-based transitions.⁵ The exact nature and wavelength maximum of the band for compound S-5 it not disclosed in the literature, however due to the similarity of the ligands, one might postulate that the ≈ 310 nm absorption band is LMCT-based.

4.3.1 Objectives

The primary objective was to use the electronic spectra of the compounds to investigate their biological properties. These properties include; the stability of the compounds in biologically relevant media, $\log P_{o/w}$ values, calf thymus DNA binding constants and the interaction between the compounds and relevant biomolecules such as glutathione and imidazole. The experimental electronic spectra were also compared to the DFT simulated spectra in order to determine the accuracy of the computational method.

4.3.2 Results and discussion

The electronic spectra for all the complexes investigated in this study were similar in that there was an intense $\pi-\pi^*$ band around 240 nm and a weaker $n-\pi^*$ band around 290 nm. There is also the presence of a relatively weaker LMCT band around 450 nm.

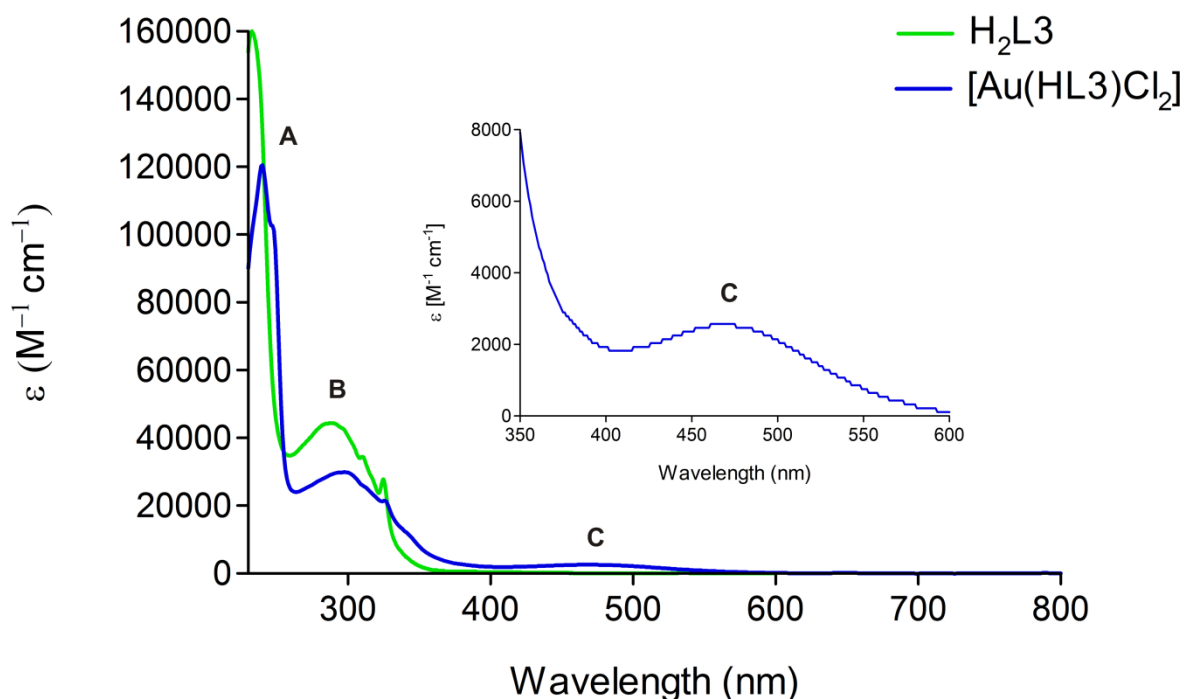


Figure 4.3.2.1: Overlaid electronic spectra of H_2L3 (green line) and $[Au(HL3)Cl_2]$ (blue line) showing the $\pi-\pi^*$ region (A and B) for both molecules and the LMCT band (inset C) for $[Au(HL3)Cl_2]$.

The electronic spectra of the ligand, H_2L3 (green line) and its metal complex, $[Au(HL3)Cl_2]$ (blue line), are shown as an example below in Figure 4.3.2.1. The peaks labelled A and B for both spectra, are assigned to the $\pi-\pi^*$ band and the $n-\pi^*$ band respectively, consistent with

Spectroscopy

the delocalised structure of the predominantly aromatic ligand. As can be seen (Figure 4.3.2.1) upon chelation of the ligand with a gold(III) ion, the $\pi-\pi^*$ peaks red-shift slightly and a new peak arises (labelled C). This comparatively less intense peak is assigned to the LMCT band associated with the metal complex. These assignments are backed up by the computational work discussed in Chapter 5.

Table 4.3.2.1: Summary of the two major λ_{\max} values in the $\pi-\pi^*$ and LMCT regions of the metal complexes reported in this work.

Compound	λ_{\max}/nm ($\epsilon/\times 10^3 \text{ M}^{-1} \text{ cm}^{-1}$)	λ_{\max}/nm ($\epsilon/\times 10^3 \text{ M}^{-1} \text{ cm}^{-1}$)
[Au(HL1)Cl ₂]	312 (5.1)	453 (0.16)
[Au(HL2)Cl ₂]	310 (3.9)	449 (0.12)
[Au(HL3)Cl ₂]	297 (30)	468 (2.9)
[Au(L4)Cl ₂]	269 (18)	477 (6.3)
[Au(L5)Cl](PF ₆)	224 (32)	317 (40)
[Au(L6)Cl](PF ₆)	226 (45)	301 (8.2)
[Au(L7)Cl](PF ₆)	244 (83)	342 (2.4)
[Au(L8)Cl](PF ₆)	256 (44)	364 (12)
[Au(L9)Cl](PF ₆)	257 (6.4)	362 (2.4)
[Au(L10)Cl](PF ₆)	248 (67)	374 (9.0)
[Au(L11)Cl](PF ₆)	248 (93)	349 (12)
[Au(L12)Cl](PF ₆)	253 (38)	369 (7.7)
[Au(L13)Cl](PF ₆)	255 (34)	369 (7.3)
[Au(L14)Cl](PF ₆)	256 (32)	362 (9)
[Au(L15)Cl](PF ₆)	N/A ^a	376 (6.3)
[Au(L16)Cl](PF ₆)	N/A ^a	379 (7.7)
[Au(Quinpy)Cl]Cl ⁵	N/A	$\approx 365^b$
[Au(Quingly)Cl]Cl ⁵	N/A	$\approx 360^b$
[Au(Quinala)Cl]Cl ⁵	N/A	$\approx 370^b$
S-5 ⁸	N/A	$\approx 310^b$

^aThe electronic spectra for complexes [Au(L15)Cl](PF₆) and [Au(L16)Cl](PF₆) were recorded in DMSO due to lack of solubility in more appropriate solvents. DMSO absorbs in the region where the $\pi-\pi^*$ absorption band would normally be positioned, hence their non-availability.^b Exact absorption maxima and extinction coefficients not given in the literature and have therefore been estimated from figures.

Spectroscopy

The metal compounds were essentially synthesised as four different generations of compounds. Metal compounds $[\text{Au}(\text{HL1})\text{Cl}_2]$ – $[\text{Au}(\text{L4})\text{Cl}_2]$ were synthesised first followed by $[\text{Au}(\text{L5})\text{Cl}](\text{PF}_6)$ – $[\text{Au}(\text{L7})\text{Cl}](\text{PF}_6)$, $[\text{Au}(\text{L8})\text{Cl}](\text{PF}_6)$ – $[\text{Au}(\text{L14})\text{Cl}](\text{PF}_6)$ and finally $[\text{Au}(\text{L15})\text{Cl}]$ – $[\text{Au}(\text{L16})\text{Cl}]$. The λ_{max} values for these complexes are similar within a generation, and even between generations. For example, metal compounds $[\text{Au}(\text{HL1})\text{Cl}_2]$ – $[\text{Au}(\text{L4})\text{Cl}_2]$ all contain a weak LMCT band in the ~450 nm region whereas $[\text{Au}(\text{L5})\text{Cl}](\text{PF}_6)$ – $[\text{Au}(\text{L7})\text{Cl}](\text{PF}_6)$ absorb in the lower 300 nm range and $[\text{Au}(\text{L8})\text{Cl}](\text{PF}_6)$ – $[\text{Au}(\text{L16})\text{Cl}]$ absorb in the mid-to-higher 300 nm range. This is because there are only slight structural changes between generations and even smaller structural changes within a generation. The spectra for the cis-dichloro compounds, $[\text{Au}(\text{HL1})\text{Cl}_2]$ – $[\text{Au}(\text{L4})\text{Cl}_2]$, were similar to that of an analogous gold(III) amide compound presented in the literature, $[\text{Au}(\text{HL})\text{Cl}_2]$ ($\text{H}_2\text{L} = 2,2'$ -bis(2-pyridylcarboxamide)-1,1'-binaphthyl), with absorption maxima at 250, 350 and 470 nm.⁹ The tridentate compounds from this work were also found to follow the trend set by literature compounds, $[\text{Au}(\text{Quinpy})\text{Cl}]\text{Cl}$, $[\text{Au}(\text{Quinpy})\text{Cl}]\text{Cl}$, $[\text{Au}(\text{Quinpy})\text{Cl}]\text{Cl}$ and *S*-5, which similarly obtain absorption maxima at approximately 360 nm.⁵

4.4 Stability and reactivity

The metal complexes described in this work were synthesised with the aim of being metallotherapeutic drugs in the fight against cancer. One of the primary characteristics one has to consider and evaluate when testing such drugs is their solution stability, in traditional solvents such as acetonitrile, methanol and ethanol, as well as biologically relevant solvents such as buffered aqueous media. This is particularly pertinent in the field of gold(III)-based metallo-therapeutics.¹⁶⁻¹⁸ This is because gold in its +3 oxidation state is electron deficient and readily undergoes hydrolysis reactions as well as reductive demetallation reactions.^{16, 17} Hydrolysis reactions generally occur when the metal complex in question contains an accessible co-ordination site such as in the $[\text{Au}^{(\text{III})}(\text{terpy})\text{Cl}]^+$ system, however it is also possible for hydrolysis reactions to occur in tetradentate systems such as the bis(pyrrole-imine) gold(III) system.¹⁹⁻²¹ For the bis(pyrrole-imine) gold(III) system this only occurs when the bridging unit of the system contains a two-carbon linker imposing geometries that deviate significantly from the norm, creating a highly strained co-ordination environment. This allows for the cleavage of one Au–N bond by a water molecule followed by hydrolysis to form the species shown below in Figure 4.4.1.

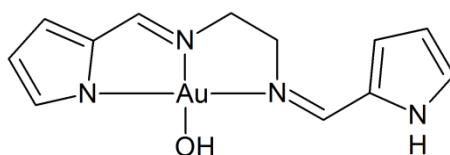


Figure 4.4.1: Chemical structure of the hydrolysis product originating from a bis(pyrrole-imine) gold(III) compound.¹⁹

Reductive demetallation in gold(III)-based compound systems is very common.^{5, 14, 17, 22} One way of avoiding this problem is via the introduction of multidentate-chelating ligands which contain strong σ -donor ability and are hence able to stabilise the gold(III) ion in its high oxidation state. An example of such a ligand is tetraphenylporphyrin (TPP).^{12, 13} This is a macrocyclic tetradentate ligand containing two anionic and two neutral N-donors. This ligand is able to stabilise the gold(III) centre in biologically relevant media as well as towards cellular reducing agents such as glutathione (GSH).^{12, 13} Most gold(III) complexes synthesised with the intention of being metallotherapeutic drugs are evaluated for their stability towards GSH. This is because GSH is one of the most prevalent intracellular reducing agents

Spectroscopy

and is present in animal cells at a concentration of approximately 5 mM.²³ GSH is a tripeptide comprising glutamate, cysteine and glycine and is used in a variety of detoxification, transport and metabolic processes.²³ An example is in its use as a substrate for peroxidase reactions in helping to destroy peroxides generated by oxidases.^{23, 24} It is present in either its reduced form (GSH) or its oxidised form (GSSH). The ratio of reduced glutathione to oxidised glutathione is often used as a measure of cellular toxicity.²⁴ Once oxidised, glutathione can be reduced back by glutathione reductase using NADPH as an electron donor.²⁴

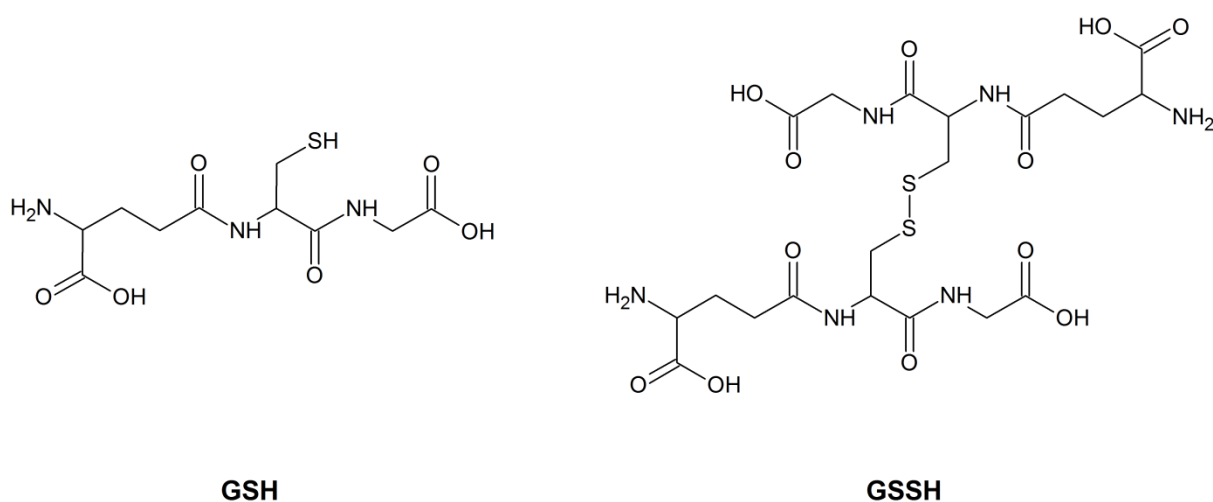


Figure 4.4.2: Chemical structures of reduced glutathione (GSH) and oxidised glutathione (GSSH).

4.4.1 Objectives

The objectives of this section are to evaluate the compounds synthesised in this work for their solution stability in biologically relevant media, such as a buffer system, using UV/Visible spectroscopy. Once the compounds were proven stable in said media they were further evaluated for their stability in the presence of certain biomolecules such as GSH and imidazole.

4.4.2 Experimental

Ultra-pure water (resistivity 18.2 MOhm.cm) was used to prepare the tris buffers used in this work. The correct amount of tris and sodium chloride to formulate a 50 mM and 10 mM solution, respectively, were weighed out and dissolved in a small amount of ultra-pure water. This solution was then placed in a jacketed conical flask which was connected to a

thermostatically regulated water bath at 37 °C. This is to mimic physiological conditions. The solution was then titrated with concentrated HCl to a pH of 7.34 and decanted into a 250 mL volumetric flask and allowed to cool to room temperature before making up to the mark. For all experiments below the chloride salt of each complex was used as it is water soluble.

4.4.3 Results and discussion

As previously mentioned, the metal compounds in this work were synthesised in four different generations. Metal compounds [Au(HL1)Cl₂]- [Au(HL4)Cl₂] were synthesised first and hence their stability was assessed first. Metal complex [Au(HL3)Cl₂] was the only one from the first generation of complexes that proceeded through to the 5-dose phase of testing at the National Cancer Institute (NCI), hence this complex was used as a representative example for analysis of its solution stability. The complex was dissolved in pure spectroscopic grade DMSO and an amount was added to a 1 cm UV/Vis quartz cuvette containing a tris buffered saline (TBS, 50 mM Tris, 10 mM NaCl, pH 7.34 at 37 °C) solution so that the final concentration of complex was 1.16×10^{-5} M. Spectra were then recorded at 30 min intervals over a period of 48 h to observe any significant spectral change and hence the solution stability of the complex. Figure 4.4.3.1 below displays graphically successive scans over this period with the orange line displaying time = 0.5 h, the purple line time = 12 h and the red line time = 48 h. It was noticed immediately that there was a shifting baseline which is characteristic of precipitation, and indeed this was observed. Once the 48 h period was complete the sample was removed from the spectrometer and a fine white precipitate was present along with a clear solution. This was interesting as the complex itself in solution is a dark red colour. From the figure below it is clearly visible that there is a steady decrease in absorbance over the 48 h period, specifically in the 300-400 nm region, which is where the LMCT band of the complex lies.

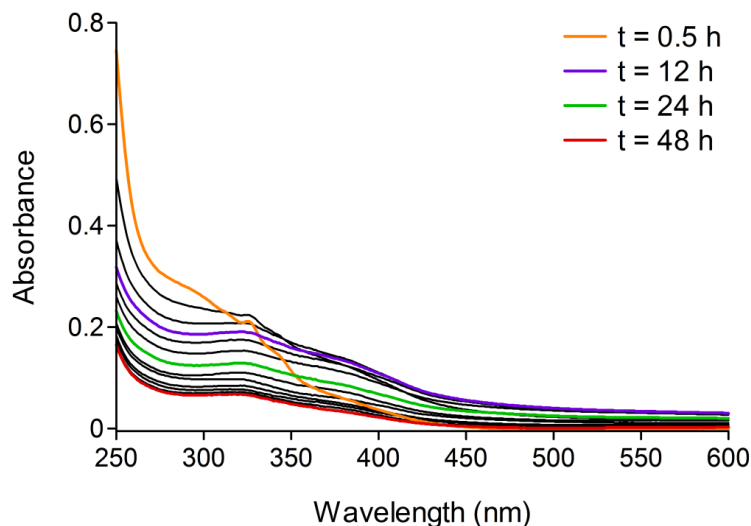


Figure 4.4.3.1: Spectra of $[\text{Au}(\text{HL}3)\text{Cl}_2]$ recorded as a function of time in TBS at a complex concentration of $1.16 \times 10^{-5} \text{ M}$, pH 7.34 and at 37°C . All spectra were corrected for any background offset by setting $A_{600} = 0$.

It is therefore clear that there is some kind of decomposition of the complex occurring in solution. There are two hypotheses that would account for the observed spectral changes. The first is reductive demetallation where no substitution of the chloride ions takes place and the metal centre is directly reduced 'out' of the ligand in one step. The second and more likely process is the substitution of the chloride ions with water followed by reductive demetallation. Substitution of the chloride ions with DMSO was ruled out by observing the ^1H NMR spectrum of the complex in pure $\text{DMSO-}d_6$ over the same time period with no noticeable change. If the second proposed mechanism was to be considered one would assume there would be at least two steps, the first comprising simultaneous substitution of both chloride ions followed by a second reductive demetallation step. If each of the chloride ions were equivalent in terms of reactivity, this assumption would hold. In the case of complex $[\text{Au}(\text{HL}3)\text{Cl}_2]$ the ligand contains two dissimilar N-donor moieties, the stronger σ -donor amide nitrogen and the weaker σ -donor heterocyclic pyridine nitrogen. This causes a structurally evident *trans* effect whereby the Au-Cl bond *trans* to the amide nitrogen donor is greatly lengthened compared to the Au-Cl bond *trans* to the pyridine nitrogen. This in effect renders the chloride ion *trans* to the amide nitrogen more labile and susceptible to nucleophilic attack. In this case there should be three steps observable, two separate distinguishable substitution steps for each chloride ion followed by reductive demetallation. The concomitant formation of a precipitate does not allow for accurate rate constants to be

determined. That being said, the absorption of the complex was monitored at 295 nm and plotted against time in order to try and discern whether the process is a two- or three-step progression (Figure 4.4.3.2). The data fits a double exponential decay function indicating that there is a two-step process with the first and second rate constants being $0.024(2) \text{ h}^{-1}$ and $0.15(3) \text{ h}^{-1}$, respectively. This result is interesting considering the *trans* effect argument mentioned above. The reaction is either truly biphasic, with the substitution of the chloride ions occurring simultaneously, or the first step in the three step process occurs extremely fast and takes place in under half an hour, which is the first time point in the experiment. The kinetic trace, however, does confirm a multi-step process over the single-step demetallation process. Water suppression ^1H NMR experiments were performed in order to deconvolute the mechanistic detail. However a high enough concentration was not achievable in order to observe a spectrum at a reasonable signal-to-noise ratio in relation to acquisition time. Complexes $[\text{Au}(\text{HL1})\text{Cl}_2]$, $[\text{Au}(\text{HL2})\text{Cl}_2]$ and $[\text{Au}(\text{L4})\text{Cl}_2]$ were similarly monitored. A similar trend to $[\text{Au}(\text{HL3})\text{Cl}_2]$ was observed for $[\text{Au}(\text{HL1})\text{Cl}_2]$ and $[\text{Au}(\text{HL2})\text{Cl}_2]$ while $[\text{Au}(\text{L4})\text{Cl}_2]$ exhibited a marked increase in comparable stability.

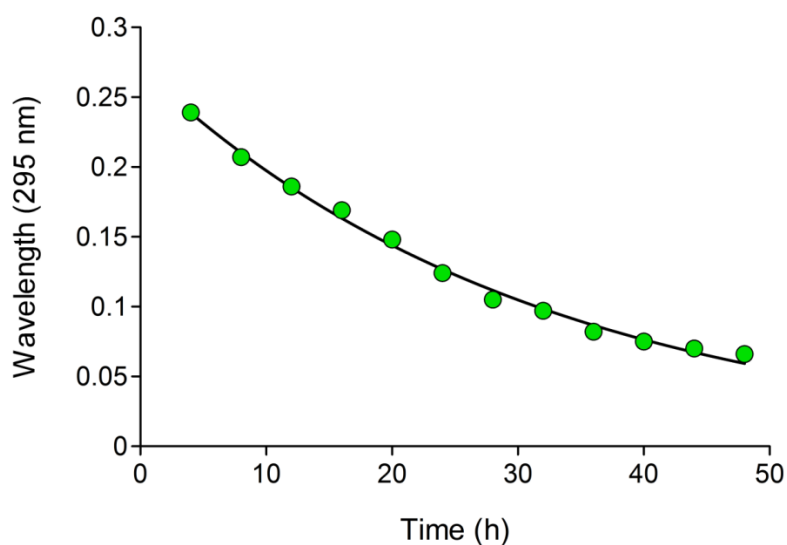


Figure 4.4.3.2: Double exponential decay curve for $[\text{Au}(\text{HL3})\text{Cl}_2]$ at 295 nm in TBS at a complex concentration of $1.16 \times 10^{-5} \text{ M}$, pH 7.34 and at $37 \text{ }^\circ\text{C}$ over a period of 48 h. Non-linear equation used: $Y = A1 \times 10^{(-A2*t)} + A3 \times 10^{(-A4*t)}$ where t = time, $A1$ and $A3$ are Y spans; $A2$ and $A4$ are rate constants. R is 0.9987, $A1$ is 0.18(1), $A2$ is $0.024(2) \text{ h}^{-1}$, $A3$ is 0.10(1) and $A4$ is $0.15(3) \text{ h}^{-1}$.

Due to the lack of stability and relatively poor cytotoxicity for $[\text{Au}(\text{HL3})\text{Cl}_2]$, the cis-dichloro compounds were abandoned and the aminomethyl-based tridentate compounds,

Spectroscopy

[Au(L5)Cl](PF₆)-[Au(L7)Cl](PF₆) were synthesised. All three of these compounds were accepted at the NCI for 1-dose testing against their panel of 60 human cancer cell lines with both [Au(L6)Cl](PF₆) and [Au(L7)Cl](PF₆) progressing further to the repeat 5-dose phase. It has already been shown, by NMR, that this generation of complexes are unstable in DMSO-*d*₆ (see chapter 4.2). It was therefore expected that they would be similarly unstable in TBS, and indeed they were. Complex [Au(L6)Cl](PF₆) is used as an example (see Figure 4.4.3.3 below). An appropriate amount of the complex was dissolved in 1 mL spectroscopic grade DMSO and 19 mL of TBS added to make a solution containing 5% DMSO. This solution was then monitored by UV/Vis spectroscopy over a period of 12 h. As one can see below, the absorption peak at 365 nm displays a 57% reduction in absorbance over the 12 h. This agrees with the NMR data and can be attributed to reductive demetallation of the complex.

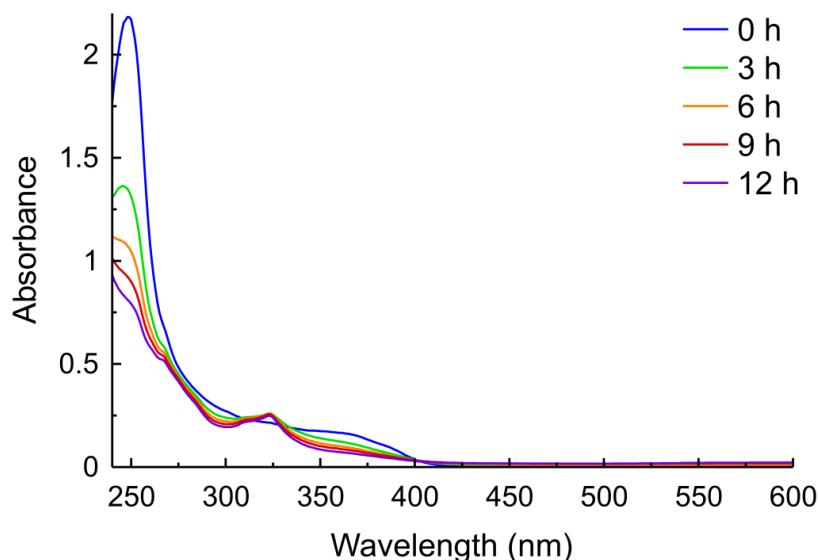


Figure 4.4.3.3: UV/Vis absorption spectrum for complex [Au(L6)Cl](PF₆) at a concentration of 2.32×10^{-5} M, pH 7.34 and at 37 °C. The spectra were recorded over a period of 12 h displaying a 57% drop in absorbance at 365 nm.

Complexes [Au(L5)Cl](PF₆)-[Au(L7)Cl](PF₆) were similarly abandoned due to their instability and the next generation of complexes, [Au(L8)Cl](PF₆)-[Au(L14)Cl](PF₆), were synthesised to circumvent solution and redox instability; these complexes all contain an 8-aminoquinoline group in place of the aminomethyl moiety. All the complexes bar [Au(L9)Cl](PF₆) and [Au(L13)Cl](PF₆) were accepted through to the 5-dose phase of testing at the NCI with [Au(L10)Cl](PF₆), [Au(L12)Cl](PF₆) and [Au(L13)Cl](PF₆) exhibiting particularly encouraging results (see Chapter 7). It was therefore imperative that the stability of these complexes be

evaluated in TBS. The chloride salts of each of the complexes were used as they are readily soluble in TBS. All complexes were dissolved directly in TBS, as their chloride salts, and their spectra observed over a period of 24 h. Complex $[\text{Au}(\text{L12})\text{Cl}](\text{PF}_6)$ is used as an example below (Figure 4.4.3.4). As Figure 4.4.3.4 depicts, complex $[\text{Au}(\text{L12})\text{Cl}](\text{PF}_6)$ displays a 2% decrease in absorbance at 362 nm over a 24 h period. This decrease is effectively negligible and is comparable to $\text{Au}[\text{Por}]^+$,^{12, 13} indicating complexes $[\text{Au}(\text{L8})\text{Cl}](\text{PF}_6)$ – $[\text{Au}(\text{L14})\text{Cl}](\text{PF}_6)$ are stable in the tested media. All complexes displayed similar stability with complex $[\text{Au}(\text{L13})\text{Cl}](\text{PF}_6)$ showing the largest percentage decrease in absorbance (2.5%) at 362 nm.

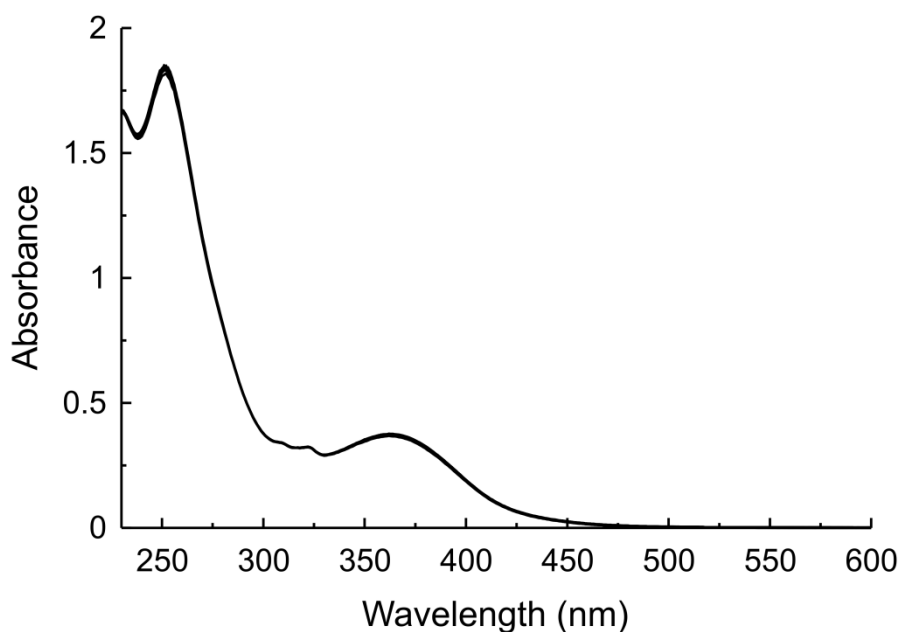


Figure 4.4.3.4: UV/Vis absorption spectrum taken over a period of 24 h at 37 °C in TBS, pH 7.34, for complex $[\text{Au}(\text{L12})\text{Cl}](\text{PF}_6)$ (1.52×10^{-5} M) displaying a 2% drop in absorbance.

Due to the marked increase in stability of complexes $[\text{Au}(\text{L8})\text{Cl}](\text{PF}_6)$ – $[\text{Au}(\text{L14})\text{Cl}](\text{PF}_6)$ in TBS, complex $[\text{Au}(\text{L7})\text{Cl}](\text{PF}_6)$ was used as a representative example due to its potent cytotoxicity and evaluated further for its stability in the presence of glutathione and imidazole. Glutathione, as mentioned in the introduction to this section, is a biologically relevant reducing agent and as such it is of vital importance to assess the stability of the complexes towards it. Imidazole is a heterocyclic aromatic N-donor that is intended to mimic relevant biomolecules such as the amino acid histidine as well as the nucleobases adenine, thymine, guanine and cytosine.²⁴ This would give us an idea whether the nucleobases are able to substitute the chloride ion in the fourth co-ordination site and hence be able to form DNA-

drug adducts as cisplatin does.²⁵ Figure 4.4.3.5 A below displays the spectra of complex $[\text{Au}(\text{L12})\text{Cl}](\text{PF}_6)$ collected over a 24 h period in the presence of a tenfold higher concentration of imidazole while Figure 4.4.3.5 B displays complex $[\text{Au}(\text{L12})\text{Cl}](\text{PF}_6)$ in the presence of a tenfold higher concentration of glutathione at 10 minute intervals over a 12 h period. As can be seen from 4.4.3.5 A, there is a minimal 3.5% decrease in the LMCT absorption band positioned at 364 nm. This indicates that there is no chemical reaction taking place under the chosen reaction conditions and complex $[\text{Au}(\text{L12})\text{Cl}](\text{PF}_6)$ is stable towards nucleophilic substitution of the chloride ion by imidazole. This further suggests that if the complex does interact with DNA through intercalation, as it was intended by design, the complex will not form DNA-complex biomolecule adducts and the DNA-complex interaction will be driven purely by electrostatic and van der Waals forces. Figure 4.4.3.5 B displays effectively a 100% reduction in the LMCT absorption band in the presence of glutathione. After 12 h (Figure 4.4.3.5 B, red line) the reaction is effectively complete. This is indicative of reductive decomposition of the complex. It is interesting to note that upon mixing the individual solutions a fine milky white precipitate formed immediately. This was confirmed by the presence of a shifting baseline seen in the representative figure below.

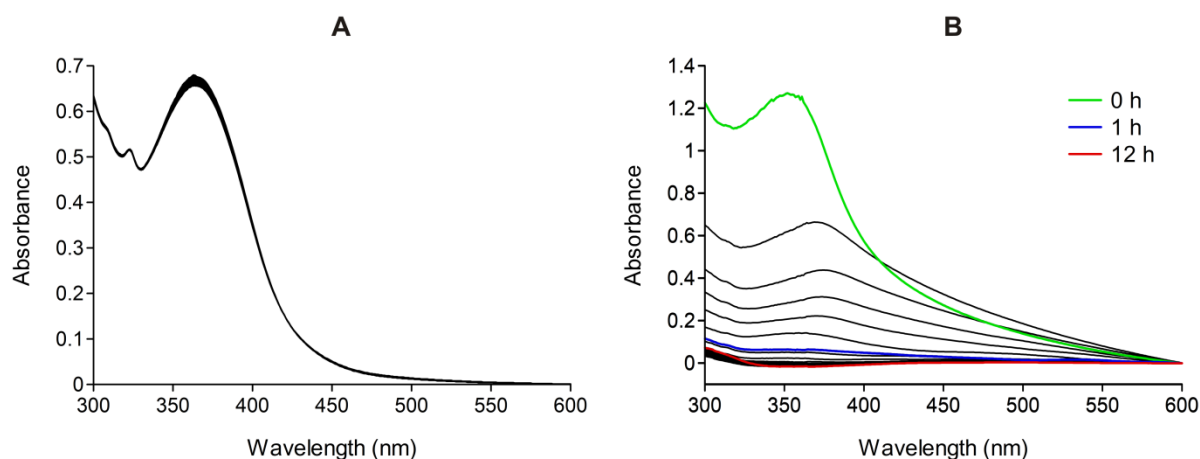


Figure 4.4.3.5: UV/Vis spectra of $[\text{Au}(\text{L12})\text{Cl}](\text{PF}_6)$ in the presence of a tenfold increase in concentration of imidazole over a period of 24 h (A) and in the presence of a tenfold increase in concentration of glutathione (B) over 12 h. Both sets of spectra were recorded at 37 °C in TBS at pH 7.34. All spectra were corrected for any background offset by setting $A_{600} = 0$.

After the 12 h period was complete the contents of the cuvette were centrifuged and both the precipitate and supernatant liquid were analysed by mass spectrometry. The supernatant liquid contained both oxidized and reduced glutathione as well as $[\text{AuCl}_2]^-$ while

Spectroscopy

the precipitate contained free ligand and $[\text{AuCl}_2]^-$. It is therefore clear that the complex undergoes reductive demetallation, presumably, through a multistep process. The proposed mechanism is substitution of the chloride ion by the S-H moiety of glutathione followed by electron transfer and reduction of the gold(III) centre to gold(I), then further substitution by chloride ions on the gold centre to form $[\text{AuCl}_2]^-$. The stabilities of complexes $[\text{Au}(\text{L15})\text{Cl}]$ and $[\text{Au}(\text{L16})\text{Cl}]$ were unable to be evaluated due to their inherent insolubility in up to 15% DMSO/TBS solutions at concentrations as low as 10^{-6} M.

4.5 Octanol/Water partition coefficients

The transport of a drug to its site of action normally involves the drug having to pass through several lipid membrane systems.^{26, 27} As a result of this, the solubility of a drug in aqueous media relative to lipids is of considerable significance in the transport of that drug to its site of action.^{26, 27} This is specifically important at the aqueous medium/lipid interface. Partition coefficients are therefore a way to measure the distribution of a compound between two immiscible solvents in the attempt to correlate the activities of the drugs with their partition coefficient.²⁸ Such correlations have been used with some success in the prediction of the activities of some potential drugs; however, the results are generally only valid when the solubility and transport by diffusion through a membrane are the main factors controlling the drug action.^{26, 27}

It is not easy to measure partition coefficients *in situ* and so instead the less accurate organic solvent/aqueous solution model system is used.^{26, 27} The octanol/water partition coefficient is the ratio between the amount of drug present in the octanol layer and the amount of drug present in the aqueous layer at equilibrium. Octanol/water partition coefficients are shown below (Figure 4.5.1) for selected literature compounds.

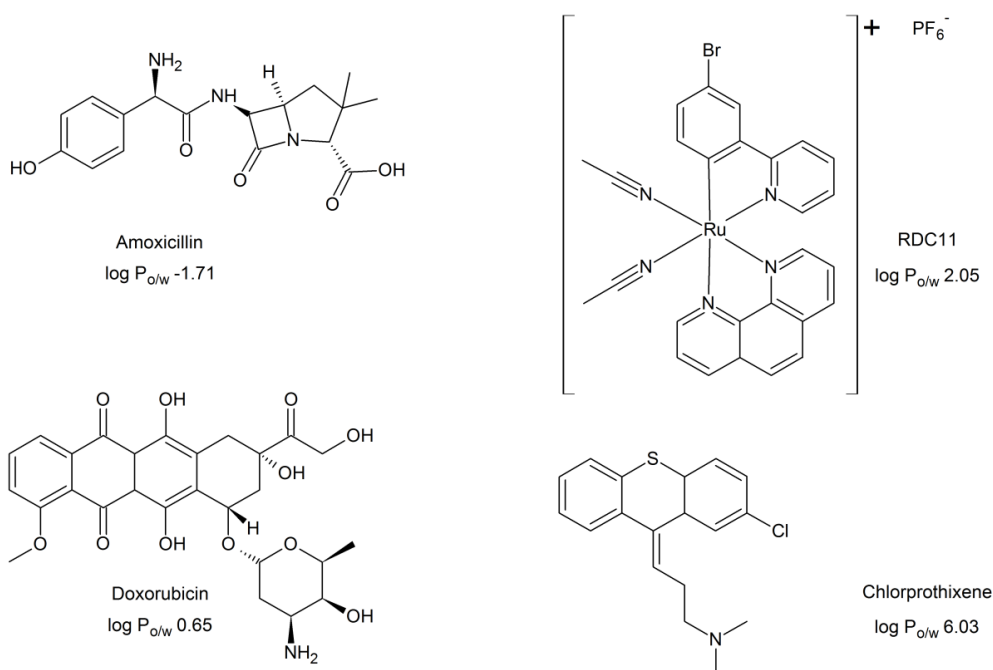


Figure 4.5.1: Structures and $\log P_{o/w}$ values of an anti-biotic (amoxicillin), two anti-cancer chemotherapeutic drugs (doxorubicin and RDC11) and an anti-psychotic drug (chlorprothixene).

The log of this value ($\log P_{o/w}$) is the value that is normally quoted and used in quantitative-structural-activity relationship studies.^{26, 27} The ratio is essentially independent of concentration and is generally calculated using the shake flask method.²⁶⁻²⁸ The use of *n*-octanol as the representative hydrophobic phase is due to its similar structure to phospholipids present in cell membranes. The eight carbon chain mimics the hydrophobic tail while the alcohol group mimics the hydrophilic head. The second phase is water, since the main constituent of blood serum is water. The more hydrophobic a drug is, the more likely it is to be found in lipid membranes while the more hydrophilic a drug is, the more likely it is to be found in blood serum. Generally a drug must contain some hydrophobic character since some of the most important interactions between drugs and a biological system depend on its hydrophobicity. Some examples of such interactions are enzyme-ligand, drug-receptor interactions and transport through biological membranes.^{26, 27} The efficient penetration through membranes is a prerequisite for most drugs, but, particularly important in the case of orally ingested candidates which must move from the intestine to the blood and on to their intended target.²⁹ The ability of a drug candidate to cross these barriers until it finds its intended target and performs its function is most often described by the octanol/water partition coefficient.

4.5.1 Objectives

The objective in determination of the octanol/water partition coefficients of the metal compounds presented in this work is to determine whether they are hydrophilic or hydrophobic in nature. This will hopefully allow us to better understand the activity profiles of the compounds and to correlate their relative activities with their structures.

4.5.2 Experimental

The method that was chosen for the determination of octanol/water partition coefficients in this work was the 'shake-flask' method. This method is the most labour intensive but also the most reliable and accurate method. There are other methods for determination of octanol/water partition coefficients, such as by means of HPLC.^{26, 27} This method is based on the retention time of the candidate on the column and comparing this value to structurally similar compound's retention times.^{26, 27} The problem with this method is that there are not many, if any, gold(III) metal compounds that are structurally similar to the ones developed

in this work who's octanol/water partition coefficients have been determined. The 'shake flask' method requires the use of octanol-saturated water and water-saturated octanol. This is to avoid artificial carry-over between phases during the experimental procedure. The solvents were prepared by vigorously shaking high grade octanol with ultra-pure water (resistivity = 18.3 MOhm.cm). The two phases were allowed to separate over a period of 24 h and then were centrifuged and collected as the individual saturated phases. These are the solvents that were used in the determinations. Ideally, extinction coefficients from a Beer-Lambert plot of the candidate in both octanol-saturated water and water-saturated octanol should be determined in order to determine the concentration of the candidate in each phase so that equation 4.5.2.1 is used to determine the octanol/water partition coefficient.

$$\log P_{o/w} = \log\left(\frac{[Complex]_{octanol}}{[Complex]_{water}}\right) \quad 4.5.2.1$$

However, this was not possible for the metal compounds studied in this work as they were not sufficiently soluble in octanol to determine their extinction coefficients. It was therefore assumed that each complex exhibits a similar extinction coefficient in both solvents and the respective absorbance values were used to determine the octanol/water partition coefficients using equation 4.5.2.2.

$$\log P_{o/w} = \log\left(\frac{A_{octanol}}{A_{water}}\right) \quad 4.5.2.2$$

An aqueous solution of approximately 10^{-5} M for each complex was prepared and vigorously shaken with an equal volume of octanol, then allowed to stand for 2 h before the solution was centrifuged and the individual layers isolated. The absorbance of each of the phases was determined in triplicate and the average used to determine the $\log P_{o/w}$ for each compound.

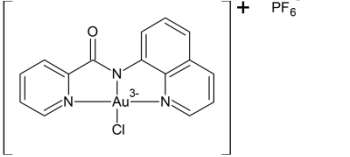
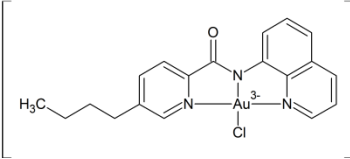
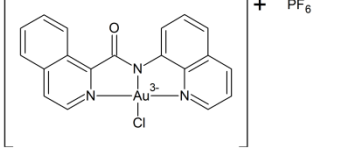
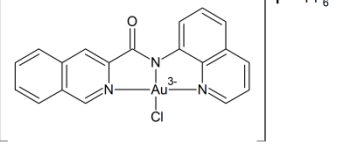
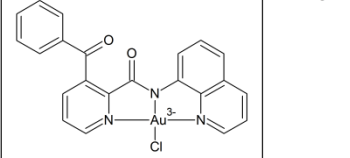
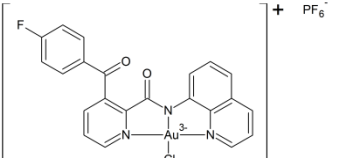
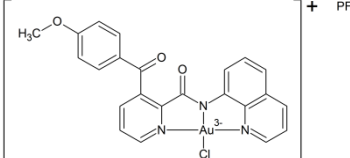
4.5.3 Results and discussion

As has been discussed previously, metal compounds $[Au(HL1)Cl_2]$ – $[Au(L7)Cl](PF_6)$ and $[Au(L15)Cl]$ – $[Au(L16)Cl]$ are all either unstable in solution and/or not soluble in the media required. Both these factors are critical for determining octanol/water partition coefficients. Due to this constraint, only the octanol/water partition coefficients for metal compounds

Spectroscopy

[Au(L8)Cl](PF₆)-[Au(L14)Cl](PF₆) were determined. The results for all the complexes studied are displayed in Table 4.5.3.1.

Table 4.5.3.1: Summary of the average log P_{o/w} values for the indicated gold(III) compounds synthesised in this work.

Metal compound structure	Metal complex	log P _{o/w}
	[Au(L8)Cl](PF ₆)	-2.06
	[Au(L9)Cl](PF ₆)	-0.80
	[Au(L10)Cl](PF ₆)	-0.91
	[Au(L11)Cl](PF ₆)	-2.16
	[Au(L12)Cl](PF ₆)	-1.41
	[Au(L13)Cl](PF ₆)	-1.33
	[Au(L14)Cl](PF ₆)	-1.00

Spectroscopy

All the metal compounds analysed in this work display large negative log $P_{o/w}$ values indicating they are extremely hydrophilic in nature and are likely to localise in the blood serum *in vivo*. This result is an expected one as the compounds studied are charged cationic metal compounds and will therefore be more soluble in polar solvents rather than non-polar solvents. Compound $[\text{Au}(\text{L11})\text{Cl}](\text{PF}_6)$ has the lowest log $P_{o/w}$ value at -2.16 while complex $[\text{Au}(\text{L9})\text{Cl}](\text{PF}_6)$ has the highest log $P_{o/w}$ value at -0.80. This result again is an expected one as complex $[\text{Au}(\text{L9})\text{Cl}](\text{PF}_6)$ contains an aliphatic butyl chain which would increase its solubility in non-polar solvents while $[\text{Au}(\text{L11})\text{Cl}](\text{PF}_6)$ contains a polar fully aromatic structure that would tend towards dissolution in more polar solvents. Within this generation, complexes $[\text{Au}(\text{L8})\text{Cl}](\text{PF}_6)$ – $[\text{Au}(\text{L11})\text{Cl}](\text{PF}_6)$ were synthesised first with complexes $[\text{Au}(\text{L11})\text{Cl}](\text{PF}_6)$ – $[\text{Au}(\text{L13})\text{Cl}](\text{PF}_6)$ being synthesised subsequently. There does not appear to be any correlation between cytotoxicity and log $P_{o/w}$ for compounds $[\text{Au}(\text{L8})\text{Cl}](\text{PF}_6)$ – $[\text{Au}(\text{L11})\text{Cl}](\text{PF}_6)$. Complexes $[\text{Au}(\text{L8})\text{Cl}](\text{PF}_6)$, $[\text{Au}(\text{L10})\text{Cl}](\text{PF}_6)$ and $[\text{Au}(\text{L11})\text{Cl}](\text{PF}_6)$ display vastly different log $P_{o/w}$ values of -2.06, -0.91 and -2.16 yet all made it through to the repeat 5-dose phase of testing while complex $[\text{Au}(\text{L9})\text{Cl}](\text{PF}_6)$ failed at the 1-dose phase even though it exhibited the most hydrophobic log $P_{o/w}$ value of -0.80. Complexes $[\text{Au}(\text{L12})\text{Cl}](\text{PF}_6)$ – $[\text{Au}(\text{L14})\text{Cl}](\text{PF}_6)$ all displayed log $P_{o/w}$ values between 1 and 1.41. The reason for the addition of the fluoro and methoxy groups in the *para* position of the phenyl ketone ring was to try to increase the lipophilicity of the compounds and hence their activity, as was observed for some β -tryptase inhibitors as well as μ and κ opioid analgesics.^{30, 31} This imparted the desired effect with the fluoro and methoxy substituted complexes $[\text{Au}(\text{L13})\text{Cl}](\text{PF}_6)$ and $[\text{Au}(\text{L14})\text{Cl}](\text{PF}_6)$ exhibiting higher log $P_{o/w}$ values. They were however less cytotoxic and little correlation between cytotoxicity and log $P_{o/w}$ values for these three complexes was observed since $[\text{Au}(\text{L12})\text{Cl}](\text{PF}_6)$ and $[\text{Au}(\text{L13})\text{Cl}](\text{PF}_6)$ both made it through to the repeat 5-dose phase of testing (NCI-60 cytotoxicity screen) despite exhibiting the two lowest log $P_{o/w}$ values, while $[\text{Au}(\text{L14})\text{Cl}](\text{PF}_6)$ exhibited the highest log $P_{o/w}$ value but failed at the 1-dose phase of the NCI cytotoxicity screen against their panel of 60 human cancer cell lines.

When compared to other organic drugs the hydrophilicity of the metal compounds in this work is considerably higher. The organic drugs, gabapentin and amoxicillin, are some of the more hydrophilic drugs with a log $P_{o/w}$ values of -1.25 and -1.71.³² This value is similar to the complexes $[\text{Au}(\text{L12})\text{Cl}](\text{PF}_6)$ and $[\text{Au}(\text{L13})\text{Cl}](\text{PF}_6)$ with values of -1.41 and -1.33 respectively.

The vast majority of anti-cancer drugs that are in clinical use today are highly lipophilic, much more so than the metal compounds studied in this work, since they are generally organic in nature with $\log P_{o/w}$ values as high as 6.03 for chlorproxithene.²⁸ A much more realistic comparison of the $\log P_{o/w}$ values could be drawn against other metallo-drugs such as cisplatin or octahedral ruthenium based complexes. There are very few sources of such information for such complexes, however, Gaiddon and co-workers have recently reported a large library of second generation octahedral ruthenium complexes and their correlation between $\log P_{o/w}$ values, reduction potentials and IC_{50} values.³³ Of the 32 metal compounds synthesised, most displayed positive $\log P_{o/w}$ values despite being positively charged.³³ Specifically, metal compounds with reduction potentials between 0.4–0.6 V (vs. SCE) and $\log P_{o/w}$ above 2.0 display the lowest IC_{50} values.³³ When looking to correlate the $\log P_{o/w}$ values for all compounds studied with cytotoxic activity (via mean growth percentage values), no immediate correlation was evident. Upon further investigation, a correlation within the phenyl ketone class of compounds was observed, albeit an unconventional one. A plot of $\log P_{o/w}$ vs mean growth percent revealed that the more negative the $\log P_{o/w}$ value, the more cytotoxic the compound was. This was an unusual result as, in general, it is observed that an increase in $\log P_{o/w}$ value for a certain class of drugs (particularly cationic metallotherapeutic drugs) results in an increase in cytotoxic activity.³³

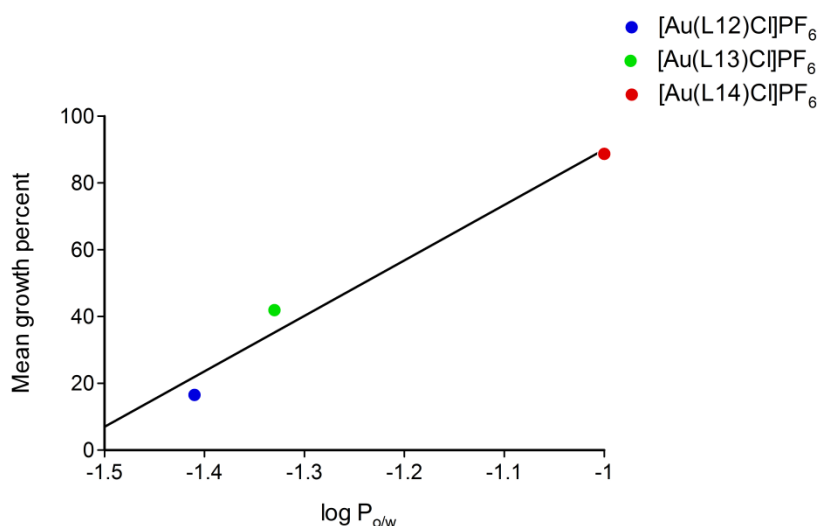


Figure 4.5.3.1: Plot of the mean growth percent values versus their $\log P_{o/w}$ values showing the unconventional correlation. The correlation coefficient of the fit is 0.985.

4.6 DNA binding studies

The gold(III) metal compounds in this work were designed to be novel and effective metallotherapeutic agents in the fight against cancer. The mode of action through which they were intended to exert their cytotoxicity was topoisomerase inhibition or poisoning. There are several methods and steps in the topoisomerase catalytic cycle where a drug can effect its action.³⁴⁻³⁶ In the case for the compounds presented in this work, they are anticipated to effect their action via DNA intercalation. For DNA intercalation to occur the drug should contain two important features. Firstly; the drug must contain an extended planar aromatic region in order to insert itself between base pairs of the DNA and stabilise itself within the DNA through van der Waals interactions such as π -stacking, and secondly, the drug should contain a positive charge in order to interact electrostatically with the negatively charged phosphate backbone of the DNA.³⁷ If a drug is to inhibit or poison topoisomerase through intercalation it must also to be able to interact with the enzyme while intercalated into DNA.

Since DNA is the blueprint for life it is a common target for numerous drugs and biological agents. Some common antibiotics and anti-cancer agents such as doxorubicin and actinomycin affect their biological action through DNA intercalation.³⁸ There are also numerous biological agents that are used to visualise DNA via enhanced fluorescence during an intercalation event when performing certain assays. These compounds include ethidium bromide (EB) and acridine orange. DNA intercalation can be described and quantified by the following parameters:

K_b = binding constant at equilibrium

r_f = ratio of intercalator to total nucleotide concentration

r = ratio of bound intercalator to total nucleotide concentration

Calf thymus and salmon testes DNA are widely used as analogues to human DNA for determining the binding affinity of drugs.³⁹⁻⁴³ In this work, calf thymus DNA was chosen and used for all DNA binding experiments. There are two general methods through which a binding constant between DNA and drug can be determined. The first and more accurate method is conducted via UV/Visible spectroscopy. The drug is dissolved in a buffered aqueous system while increasing amounts of a DNA solution are added. A spectrum is

recorded after every addition of DNA and the LMCT region monitored for a red shift as well as hypochromism. Analysis of these spectral changes results in the determination of a binding constant K_b (see Experimental for details). The second method is through competitive binding experiments with EB.⁴⁴ EB displays a marked increase in fluorescence while intercalated between base pairs. It has been shown that the presence of a second intercalator is able to quench the fluorescence of the EB by displacing it from the DNA. From this characteristic, a less accurate, apparent binding constant is calculated (see Experimental for details).

Molecules that intercalate DNA have traditionally been organic in nature such as EB and acridine. In more recent years however, metallo-intercalators have become a keen area of interest. Three proven metallo-intercalators are shown below in Figure 4.6.1.

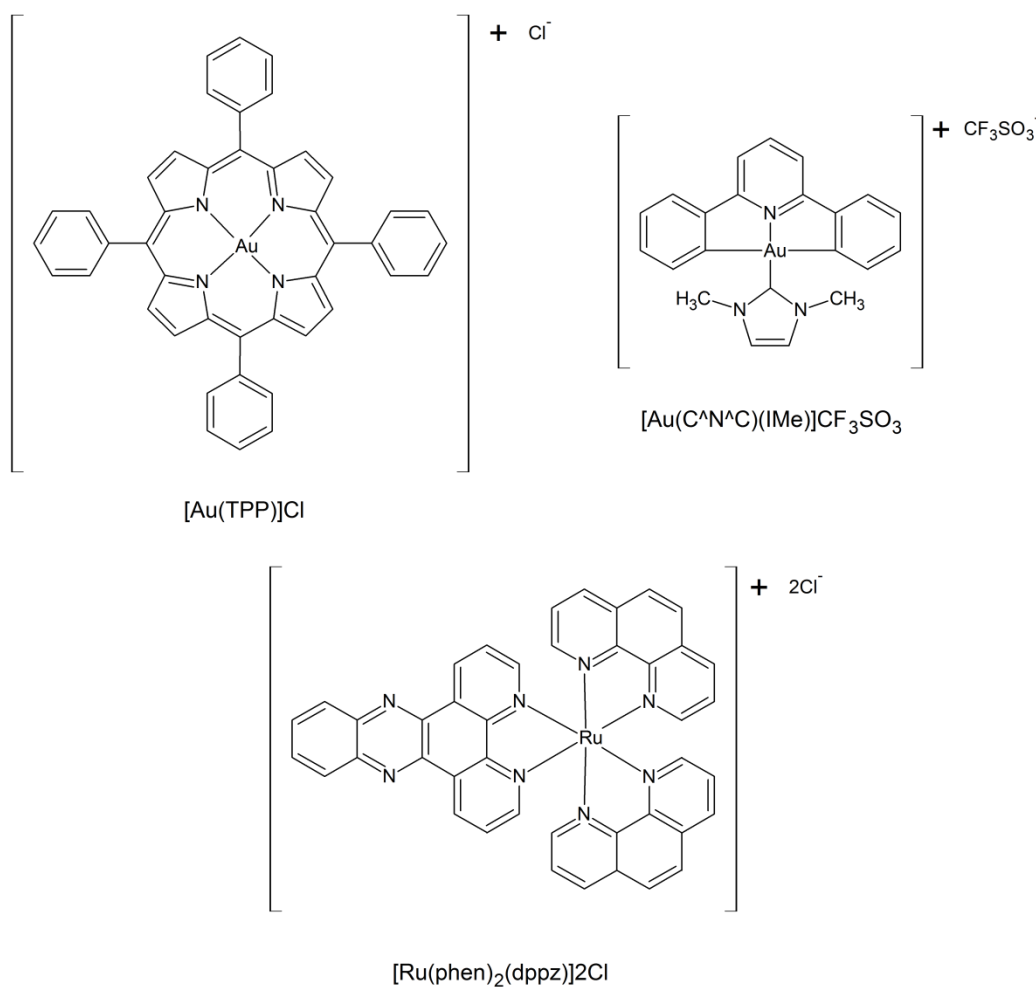


Figure 4.6.1: Chemical structures of three proven metal-based DNA intercalators.

Spectroscopy

All three compounds shown in Figure 4.6.1 have been shown to have great therapeutic or diagnostic potential. Compounds $[\text{Au}(\text{TPP})]\text{Cl}$ and $[\text{Au}(\text{C}^{\wedge}\text{N}^{\wedge}\text{C})(\text{IMe})]\text{CF}_3\text{SO}_3$ have been shown to intercalate ctDNA with binding affinities of $2.8 \times 10^6 \text{ M}^{-1}$ and $5.4 \times 10^5 \text{ M}^{-1}$ respectively, with both compounds demonstrating encouraging *in vivo* activity against solid tumours.^{13, 45, 46} The activity of these compounds is said to be based on their intercalative ability. The compound $[\text{Ru}(\text{phen})_2(\text{dppz})]2\text{Cl}$ is well known in the literature as the 'light switch' compound for its enhanced emission in the presence of calf thymus DNA (ctDNA).⁴⁷ It binds ctDNA with a large binding constant of $5.1 \times 10^6 \text{ M}^{-1}$ and its binding mode to DNA has been meticulously characterised via the publication of several X-ray structures of the complex intercalated into different DNA oligomers.^{48, 49}

4.6.1 Objectives

The objectives of these experiments are to investigate the interaction of the metal compounds synthesised in this work with DNA and to try and determine the specific mode by which this interaction occurs. The binding constants between the complexes and DNA will be determined and related to their three-dimensional structure and cytotoxicity profiles if possible.

4.6.2 Experimental

Calf thymus DNA was purchased from Sigma Aldrich as the high purity, highly polymerised sodium salt. The ratio of absorbance in the 260 and 280 nm region of the UV spectrum was always calculated to be between 1.8-2:1 when performing DNA binding experiments. This value falls between the reported range of 1.80-2:1 which indicates the DNA is sufficiently free of protein so that no additional purification was required. The concentration of the stock solution was determined spectrophotometrically using the extinction coefficient of $13200 \text{ M}^{-1} \text{ cm}^{-1}$ at 260 nm.

UV/VISIBLE SPECTROPHOTOMETRIC TITRATIONS:

Generally, a complex concentration of approximately 10^{-5} M (TBS, pH 7.34, 37 °C, 10 mM NaCl) was prepared in 1cm quartz cuvette with an initial volume of 2.2 mL. Aliquots (5-100 μL) of a concentrated DNA stock solution were added at 10 minute intervals to the reaction cuvette as well as to the reference cuvette. This was to correct for the absorbance of the

Spectroscopy

DNA and to ensure the interaction/binding process was complete and equilibrium had been reached before the spectra were recorded. The absorbance of the LMCT band at approximately 350 nm (compound dependent) was corrected for dilution and monitored as a function of ctDNA concentration. The function below was fitted to the data using non-linear regression.⁴²

$$(\varepsilon_a - \varepsilon_f) / (\varepsilon_b - \varepsilon_f) = (b - (b^2 - 2K_a^2 Ct [DNA] / s)^{\frac{1}{2}}) / 2K_a Ct \quad 4.6.2.1a$$

$$b = 1 + K_b Ct + K_b [DNA] / 2s \quad 4.6.2.1b$$

Where:

- [DNA] = concentration of DNA
- ε_a = extinction coefficient of LMCT band at a given [DNA]
- ε_f = extinction coefficient of the free gold(III) compound
- ε_b = extinction coefficient of the fully intercalated compound
- K_b = equilibrium binding constant in M^{-1}
- Ct = total concentration of gold(III) compound
- s = binding site size; number of nucleotides per compound

COMPETITIVE BINDING TITRATIONS:

The gold(III) complexes were found to be non-emissive in the presence or absence of DNA and had no effect on the emission properties of EB; because of this, competitive binding experiments were able to be performed reliably. A 1:1 or 15:15 μM ratio between DNA and EB was used in the displacement titrations. Aliquots (30-200 μL) of metal complex were added at 10 minute intervals to the EB-DNA mixture. This was to ensure the intercalation process was complete and equilibrium had been reached before the spectra were recorded. The individual spectra were recorded from 530-800 nm as the average of 10 scans at 37 °C with the excitation wavelength at 500 nm. The apparent binding constant, K_{app} , is then calculated from the equation below.

$$K_{EtBr}[EB] = K_{app}[Complex] \quad 4.6.2.2$$

Where:

Spectroscopy

K_{EB}	=	binding constant of EB to DNA: $1 \times 10^{-7} \text{ M}^{-1}$ ⁴⁴
[EB]	=	concentration of EB
K_{app}	=	apparent binding constant
[Complex]	=	concentration of gold(III) complex that causes 50% reduction of initial EB fluorescence intensity

The intensity of the emission peak at 610 nm was recorded and monitored as a function of gold(III) complex concentration and an IC₅₀ function with a Hill coefficient fitted to the data in order to determine [Complex].

$$Y = 100/[1 + (\frac{x}{A1})]^{A2} \quad 4.6.2.3$$

Where:

Y = response ($Y=100\%$ when $X=0$)

X = inhibitor concentration

$A1$ = IC₅₀ value

$A2$ = hill coefficient.

4.6.3 Results and discussion

As mentioned above (4.4 Stability and Reactivity), only metal compounds [Au(L8)Cl](PF₆)–[Au(L14)Cl](PF₆) were stable enough in solution to perform reliable spectroscopic experiments. The UV/Visible absorption spectra of each of the complexes were monitored upon the addition of DNA and a decrease in the intensity of both the π - π^* and LMCT region were observed. The percentage hypochromism ($H\%$) is defined as:

$$H\% = 100\% \times (A_{free} - A_{bound})/A_{free} \quad 4.6.3.1$$

Metal compound [Au(L10)Cl](PF₆) displays hypochromism of 28.11% which is similarly observed for the proven DNA intercalator [Ru(Im)(dppz)]²⁺.⁴² The hypochromism values for the rest of the compounds are summarised in Table 4.6.3.1. Identical aliquots of DNA were added to the reference cell to counter absorbance of the DNA itself. The DNA additions were continued until there where minimal spectral changes for at least three consecutive additions. Dilution effects of the gold(III) compounds where corrected for using absorption

Spectroscopy

correction techniques. The spectral changes observed for [Au(L10)Cl](PF₆) upon the addition of DNA are displayed below (Figure 4.6.3.1).

Table 4.6.3.1: Summary of binding affinities, binding site size, hypochromism and bathochromic shift for stable gold(III) compounds from this work as well as some literature metallointercalators determined by UV/Visible DNA titrations.

Metal Complex	<i>s</i>	<i>K_b</i> (x 10 ⁵ M ⁻¹)	<i>H</i> (%)	Bathochromic shift (nm)
[Au(L8)Cl](PF ₆)	1.9(9)	3.6(6)	27.2	6
[Au(L9)Cl](PF ₆)	1.4(9)	2.8(6)	33.5	8
[Au(L10)Cl](PF ₆)	1.3(5)	4.7(6)	28.1	17
[Au(L11)Cl](PF ₆)	1.2(9)	2.7(5)	31.2	6
[Au(L12)Cl](PF ₆)	2(5)	1(1)	23.6	8
[Au(L13)Cl](PF ₆)	6(6)	3(1)	51.1	8
[Au(L14)Cl](PF ₆)	2(3)	2(1)	18.3	3
[Au(C ^N ^N^C)(IMe)]CF ₃ SO ₃ ⁴⁵	N/A	5.4(8)	N/A	N/A
[Ru(phen) ₂ (dppz)]2Cl ⁴⁷	0.6	51(4)	N/A	N/A
[Au(TPP)]Cl ¹³	N/A	28(2)	53	N/A

Generally, the larger the binding affinity (*K_b*) and the binding site size (*s*), the stronger the intercalation interaction between the complex and DNA is. The percentage hypochromism of the LMCT bands between the different gold(III) compounds varies quite significantly. Metal compound [Au(L13)Cl](PF₆) displays the largest hypochromism at 51.10% while complex [Au(L14)Cl](PF₆) exhibited the smallest hypochromism at 18.28%. The rest of the gold(III) complexes displayed hypochromism in the 30% region which is similarly observed for some anti-cancer gold(III) porphyrin complexes reported by Che and co-workers.¹³ The characteristic traits observed when a drug intercalates DNA are a red shift in the charge transfer band as well as hypochromism. A red shift occurs because as the metal complex intercalates DNA, there are strong π-π stacking interactions between base pairs of the DNA and the aromatic structure of the complex which results in a drop in energy of the LUMO. The end result is a slight red shift in the charge transfer band of the metal complex. It is generally accepted in literature that the larger the hypochromism, the stronger the intercalation event.⁴²

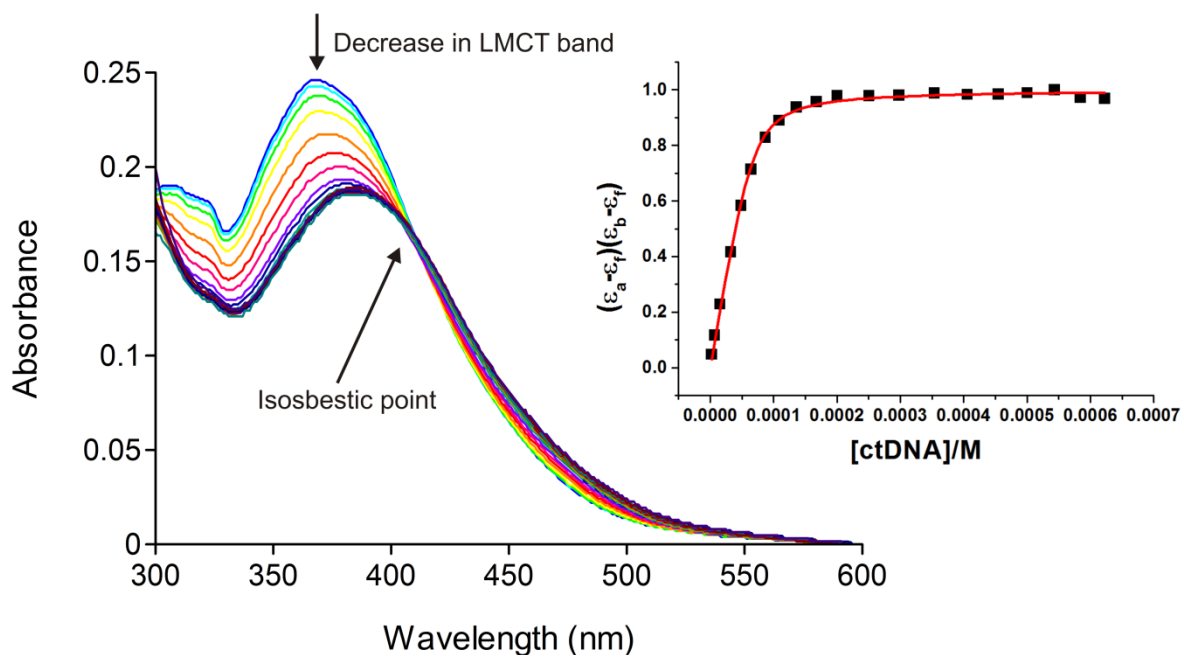


Figure 4.6.3.1: UV/Visible spectrum of $[\text{Au}(\text{L10})\text{Cl}](\text{PF}_6)$ in pH 7.34 TBS at 37°C showing the hypochromism and bathochromic shift of the LMCT band upon addition of consecutive aliquots of ctDNA. Inset displays a plot of $(\epsilon_a - \epsilon_f)/(\epsilon_b - \epsilon_f)$ vs $[\text{ctDNA}]/\text{M}$ and the non-linear fit of the data resulting in the determination of K_b and s .

However, this was not observed for the compounds in this work with $[\text{Au}(\text{L10})\text{Cl}](\text{PF}_6)$ displaying the largest binding constant of $4.7(6) \times 10^5 \text{ M}^{-1}$ while its hypochromism was mid-range for the complexes studied (28.1%).

It has been shown that the binding affinity of $[\text{PtX}(\text{terpy})]^+$, where $x = \text{anion}$, complexes depends heavily on several structural factors such as hydrogen-bonding capability, charge, structure and steric effects.³⁸ This is highlighted in the comparison of the DNA binding affinities of various $[\text{PtX}(\text{terpy})]^+$ complexes which range from as low as 3.3×10^3 to as high as $1.8 \times 10^7 \text{ M}^{-1}$.³⁸ Direct comparisons between separate studies are however difficult due to the fact that K_b values are sensitive towards ionic strength, pH and temperature.³⁸ For the metal compounds described in this work, compounds $[\text{Au}(\text{L8})\text{Cl}](\text{PF}_6)$ - $[\text{Au}(\text{L11})\text{Cl}](\text{PF}_6)$ all displayed the expected red-shift and hypochromism consistent with intercalation of the complexes between DNA base pairs. The non-linear curve fit to a plot of $(\epsilon_a - \epsilon_f)/(\epsilon_b - \epsilon_f)$ vs $[\text{ctDNA}]$ resulted in binding constants ranging from $2.7(5) \times 10^5 \text{ M}$ for $[\text{Au}(\text{L11})\text{Cl}](\text{PF}_6)$, to $4.7(6) \times 10^5 \text{ M}$ for $[\text{Au}(\text{L10})\text{Cl}](\text{PF}_6)$. Metal compounds $[\text{Au}(\text{L8})\text{Cl}](\text{PF}_6)$ - $[\text{Au}(\text{L10})\text{Cl}](\text{PF}_6)$ follow a trend based on structural effects with $[\text{Au}(\text{L10})\text{Cl}](\text{PF}_6)$ exhibiting the largest binding constant consistent with its extended aromatic structure compared to compounds

[Au(L8)Cl](PF₆) and [Au(L9)Cl](PF₆). Metal compound [Au(L9)Cl](PF₆) exhibits the weakest binding constant of $2.8(6) \times 10^5$ M. This weaker binding constant is consistent with the steric bulk introduced by the butyl chain in the *para* position of the pyridine ring. Compound [Au(L8)Cl](PF₆) exhibits a binding constant of $3.8(6) \times 10^5$ M, which is less than that for [Au(L10)Cl](PF₆), consistent with its less aromatic structure. The binding constant is however higher than [Au(L9)Cl](PF₆) due to less steric bulk on the pyridine ring of the complex. Metal compound [Au(L11)Cl](PF₆) does not follow the trend with the weakest binding constant of all four at $2.7(5) \times 10^5$ M. This was not expected as it shares the extended aromatic structure of [Au(L10)Cl](PF₆) without the steric bulk of [Au(L10)Cl](PF₆). The only obvious difference between [Au(L10)Cl](PF₆) and [Au(L11)Cl](PF₆) is that they contain different isoquinoline isomers. Compound [Au(L10)Cl](PF₆) contains the 1-isoquinoline moiety while [Au(L11)Cl](PF₆) contains the 3-isoquinoline moiety. It is known that small structural difference can cause fairly large difference in binding constants.³⁸ The difference in binding constants between these two complexes may be associated with the difference in isoquinoline motifs. It is also conceivable that [Au(L10)Cl](PF₆) may have a shape that energetically and sterically favours the left handed DNA helical structure, more so than that of [Au(L11)Cl](PF₆), and therefore as a result obtains a higher K_b value.

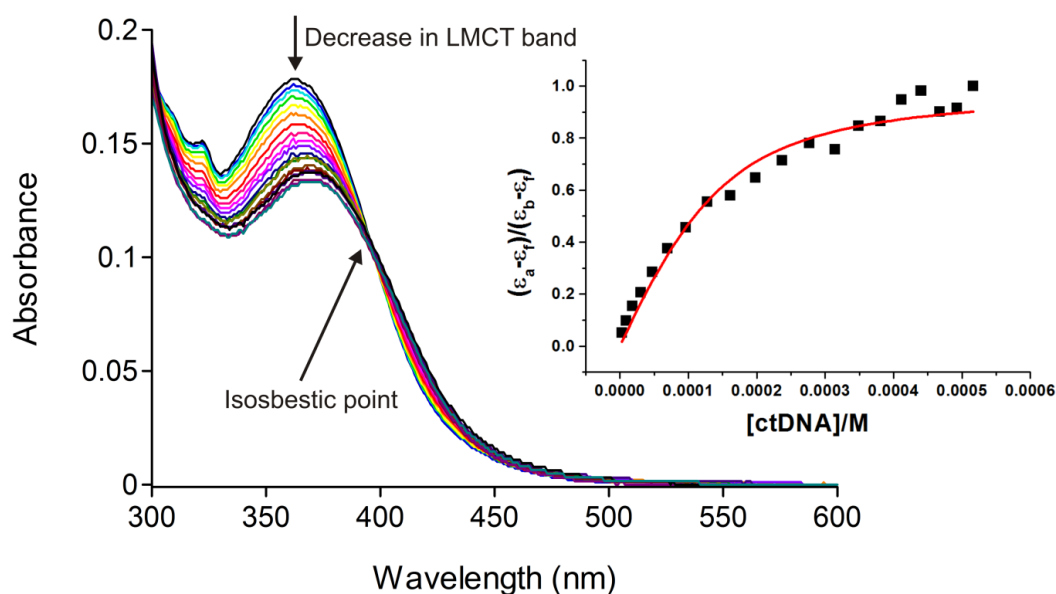


Figure 4.6.3.2: UV/Visible spectrum of [Au(L12)Cl](PF₆) in pH 7.34 TBS at 37 °C showing the hypochromism and bathochromic shift of the LMCT band upon addition of consecutive aliquots of ctDNA. Inset displays a plot of $(\epsilon_a - \epsilon_f) / (\epsilon_b - \epsilon_f)$ vs [ctDNA] and the non-linear fit of the data resulting in the determination of K_b and s .

Complexes [Au(L11)Cl](PF₆)-[Au(L13)Cl](PF₆) displayed the characteristic spectral features of a red shift in the LMCT band as well as hypochromism. However, the non-linear curve fit to a plot of $(\epsilon_a - \epsilon_f)/(\epsilon_b - \epsilon_f)$ vs [ctDNA] resulted in binding constants with extremely poor data fits and large errors in K_b and s (Figure 4.6.3.2), rendering the information effectively quantitatively useless. This was interesting and suggestive of more than one type of drug-DNA interaction occurring in solution. This is feasible as the structure of complexes [Au(L12)Cl](PF₆)-[Au(L14)Cl](PF₆) contain a phenyl ketone moiety which in itself would be able to intercalate DNA. This has recently been shown by Niyazi and co-workers for Λ -[Ru(phen)₂dppz]⁺. X-ray crystallographic studies show that the complex Λ -[Ru(phen)₂dppz]⁺ is able to intercalate DNA via both the dppz and phen moieties in separate binding events.⁴⁸ Due to the poor data obtained from the UV/Visible DNA titrations, another method was sought to investigate the ability of the metal compounds [Au(L12)Cl](PF₆)-[Au(L14)Cl](PF₆) to intercalate DNA. Another common method is based on emission spectroscopy. Ethidium bromide is an organic molecule that exhibits a marked increase in emission intensity when intercalated between base pairs.

Therefore by titrating a drug into a solution containing EB intercalated into DNA we are able to displace the EB and observe a steady reduction in emission intensity upon successive additions of the drug.⁴⁴ All three complexes, [Au(L12)Cl](PF₆)-[Au(L13)Cl](PF₆) displayed the characteristic steady decrease in emission intensity of EB upon an increase in concentration of metal complex (Figure 4.6.3.3 displays this for [Au(L12)Cl](PF₆). The binding constants determined are summarised below (Table 4.6.3.2) along with the correlation coefficients of the IC₅₀ fits for emission vs [metal complex] used to determine [complex]. Complex [Au(L14)Cl](PF₆) exhibited the highest K_{app} value at $8.42 \times 10^5 \text{ M}^{-1}$ while [Au(L13)Cl](PF₆) displayed the lowest K_{app} value at $4.51 \times 10^5 \text{ M}^{-1}$. The K_{app} values obtained for the emission displacement titrations were in the same order of magnitude as for those determined via UV/Visible spectroscopic titrations and therefore it is safe to assume that metal compounds [Au(L12)Cl](PF₆)-[Au(L14)Cl](PF₆) are able to interact with the DNA fairly strongly. The emission displacement titrations however further enforced the idea that there is more than one DNA-drug interaction occurring in solution.

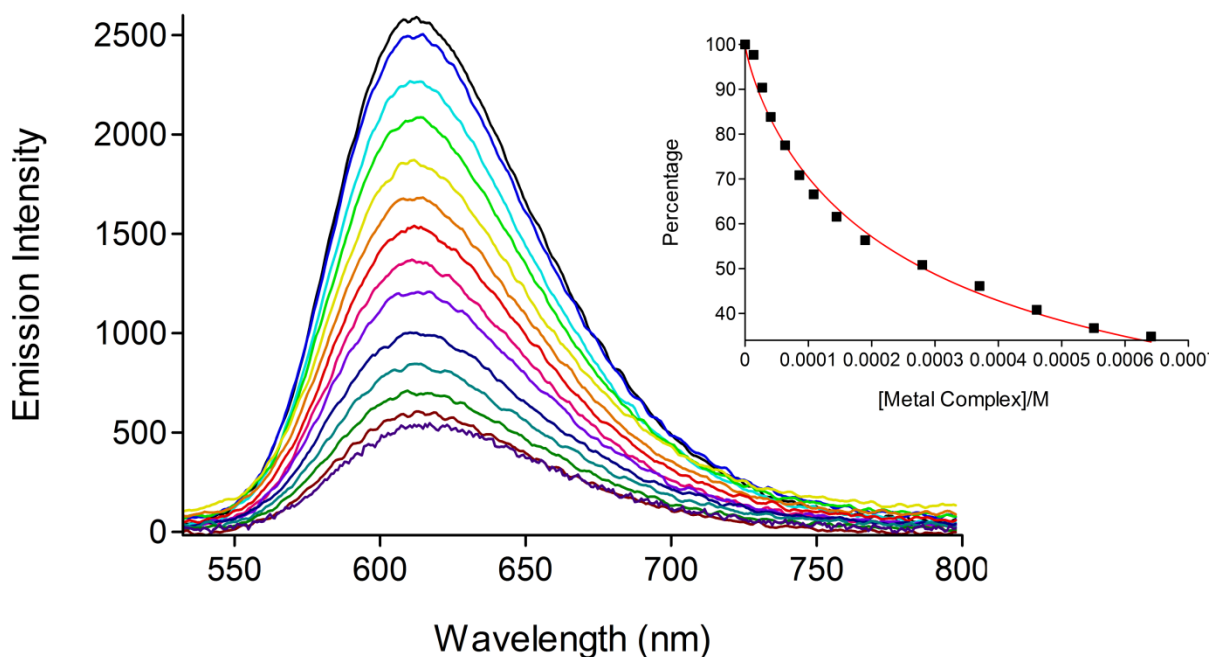


Figure 4.6.3.3: Emission spectrum of EB in pH 7.34 TBS at 37 °C, showing the reduction in intensity upon increasing the concentration of $[\text{Au}(\text{L12})\text{Cl}](\text{PF}_6)$. Inset displays a plot of emission intensity as a percentage vs $[\text{Au}(\text{L12})\text{Cl}](\text{PF}_6)$ and the IC_{50} fit of the data.

If one observes the first and second additions of metal compound (equal amounts of 30 μl) in Figure 4.6.3.3, it can be seen that the drops in emission intensity are not equivalent. There is a much greater drop in intensity after the second addition compared to that of the first. This suggests that the complex interacts with the DNA in a different manner at lower concentrations (approximately 1×10^{-5} M), perhaps via intercalation of the phenyl ketone moiety. As the concentration of the metal complex is increased, the traditional characteristics of an intercalative binding mode are observed. In order to unequivocally determine whether the metal compounds $[\text{Au}(\text{L12})\text{Cl}](\text{PF}_6)$ - $[\text{Au}(\text{L14})\text{Cl}](\text{PF}_6)$ in fact intercalate DNA, electrophoretic gel mobility shift assays (EMSA) were performed (see Chapter 7). The EMSA results show that there is no evidence for DNA intercalation or groove binding and therefore contradict the spectroscopic data obtained (*vide supra*). There is no doubt that there is an interaction between complexes $[\text{Au}(\text{L12})\text{Cl}](\text{PF}_6)$ - $[\text{Au}(\text{L14})\text{Cl}](\text{PF}_6)$ and DNA, however, from the collective data we may only hypothesise that the interaction may be electrostatic (see Chapter 7 for further discussion).

Spectroscopy

Table 4.6.3.2: Summary of ctDNA binding affinities, binding site size and hypochromism for the selected metal compounds, determined by ethidium bromide displacement titrations.

Metal Complex	$K_{app} / M^{-1} (x 10^5)$	Correlation coefficient*
[Au(L12)Cl](PF ₆)	5.3(5)	0.995
[Au(L13)Cl](PF ₆)	4.5(8)	0.997
[Au(L14)Cl](PF ₆)	8.4(6)	0.987

*Correlation coefficient of the IC₅₀ curve fit when determining [Complex].

Overall metal compounds [Au(L8)Cl](PF₆)–[Au(L11)Cl](PF₆) have been identified to intercalate DNA while metal compounds [Au(L12)Cl](PF₆)–[Au(L14)Cl](PF₆) display a spectral signature consistent with DNA–complex interactions; however, the complex nature of the spectral changes associated with DNA binding by the latter complexes suggest that further investigations might be required to fully elucidate the nature of the binding process (e.g. the use of circular dichroism spectroscopy and/or micro viscosity measurements). The binding affinities of the metal compounds are all in the order of 10⁵ M and therefore can be classified as relatively strong DNA intercalators and are in the same region as the gold(III) compound, [Au(C[^]N[^]C)(IMe)]CF₃SO₃, which is a topoisomerase I inhibitor that shows encouraging *in vivo* results. It is therefore inferred that the interaction of the compounds with DNA forms the basis via which the metal compounds affect their cytotoxic activity described in Chapter 7.

4.7 References

1. D. A. Skoog, D. M. West, J. F. Holler and S. R. Crouch, *Fundamentals of Analytical Chemistry*, Brooks/Cole, 2004.
2. P. Y. Bruice, *Organic Chemistry*, Pearson, 2004.
3. G. McMahon, *Analytical Instrumentation*, Wiley and Sons, 2007.
4. D. L. Pavia, G. M. Lampman, G. S. Kriz and J. R. Vyvyan, Brooks/Cole, 2009, vol. 4th Edition.
5. T. Yang, C. Tu, J. Zhang, L. Lin, X. Zhang, Q. Liu, J. Ding, Q. Xu and Z. Guo, *Dalton Trans.*, 2003, 3419-3424.
6. Y. Shao, J. Zhang, C. Tu, C. Dai, Q. Xu and Z. Guo, *J. Inorg. Biochem.*, 2005, **99**, 1490-1496.
7. J. Zhang, X. Ke, C. Tu, J. Lin, J. Ding, L. Lin, H.-K. Fun, X. You and Z. Guo, *BioMetals*, 2003, **16**, 485-496.
8. M. A. Cinellu, L. Maiore, G. Minghetti, F. Cocco, S. Stoccoro, A. Zucca, M. Manassero and C. Manassero, *Organometallics*, 2009, **28**, 7015-7024.
9. T.-C. Cheung, T.-F. Lai and C.-M. Che, *Polyhedron*, 1994, **13**, 2073-2077.
10. A. Rosenberg, *Acta Chemica Scandinavica Series a-Physical and Inorganic Chemistry*, 1957, **11**, 1390-1404.
11. J. Keeler, *Understanding NMR spectroscopy*, Wiley and Sons, 2010.
12. R. W.-Y. Sun and C.-M. Che, *Coord. Chem. Rev.*, 2009, **253**, 1682-1691.
13. R. W.-Y. Sun, C. K.-L. Li, D.-L. Ma, J. J. Yan, C.-N. Lok, C.-H. Leung, N. Zhu and C.-M. Che, *Chem.--Eur. J.*, 2010, **16**, 3097-3113, S3097/3091-S3097/3030.
14. P. J. Sadler and R. E. Sue, *Met.-Based Drugs*, 1994, **1**, 107-144.
15. D. F. Shriver and P. W. Atkins, *Inorganic Chemistry*, 4th Edition edn., Oxford University Press, 2006.
16. A. N. Wein, A. T. Stockhausen, K. I. Hardcastle, M. R. Saadein, S. Peng, D. Wang, D. M. Shin, Z. Chen and J. F. Eichler, *J. Inorg. Biochem.*, 2011, **105**, 663-668.
17. L. Messori, F. Abbate, G. Marcon, P. Orioli, M. Fontani, E. Mini, T. Mazzei, S. Carotti, T. O'Connell and P. Zanello, *J. Med. Chem.*, 2000, **43**, 3541-3548.
18. L. Maiore, M. A. Cinellu, E. Michelucci, G. Moneti, S. Nobili, I. Landini, E. Mini, A. Guerri, C. Gabbiani and L. Messori, *J. Inorg. Biochem.*, 2011, **105**, 348-355.
19. M. P. Akerman, University of KwaZulu-Natal, 2009.
20. A. Djekovic, B. Petrovic, Z. D. Bugarcic, R. Puchta and E. R. van, *Dalton Trans.*, 2012, **41**, 3633-3641.
21. B. Pitteri, G. Marangoni, F. Visentin, T. Bobbo, V. Bertolasi and P. Gilli, *J. Chem. Soc., Dalton Trans.*, 1999, 677-682.
22. L. Messori, G. Marcon and P. Orioli, *Bioinorg. Chem. Appl.*, 2003, 177-187.
23. B. Halliwell and J. M. C. Halliwell, Clarendon Press, Oxford, 1989, vol. 2nd Edition.
24. D. Voet and J. G. Voet, *Biochemistry*, Wiley and Sons, 2004.
25. C. J. Jones and J. R. Thornback, *Medicinal Applications of Coordination Chemistry*, RSC Publishing, 2007.
26. G. L. Patrick, *An Introduction to Medicinal Chemistry*, Oxford University Press, 2005.
27. G. Thomas, *Medicinal Chemistry*, Wiley and Sons, 2002.
28. C. J. P. Monteiro, M. M. Pereira, S. M. A. Pinto, A. V. C. Simoes, G. F. F. Sa, L. G. Arnaut, S. J. Formosinho, S. Simoes and M. F. Wyatt, *Tetrahedron*, 2008, **64**, 5132-5138.

29. A. V. Rudnev, L. S. Foteeva, C. Kowol, R. Berger, M. A. Jakupec, V. B. Arion, A. R. Timerbaev and B. K. Keppler, *J. Inorg. Biochem.*, 2006, **100**, 1819-1826.
30. C. R. Clark, P. R. Halfpenny, R. G. Hill, D. C. Horwell, J. Hughes, T. C. Jarvis, D. C. Rees and D. Schofield, *J. Med. Chem.*, 1988, **31**, 831-836.
31. Y. Miyazaki, Y. Kato, T. Manabe, H. Shimada, M. Mizuno, T. Egusa, M. Ohkouchi, I. Shiromizu, T. Matsusue and I. Yamamoto, *Bioorg. Med. Chem. Lett.*, 2006, **16**, 2986-2990.
32. J. Ghasemi and S. Saaidpour, *Anal. Chim. Acta*, 2007, **604**, 99-106.
33. L. Fetzer, B. Boff, M. Ali, X. Meng, J.-P. Collin, C. Sirlin, C. Gaiddon and M. Pfeffer, *Dalton Trans.*, 2011, **40**, 8869-8878.
34. Y. Pommier, E. Leo, H.-L. Zhang and C. Marchand, *Chem. Biol.*, 2010, **17**, 421-433.
35. J. L. Nitiss, *Nat. Rev. Cancer*, 2009, **9**, 338-350.
36. J. L. Nitiss, *Nat. Rev. Cancer*, 2009, **9**, 327-337.
37. B. M. Zeglis, V. C. Pierre and J. K. Barton, *Chem. Comm.*, 2007, 4565-4579.
38. S. D. Cummings, *Coord. Chem. Rev.*, 2009, **253**, 1495-1516.
39. C. A. Mitsopoulou, C. E. Dagas and C. Makedonas, *J. Inorg. Biochem.*, 2008, **102**, 77-86.
40. X.-W. Liu, J. Li, H. Li, K.-C. Zheng, H. Chao and L.-N. Ji, *J. Inorg. Biochem.*, 2005, **99**, 2372-2380.
41. K. Andrews and D. R. McMillin, *Biochemistry*, 2008, **47**, 1117-1125.
42. L.-M. Chen, J. Liu, J.-C. Chen, C.-P. Tan, S. Shi, K.-C. Zheng and L.-N. Ji, *J. Inorg. Biochem.*, 2008, **102**, 330-341.
43. J. P. Dheyongera, W. J. Geldenhuys, T. G. Dekker and d. S. C. J. Van, *Bioorg. Med. Chem. Lett.*, 2005, **13**, 689-698.
44. G.-G. J. Luis, M. Gonzalez-Alvarez, M. Liu-Gonzalez, B. Macias, J. Borrás and G. Alzuet, *J. Inorg. Biochem.*, 2009, **103**, 923-934.
45. J. J. Yan, A. L.-F. Chow, C.-H. Leung, R. W.-Y. Sun, D.-L. Ma and C.-M. Che, *Chem. Comm.*, 2010, **46**, 3893-3895.
46. C.-M. Che, R. W.-Y. Sun, W.-Y. Yu, C.-B. Ko, N. Zhu and H. Sun, *Chem. Comm.*, 2003, 1718-1719.
47. R. B. Nair, E. S. Teng, S. L. Kirkland and C. J. Murphy, *Inorg. Chem.*, 1998, **37**, 139-141.
48. H. Niyazi, J. P. Hall, K. O'Sullivan, G. Winter, T. Sorensen, J. M. Kelly and C. J. Cardin, *Nat. Chem.*, 2012, **4**, 621-628.
49. H. Song, J. T. Kaiser and J. K. Barton, *Nat. Chem.*, 2012, **4**, 615-620.

5. X-Ray crystallography

5.1 Introduction

There are relatively few crystal structures of gold(III)-bis(amides) and mono(amides) in the CSD¹ (Cambridge Structural Database, September 2011 release).²⁻⁸ Although there are many gold(III) structures in the literature, few involve the ligand systems investigated in this project. This is unusual as the ligand systems would appear to be ideally suited to the chelation of gold(III). Specifically, the amide N–H binding sites, when deprotonated, produce strong σ -donors. This coupled with the pyridine nitrogen's σ -donor/ π -acceptor qualities afford a powerful stabilising compound. With two negative and two neutral binding sites the bis(amide) compounds would be expected to acquire a net positive charge for the complex (ideal for electrostatically targeting the polyphosphate backbone of DNA). The mono(amide) ligands contain a single negative binding site for ligands $[\text{Au}(\text{L4})\text{Cl}_2]$ – $[\text{Au}(\text{L14})\text{Cl}](\text{PF}_6)$. This coupled with the co-ordination of a chloride ion similarly afford singly positively charged complexes. Ligands $\text{H}_2\text{L15}$ and $\text{H}_2\text{L16}$ contain two anionic binding sites, N^- and C^- , resulting in the formation of neutral complexes.

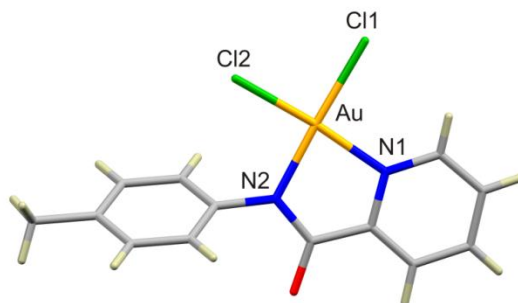


Figure: 5.1.1: Diagram of a single molecular unit of $[\text{Au}(\text{L-N,N}')\text{Cl}_2]$, showing the coordination geometry of the gold(III) centre. Redrawn from the CSD¹ co-ordinates of Yang *et al.*'s structure.⁶

There are only a handful of gold(III)-mono(amide) complexes listed in the CSD,¹⁻⁸ of which $[\text{Au}(\text{L-N,N}')\text{Cl}_2]$ (where L = *N*-(4-methylphenyl)pyridine-2-carboxamide, CSD ref code: UKETUZ) was reported by Yang *et al.* in 2003.⁶ It crystallised in the monoclinic space group $P2_1/c$ with $Z = 8$. These workers reported a 1:1 gold(III):amide complex where the gold(III) metal centre is bound to the amide and pyridine nitrogen units of the ligand along with two chloride ions to complete the distorted square planar geometry (Fig. 5.1.1).⁶

X-ray Crystallography

The only gold(III) bis(amide) complex, $[\text{Au}(\text{XL})\text{Cl}_2]$ (where $\text{X} = 2,2'$ -bis(pyridylcarboxamide)-1,1'-binaphthyl), reported in the CSD¹ (CSD ref code: YEHLEC) was by Che *et al.* in 1994. It crystallised in the monoclinic space group $P2_1/c$ with $Z = 4$. He reported that the gold(III) centre was only bound to half the tetradentate ligand with two chloride ions completing the distorted square planar geometry (Fig. 5.1.2) in a similar binding fashion to that of Yang's complex. This was presumably due to the steric constraints of the ligand. The 5-carbon bridge would induce a 7-membered compound upon binding to gold(III). The seven membered compound is evidently too strained to accommodate the square planar geometry required by the gold(III) centre, hence the gold(III) ion only binding to half the ligand.

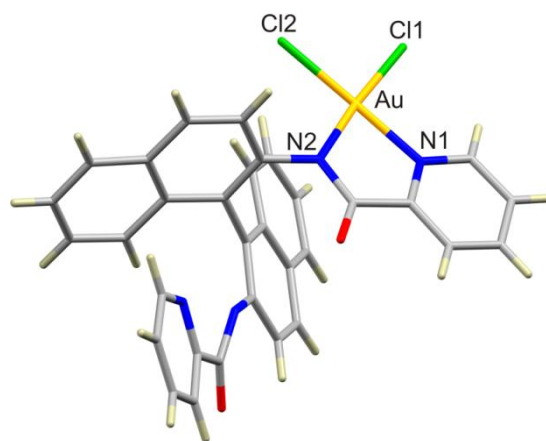


Figure: 5.1.2: Diagram of a single molecular unit of $[\text{Au}(\text{XL})\text{Cl}_2]$, showing the coordination geometry of the gold(III) centre. Redrawn from the CSD¹ co-ordinates of Che *et al.*'s structure.²

The distortion from the ideal square planar geometry for compounds $[\text{Au}(\text{L-N,N}')\text{Cl}_2]$ and $[\text{Au}(\text{XL})\text{Cl}_2]$ arises from the bite angle of the co-ordinating ligands, which cannot accommodate the gold ion in a perfect square plane. The $\text{N1}-\text{Au}-\text{N2}$ angle is significantly smaller than the ideal 90° and the $\text{Cl2}-\text{Au}-\text{Cl1}$ angle approximately equal to the expected 90° in both complexes (Table 5.1.1). The *trans* effect arising from the stronger σ -donor ability of the amide nitrogen is evident in the longer $\text{Cl2}-\text{Au}$ bond lengths of both complexes (Table 5.1.1).

X-ray Crystallography

Table 5.1.1: Co-ordination sphere bond lengths and bond angles for CSD-reported gold(III) structures.

CSD Ref Code: YEHLEC		CSD Ref Code: UKETUZ
Co-ordination bond lengths (Å)		
N1–Au	2.018	2.018
N2–Au	2.033	2.047
Cl1–Au	2.272	2.258
Cl2–Au	2.302	2.286
Co-ordination bond angles (°)		
N1–Au–N2	81.47	81.66
N2–Au–Cl2	93.70	95.49
Cl2–Au–Cl1	90.03	88.73
Cl1–Au–N1	94.85	94.18

Yang *et al.* published a paper entitled ‘Novel gold(III) complexes of aminoquinoline derivatives: crystal structure, DNA binding and cytotoxicity against melanoma and lung tumour cells’ in 2008 which they report the crystal structures of two 8-aminoquinoline amide-based tridentate compounds of gold(III) (Figure 5.1.3): [Au(Quingly)Cl]Cl (CSD ref code: ILIGUF) and [Au(Quinala)Cl]Cl (CSD ref code: ILIHAM).⁵ The former is chiral and thus crystallised in the monoclinic space group $P2_12_12_1$ while the latter crystallised in the monoclinic space group $P2_1/c$.

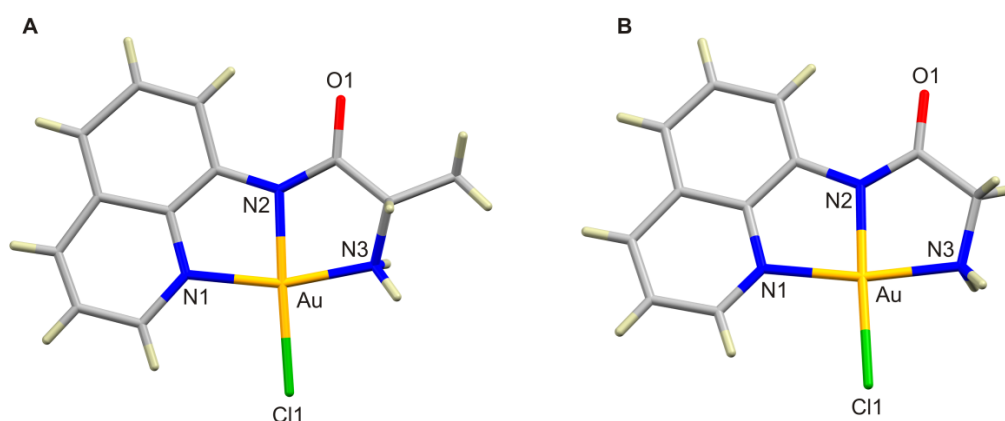


Figure: 5.1.3: Diagram of a single molecular unit of [Au(Quingly)Cl]Cl (A) and [Au(Quinala)Cl]Cl (B), showing the co-ordination geometry of the gold(III) centre. Redrawn from the CSD¹ co-ordinates of Yang *et al.*'s structures.⁵

X-ray Crystallography

Table 5.1.2: Co-ordination sphere bond lengths and bond angles for CSD-reported gold(III) structures.

	CSD Ref Code: ILIGUF	CSD Ref Code: ILIHAM
Co-ordination bond lengths (Å)		
N1–Au	2.020	2.021
N2–Au	1.953	1.973
N3–Au	2.024	1.975
Cl1–Au	2.277	2.278
Co-ordination bond angles (°)		
N1–Au–N2	83.54	81.66
N2–Au–N3	83.09	95.49
N3–Au–Cl1	94.81	88.73
Cl1–Au–N1	98.54	94.18

Once again the distortion from the ideal square planar geometry for compounds [Au(Quingly)Cl]Cl and [Au(Quinala)Cl]Cl arises from the bite angle of the co-ordinating ligands, which cannot accommodate the gold ion in a perfect square plane. The N–Au–N angles are significantly smaller than the ideal 90° while the N–Au–Cl1 angles are fairly obtuse (Table 5.1.2). The *trans* effect arising from the stronger σ -donor ability of the amide nitrogen is evident in the longer Cl1–Au bond lengths of both complexes (Table 5.1.2).

5.2 Objectives

The first objective of the single crystal X-ray analysis was to elucidate the solid state structures of the metal compounds studied in this work and their molecular conformations. The second objective was to use the solid state structures as a starting point for the gas phase geometry optimisation calculations. This was performed in order to investigate the crystal packing effects on the solid state structure compared to that of the gas phase optimised structure. The geometry optimised structures were then used to delineate the electronic structure of the complexes along with NMR shielding tensors and IR frequencies.

5.3 Experimental

X-Ray diffraction data were collected on an Oxford Diffraction Xcalibur2 CCD 4-circle diffractometer equipped with an Oxford Instruments Cryojet for H₂L3, HL13, [Au(HL1)Cl₂], [Au(HL2)Cl₂], [Au(HL3)Cl₂], [Au(L4)Cl₂], [Au(L5)Cl](PF₆), [Au(L6)Cl](PF₆), [Au(L7)Cl](PF₆), [Au(L12)Cl](PF₆) and [Au(L13)Cl](PF₆). The data were collected at room temperature unless otherwise stated, with Mo K α ($\lambda = 0.71073 \text{ \AA}$) radiation at a crystal-to-detector distance of 50 mm using omega scans at $\theta = 29.389^\circ$, with varying exposure times taken at 2.01 kW X-ray power with 0.75° frame widths. The data were reduced with the program CrysAlis RED⁹ using outlier rejection, scan speed scaling, as well as standard Lorentz and polarisation correction factors. Unless otherwise stated, direct methods (SHELXS-97, WinGX32)^{10, 11} were used to solve the structures. All non-H atoms were located in the E-map and refined anisotropically with SHELXL-97.¹² All hydrogen atoms in each of the structures resolved were included as idealised contributors in the least squares process with standard SHELXL-97¹² parameters, unless otherwise stated. The X-Ray diffraction data for compounds [Au(L8)Cl](PF₆), [Au(L11)Cl](PF₆) and [Au(L15)Cl] were collected on a Bruker Smart APEX II Duo CCD 3-circle diffractometer equipped with an Oxford Instruments Cryojet. The data were collected at room temperature unless otherwise stated ($\lambda = 0.71073 \text{ \AA}$, μS Mo microsource) at a crystal-to-detector distance of 50 mm using omega and psi scans, with varying exposure times. The frames were integrated with the Bruker SAINT software package using a narrow-frame algorithm. Data were corrected for absorption effects using the multi-scan method (SADABS). Unless otherwise stated, direct methods (SHELXS-97, WinGX32)^{10, 12} were used to solve the structures. All non-H atoms were located in the E-map and refined anisotropically with SHELXL-97.¹² All hydrogen atoms in each of the structures resolved were included as idealised contributors in the least squares process with standard SHELXL-97 parameters, unless otherwise stated. X-Ray diffraction data for compound [Au(L9)Cl]AuCl₂ were collected on a X8 Prospector CCD 4-circle system equipped with an Oxford Instruments Cryojet, multilayer monochromator ($\lambda = 1.54178 \text{ \AA}$, μS Co microsource) at a crystal-to-detector distance of 50 mm using omega and psi scans, with varying exposure times. The frames were integrated with the Bruker SAINT software package using a narrow-frame algorithm. Data were corrected for absorption effects using the multi-scan method (SADABS). The structure was solved and refined using the Bruker SHELXTL Software Package.

5.4 Results and discussion

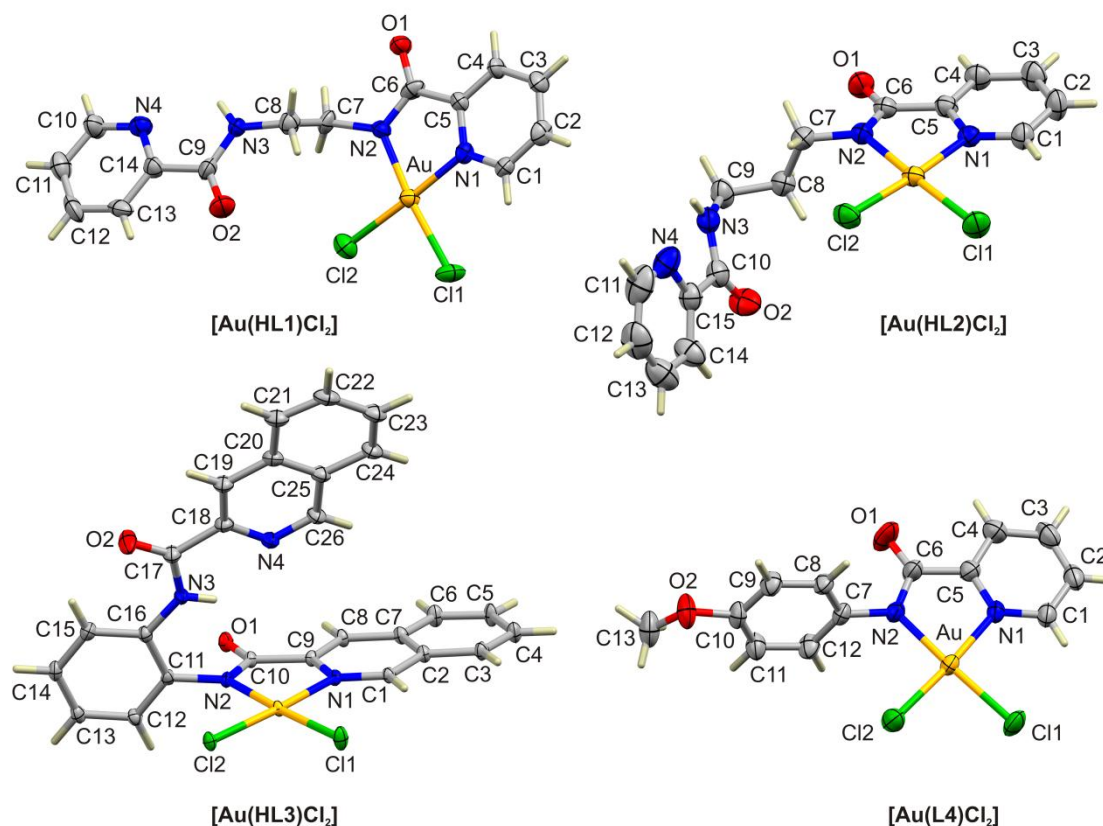
MOLECULAR STRUCTURES $[\text{Au}(\text{HL1})\text{Cl}_2]$ – $[\text{Au}(\text{L4})\text{Cl}_2]$:

Figure: 5.4.1: Labelled views of the single crystal X-ray structures of gold(III) compounds $[\text{Au}(\text{HL1})\text{Cl}_2]$, $[\text{Au}(\text{HL2})\text{Cl}_2]$, $[\text{Au}(\text{HL3})\text{Cl}_2]$ and $[\text{Au}(\text{L4})\text{Cl}_2]$. Hydrogen atoms are rendered as sticks and bonds are represented as cylinders. Thermal ellipsoids are represented as 50% probability surfaces for $[\text{Au}(\text{HL1})\text{Cl}_2]$, $[\text{Au}(\text{HL2})\text{Cl}_2]$, and $[\text{Au}(\text{HL3})\text{Cl}_2]$.

The X-ray structures of $[\text{Au}(\text{HL1})\text{Cl}_2]$ – $[\text{Au}(\text{L4})\text{Cl}_2]$ are shown in Figure 5.4.1. The gold(III) ion is nominally square planar in each complex with a pair of *cis*-chloride ions co-ordinated *trans* to the single pyridyl-amido chelating moiety of the ligand in the case of $[\text{Au}(\text{L4})\text{Cl}_2]$, and one of the pair of such chelating groups in $[\text{Au}(\text{HL1})\text{Cl}_2]$ – $[\text{Au}(\text{HL3})\text{Cl}_2]$. The substituent groups attached to the deprotonated metal-bound amide nitrogen atom (N2) in $[\text{Au}(\text{HL1})\text{Cl}_2]$ – $[\text{Au}(\text{L4})\text{Cl}_2]$ adopt structure-dependent conformations that have an essentially minimal impact on the co-ordination geometry of the gold(III) ion in each case (Table 5.4.1). The aryl-substituted derivatives $[\text{Au}(\text{HL3})\text{Cl}_2]$ and $[\text{Au}(\text{L4})\text{Cl}_2]$ have co-ordination group parameters that are structurally and statistically equivalent to the alkyl-substituted analogues

X-ray Crystallography

[Au(HL1)Cl₂] and [Au(HL2)Cl₂], despite having a substituent that is potentially capable of conjugation with the amide-based compound ring.

Table 5.4.1: Selected Crystallographic Bond Distances and Bond Angles for [Au(HL1)Cl₂]-[Au(L4)Cl₂].

	[Au(HL1)Cl ₂]	[Au(HL2)Cl ₂]	[Au(HL3)Cl ₂]	[Au(L4)Cl ₂]
Bond distances				
Au1–N1	2.036(5)	2.037(3)	2.048(3)	2.031(4)
Au1–N2	2.019(4)	2.014(3)	2.035(3)	2.009(5)
Au1–Cl1	2.290(2)	2.287(1)	2.303(1)	2.295(2)
Au1–Cl2	2.285(2)	2.263(1)	2.270(1)	2.261(2)
C=O ^a	1.211(7)	1.230(5)	1.232(4)	1.21(1)
C=O ^b	1.228(7)	1.217(5)	1.240(6)	–
N–C ^a	1.345(8)	1.341(5)	1.362(5)	1.343(9)
N–C ^b	1.340(7)	1.346(6)	1.391(5)	–
Bond angles				
N1–Au1–Cl1	94.0(1)	94.85(9)	95.68(8)	95.3(1)
Cl1–Au1–Cl2	89.11(7)	89.00(4)	89.42(2)	88.87(6)
Cl2–Au1–N2	95.8(1)	94.90(9)	93.83(9)	94.4(1)
N2–Au1–N1	81.0(2)	81.3(1)	81.1(1)	81.5(2)
Au1–N1–C5 ^c	112.9(4)	112.9(3)	112.7(2)	113.2(4)
Au1–N2–C6 ^d	115.3(4)	115.0(3)	116.0(2)	115.2(4)
N1–C5–C6 ^e	115.9(5)	115.9(4)	116.7(3)	116.2(5)
N2–C6–C5 ^f	113.6(5)	113.7(3)	113.0(3)	113.9(6)

^a Metal-bound amide group. ^b Free amide group. ^c For [Au(HL3)Cl₂], this angle is Au1–N1–C9. ^d For [Au(HL3)Cl₂], this angle is Au1–N2–C9. ^e For [Au(HL3)Cl₂], this angle is N1–C9–C10. ^f For [Au(HL3)Cl₂], this angle is N2–C10–C9.

For compound [Au(HL3)Cl₂] the dihedral angle between the aryl ring (C11–C16) attached to the metal-bound amido group (N2) and the 13-atom mean plane of the isoquinoline-amido gold(III) compound (Au1, N1, C1–C10, N2) is near-orthogonal, measuring 80.7°, while for compound [Au(L4)Cl₂], the dihedral angle between the aryl substituent, C7–C12, and the 9-atom mean plane of the pyridine-amido compound, defined by the atoms Au1, N1, C1–C6, and N2, measures 75.8°. Both angles are consistent with an unconjugated aryl group. The more perpendicular dihedral angle for [Au(HL3)Cl₂] presumably reflects the intradimer C–H⋯Cl hydrogen-bonding observed in the π-stacked inversion pair, as discussed later, while the aryl ring orientation in [Au(L4)Cl₂] is possibly marginally influenced by an unconventional C–H⋯O hydrogen bond involving C11, H11, and the amide oxygen acceptor atom O1 of a

X-ray Crystallography

neighbouring molecule in the lattice (*vide infra*); as indicated above, this interaction does not significantly disturb the structure of the chelating group or its co-ordination of the gold(III) ion. The Au–N_{pyridine} and Au–N_{amido} distances for compounds [Au(HL1)Cl₂], [Au(HL2)Cl₂] and [Au(L4)Cl₂] average 2.03(7) Å and 2.014(5) Å, respectively, while the Au–N_{Qu} and Au–N_{amido} distances for compound [Au(HL3)Cl₂] measure 2.048(3) Å and 2.035(3) Å, respectively. These values indicate crystallographically and chemically distinct co-ordination interactions. Both N-donor atom types (pyridine and amido) are sp²-hybridised; however as might be anticipated for an anionic N-donor atom (and consequently a more powerful σ -donor). The Au–N_{amido} bond of [Au(HL3)Cl₂] measures 2.035(3) Å and is more than four standard deviations (4 σ) longer than the mean Au–N_{amido} bond of [Au(HL1)Cl₂], [Au(HL2)Cl₂] and [Au(L4)Cl₂] (2.014(5) Å); similarly, the Au–N_{IQ} bond of [Au(HL3)Cl₂] (2.048(3) Å) is more than 4(σ) longer than the mean Au–N_{pyridine} bond distance for AuL1, AuL2 and AuL4 (2.035(3) Å). Note that this structural difference exists despite the pK_a of pyridine (5.2) being roughly the same as that for isoquinoline (5.5). The underlying reasons for elongation of the Au–N bond distances in [Au(HL3)Cl₂] are therefore likely to be electronic, as opposed to structural, in origin. Overall, the shorter Au–N_{amido} bond and longer Au–N_{pyridine/Qu} phenomenon in amide based compounds has been observed in the crystal structure of another N-alkylated pyridyl-amido gold(III) compound, notably AuCl₂(N-NP2C), where N-NP2C = N-nonylpyridine-2-carboxamido anion, Au–N_{pyridine} = 2.032(2) Å, and Au–N_{amido} = 2.011(2) Å.⁴ The co-ordination group asymmetry for amido-pyridine compounds of gold(III) is even more pronounced for the simplest amide derivative AuCl₂(P2C), where P2C = pyridine-2-carboxamido anion, Au–N_{pyridine} = 2.047(5) Å, and Au–N_{amido} = 1.969(5) Å.⁷ Evidently, the sterically unencumbered amido nitrogen atom of the latter complex is capable of a particularly close approach to the gold(III) ion, a structural feat that apparently requires simultaneous elongation of the Au–N_{pyridine} bond within the five-membered compound ring. Regarding the different Au–N bonds in these pyridyl-amido compounds, it is noteworthy that symmetric bipyridine (bipy) complexes of gold(III) such as [AuCl₂(DMbipy)][PF₆] and [AuCl₂(DMObipy)][PF₆], where DMbipy = 4,4'-dimethyl-2,2'-bipyridine and DMObipy = 4,4'-dimethoxy-2,2'-bipyridine, exhibit equivalent Au–N_{pyridine} distances of 2.03(1) and 2.02(2) Å, respectively.¹³ This confirms the idea that the amido and pyridine nitrogen atoms are chemically distinct (despite equivalent hybridisation), with the former acting as a strong σ -donor and the latter as a more balanced σ -donor/ π -acceptor,¹⁴ and that this electronic

X-ray Crystallography

distinction reinforces dissymmetric co-ordination of the gold(III) ion in the present compounds.

The Au–Cl1 (*trans* to the amido group) and Au–Cl2 (*trans* to the pyridine or quinoline group) bond distances for [Au(HL1)Cl₂]-[Au(L4)Cl₂] average 2.293(6) and 2.260(13) Å, respectively. Closer inspection of the Au–Cl distances indicates that a significant “*trans* effect”¹⁵ is structurally manifest in these complexes, as briefly noted in an earlier paper by Fan *et al.* for AuCl₂(P2C).⁷ More specifically, the Au–Cl bond *trans* to the stronger σ -donor atom (N2, or N_{amido}) is considerably longer than that *trans* to the pyridine nitrogen; in the case of [Au(L4)Cl₂] this difference is as large as 0.034 Å and thus statistically significant relative to the standard uncertainties of the experimental Au–Cl bond distances. The difference between the co-ordination of chloride *trans* to the amido group relative to the pyridine or quinoline group becomes particularly apparent if we compare the mean Au–Cl1 distance above to the mean Au–Cl distance of 2.255(7) Å reported for the symmetric bipy derivatives [AuCl₂(DMbipy)][PF₆] and [AuCl₂(DMObipy)Cl₂][PF₆].¹³ These complexes epitomise the expected bond lengths for the co-ordination of chloride *trans* to an Au–N_{pyridine} bond in a symmetric five-membered compound ring system and highlight the marked elongation of the Au–Cl bonds *trans* to the amido nitrogen donor in the present complexes (especially [Au(L4)Cl₂]). Interestingly, if the chelating σ -donor anion co-ordinated to gold(III) is switched to carbon, as in the complex AuCl₂(2-phenylpyridine),¹⁶ then a very large structural *trans* effect occurs with the Au–Cl distance *trans* to the Au–C bond elongating beyond that observed for the pyridyl-amido complexes reported here to 2.361(8) Å. As might be anticipated, the structural *trans* effect discussed above for organo-gold complexes is paralleled by a kinetic *trans* effect in the substitution reactions of the gold(III) ion. Anions such as chloride co-ordinated *trans* to a powerful σ -donor (e.g. C₆H₅⁻) are kinetically more labile than those co-ordinated *cis* to the “labilising” ligand. This reactivity pattern clearly correlates with a longer, weaker Au–Cl bond *trans* to the strong σ -donor ligand in the structures of such compounds. One might logically expect that for [Au(HL1)Cl₂], [Au(HL2)Cl₂] and [Au(L4)Cl₂], substitution of at least one of the chloride ions (the one *trans* to the amido group (presumably being the more reactive) might be possible for some nucleophiles.

The bond angles (Table 5.4.1) subtended at the metal ion in [Au(HL1)Cl₂]-[Au(L4)Cl₂] are normal for five-membered ring compounds of gold(III) with two N-donor atoms. The mean

X-ray Crystallography

cis Cl–Au–Cl bond angle, 89.1(2)°, falls within 1° of 90°, while the mean *cis* N–Au–N angle is quite acute, measuring 81.2(2)°. The latter bond angle, which deviates significantly from 90°, clearly reflects the geometric constraints on metal ion co-ordination imposed by the five-membered chelate ring for the complexes. In each complex, the *cis* N–Au–Cl bond angles are crystallographically equivalent, averaging 95.0(7)° and 94.7(8)° for the angles to Cl1 and Cl2 for [Au(HL1)Cl₂–[Au(L4)Cl₂], respectively. Both angles are slightly obtuse; this is expected if the sum of the angles at the metal center is required to equate to 360° for a square-planar metal center. The metrics of the co-ordination sphere bond angles for [Au(HL1)Cl₂–[Au(L4)Cl₂] compare favorably with other complexes of gold(III) comprising five-membered chelate rings with two N-donors. The *cis* N–Au–N bond angle is, in fact, a good measure of chelation by such ligands: values of 81.42(7)° for AuCl₂(N-NP2C),⁴ 81.2(2)° for AuCl₂(P2C),⁷ 80.9(4)° for [AuCl₂(DMbipy)][PF₆],¹³ and 80.6(2)° for [AuCl₂(bipy)][NO₃]¹⁷ have been determined and indicate that both amido-pyridine and bipy-type ligands have similar “bite” angles to gold(III).

Gold compounds [Au(HL1)Cl₂–[Au(L4)Cl₂] are polyfunctional in the sense that they possess hydrogen bond donor and acceptor groups as well as aromatic ring systems. The supramolecular structures of the compounds are accordingly both diverse and quite complex. The extended structures of [Au(HL1)Cl₂–[Au(L4)Cl₂] are dominated by unconventional C–H···O and C–H···Cl hydrogen bonds in all cases, which culminates in the formation of one-dimensional (1D) hydrogen-bonded chains in the solid state.

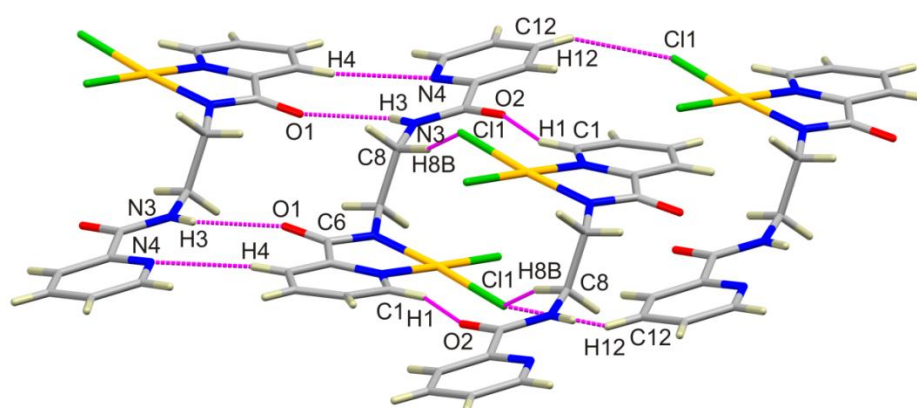


Figure 5.4.2: Key intermolecular H-bonds (labeled atoms) for [Au(HL1)Cl₂]. Atoms and bonds are shown as sticks. Hydrogen bonds are shown as broken magenta cylinders.

Compound [Au(HL1)Cl₂], furthermore, forms inversion-related H-bonded dimers linked by conventional N–H···O hydrogen bonds involving the amide groups as part of interlinked 1D

X-ray Crystallography

H-bonded chains in the solid state (Figure 5.4.2). Several π -stacking interactions are also prevalent; these span lateral shift (LS) and mean plane separation (MPS) values of 1.37–2.42 Å and 3.34–3.50 Å, respectively, and involve both the free- and Au-bound pyridine rings of [Au(HL1)Cl₂], [Au(HL2)Cl₂] and [Au(L4)Cl₂]. In the case of [Au(L4)Cl₂] (Figure 5.4.3), benzene...pyridine π - π stacking occurs and is structurally akin to that reported for the 4-methylbenzene-substituted analogue of [Au(L4)Cl₂].⁶

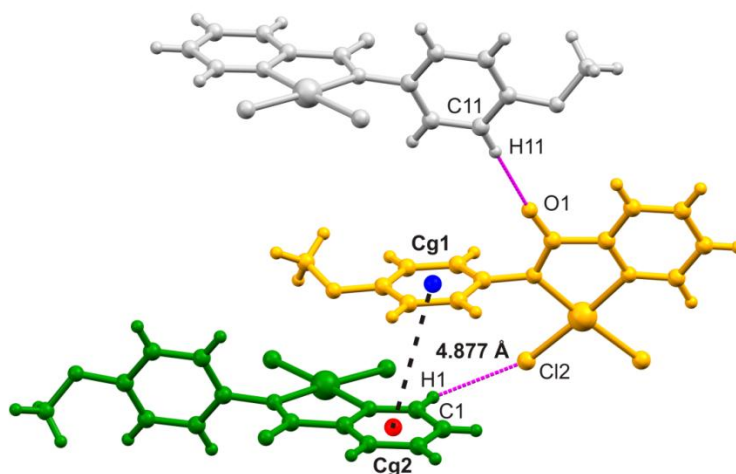


Figure 5.4.3: View of the hydrogen-bonding and π - π stacking interactions between molecules of [Au(L4)Cl₂]. The distance between the two ring centers of gravity (Cg) is indicated. Atoms and bonds are shown as spheres and sticks, respectively. Hydrogen bonds are shown as broken magenta cylinders and individual molecules are colored according to their symmetry operators. A mean plane separation (MPS) for the stacked rings cannot be determined as the rings are not parallel.

Given that there are no especially short intermolecular contacts for the π -stacked rings of [Au(HL1)Cl₂], [Au(HL2)Cl₂] and [Au(L4)Cl₂], a situation that may partly reflect the temperature of the X-ray experiments, but that the interaction metrics fall within the range expected for π -stacked aromatic rings (MPS values of 3.3–3.8 Å),¹⁸⁻²⁰ we conclude that multiple ring-stacking associations stabilised by attractive “ π - π ” occur for [Au(HL1)Cl₂], [Au(HL2)Cl₂] and [Au(L4)Cl₂].¹⁸ For compound [Au(HL3)]Cl₂, however, a more interesting centrosymmetric hydrogen bond-stabilised π -stacked dimer formed (Figure 5.4.4).

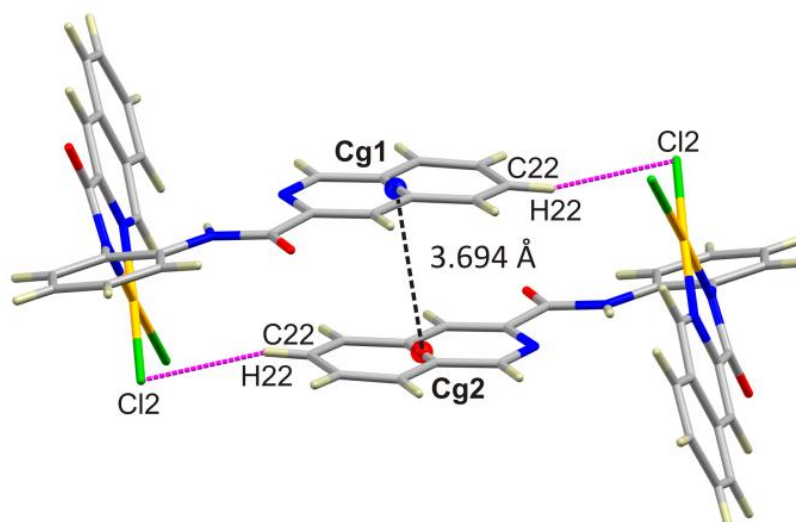


Figure 5.4.4: Partially labeled view of the centrosymmetric π -stacked dimer formed by $[\text{Au}(\text{HL}3)\text{Cl}_2]$. The isoquinoline ring planes are parallel; the distance between the isoquinoline ring centers of gravity ($\text{Cg}1 \cdots \text{Cg}1^i$) is indicated. The dimer is additionally stabilised by C–H \cdots Cl hydrogen bonds: $\text{H}22 \cdots \text{Cl}2^i$, 2.960(1) Å; $\text{C}22 \cdots \text{Cl}2^i$, 3.864(4) Å; $\text{C}22\text{--H}22 \cdots \text{Cl}2^i$, 159.5(3) $^\circ$. Crystallographic symmetry code: (i) $-x, 1-y, 1-z$.

The metal-free isoquinoline rings of two neighbouring molecules of $[\text{Au}(\text{HL}3)\text{Cl}_2]$ stack with exactly parallel ring planes about a centre of inversion to form a relatively tight interaction with a MPS of 3.523 Å that is well within the 3.35–3.8 Å range expected for π -stacked aryl rings.¹⁹ If the isoquinoline nitrogen atom N4 is used as a frame of reference, then the geometry of the interacting isoquinoline rings is the typical offset antiparallel arrangement (N4 atoms pointing in opposite directions) for aromatic N-heterocycles.¹⁸ This particular ring \cdots ring arrangement evidently represents energetically favourable dipole alignments in the two ring systems. The distance between the centres of gravity of the two isoquinoline rings, $\text{Cg}1 \cdots \text{Cg}1^i$, measures 3.694 Å such that the lateral shift of the ring systems is 1.111 Å. As clearly presented and discussed by Janiak,¹⁸ the laterally-displaced ring systems seen in AuL4 would permit optimal π - π attraction between stacked isoquinoline groups in addition to normal van der Waals attraction and London forces of attraction.

Collectively, the interactions appear to be structurally rather modest. A further conclusion based on our analysis of the extended structures of $[\text{Au}(\text{HL}1)\text{Cl}_2]$ and $[\text{Au}(\text{HL}2)\text{Cl}_2]$ is that the involvement of the metal-free pyridyl-amide side-chain groups in intermolecular H-bonding and π -stacking interactions most likely accounts for the different solid-state conformations of these groups evident in Figure 5.4.1 (e.g. the N–H hydrogen atom of $[\text{Au}(\text{HL}2)\text{Cl}_2]$, H3,

X-ray Crystallography

eclipses the adjacent methylene group's C–H hydrogen atom, as opposed to adopting a staggered conformation as in [Au(HL1)Cl₂].

Table 5.4.2: Hydrogen bond distances and angles for compounds [Au(HL1)Cl₂]-[Au(L4)Cl₂]

Donor–H···A	D–H/Å	H···A/Å	D···A/Å	D–H···A/°
[Au(HL1)Cl₂]				
N3–H3···O1 ⁱ	0.8	2.33	2.933(7)	133
C1–H1···O2 ⁱⁱ	0.93	2.41	3.140(7)	136
C8–H8B···Cl1 ⁱⁱ	0.97	2.73	3.580(7)	147
C12–H12···Cl1 ⁱⁱ	0.93	2.75	3.602(8)	152
Symmetry codes: (i) 1–x, 1–y, 1–z; (ii) –x, 1–y, 2–z.				
[Au(HL2)Cl₂]				
C1–H1···O2 ⁱ	0.93	2.50	3.088(6)	121
C3–H3A···O1 ⁱⁱ	0.93	2.47	3.187(6)	133
C12–H12···Cl2 ⁱⁱ	0.93	2.86	3.566(5)	133
Symmetry codes: (i) –1/2+x, 1/2–y, 1/2+z; (ii) 3/2–x, –1/2+y, 3/2–z.				
[Au(HL3)Cl₂]				
C3–H3A···O1 ⁱⁱ	0.95	2.37	3.269(4)	158
C8–H8···Cl1 ⁱⁱ	0.93	2.67	3.554(3)	156
C1–H1···Cl1 (intramol.)	0.95	2.71	3.303(4)	121
C15–H15···O2 (intramol.)	0.95	2.39	2.999(5)	122
N3–H3···N2 (intramol.)	0.88(5)	2.42(5)	2.804(5)	107(4)
N3–H3···N4 (intramol.)	0.88(5)	2.09(4)	2.619(5)	118(4)
Symmetry codes: (i) x, 1/2–y, –1/2+z; (ii) x, 1/2–y, 1/2+z.				
[Au(L4)Cl₂]				
C1–H1···Cl2 ⁱ	0.93	2.81	3.522(6)	134
C11–H11···O1 ⁱⁱ	0.93	2.26	3.19(1)	176
Symmetry codes: (i) 1/2–x, –1/2+y, 1.5–z; (ii) –1/2+x, 1/2–y, –1/2+z.				

X-ray Crystallography

Table 5.4.3: Crystal Structure, X-ray Data, and Structure Model Refinement Parameters for and [Au(HL1)Cl₂]-[Au(L4)Cl₂].^a

	[Au(HL1)Cl]	[Au(HL2)Cl]	[Au(HL3)Cl ₂]	[Au(L4)Cl ₂]
Chemical formula	C ₁₄ H ₁₃ AuCl ₂ N ₄ O ₂	C ₁₅ H ₁₅ AuCl ₂ N ₄ O ₂	C ₂₆ H ₁₇ AuCl ₂ N ₄ O ₂ ·C ₄ H ₁₀ O	C ₁₃ H ₁₁ AuCl ₂ N ₂ O ₂
<i>M_r</i>	537.15	551.18	759.42	495.10
Crystal system	Triclinic	Monoclinic	Monoclinic	Monoclinic
SG	<i>P</i> -1	<i>P</i> 2 ₁ / <i>n</i>	<i>P</i> 2 ₁ / <i>c</i>	<i>P</i> 2 ₁ / <i>n</i>
Temperature (K)	296 (2)	296 (2)	100 (1)	296 (2)
<i>a</i> , <i>b</i> , <i>c</i> (Å)	7.477 (5), 10.210 (5), 11.023 (5)	11.188 (5), 10.192 (5), 15.132 (5)	15.990 (5), 12.445 (5), 15.602 (5)	12.971 (5), 8.701 (5), 14.068 (5)
α , β , γ (°)	85.443 (5), 79.313 (5), 72.383 (5)	90, 93.350 (5), 90	90, 104.487 (5), 90	90, 114.723 (5), 90
<i>V</i> (Å ³)	787.9 (7)	1722.5 (13)	3006.0 (18)	1442.2 (11)
<i>Z</i>	2	4	4	4
Radiation type	Mo <i>K</i> α	Mo <i>K</i> α	Mo <i>K</i> α	Mo <i>K</i> α
μ (mm ⁻¹)	9.69	8.87	5.11	10.57
Crystal size (mm)	0.4 × 0.35 × 0.15	0.60 × 0.20 × 0.18	0.50 × 0.45 × 0.15	0.50 × 0.40 × 0.20
Abs. correction	Multi-scan	Multi-scan	Multi-scan	Multi-scan
<i>T_{min}</i> , <i>T_{max}</i>	0.507, 1.000	0.076, 0.298	0.184, 0.515	0.077, 0.226
<i>N_m</i> , <i>N_i</i> , <i>N_o</i>	6130, 3427, 3043	26661, 6154, 4240	45814, 10638, 7698	14511, 2837, 2494
<i>R_{int}</i>	0.040	0.045	0.058	0.045
<i>R₁</i> , <i>wR(F²)</i> , <i>S</i>	0.034, 0.083, 1.01	0.032, 0.080, 0.96	0.039, 0.096, 0.96	0.036, 0.10, 1.05
<i>N_p</i> , <i>N_{res}</i>	212, 0	217, 0	367, 4	182, 0
$\Delta\rho_{max}$, $\Delta\rho_{min}$ (e Å ⁻³)	1.02, -1.91	1.47, -1.97	1.98, -4.55	1.38, -2.94

^aAbbreviations: SG, space group; *V*, volume; *Z*; number of formula units per unit cell; μ , absorption coefficient; *T*, transmission coefficient; *N_m*, number of measured reflections, *N_i*, number of independent reflections; *N_o*, number of observed reflections with $I > 2\sigma(I)$; *I*, intensity; *R_{int}*, internal *R*-factor for data set (based on the intensity match between symmetry equivalent reflections); *R₁* = $R[F^2 > 2\sigma(F^2)]$; *wR(F²)*, weighted *R*-factor based on F^2 ; *F*, structure factor; *S*, goodness-of-fit of model to experimental data; *N_p*, number of parameters, *N_{res}*, number of restraints; $\Delta\rho$, electron density difference.

X-ray Crystallography

MOLECULAR STRUCTURES [Au(L5)Cl](PF₆)-[Au(L7)Cl](PF₆):

The X-ray structures of [Au(L5)Cl](PF₆)-[Au(L7)Cl](PF₆) are shown in Figure 5.4.6. The gold(III) ion is again nominally square planar in each complex with the gold(III) ion coordinated by the three N-donor atoms of the chelating ligand and a chloride ion coordinated to the fourth co-ordination site, *trans* to the amido chelating moiety to complete the geometry.

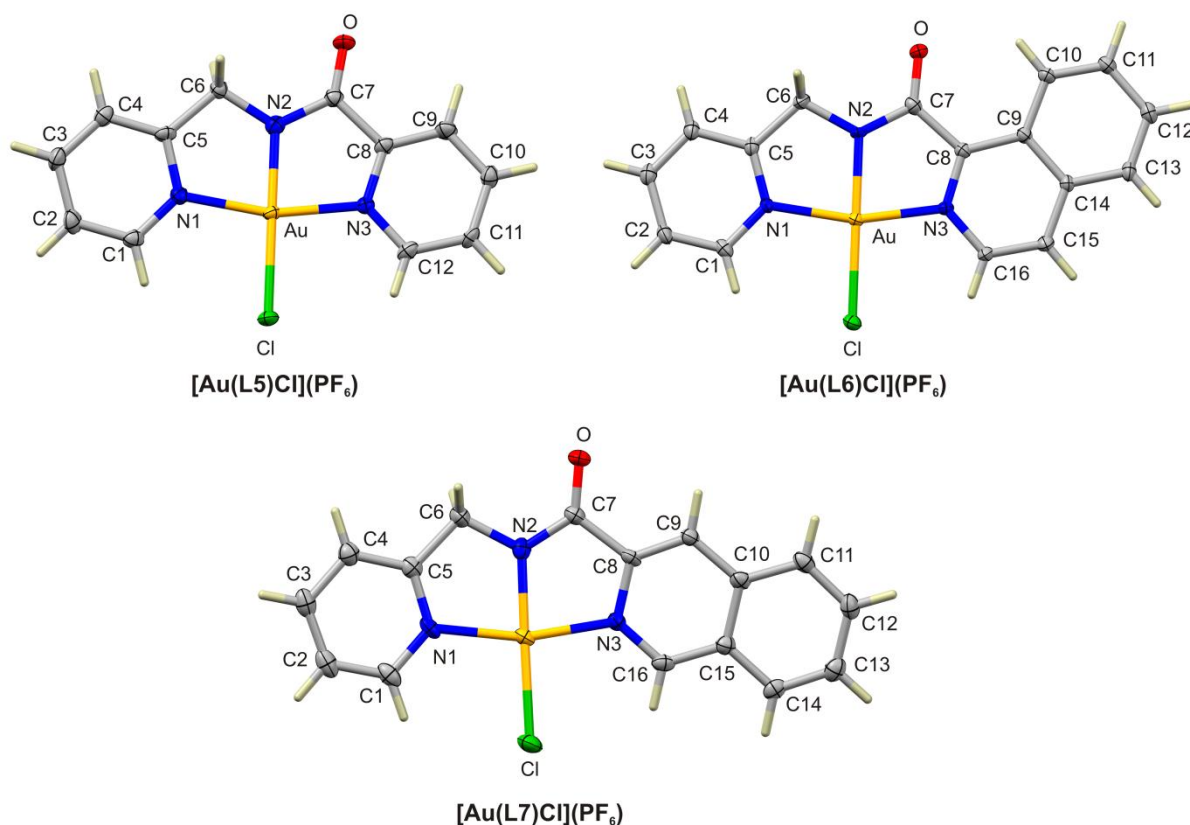


Figure: 5.4.6: Labelled views of the single crystal X-ray structures of gold(III) compounds [Au(L5)Cl](PF₆)-[Au(L7)Cl](PF₆). Hydrogen atoms are rendered as sticks and bonds are represented as cylinders. Thermal ellipsoids are represented as 50% probability surfaces.

All three compounds, [Au(L5)Cl](PF₆)-[Au(L7)Cl](PF₆), contain a picolyl-amide chelating moiety along with either a pyridine or isoquinoline moiety as the structural variation within the series. The compounds are planar in nature with slight deviation for certain atoms from an all-atom mean plane. This deviation could partially be due to the flexibility introduced by the picolyl-amide functionality as opposed to the more rigid and aromatic 8-aminoquinoline moiety for compounds [Au(L8)Cl](PF₆)-[Au(L16)Cl]. The largest single-atom deviation from the above all atom mean plane for each compound is 0.220 Å for atom C11 of compound [Au(L7)Cl](PF₆). The structural variation between compounds seems to impart minimal

X-ray Crystallography

effect on the overall planarity as well as co-ordination geometry of the gold(III) ion in each compound (Table 5.4.4).

Table 5.4.4: Selected Crystallographic Bond Distances and Bond Angles for [Au(L5)Cl](PF₆)-[Au(L6)Cl](PF₆).

	[Au(L5)Cl](PF ₆)	[Au(L6)Cl](PF ₆)	[Au(L7)Cl](PF ₆)
Bond distances			
Au1–N1	2.024(5)	2.013(5)	2.031(6)
Au1–N2	1.918(5)	1.933(5)	1.888(6)
Au1–N3	2.013(5)	2.015(6)	2.000(5)
Au1–Cl1	2.292(1)	2.298(2)	2.286(2)
C=O	1.206(7)	1.223(9)	1.231(8)
N–C	1.390(7)	1.360(9)	1.360(8)
Bond angles			
N1–Au1–N2	81.4(2)	82.8(2)	82.5(2)
N2–Au1–N3	83.1 (2)	80.7(2)	82.5(2)
N3–Au1–Cl1	96.8(1)	99.3(2)	96.8(1)
Cl1–Au1–N1	98.8(1)	97.2(2)	98.4(2)
N1–C5–C6	117.8(5)	117.4(5)	119.2(6)
C5–C6–N2	107.4(4)	108.9(5)	106.0(6)
N2–C7–C8	111.1(5)	111.2(6)	110.4(5)
C7–C8–N3	116.4(5)	115.4(5)	114.3(5)

This was to be expected as the structural derivatives incorporating pyridine, 1- and 3-isoquinoline amide moieties were specifically chosen so that minimal steric effects between the co-ordinated chloride ion and adjacent hydrogen atoms (associated with the above mentioned heterocyclic N-donor chelate rings) would be encountered. This, opposed to what would be envisaged for a ligand incorporating a quinoline amide moiety. The pKa of pyridine (5.2) and isoquinoline (5.5) are similar (*vide supra*) and are therefore not expected to impart any significant difference between gold(III)-aminomethyl pyridine (Au–N_{AMP}) and gold(III)-pyridine or isoquinoline (Au–N_{Py/IQ}) bond lengths, particularly for [Au(L5)Cl](PF₆) which contains two N_{pyridine} donor atoms within the ligand scaffold. This statement, in part, holds true as the average Au–N_{AMP} and Au–N_{Py/IQ} bond distances are 2.022(9) Å and 2.009(8) Å, respectively, which are statistically and metrically similar. This is in agreement with the

X-ray Crystallography

equivalent bond distances observed for the similar copper complexes [Cu(pmpa)(4MImH)(H₂O)](H₂O)(ClO₄) and [Cu(pmpa)(4MPy)(H₂O)](H₂O)(ClO₄), where pmpa = *N*-(2-picolyl)picolinamide, 4MImH = 4-methylimidazole and 4MPy = 4-methylpyridine.²¹ It must also be noted that the Au–N_{AMP} bond distances compare well to the Au–N bond distances observed in the symmetrical gold(III) compounds, [AuCl₂(DMbipy)][PF₆] and [AuCl₂(DMObipy)][PF₆] (*vide supra*)¹³, which suggests the N-donor atoms are chemically similar to each other in terms of σ -donor/ π -acceptor ability. The average Au–N_{amide} amide distance (1.91(2) Å) is, however, significantly shorter than the corresponding Au–N_{Py/IQ} or Au–N_{AMP} distances despite their similar hybridisation (sp^2). This renders the Au–N_{amide} and Au–N_{Py/IQ} co-ordination interactions chemically and crystallographically distinct from each other, as was the case for [Au(HL1)Cl₂]-[Au(L4)Cl₂]. This effect once again arises from the fact that the anionic amido nitrogen is a significantly stronger σ -donor than the corresponding heterocyclic nitrogen atoms and is observed for a similar gold(III) amide compound, AuCl₂(*N*-NP2C) (*vide supra*).⁴ This further reiterates the statements made (*vide supra*) regarding the dissimilar co-ordinating abilities and environments provided by the N_{amido} and N_{Py/IQ} atoms. The Au–Cl1 bond distance for compounds [Au(L5)Cl](PF₆)-[Au(L7)Cl](PF₆) average 2.292(6) Å, closely matching the Au–Cl bond lengths observed *trans* to the N_{amido} atom for compounds [Au(HL1)Cl₂]-[Au(L4)Cl₂], consistent with a significant “*trans* effect”¹⁵. This is similarly observed for the analogous Pt(II) complex PtCl(pmpa)·2H₂O where the Au–Cl bond distance is slightly longer at 2.308(3). This may, in part, be due to the slightly larger atomic radius of platinum (139 pm) compared to gold (135 pm).²² The average C6–N2 bond length, 1.46(2) Å, is markedly longer, 9(σ), than the N2–C7 bond length at 1.37(1) Å. This suggests that the lone pair of electrons associated with N2 is partially delocalised over the N2–C7 bond, increasing its bond order and subsequently allowing for the shorter length observed. These structural parameters are highlighted for the analogous Pt(II) complex, PtCl(pmpa)·2H₂O, where the C6–N2 and N2–C7 bond lengths are 1.31(2) Å and 1.44(2) Å respectively.²³

The bond angles (Table 5.4.4) subtended at the metal ion in [Au(L5)Cl](PF₆)-[Au(L7)Cl](PF₆) are normal for five-membered ring compounds of gold(III) with three N-donor atoms. The mean N–Au–Cl bond angle, 97.8(9)°, is fairly obtuse, while the mean N–Au–N angle is quite acute, measuring 82.1(9)°. This is expected since the sum of the angles at the metal center are required to equate to 360° for a square-planar metal center. Both angles deviate

X-ray Crystallography

significantly from 90°, clearly reflecting the geometric constraints on metal ion co-ordination imposed by the two five-membered chelate rings for the three complexes. The metrics of the co-ordination spheres for [Au(L5)Cl](PF₆)-[Au(L7)Cl](PF₆) compare favorably with the mean N–Au–Cl and N–Au–N angles observed for other gold(III) complexes comprising five-membered chelate rings with three N-donor atoms, such as [Au(terpy)Cl]Cl₂·3H₂O (N–Au–Cl, 98.6(1)°; N–Au–N, 81.4(1)°)^{24, 25}. Since the anionic bridgehead nitrogen (N_{amido}) in the case of [Au(L5)Cl](PF₆)-[Au(L7)Cl](PF₆) is a more powerful σ-donor than that of the pyridine atom in [Au(terpy)Cl]Cl₂·3H₂O, one might expect the bridgehead-to-gold(III) distance to be shorter for compounds [Au(L5)Cl](PF₆)-[Au(L7)Cl](PF₆), therefore influencing their co-ordination geometries. This is, however, not the case as it is well known that the bridgehead atom-to-metal (metal = gold(III) or platinum(II)) distance (in terpyridine-based metal compounds) is significantly shortened compared with the rest of the metal-N distances of the co-ordination sphere, so much so that there is essentially negligible difference between bridgehead atom-to-metal distance whether the bridgehead atom is a neutral pyridine (1.950(3) Å)^{24, 25} anionic pyridine (compounds in this work) or even an anionic carbon (1.950(5) Å).²⁶

The supramolecular structures of compounds [Au(L5)Cl](PF₆)-[Au(L7)Cl](PF₆) are modest at best as they do not contain the same functional variety that compounds [Au(HL1)Cl₂]-[Au(L4)Cl₂] do. Their only conventional hydrogen bond donor functional group (amide N–H) is lost upon chelation to the gold(III) ion. They do, however, contain conventional hydrogen bond acceptor functionalities in the amide oxygen and gold(III)-bound chloride ion along with the fluoride atoms associated with the PF₆⁻ anion. The short contact interactions within the crystal lattice for all three compounds are therefore dominated by unconventional C–H···O, C–H···Cl and C–H···F hydrogen bonding.

For all three compounds the extended solid state structures are built around centrosymmetric unconventional hydrogen-bonded dimers. Figure 5.4.7 illustrates such an interaction for compound [Au(L5)Cl](PF₆). These centrosymmetric dimers are either independent of each other and constitute dimers linked via PF₆⁻ anions to form 1D unconventionally hydrogen bonded chains as for [Au(L6)Cl](PF₆) or comprise part of a more complex 2D network of molecules linked via unconventional hydrogen bonds as for [Au(L5)Cl](PF₆). This 2D network is maintained by a series of C–H···Cl (Figure 5.4.7) and bifurcated C–H···O unconventional hydrogen bonds (Table 5.4.5) to form ‘sheets’ that are

X-ray Crystallography

interlinked in the third dimension via PF_6^- anions. The solid state structure of compound $[\text{Au}(\text{L7})\text{Cl}](\text{PF}_6)$ is even more complex, containing a 3D network linked via similar unconventional hydrogen bonds.

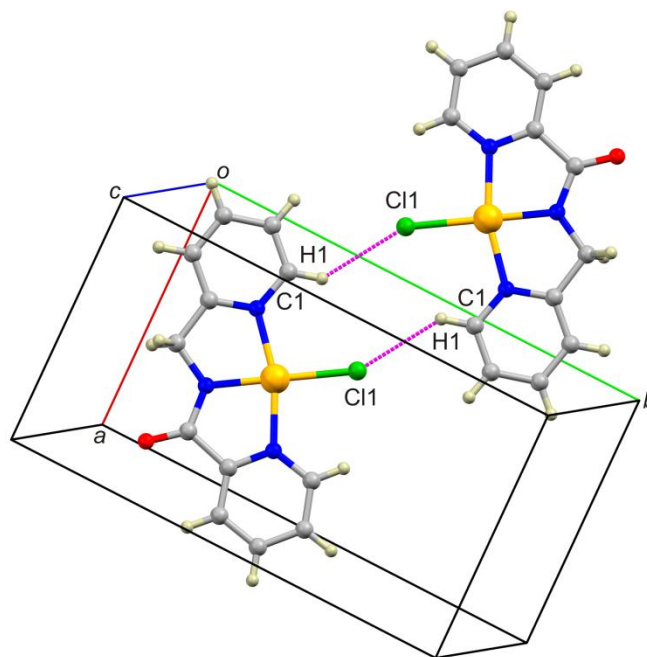


Figure 5.4.7: Partially labeled view of the centrosymmetric unconventionally hydrogen bonded dimer formed by $[\text{Au}(\text{L5})\text{Cl}](\text{PF}_6)$. The dimer is stabilized by C–H \cdots Cl hydrogen bonds: H1 \cdots Cl1ⁱ, 2.746(1) Å; C1 \cdots Cl1ⁱ, 3.503(6) Å; C1–H1 \cdots Cl1ⁱ, 137.1(3)°. Crystallographic symmetry code: (i) $-x, -y, -z$.

The π -stacking interactions for compounds $[\text{Au}(\text{L5})\text{Cl}](\text{PF}_6)$ – $[\text{Au}(\text{L6})\text{Cl}](\text{PF}_6)$ are similarly modest with no especially short intermolecular contacts for the π -stacked rings present. This could be expected for $[\text{Au}(\text{L5})\text{Cl}](\text{PF}_6)$ as the molecule is relatively small and contains only two aromatic substituents capable of π -stacking interactions that are separated by a more bulky methylene group which is capable of hindering the approach of the respective aromatic rings, and therefore the presence of strong π - π interactions. This was, however, not expected for $[\text{Au}(\text{L6})\text{Cl}](\text{PF}_6)$ as it contains an extended aromatic quinoline ring system that is well known for its π -stacking ability. Compound $[\text{Au}(\text{L7})\text{Cl}](\text{PF}_6)$ was the only complex of the three that displayed any significant π -stacking interactions, the most notable of which is the centrosymmetric interaction between two, exactly parallel, neighbouring isoquinoline rings incorporating atoms N3 and C8–C16 (Figure 5.4.8). The MPS between the rings is 3.380 Å which is well within the 3.35–3.8 Å range expected for π -stacked aryl rings.²⁰ With isoquinoline nitrogen atom N3 used as a frame of reference, the geometry of the interacting

X-ray Crystallography

isoquinoline rings is the typical offset antiparallel arrangement (N3 atoms pointing in opposite directions for aromatic N-heterocycles) as was the case in the similar interaction for compound $[\text{Au}(\text{HL3})\text{Cl}_2]$.¹⁸ The distance between the centers of gravity of the two isoquinoline rings, $\text{Cg1}\cdots\text{Cg1}^i$, measures 3.702 Å such that the lateral shift of the ring systems is 1.510 Å. As mentioned before, Janiak¹⁸ states that the laterally-displaced ring systems seen in $[\text{Au}(\text{L7})\text{Cl}](\text{PF}_6)$ would permit optimal π - π attraction between stacked isoquinoline groups in addition to normal van der Waals attraction and London forces of attraction.

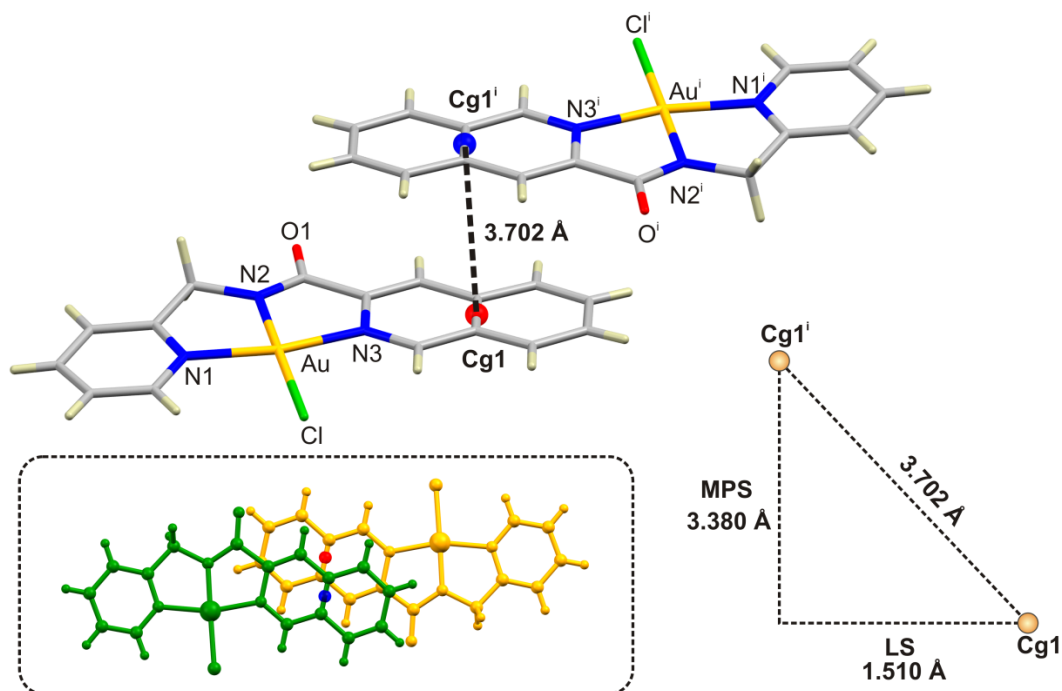


Figure 5.4.8: Partially labeled view of the centrosymmetric π -stacked dimer formed by $[\text{Au}(\text{L7})\text{Cl}](\text{PF}_6)$. The isoquinoline ring planes are parallel; the distance between the isoquinoline ring centers of gravity ($\text{Cg1}\cdots\text{Cg1}^i$) is indicated. The mean plane separation (MPS) and lateral shift (LS) of the stacked isoquinoline rings (calculated from the coordinates of Cg1 and Cg1^i) are depicted graphically on the triangle to the right of the top-down view of the dimer (lower left).

X-ray Crystallography

Table 5.4.5: Hydrogen bond distances and angles for compounds [Au(L5)Cl](PF₆)-[Au(L7)Cl](PF₆).

Donor-H...A	D-H/Å	H...A/Å	D...A/Å	D-H...A/°
[Au(L5)Cl](PF₆)				
C1-H1...Cl ⁱ	0.95	2.75	3.503(6)	137
C2-H2...F3 ⁱⁱ	0.95	2.52	3.293(8)	139
C9-H9...F2 ⁱⁱⁱ	0.95	2.44	3.344(7)	159
C10-H10...O1 ^{vi}	0.95	2.38	2.993(8)	122
C11-H11...O1 ^v	0.95	2.52	3.186(8)	116
C12-H12...F1 ^v	0.95	2.44	3.238(8)	141
C1-H1...Cl1 (intramol.)	0.95	2.78	3.365(7)	121
C12-H12...Cl1 (intramol.)	0.95	2.76	3.331(7)	119
Symmetry codes: (i) -x,-y,-z; (ii) -1+x,1/2-y,-1/2+z; (iii) 1+x,y,z; (vi) 2-x,-1/2+y,1/2-z, (v) 1-x,-1/2+y,1/2-z				
[Au(L6)Cl](PF₆)				
C2-H2...F1 ⁱ	0.95	2.38	3.332(9)	176
C11-H11...O1 ⁱⁱ	0.95	2.55	3.357(8)	143
C12-H12...F5 ⁱⁱⁱ	0.95	2.49	3.428(9)	170
C16-H16...F1 ^{vi}	0.95	2.35	3.208(8)	149
C1-H1...Cl (intramol.)	0.95	2.71	3.299(7)	121
C2-H2...F1 (intramol.)	0.95	2.27	2.916(9)	125
C2-H2...F1 (intramol.)	0.95	2.74	3.347(7)	122
Symmetry codes: (i) -1+x,y,z; (ii) 2-x,1-y,1-z; (iii) 1+x,1+y,z; (vi) 1-x,1-y,-z				
[Au(L7)Cl](PF₆)				
C14-H14...F2 ⁱ	0.95	2.32	3.209(9)	155
C13-H13...Cl1 ⁱⁱ	0.95	2.83	3.595(8)	139
C12-H12...F5 ⁱⁱⁱ	0.95	2.52	3.365(10)	148
C11-H11...O1 ^{iv}	0.95	2.55	3.314(9)	137
C9-H9...O1 ^{iv}	0.95	2.37	3.186(8)	143
C4-H4...F1 ^v	0.95	2.40	3.340(10)	169
C1-H1...Cl1 (intramol.)	0.95	2.78	3.366(8)	121
C16-H16...Cl1 (intramol.)	0.95	2.80	3.363(6)	119
Symmetry codes: (i) 1+x,y,z; (ii) 5/2-x,-1/2+y,1/2-z; (iii) 3/2-x,-1/2+y,1/2-z; (iv) 1-x,-y,1-z, (v) -1/2+x,1/2-y,1/2+z				

X-ray Crystallography

Table 5.4.6: Crystal Structure, X-ray Data, and Structure Model Refinement Parameters for and [Au(L5)Cl](PF₆)-[Au(L7)Cl](PF₆).^a

	[Au(L5)Cl](PF ₆)	[Au(L6)Cl](PF ₆)	[Au(L7)Cl](PF ₆)
Chemical formula	C ₁₂ H ₁₀ AuClN ₃ OPF ₆	C ₁₆ H ₁₂ AuClN ₃ OPF ₆	C ₁₆ H ₁₂ AuClN ₃ OPF ₆
<i>M_r</i>	589.62	551.18	639.70
Crystal system, SG	Monoclinic, <i>P</i> 2 ₁ / <i>c</i>	Triclinic, <i>P</i> -1	Monoclinic, <i>P</i> 2 ₁ / <i>n</i>
Temperature (K)	120 (2)	120 (2)	120 (1)
<i>a</i> , <i>b</i> , <i>c</i> (Å)	7.7103 (2), 13.3343 (4), 15.4971 (4)	6.8147 (1), 11.5824 (3), 12.0731 (3)	7.0730 (5), 18.4770(5), 14.3450 (5)
α , β , γ (°)	90, 100.897 (3), 90	67.202(2), 78.352 (2), 83.432(2)	90, 95.550 (5), 90
<i>V</i> (Å ³)	1564.44 (20)	859.71 (23)	1821.52(7)
<i>Z</i>	4	2	4
Radiation type	Mo <i>K</i> α	Mo <i>K</i> α	Mo <i>K</i> α
μ (mm ⁻¹)	9.75	8.88	8.185
Crystal size (mm)	0.2 × 0.15 × 0.10	0.40 × 0.20 × 0.10	0.20 × 0.20 × 0.20
Abs. correction	Multi-scan	Multi-scan	Multi-scan
<i>T_{min}</i> , <i>T_{max}</i>	0.437, 1.000	0.125, 0.470	0.291, 0.291
<i>N_m</i> , <i>N_i</i> , <i>N_o</i>	7042, 3546, 2808	8768, 5285, 4803	18077, 5787, 4425
<i>R_{int}</i>	0.044	0.041	0.038
<i>R₁</i> , <i>wR(F²)</i> , <i>S</i>	0.031, 0.075, 0.96	0.050, 0.131, 1.008	0.047, 0.132, 1.064
<i>N_p</i> , <i>N_{res}</i>	226, 5	262, 2	262, 1
$\Delta\rho_{\max}$, $\Delta\rho_{\min}$ (e Å ⁻³)	1.94, -1.72	11.67, -3.52	9.31, -2.99

^aAbbreviations: SG, space group; *V*, volume; *Z*; number of formula units per unit cell; μ , absorption coefficient; *T*, transmission coefficient; *N_m*, number of measured reflections, *N_i*, number of independent reflections; *N_o*, number of observed reflections with *I* > 2σ(*I*); *I*, intensity; *R_{int}*, internal *R*-factor for data set (based on the intensity match between symmetry equivalent reflections); *R₁* = *R*[*F*² > 2σ(*F*²)]; *wR(F²)*, weighted *R*-factor based on *F*²; *F*, structure factor; *S*, goodness-of-fit of model to experimental data; *N_p*, number of parameters, *N_{res}*, number of restraints; Δ*ρ*, electron density difference.

X-ray Crystallography

MOLECULAR STRUCTURES [Au(L8)Cl](PF₆)-[Au(L15)Cl](PF₆):

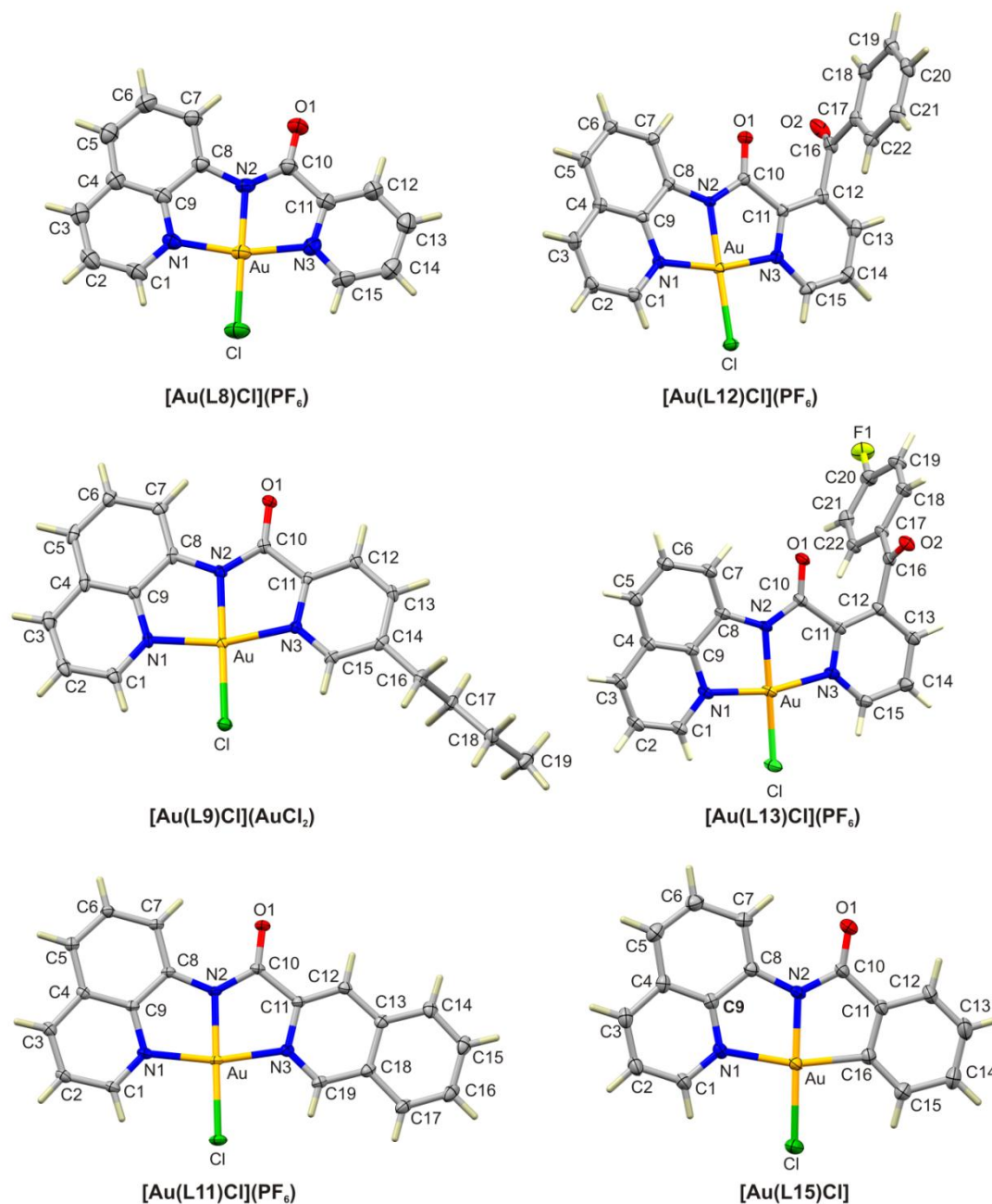


Figure: 5.4.9: Labelled views of the single crystal X-ray structures of gold(III) compounds [Au(L8)Cl](PF₆), [Au(L9)Cl](AuCl₂), [Au(L11)Cl](PF₆)-[Au(L13)Cl](PF₆) and [Au(L15)Cl]. Hydrogen atoms are rendered as sticks and bonds are represented as cylinders. Thermal ellipsoids are represented as 50% probability surfaces.

The X-ray structures of [Au(L8)Cl](PF₆), [Au(L9)Cl](AuCl₂), [Au(L11)Cl](PF₆)-[Au(L13)Cl](PF₆) and [Au(L15)Cl] are shown in Figure 5.4.9. The gold(III) ion is again nominally square planar in each complex with the gold(III) ion co-ordinated by the three N-donor atoms of the chelating ligand for complexes [Au(L8)Cl](PF₆), [Au(L9)Cl](AuCl₂), [Au(L11)Cl](PF₆)-[Au(L13)Cl](PF₆), while complex [Au(L15)Cl] comprises a NN'C donor series used to chelate

X-ray Crystallography

the gold(III) ion, followed by a chloride ion co-ordinated to the fourth co-ordination site, *trans* to the amido chelating moiety, to complete the geometry. All six compounds contain a 8-aminoquinolamide chelating moiety along with either a pyridine (unsubstituted for [Au(L8)Cl](PF₆); substituted for [Au(L9)Cl](AuCl₂), [Au(L12)Cl](PF₆) and [Au(L13)Cl](PF₆), isoquinoline ([Au(L11)Cl](PF₆) or benzene ([Au(L15)Cl]) moiety as the structural variation within the series. Deviation for individual atoms from a mean plane incorporating chelating moieties and the co-ordination sphere are minimal for all six compounds. The mean deviation for all atoms from the respective mean planes for compounds [Au(L8)Cl]PF₆, [Au(L9)Cl](AuCl₂), [Au(L11)Cl](PF₆)–[Au(L13)Cl](PF₆) and [Au(L15)Cl] is 0.03(3) Å which is less than that for compounds [Au(L5)Cl](PF₆)–[Au(L7)Cl](PF₆) (0.06(5) Å), while the largest single atom deviation from the respective mean planes for compounds [Au(L8)Cl](PF₆), [Au(L9)Cl](AuCl₂), [Au(L11)Cl](PF₆)–[Au(L13)Cl](PF₆) and [Au(L15)Cl] is 0.161 Å for atom Cl of compound [Au(L13)Cl](PF₆). This probably reflects the more rigid ligand system incorporating the 8-aminoquinoline moiety as opposed to the aminomethyl pyridine moiety which includes a flexible methylene structural motif. The structural variation between compounds seems to impart minimal effect on the overall planarity as well as co-ordination geometry of the gold(III) ion in each of the six compounds (Table 5.4.7), particularly considering the fact that [Au(L9)Cl](AuCl₂), [Au(L12)Cl](PF₆) and [Au(L13)Cl](PF₆) contain bulky substituted pyridine rings and [Au(L15)Cl] contains the markedly more powerful C₆H₅⁻ σ-donor group. This again was to be expected as the structural derivatives incorporating pyridine or substituted pyridine, 3-isoquinoline or benzene amide moieties were specifically chosen so that minimal steric effects between the co-ordinated chloride ion and adjacent protons associated with said heterocyclic N-donor chelate rings would be encountered as would be envisaged for a ligand incorporating a quinoline amide moiety. The pK_a of pyridine (5.2) and isoquinoline (5.5) are similar (*vide supra*) and are therefore not expected to impart any significant difference between gold(III)–8-aminoquinoline (Au–N_{8AMQ}) and gold(III)–pyridine or isoquinoline (Au–N_{Py/IQ}) bond lengths, particularly for [Au(L11)Cl](PF₆) which contains two N_{quinoline} donor atoms within the ligand scaffold. Compound [Au(L15)Cl] is co-ordinated via the deprotonated *ortho* carbon (C_{Bz}) of the benzene ring which is a powerful σ-donor atom, therefore it would then be expected that co-ordination metrics for [Au(L15)Cl] may differ quite significantly from the balance of the mean co-ordination metrics for the NN'N'' donor compounds discussed herein.

X-ray Crystallography

Table 5.4.7: Selected Crystallographic Bond Distances and Bond Angles for [Au(L8)Cl](PF₆), [Au(L9)Cl]AuCl₂, [Au(L11)Cl](PF₆)-[Au(L13)Cl](PF₆) and [Au(L15)Cl].

	[Au(L8)Cl](PF ₆)	[Au(L9)Cl](AuCl ₂)	[Au(L11)Cl](PF ₆)	[Au(L12)Cl](PF ₆)	[Au(L13)Cl](PF ₆)	[Au(L15)Cl]
Bond distances (Å)						
Au1–N1	2.001(4)	2.021(4)	2.010(2)	2.005(2)	2.005(3)	2.116(4)
Au1–N2	1.969(4)	1.975(4)	1.969(2)	1.971(3)	1.971(3)	1.970(4)
Au1–N3 ^a	2.024(4)	2.021(5)	2.013(2)	2.022(2)	2.013(3)	2.017(4)
Au1–Cl1	2.283(1)	2.272(1)	2.282(5)	2.283(1)	2.278(1)	2.290(2)
C=O	1.220(6)	1.223(6)	1.223(3)	1.225(5)	1.224(4)	1.221(6)
N–C	1.340(6)	1.354(7)	1.364(3)	1.352(4)	1.353(5)	1.356(5)
Bond angles (°)						
N1–Au1–N2	83.2(2)	83.0(2)	83.0(1)	83.1(1)	83.1(4)	81.7(1)
N2–Au1–N3 ^a	81.9(2)	82.3(2)	83.0(1)	83.1(1)	82.1(3)	82.6(2)
N3–Au1–Cl1 ^a	97.6(1)	97.7(1)	96.4(1)	96.3(1)	97.6(1)	96.5(1)
Cl1–Au1–N1	97.3(1)	96.9(1)	97.4(1)	97.4(1)	96.8(1)	99.2(1)
N1–C9–C8	117.8(5)	117.8(5)	118.1(2)	117.9(2)	117.6(3)	117.8(3)
C9–C8–N2	113.3(4)	114.4(5)	114.1(2)	114.1(2)	114.7(3)	115.0(3)
N2–C10–C11	111.9(4)	112.0(4)	112.6(2)	112.2(2)	112.0(3)	110.5(4)
C7–C8–N3 ^a	117.0(4)	117.0(5)	116.5(2)	116.3(2)	116.3(3)	118.4(4)

^aFor [Au(L15)Cl] atom N3 is replaced by atom C16.

X-ray Crystallography

The mean $N_{8AMQ}-Au$ and $N_{Py/IQ}-Au$ distances for the NN'N'' compounds are 2.008(7) Å and 2.018(5) Å, respectively, which are statistically alike and indicative of their similar σ -donor/ π -acceptor ability despite their structural dissimilarity. The mean $N_{8AMQ}-Au$ distance for the NN'N'' compounds in this work is slightly shorter than for those reported for similar 8-aminoquinoline based gold(III) compounds, $[Au(Quingly)Cl]Cl$ (2.027(6) Å, where Quingly = 2-amino-N-(quinolin-8-yl)acetamide) and $[Au(Quinala)Cl]Cl$ (2.02(4) Å, where Quinala = 2-amino-N-(quinolin-8-yl)propanamide) while the $N_{Py/IQ}-Au$ distance for the NN'N'' compounds compares well to the $N_{8AMQ}-Au$ distances for the reported compounds.⁵ The primary amine–Au ($N_{PA}-Au$) distances for reported compounds $[Au(Quingly)Cl]Cl$ and $[Au(Quinala)Cl]Cl$ (2.024(6) and 1.98(3) Å, respectively) differ from the N–Au distances reported for the NN'N'' compounds in this work.⁵ This may be expected since primary amine donor atoms are sp^3 hybridised as opposed to sp^2 , and are weaker Lewis bases than the pyridine quinoline and amido donor groups in this work. The $C_{Bz}-Au$ distance (2.017(4) Å) for compound $[Au(L15)Cl]$ is equivalent to the mean $N_{Py/IQ}-Au$ distance and slightly longer than the mean $N_{8AMQ}-Au$ distance for compounds $[Au(L8)Cl](PF_6)-[Au(L9)Cl](AuCl_2)$ and $[Au(L11)Cl](PF_6)-[Au(L13)Cl](PF_6)$. This is not unexpected as the $C_6H_5^-$ donor group is a strong σ -donor (Lewis base) and therefore the $C_{Bz}-Au$ bond length is expected to be shorter than that of an N–Au bond length. However the ionic radius for carbon is larger than that for nitrogen. Both these facts would account for the similar $C_{Bz}-Au$, $N_{Py/IQ}-Au$ and $N_{8AMQ}-Au$ bond lengths. The powerful σ -donor ability of the $C_6H_5^-$ donor group is manifest through a *trans* effect seen in the $N_{8AMQ}-Au$ bond length (2.116(4) Å), nearly 27 standard deviations longer than the average $N_{8AMQ}-Au$ bond length for the NN'N'' compounds. Similar C–Au and N–Au bond lengths have been observed for NN'C cyclometallated gold(III) complexes of 6-benzyl- and 6-alkyl-2,2'-bipyridines involving two five membered chelate rings.²⁶ The average $Au-N_{amide}$ amide bond distance for all six compounds measures 1.970(2) Å, which is significantly shorter than the corresponding $Au-N_{Py/IQ}$ (24(σ)) or $Au-N_{8AMQ}$ (19(σ)) distances despite their similar hybridisation (sp^2). This renders the $Au-N_{amide}$ and $Au-N_{Py/IQ}/Au-N_{8AMQ}$ co-ordination interactions chemically and crystallographically distinct from each other, as was the case for all compounds discussed above. This effect, once again, arises from the fact that the anionic amido nitrogen is a significantly stronger σ -donor (Lewis base) than the corresponding heterocyclic nitrogen atoms. This is similarly observed for gold(III) amide compounds $[Au(Quingly)Cl]Cl$ and $[Au(Quinala)Cl]Cl$.⁵ The $Au-Cl1$ bond distance for

X-ray Crystallography

compounds $[\text{Au}(\text{L8})\text{Cl}](\text{PF}_6)$ – $[\text{Au}(\text{L9})\text{Cl}](\text{AuCl}_2)$, $[\text{Au}(\text{L11})\text{Cl}](\text{PF}_6)$ – $[\text{Au}(\text{L13})\text{Cl}](\text{PF}_6)$ and $[\text{Au}(\text{L15})\text{Cl}]$ average 2.281(5) Å, closely matching the Au–Cl bond lengths observed *trans* to the N_{amido} atom for the rest of the compounds reported in this work, once again, indicating a significant “*trans* effect”¹⁵. This is similarly observed for the 8-aminoquinoline based gold(III) compounds $[\text{Au}(\text{Quingly})\text{Cl}]\text{Cl}$ and $[\text{Au}(\text{Quinala})\text{Cl}]\text{Cl}$ where the mean Au–Cl bond distance is similarly 2.277(1) Å. The average C8–N2 bond length, 1.41(1) Å, is longer, 6(σ), than the N2–C10 bond length at 1.353(7) Å. This suggests that the lone pair of electrons associated with N2 is partially delocalised over the N2–C7 bond, increasing its bond order and subsequently allowing for the shorter length observed. These structural parameters are highlighted for the similar gold(III) complexes, $[\text{Au}(\text{Quingly})\text{Cl}]\text{Cl}$ and $[\text{Au}(\text{Quinala})\text{Cl}]\text{Cl}$, where the C8–N2 and N2–C10 equivalent bond lengths are 1.339(9), 1.39(4) Å and 1.431(9), 1.40(4) Å respectively.⁵

The bond angles (Table 5.4.7) subtended at the metal ion in $[\text{Au}(\text{L8})\text{Cl}](\text{PF}_6)$, $[\text{Au}(\text{L9})\text{Cl}](\text{AuCl}_2)$, $[\text{Au}(\text{L11})\text{Cl}](\text{PF}_6)$ – $[\text{Au}(\text{L13})\text{Cl}](\text{PF}_6)$ are normal for five-membered ring compounds of gold(III) with three N-donor atoms while the angles for $[\text{Au}(\text{L15})\text{Cl}]$ are normal for five-membered gold(III) compounds containing NNC-donor ligands. For compounds $[\text{Au}(\text{L8})\text{Cl}](\text{PF}_6)$, $[\text{Au}(\text{L9})\text{Cl}](\text{AuCl}_2)$, $[\text{Au}(\text{L11})\text{Cl}](\text{PF}_6)$ – $[\text{Au}(\text{L13})\text{Cl}](\text{PF}_6)$ the mean N–Au–Cl bond angle, 97.1(5)°, is fairly obtuse, while the mean N–Au–N angle is quite acute, measuring 82.7(4). Compound $[\text{Au}(\text{L15})\text{Cl}]$ contains the strong σ -donor, C_6H_5^- moiety, which imparts a significant *trans* effect and hence a lengthening of the N1–Au bond length (*vide supra*). This bond lengthening in turn forces a decrease in the N1–Au–N2 bond angle to 81.7(1)° compared to the average 82.7(4)° and an increase in the Cl1–Au–N1 bond angle to 99.2(1)° compared to the average 97.1(5)° for the NN'N'' donor compounds. Both angles deviate significantly from 90°, clearly reflecting the geometric constraints on metal ion coordination imposed by the two five-membered chelate rings for the six complexes. The metrics of the co-ordination geometries for $[\text{Au}(\text{L8})\text{Cl}](\text{PF}_6)$, $[\text{Au}(\text{L9})\text{Cl}](\text{AuCl}_2)$, $[\text{Au}(\text{L11})\text{Cl}](\text{PF}_6)$ – $[\text{Au}(\text{L13})\text{Cl}](\text{PF}_6)$ compare favourably with the mean N–Au–Cl and N–Au–N angles observed for other gold(III) complexes comprising five-membered chelate rings with three N-donor atoms, such as $[\text{Au}(\text{terpy})\text{Cl}]\text{Cl}_2 \cdot 3\text{H}_2\text{O}$ (N–Au–Cl, 98.6(1)°; N–Au–N, 81.4(1)°). The N_{amido} –Au distances for compounds $[\text{Au}(\text{L8})\text{Cl}](\text{PF}_6)$ – $[\text{Au}(\text{L15})\text{Cl}](\text{PF}_6)$ (1.970(2) Å) are similar to compounds $[\text{Au}(\text{L5})\text{Cl}](\text{PF}_6)$ – $[\text{Au}(\text{L7})\text{Cl}](\text{PF}_6)$ (1.91(2) Å) as well as the N_{py} –Au

X-ray Crystallography

distances for $[\text{Au}(\text{terpy})\text{Cl}]\text{Cl}_2 \cdot 3\text{H}_2\text{O}$ (1.950(3) Å).^{24, 25} This is despite the more powerful σ -donor ability of a N_{amido} moiety compared to that of an N_{py} moiety. The reason for this is the well-known fact that the bridgehead atom-to-metal (metal = gold(III) or platinum(II)) distance (in terpyridine-based metal compounds) is significantly shortened compared with the rest of the metal-N distances of the co-ordination sphere. The co-ordination geometry for $[\text{Au}(\text{L15})\text{Cl}]$ compares well with the 6-substituted bipyridine complex, $[\text{Au}\{\text{N}_2\text{C}_{10}\text{H}_7(\text{CMe}_2\text{CH}_2)\text{-6}\}\text{-Cl}][\text{BF}_4] \cdot 5\text{H}_2\text{O}$ ²⁷ (where $\{\text{N}_2\text{C}_{10}\text{H}_7(\text{CMe}_2\text{CH}_2)\text{-6}\}$ = 6-tert-butyl-2,2'-bipyridine), a similar NN'C donor gold(III) compound comprising two five-membered chelate rings, with a similar decrease and increase in N1-Au-N2 and Cl1-Au-N1 bond angles respectively. The deviations are more pronounced for $[\text{Au}\{\text{N}_2\text{C}_{10}\text{H}_7(\text{CMe}_2\text{CH}_2)\text{-6}\}\text{-Cl}][\text{BF}_4] \cdot 5\text{H}_2\text{O}$.²⁷ This may be due to the different C-donor moieties, $[\text{Au}(\text{L15})\text{Cl}]$ contains a C_6H_5^- donor while $[\text{Au}\{\text{N}_2\text{C}_{10}\text{H}_7(\text{CMe}_2\text{CH}_2)\text{-6}\}\text{-Cl}][\text{BF}_4] \cdot 5\text{H}_2\text{O}$ contains a CH_2^- donor moiety. The latter is sterically unencumbered and flexible allowing a closer approach of the C-donor atom to the gold(III) centre and evidently a further elongation of the *trans* N1-Au bond. As a result the mentioned decrease and increase in N1-Au-N2 and Cl1-Au-N1 bond angles is observed.

Only compounds $[\text{Au}(\text{L9})\text{Cl}](\text{AuCl}_2)$, $[\text{Au}(\text{L12})\text{Cl}](\text{PF}_6)$ and $[\text{Au}(\text{L13})\text{Cl}](\text{PF}_6)$ contain substituent groups capable of conformational/rotational freedom that are not part of the mean plane chelating moiety capable of conformational freedom. Compound $[\text{Au}(\text{L9})\text{Cl}](\text{AuCl}_2)$ contains a *para* butyl-substituted pyridine ring (Figure 5.4.9). The butyl chain adopts a staircase motif akin with that of the similar nonyl chain present in the compound $\text{AuCl}_2(\text{N-NP2C})$ discussed above. Compounds $[\text{Au}(\text{L12})\text{Cl}](\text{PF}_6)$ and $[\text{Au}(\text{L13})\text{Cl}](\text{PF}_6)$ contain phenyl ketone moieties substituted in the *ortho* position of the chelating pyridine ring. In solution the phenyl ketone ring has free rotation around atom C12 while the phenyl motif has additional free rotation around atom C17. In the solid state the phenyl ketone moiety has to adopt a 'ring up' or 'ring down' conformation with respect to the main body of the complex. This conformation evidently arises through differences in crystal packing energies as the rings in both complexes adopt different orientations; complex $[\text{Au}(\text{L12})\text{Cl}](\text{PF}_6)$ adopts the 'ring up' orientation while complex $[\text{Au}(\text{L13})\text{Cl}](\text{PF}_6)$ adopts the 'ring down' orientation (this statement is with reference to the 8-aminoquinoline moiety being positioned on the left when viewing from above). The angle between the phenyl ketone moiety and the main

chelating body of each complex is near perpendicular at 86.9° and 85.5° for $[\text{Au}(\text{L12})\text{Cl}](\text{PF}_6)$ and $[\text{Au}(\text{L13})\text{Cl}](\text{PF}_6)$, respectively. The phenyl ring is almost co-planar with the amide group for $[\text{Au}(\text{L12})\text{Cl}](\text{PF}_6)$ with the $\text{C12}-\text{C16}-\text{C17}-\text{C18}$ dihedral angle measuring $1.5(6)^\circ$, while for $[\text{Au}(\text{L13})\text{Cl}](\text{PF}_6)$ the 4-fluorophenyl ring is slightly out of plane to the amide group with a $\text{C12}-\text{C16}-\text{C17}-\text{C18}$ dihedral angle of $19.0(6)^\circ$.

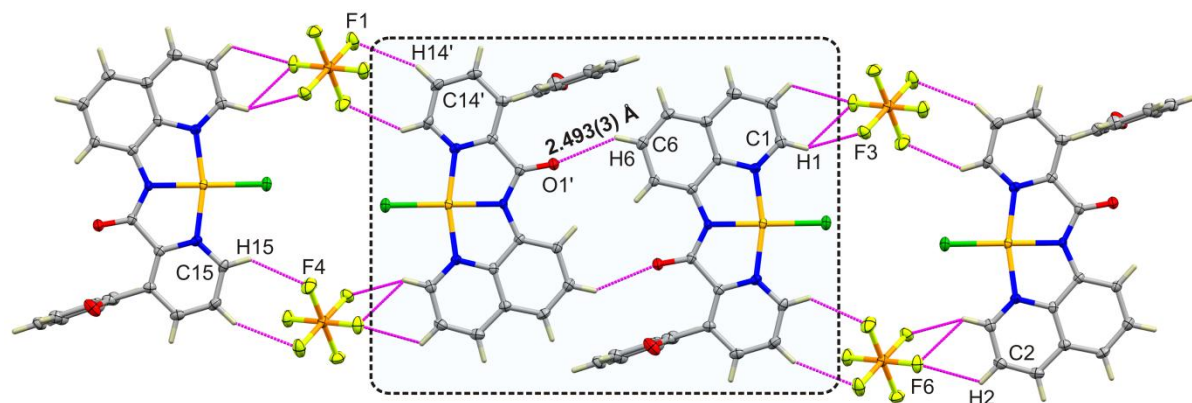


Figure 5.4.10: Partially labelled view of a discrete unconventionally hydrogen-bonded centrosymmetric dimer of $[\text{Au}(\text{L12})\text{Cl}](\text{PF}_6)$. Hydrogen atoms are represented as sticks; all other atoms are represented as thermal ellipsoids (50% probability). The dimer is stabilised by $\text{C}-\text{H}\cdots\text{O}$ hydrogen bonds: $\text{H6}\cdots\text{O1}^i$, 2.49 Å; $\text{C6}\cdots\text{O1}^i$, 3.318(5) Å; $\text{C6}-\text{H6}\cdots\text{O1}^i$, 145° . Crystallographic symmetry code: (i) $1-x, 1-y, -z$.

Consistent with the structural data for the compounds discussed earlier, compounds $[\text{Au}(\text{L8})\text{Cl}](\text{PF}_6)-[\text{Au}(\text{L15})\text{Cl}](\text{PF}_6)$ contain no traditional hydrogen bond donors due to the N-H donor being lost upon chelation of the ligand to the gold(III) centre. The short contact interactions within the crystal lattice for all compounds are therefore dominated by unconventional $\text{C}-\text{H}\cdots\text{O}$, $\text{C}-\text{H}\cdots\text{Cl}$ and $\text{C}-\text{H}\cdots\text{F}$ hydrogen bonding as was the case for $[\text{Au}(\text{L5})\text{Cl}](\text{PF}_6)-[\text{Au}(\text{L7})\text{Cl}](\text{PF}_6)$. The supramolecular structures of $[\text{Au}(\text{L8})\text{Cl}](\text{PF}_6)$, $[\text{Au}(\text{L9})\text{Cl}](\text{AuCl}_2)$ and $[\text{Au}(\text{L11})\text{Cl}](\text{PF}_6)-[\text{Au}(\text{L13})\text{Cl}](\text{PF}_6)$ are again similarly dominated by centrosymmetric unconventionally hydrogen-bonded dimers. The centrosymmetric dimers for compounds $[\text{Au}(\text{L8})\text{Cl}](\text{PF}_6)$, $[\text{Au}(\text{L9})\text{Cl}](\text{AuCl}_2)$ and $[\text{Au}(\text{L12})\text{Cl}](\text{PF}_6)$ are linked via unconventional hydrogen bonds that are restricted to single $\text{C}-\text{H}\cdots\text{O}$ interactions between individual molecules of each dimer and are not extended continuously through the lattice (Figure 5.4.10). For compound $[\text{Au}(\text{L8})\text{Cl}](\text{PF}_6)$, the individual dimers are linked to each other in three dimensions via PF_6^- anions to form the extended structure observed in the lattice. For compound $[\text{Au}(\text{L9})\text{Cl}](\text{AuCl}_2)$ the individual dimers are successively linked to neighbouring molecules above and below in a staircase fashion via $\text{C}-\text{H}\cdots\text{Cl}$ unconventional

hydrogen bonds and C–Cl short contact interactions associated with the AuCl₂ counterions. Individual dimers for [Au(L12)Cl](PF₆) are linked to each other via PF₆[−] anions to form discrete 1D linear chains. These chains are then interconnected to similar chains above and below via strong N–O (2.887(5) Å) short contact interactions. The extended structures for compounds [Au(L11)Cl](PF₆) and [Au(L13)Cl](PF₆) similarly revolve around centrosymmetric dimers linked via unconventional hydrogen bonds, however the distinction between the C–H···O unconventional hydrogen bonds between dimers for these compounds compared to [Au(L8)Cl](PF₆), [Au(L9)Cl](AuCl₂) and [Au(L12)Cl](PF₆) is that they are three-centred, bifurcated hydrogen bonds which form a 1D hydrogen-bonded polymer. For compound [Au(L9)Cl](AuCl₂), the hydrogen bond acceptor is atom O1 while the donor atoms are H6 and H7, full metrics of the interactions are available in Table 5.4.8. The 3D extended structure consists of C–H···O, C–H···F and C–H···Cl unconventional hydrogen bonds as well as C–C and C–Cl short contact interactions between PF₆[−] anions, MeNO₂ solvent molecules and cations.

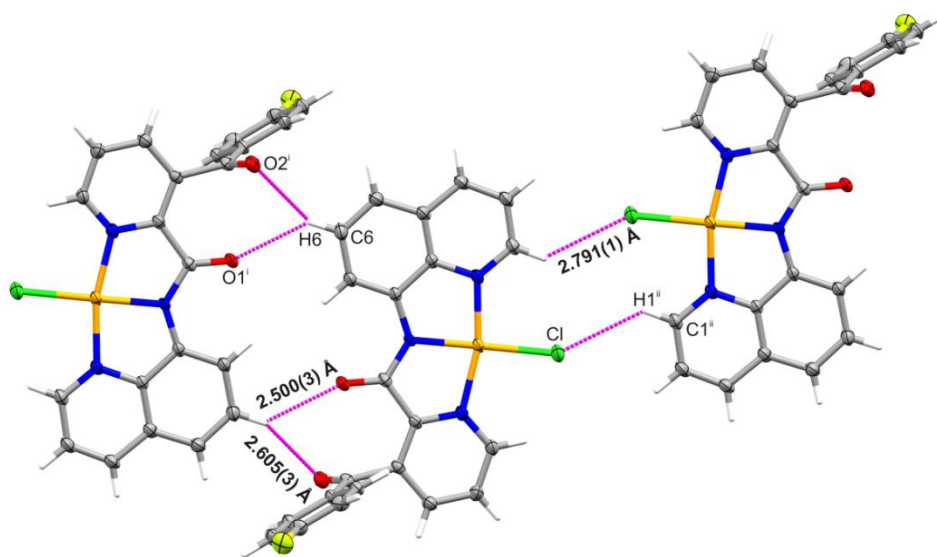


Figure 5.4.11: Partially labelled view of both types of unconventionally hydrogen bonded centrosymmetric dimers of [Au(L12)Cl](PF₆). Hydrogen atoms are represented as sticks; all other atoms are represented as thermal ellipsoids (50% probability). The dimer on the left is stabilised by bifurcated C–H···O hydrogen bonds: H6···O1ⁱ, 2.50 Å; C6···O1ⁱ, 3.240(5) Å; C6–H6···O1ⁱ, 135°; H6···O2ⁱ, 2.60 Å; C6···O2ⁱ, 3.443(5) Å; C6–H6···O2ⁱ, 147°. Crystallographic symmetry code: (i) -x,-y,-z. The dimer on the right is stabilized by C–H···Cl hydrogen bonds: H1···Clⁱⁱ, 2.79 Å; C1···Clⁱⁱ, 3.516(4) Å; C6–H6···O1ⁱⁱ, 134°. Crystallographic symmetry code: (ii) 2-x,1-y,-z.

The extended structure of compound [Au(L13)Cl](PF₆) (Figure 5.4.11) comprises discrete infinite chains containing alternating centrosymmetric dimers linked via bifurcated C–H···O

and C–H···Cl unconventional hydrogen bonds (metrics of the bonds can be found in Table 5.4.8.) so that each individual molecule is simultaneously part of each type of cation pair (Figure 5.4.11). Compound [Au(L15)Cl] contains no appreciable (less than the sum of the van der Waals radii) short contact or hydrogen bond interactions.

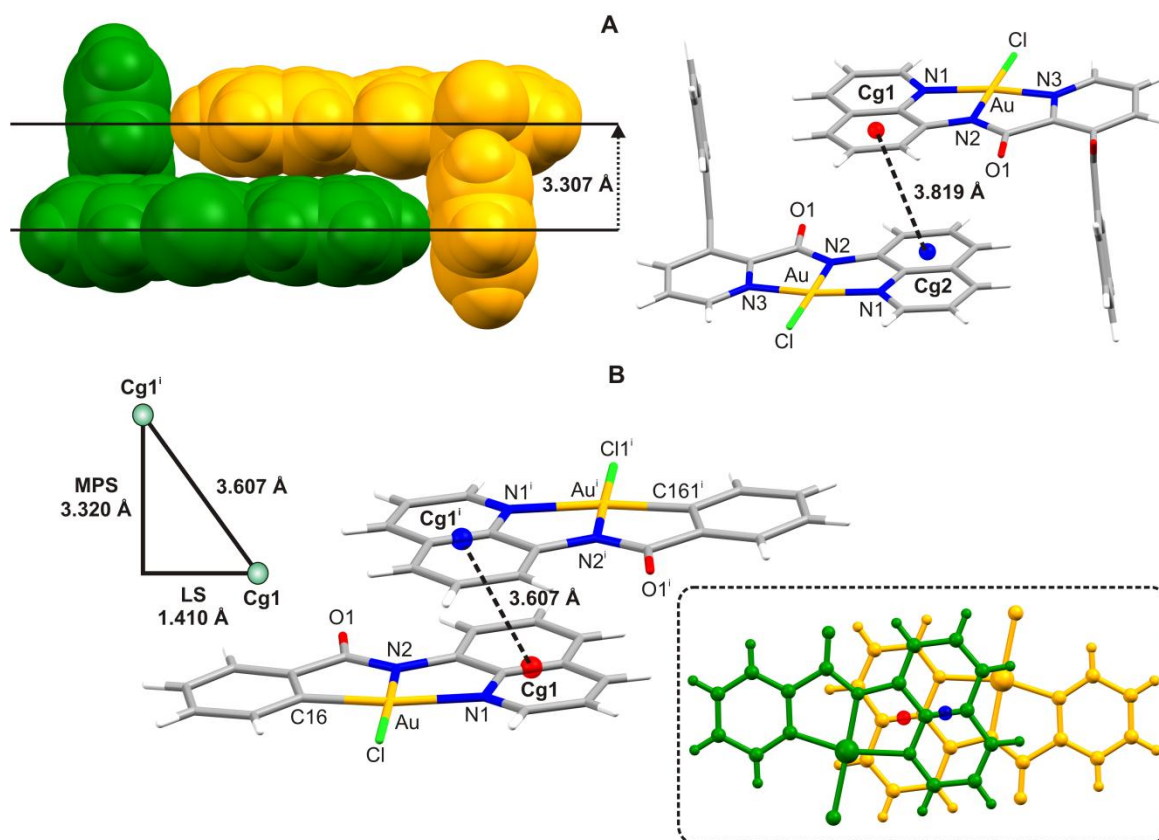


Figure 5.4.12: A: Spacefill (left) and stick (right) representation of the centrosymmetric π -stacked dimer between two quinoline rings in compound [Au(L12)Cl](PF₆). The metrics of the interaction are as follows: Cg1···Cg2, 3.819 Å; MPS, 3.307 Å; LS, 1.911. B: Partially labelled view of the centrosymmetric π -stacked dimer formed by [Au(L15)Cl]. The metrics of the interaction are depicted in the triangle inset on the left hand side while the inset on the right displays the interaction from a point of view perpendicular to a mean plane through an isoquinoline ring

Several π -stacking interactions are also prevalent for all compounds bar [Au(L8)Cl](PF₆); these span lateral shift (LS) and mean plane separation (MPS) values of 0.88–1.92 Å and 3.26–3.42 Å, respectively, and involve both the free- and Au-bound pyridine rings. For compound [Au(L12)Cl](PF₆), the most prominent π - π interaction occurs between the phenyl rings of neighbouring isoquinoline moieties. The interaction forms the basis of a π -stacked centrosymmetric dimer similar to that seen for compound [Au(HL3)Cl]₂. In the case of [Au(L12)Cl](PF₆), however, the dimer is not further stabilised by unconventional hydrogen

bond interactions as for $[\text{Au}(\text{HL3})\text{Cl}_2]$. The interaction is such that each individual L-shaped molecule of $[\text{Au}(\text{L12})\text{Cl}](\text{PF}_6)$ interlocks via the π -stacking interaction with a neighbouring molecule to create the rectangle-shaped dimer seen in Figure 5.4.12 (Part A). Although the interacting rings do not contain any heteroatoms, a characteristic offset parallel geometry discussed by Janiak is observed.¹⁸ The interplanar spacing between rings is 3.307 Å, which is smaller than the 3.35-3.8 Å separation expected for such rings and indicates the interaction is particularly strong.¹⁹ The only intermolecular interaction of significance within the crystal lattice of compound $[\text{Au}(\text{L15})\text{Cl}]$ is a π - π interaction. It occurs between two exactly parallel quinoline rings of neighbouring molecules, once again, so that a centrosymmetric π -stacked dimer is formed. The interplanar spacing between rings is 3.320 Å which is also less than the typical MPS of 3.35-3.8 Å, and indicates, the interaction is particularly strong.¹⁹ The LS and centroid-centroid distances are represented in Figure 5.4.12 (Part B). The heteroaromatic rings display the characteristic offset antiparallel geometry discussed by Janiak so that the respective nitrogen atoms (N1) are pointing in opposite directions with respect to each other.¹⁸

The last intermolecular interaction that is noteworthy is that of an aurophilic interaction present for compound $[\text{Au}(\text{L9})\text{Cl}](\text{AuCl}_2)$. Aurophilic interactions between gold(III) cations are very rare.²⁸ This is evident through the absence of such interactions for all thirteen single crystal X-ray structures presented in this work. By far the most common Au-Au interactions occur between gold(I) ions, where the Au-Au bond distance and strength (3.0 Å and ca. 6-12 kcal, respectively) has been calculated and experimentally found to be similar to that of a common hydrogen bond.²⁹⁻³¹ There are also reports in the literature of aurophilic interactions between mixed oxidation state complex salts such as $[\text{Au}(\text{terpy})\text{Cl}]_2[\text{AuCl}_2]_3[\text{AuCl}_4]$.²⁵ Initial synthetic attempts for compound $[\text{Au}(\text{L9})\text{Cl}](\text{PF}_6)$ resulted in the linear AuCl_2 salt of the complex, $[\text{Au}(\text{L9})\text{Cl}](\text{AuCl}_2)$. Single crystal analysis revealed the presence of Au(I)-Au(III) aurophilic interactions. The interatomic distance between the two gold atoms is 3.277(1) Å which compares closely with the similar Au(I)-Au(III) aurophilic interaction (3.299(1) Å) present in the gold(III)terpy complex $[\text{Au}(\text{terpy})\text{Cl}]_2[\text{AuCl}_2]_3[\text{AuCl}_4]$.²⁵ The interaction is a centrosymmetric one with the gold(I) anion 'sandwiched' between two gold(III) cations (Figure 5.4.13 (Right)). The Au(I)-Au(III) interactions are discrete events restricted to individual 'sandwiches' and hence are not

extended throughout the lattice. When viewed from above, perpendicular to a plane comprising all atoms of the co-ordinating moiety, the Au atoms partially eclipse one another (Figure 5.4.13).

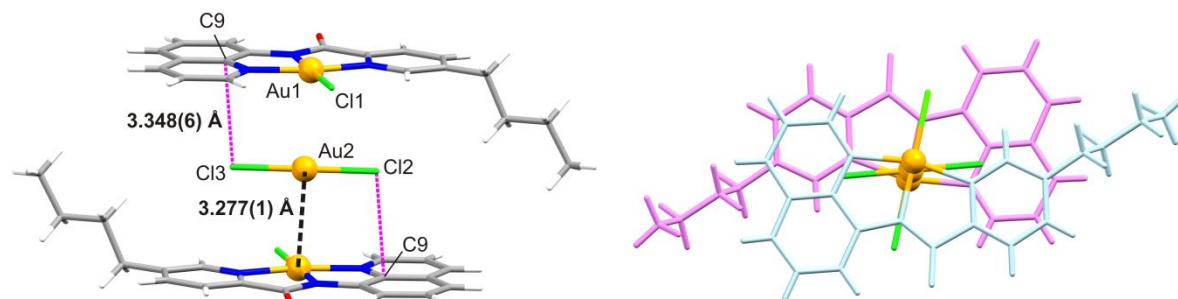


Figure 5.4.13: Centrosymmetric ‘sandwich’ structure observed for compound $[\text{Au}(\text{L9})\text{Cl}](\text{AuCl}_2)$ showing a linear gold(I) anion symmetrically sandwiched between two gold(III) cations (left). A top view of the ‘sandwich’ structure viewed perpendicular to a co-ordination motif mean plane.

The laterally-displaced ring systems seen in most compounds discussed would permit optimal π - π attraction between stacked isoquinoline, quinoline or pyridine groups in addition to normal van der Waals attraction and London forces of attraction. Isoquinoline and quinoline ring systems are, of course, well-known for their π -stacking ability and are often key pharmacophores prevalent in many anti-cancer,³² anti-viral,³³ and anti-malarial³⁴ compounds with a mechanism of action (MOA) involving DNA binding by intercalation.³⁵ Of special relevance to the present work, we note that the clinically-deployed anti-cancer drug camptothecin (a quinoline alkaloid) poisons human topoisomerase I (TOP1) by DNA intercalation at a 5'-TA-3' dinucleotide site targeted for covalent binding by the enzyme during its catalytic cycle.³⁶ In short, the isoquinoline, quinoline or pyridine rings of the compounds discussed are clearly potentially useful functional groups that may engage in interactions with biological targets such as DNA by π -stacking as well as hydrogen-bonding.

X-ray Crystallography

Table 5.4.8: Hydrogen bond distances and angles for compounds [Au(L8)Cl](PF₆), [Au(L9)Cl](AuCl₂), [Au(L11)Cl](PF₆)-[Au(L13)Cl](PF₆) and [Au(L15)Cl].

Donor-H...A	D-H/Å	H...A/Å	D...A/Å	D-H...A/°
[Au(L8)Cl](PF₆)				
C14-H14...F2 ⁱ	0.95	2.36	3.190(8)	145
C12-H12...F6 ⁱⁱ	0.95	2.52	3.300(7)	138
C7-H7...O1 ⁱⁱⁱ	0.95	2.55	3.186(7)	125
C1-H1...F2 ^{iv}	0.95	2.44	3.265(7)	145
C1-H1...Cl (intramol.)	0.95	2.80	3.372(6)	119
C8-H8...O1 (intramol.)	0.95	2.44	3.008(7)	119
C14-H14...Cl1 (intramol.)	0.95	2.79	3.354(6)	119
Symmetry codes: (i) -1+x,y,z; (ii) 1-x,1/2+y,1/2-z; (iii) 2-x,1-y,1-z; (iv) 1-x,-1/2+y,1/2-z				
[Au(L9)Cl](AuCl₂)				
C5-H5...Cl3 ⁱ	0.95	2.83	3.775(6)	175
C12-H12...O1 ⁱⁱ	0.95	2.36	3.216(7)	149
C1-H1...Cl (intramol.)	0.95	2.78	3.341(7)	119
C7-H7...O1 (intramol.)	0.95	2.43	3.002(7)	118
C15-H15...Cl1 (intramol.)	0.95	2.79	3.371(6)	120
Symmetry codes: (i) 1-x,1-y,-z; (ii) -1-x,-y,1-z				
[Au(L11)Cl](PF₆)				
C2-H2...F3 ⁱ	0.93	2.29	3.170(4)	158
C3-H3...F5 ⁱⁱ	0.93	2.45	2.908(5)	110
C3-H3...F1 ⁱⁱⁱ	0.93	2.51	3.304(4)	143
C6-H6...O1 ^{iv}	0.93	2.49	3.122(4)	125
C16-H16...Cl1 ^v	0.93	2.74	3.609(4)	156
C17-H17...F6 ^{vi}	0.93	2.48	3.247(4)	140
C1-H1...Cl1 (intramol.)	0.93	2.78	3.344(3)	120
C16-H16...Cl1 (intramol.)	0.93	2.43	2.991(4)	119
C19-H19...Cl1 (intramol.)	0.93	2.72	3.301(3)	122
Symmetry codes: (i) 1/2-x,1/2-y,1-z; (ii) 1/2-x,1/2+y,1/2-z; (iii) -1/2+x,1/2-y,-1/2+z; (iv) -x,-y,-z, (v) 1/2-x,1/2+y,1/2-z; (vi) x,-y,1/2+z				

X-ray Crystallography

Table 5.4.8 continued: Hydrogen bond distances and angles for compounds [Au(L8)Cl](PF₆), [Au(L9)Cl](AuCl₂), [Au(L11)Cl](PF₆)-[Au(L13)Cl](PF₆) and [Au(L15)Cl].

Donor-H...A	D-H/Å	H...A/Å	D...A/Å	D-H...A/°
[Au(L12)Cl](PF₆)				
C1-H1...F3 ⁱ	0.95	2.44	3.204(5)	137
C1-H1...F6 ⁱ	0.95	2.47	3.074(5)	121
C2-H2...F6 ⁱ	0.95	2.54	3.102(5)	118
C6-H6...O1 ⁱⁱ	0.95	2.49	3.318(5)	145
C14-H14...F1 ⁱⁱⁱ	0.95	2.54	3.432(5)	156
C14-H14...F3 ^{iv}	0.95	2.42	3.084(5)	126
C15-H15...F4 ⁱⁱⁱ	0.95	2.40	3.169(5)	138
C19-H19...F2 ^v	0.95	2.44	3.300(5)	151
C1-H1...Cl (intramol.)	0.95	2.77	3.340(4)	119
C7-H7...O1 (intramol.)	0.95	2.43	2.999(5)	119
C15-H15...Cl (intramol.)	0.95	2.79	3.358(4)	120
Symmetry codes: (i) -1+x,y,z; (ii) 1-x,1-y,-z; (iii) -x,1-y,1-z; (iv) 1-x,1-y,1-z, (v) 1+x,1+y,z				
[Au(L13)Cl](PF₆)				
C1-H1...Cl ⁱ	0.95	2.79	3.516(4)	134
C2-H2...F5 ⁱⁱ	0.95	2.48	3.307(5)	146
C6-H6...O1 ⁱⁱⁱ	0.95	2.50	3.240(5)	135
C15-H15...F7 ^{iv}	0.95	2.50	3.182(5)	129
C1-H1...Cl (intramol.)	0.95	2.77	3.333(5)	119
C7-H7...O1 (intramol.)	0.95	2.43	3.004(5)	119
C15-H15...Cl (intramol.)	0.95	2.74	3.182(5)	120
Symmetry codes: (i) 2-x,1-y,-z; (ii) 1-x,1-y,-z; (iii) -x,-y,-z; (iv) 1+x,y,z				
[Au(L14)Cl](PF₆)				
C7-H7...O1 (intramol.)	0.95	2.31	2.905(7)	120
C15-H15...Cl1 (intramol.)	0.95	2.81	3.355(6)	117

X-ray Crystallography

Table 5.4.9: Crystal Structure, X-ray Data, and Structure Model Refinement Parameters for and [Au(L8)Cl](PF₆), [Au(L9)Cl](AuCl₂), [Au(L11)Cl](PF₆)-[Au(L13)Cl](PF₆) and [Au(L15)Cl].

	[Au(L8)Cl](PF ₆)	[Au(L9)Cl](AuCl ₂)	[Au(L11)Cl](PF ₆)	[Au(L12)Cl](PF ₆)	[Au(L13)Cl](PF ₆)	[Au(L15)Cl]
Chemical formula	C ₁₅ H ₁₀ AuClN ₃ OPF ₆	C ₁₉ H ₁₈ Au ₂ Cl ₃ N ₃ O	C ₃₈ H ₂₄ Au ₂ Cl ₂ N ₆ O ₂ P ₂ F ₁₂ ·C ₃ H ₃ NO ₂	C ₁₆ H ₁₀ AuClN ₂ O	C ₂₂ H ₁₄ AuClN ₃ O ₂ PF ₆	C ₂₂ H ₁₃ AuClN ₃ O ₂ PF ₇
<i>M_r</i>	625.65	804.65	1412.45	478.68	729.75	829.85
Crystal system, SG	Monoclinic, <i>P</i> 2 ₁ / <i>c</i>	Triclinic <i>P</i> -1	Monoclinic <i>C</i> 2/ <i>c</i>	Triclinic <i>P</i> -1	Triclinic <i>P</i> -1	Triclinic <i>P</i> -1
Temperature (K)	298	100	100	100	120	120
<i>a</i> , <i>b</i> , <i>c</i> (Å)	6.7497(7), 14.7513(14), 17.1367(18)	7.4524(3), 10.6317(4), 13.3822(5)	20.1340(17), 17.1599(15), 13.1051(12)	7.5857(5), 9.1675(5), 11.1274(7)	6.1536(1), 14.2281(4), 15.0781(4)	7.5635(1), 13.7007(3), 14.0072(3)
α , β , γ (°)	90, 93.799(6), 90	95.219(1), 98.244(1), 95.537(1)	90, 110.810(2), 90	99.443(3), 101.633(3), 112.353(2)	109.117(2), 94.755(2), 94.470(2)	93.283(1), 97.933(1), 104.144(1)
<i>V</i> (Å ³)	1702.5(3)	1038.51(7)	4232.4(6)	675.76(7)	1235.29(5)	1387.77(5)
<i>Z</i>	4	2	4	2	2	2
Radiation type	Mo <i>K</i> α	Cu <i>K</i> α	Mo <i>K</i> α	Mo <i>K</i> α	Mo <i>K</i> α	Mo <i>K</i> α
μ (mm ⁻¹)	8.967	29.862	7.232	11.081	6.198	5.537
Crystal size (mm)	0.30, 0.10, 0.05	0.09, 0.08, 0.05	0.40, 0.20, 0.10	0.30, 0.10, 0.05	0.30, 0.20, 0.20	0.30, 0.30, 0.05
Abs. correction	SADABS	SADABS	SADABS	SADABS	Multi-Scan	Multi-Scan
<i>T_{min}</i> , <i>T_{max}</i>	0.174, 0.663	0.115, 0.199	0.420, 0.749	0.400, 0.751	0.258, 0.370	0.287, 0.769
<i>N_m</i> , <i>N_i</i> , <i>N_o</i>	24990, 8115, 5597	3508, 3508, 3383	52994, 17898, 13385	30618, 16888, 9811	12640, 7581, 6793	14195, 8529, 7158
<i>R_{int}</i>	0.053	0.025	0.0417	0.057	0.032	0.033
<i>R₁</i> , <i>wR(F²)</i> , <i>S</i>	0.052, 0.156, 1.025	0.026, 0.069, 1.128	0.040, 0.150,	0.067, 0.206, 1.011	0.033, 0.082, 0.992	0.036, 0.085, 0.963
<i>N_p</i> , <i>N_{res}</i>	254, 0	259, 0	309, 0	190, 0	325, 0	390, 0
$\Delta\rho_{max}$, $\Delta\rho_{min}$ (e Å ⁻³)	4.55, -3.30	1.069, -1.471	6.170, -3.410	7.400, -6.830	1.950, -3.010	1.980, -2.820

^aAbbreviations: SG, space group; *V*, volume; *Z*; number of formula units per unit cell; μ , absorption coefficient; *T*, transmission coefficient; *N_m*, number of measured reflections, *N_i*, number of independent reflections; *N_o*, number of observed reflections with $I > 2\sigma(I)$; *I*, intensity; *R_{int}*, internal *R*-factor for data set (based on the intensity match between symmetry equivalent reflections); $R_1 = R[F^2 > 2\sigma(F^2)]$; *wR(F²)*, weighted *R*-factor based on F^2 ; *F*, structure factor; *S*, goodness-of-fit of model to experimental data; *N_p*, number of parameters, *N_{res}*, number of restraints; $\Delta\rho$, electron density difference.

5.5 References

1. C. C. D. Centre, ed. CCDC, September 2011 edn., 2011.
2. T.-C. Cheung, T.-F. Lai and C.-M. Che, *Polyhedron*, 1994, **13**, 2073-2077.
3. A. Dogan, B. Schwederski, T. Schleid, F. Lissner, J. Fiedler and W. Kaim, *Inorg. Chem. Commun.*, 2004, **7**, 220-223.
4. A. S. K. Hashmi, M. Rudolph, J. W. Bats, W. Frey, F. Rominger and T. Oeser, *Chem.--Eur. J.*, 2008, **14**, 6672-6678.
5. T. Yang, C. Tu, J. Zhang, L. Lin, X. Zhang, Q. Liu, J. Ding, Q. Xu and Z. Guo, *Dalton Trans.*, 2003, 3419-3424.
6. T. Yang, J.-Y. Zhang, C. Tu, J. Lin, Q. Liu and Z.-J. Guo, *Wuji Huaxue Xuebao*, 2003, **19**, 45-48.
7. D. Fan, C.-T. Yang, J. D. Ranford and J. J. Vittal, *Dalton Trans.*, 2003, 4749-4753.
8. M. A. Cinellu, L. Maiore, G. Minghetti, F. Cocco, S. Stoccoro, A. Zucca, M. Manassero and C. Manassero, *Organometallics*, 2009, **28**, 7015-7024.
9. *CrysAlis CCD and CrysAlis RED*, (2002) Oxford Diffraction Ltd., Abington, UK.
10. G. M. Sheldrick, *SHELXS-97, Program for the solution of crystal structures*, (1997), University of Gottingen, Germany.
11. L. J. Farrugia, *J. Appl. Crystallogr.*, 1999, **32**, 837-838.
12. G. M. Sheldrick, *SHELXL-97, Program for refinement of crystal structures*, (1997), University of Gottingen, Germany.
13. A. Casini, M. C. Diawara, R. Scopelliti, S. M. Zakeeruddin, M. Gratzel and P. J. Dyson, *Dalton Trans.*, 2010, **39**, 2239-2245.
14. R. E. Shepherd, A. Proctor, W. W. Henderson and T. K. Myser, *Inorg. Chem.*, 1987, **26**, 2440-2444.
15. Z. Y. Lin and M. B. Hall, *Inorg. Chem.*, 1991, **30**, 646-651.
16. D. M. Fan, C. T. Yang, J. D. Ranford, P. F. Lee and J. J. Vittal, *Dalton Trans.*, 2003, 2680-2685.
17. J. K. Bjernemose, P. R. Raithby and H. Toftlund, *Acta Crystallogr., Sect. E: Struct. Rep. Online*, 2004, **60**, M1719-M1721.
18. C. Janiak, *J. Chem. Soc., Dalton Trans.*, 2000, 3885-3896.
19. G. Bacon, *Acta Crystallographica*, 1951, **4**, 558-561.
20. C. A. Hunter and J. K. M. Sanders, *Journal of the American Chemical Society*, 1990, **112**, 5525-5534.
21. C.-Y. Wu and C.-C. Su, *Polyhedron*, 1996, **16**, 383-392.
22. F. A. Cotton and G. Wilkinson, *Advanced Inorganic Chemistry*, 5th Edition edn., Wiley and Sons, 1988.
23. M. P. J. Sanz, M. Roitzsch, L. Yin, P. M. Lax, L. Holland, O. Krizanovic, M. Lutterbeck, M. Schuermann, E. C. Fusch and B. Lippert, *Dalton Trans.*, 2009, 10774-10786.
24. H. B. Friedrich, G. E. M. Maguire, B. S. Martincigh, M. G. McKay and L. K. Pietersen, *Acta Crystallogr., Sect. E: Struct. Rep. Online*, 2008, **E64**, m1240, m1240/1241-m1240/1248.
25. L. S. Hollis and S. J. Lippard, *J. Am. Chem. Soc.*, 1983, **105**, 4293-4299.
26. S. Stoccoro, G. Alesso, M. A. Cinellu, G. Minghetti, A. Zucca, M. Manassero and C. Manassero, *Dalton Trans.*, 2009, 3467-3477.
27. M. A. Cinellu, A. Zucca, S. Stoccoro, G. Minghetti, M. Manassero and M. Sansoni, *J. Chem. Soc., Dalton Trans.*, 1996, 4217-4225.

28. A. Laguna, *Modern Supramolecular Gold Chemistry: Gold-Metal Interactions and Applications*, Wiley and Sons, 2008.
29. C. Hollatz, A. Schier and H. Schmidbaur, *J. Am. Chem. Soc.*, 1997, **119**, 8115-8116.
30. D. B. Leznoff, B.-Y. Xue, R. J. Batchelor, F. W. B. Einstein and B. O. Patrick, *Inorg. Chem.*, 2001, **40**, 6026-6034.
31. H. Schmidbaur, *Chem. Soc. Rev.*, 1995, **24**, 391-400.
32. S. Antony, K. K. Agama, Z. H. Miao, M. Hollingshead, S. L. Holbeck, M. H. Wright, L. Varticovski, M. Nagarajan, A. Morrell, M. Cushman and Y. Pommier, *Mol. Pharmacol.*, 2006, **70**, 1109-1120.
33. I. Orhana, B. Ozcelik, T. Karaoglu and B. Sener, *Zeitschrift fur Naturforschung. C, Journal of biosciences*, 2007, **62**, 19-26.
34. V. Rosenkranz and M. Wink, *Molecules*, 2008, **13**, 2462-2473.
35. M. F. Brana, J. M. Castellano, M. Moran, F. Emling, M. Kluge, E. Schlick, G. Klebe and N. Walker, *Arzneimittel-Forschung*, 1995, **45**, 1311-1318.
36. B. L. Staker, M. D. Feese, M. Cushman, Y. Pommier, D. Zembower, L. Stewart and A. B. Burgin, *J. Med. Chem.*, 2005, **48**, 2336-2345.

6. Computational chemistry

6.1 Introduction

Computational chemistry involves the use of mathematical methods, combined with the basic laws of physics, and is used to solve chemically related problems by calculation. It is a subfield of theoretical chemistry that falls under the broader field of physical chemistry.¹

In trying to understand how molecules behave, one has to understand the underlying contributing factors that affect how molecules behave, this being the electron. Quantum mechanics (QM) is the most correct mathematical description of the behaviour of electrons and their ability to behave in both a particle-like fashion and a wave-like fashion.² In theory, QM can predict any property of an individual atom or molecule but in practice the QM equations have only been solved exactly for one-electron systems. There are several different methods that have been developed for approximating the solution for multiple-electron systems. One of these methods was formulated by Schrödinger:³

$$\hat{H}\psi = E\psi \quad 6.1.1$$

where \hat{H} is the Hamiltonian operator, ψ a wave function and E the energy.³

The wave function ψ , as the name implies, is the description of an electron as a wave and can describe the probability of electrons being in certain locations, but it cannot predict exactly where electrons are located. Once the wave function has been calculated, almost any property of the individual molecule can be determined with varying degrees of accuracy dependent upon the approximations used to simplify the calculations.³ Density functional theory (DFT) is an indirect method of calculating the wave function and focuses on optimising electron density. From the basic premises of DFT, the charge distribution determines the external potential, which in turn determines the Hamiltonian operator, which ultimately leads to the wave function.⁴ DFT theory is based upon a strategy of modelling electron correlation via general functional of the electron density. Electron correlation is based on the fact that electrons in a molecular system react to one another's motion and attempt to avoid each other.² DFT is frequently used as the method of choice when predicting properties of metal complexes. The most common type of functional used in modern DFT calculations of small molecules is a gradient-corrected functional (the

Computational

generalised gradient approximation (GGA)).³⁻⁵ This is over the older functionals such as the local density approximation (LDA) as well as the local spin density approximation (LSDA). Both these functionals are based on the assumption that at every point in the molecule the energy density has the value that would be given by a homogeneous electron gas which had the same electron density at that point.⁵ The LSDA functional extends this further and assigns a spin orientation to electrons similar to the Hartree-Fock (HF) method.^{1, 3-5} HF is another quantum mechanical method used to calculate the wave function and is the product of one-electron functions called spatial orbitals.^{1, 3-5} Further functionals, and the type used for the calculations performed in this thesis, are the hybrid GGA functionals. This is a GGA functional to which HF exchange has been added.⁵ In general the most frequently used hybrid-functionals are B3LYP⁶⁻⁸ (Becke 88 3-parameter exchange functional and the Lee, Yang, Parr correlation functional), PBE1PBE⁹ (the Adamo hybrid of the 1996 pure functional of Perdew, Burke and Ernzerhof) and HSEh1PBE¹⁰⁻¹³ (the full Heyd-Scuseria-Ernzerhof) functional. These functionals are used in conjunction with a basis set which are the set of mathematical functions from which the wave function is constructed. For molecules that only contain light atoms (up to the first row of transition metals) the 6-311G¹⁴⁻¹⁶ basis set is commonly used. For heavy elements, however, the situation is slightly different as they contain numerous core electrons which would require a large number of basis functions to describe them. In addition to this, the core electrons of such heavy elements approach velocities nearing the speed of light so that they may manifest relativistic effects. The solution to this problem is to use an effective core potential (ECP) which uses an analytical function to replace the core electrons. The most commonly used ECP basis sets for the study of heavy metal complexes are the Los Alamos¹⁷⁻¹⁹ (LanL2DZ), and the Stuttgart/Dresden²⁰ (SDD) ECP's. There is, however, no obvious choice of functional and basis set combination when examining the literature and one has to pick a combination which is relevant to the system being investigated. In the case of gold(III) d⁸ metal complexes there is a precedent for all functionals (*vide supra*). We have chosen the HSEh1PBE¹⁰⁻¹³ functional as it is the most modern of the three described, along with the use of a split basis set, 6-311G(d,p)¹⁴⁻¹⁶ being used for all atoms except the gold(III) ion, for which the LanL2DZ¹⁷⁻¹⁹ ECP was used.

Literature reports on the use of DFT calculations on gold complexes are fairly prevalent with the most common use being as an aid in understanding the experimental physical properties such as luminescence, reactivity, stability and UV-vis spectra of the respective complexes.²¹⁻²⁶ DFT calculations are, however, also regularly used to try and understand the mechanistic detail underlying chemical reactions that involve gold complexes as a catalyst.^{27,}
28

One such example on the use of DFT computations as an aid to understanding the physical properties of gold complexes is reported by Au and co-workers and titled 'Luminescent Cyclometalated Alkynylgold(III) Complexes with 6-Phenyl-2,2'-Bipyridine Derivatives: Synthesis, Characterisation, Electrochemistry, Photophysics, and Computational Studies' (Figure 6.1.1).²¹

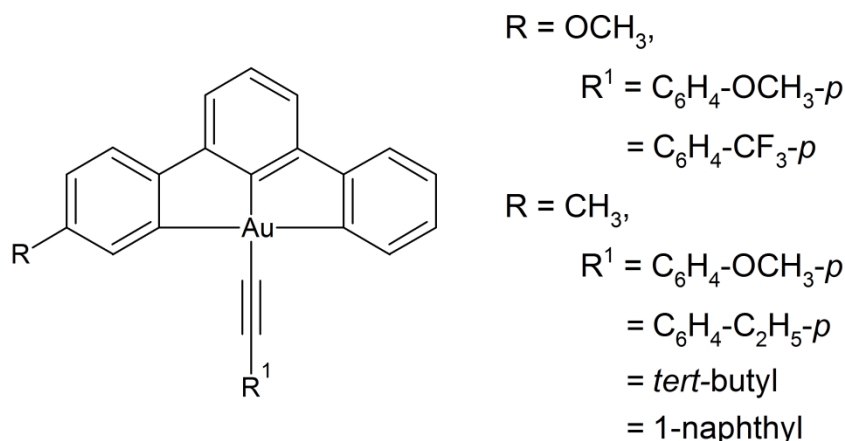


Figure 6.1.1: Chemical structures of some gold(III) alkynyl complexes studied by Yam and co-workers.

The authors found that the electronic absorption spectra (acetonitrile, room temperature) of the complexes (Figure 6.1.1) revolved around an intense absorption at the higher energy region (wavelength < 320 nm) and a moderately intense broad adsorption band at 374-406 nm, assigned to a metal-perturbed intraligand $\pi\text{-}\pi^*$ transition of the ligand.²¹ The transitions were found to be based on a charge transfer from the aryl ring to the bipy moiety.²¹ The complexes were all found to be emissive in butyronitrile glass (77K) with emission bands between 469-550 nm.²¹ These were assigned to an intraligand excited state of the ligand with some charge transfer character from the aryl ring to the bipy moiety.²¹

Computational

A recent example of the application of DFT computations in the elucidation of a catalytic mechanism, Ye and co-workers describe the generation of vinylidenes from terminal alkynes via a bifurcation pathway and facile C-H insertion (Figure 6.1.2).²⁸

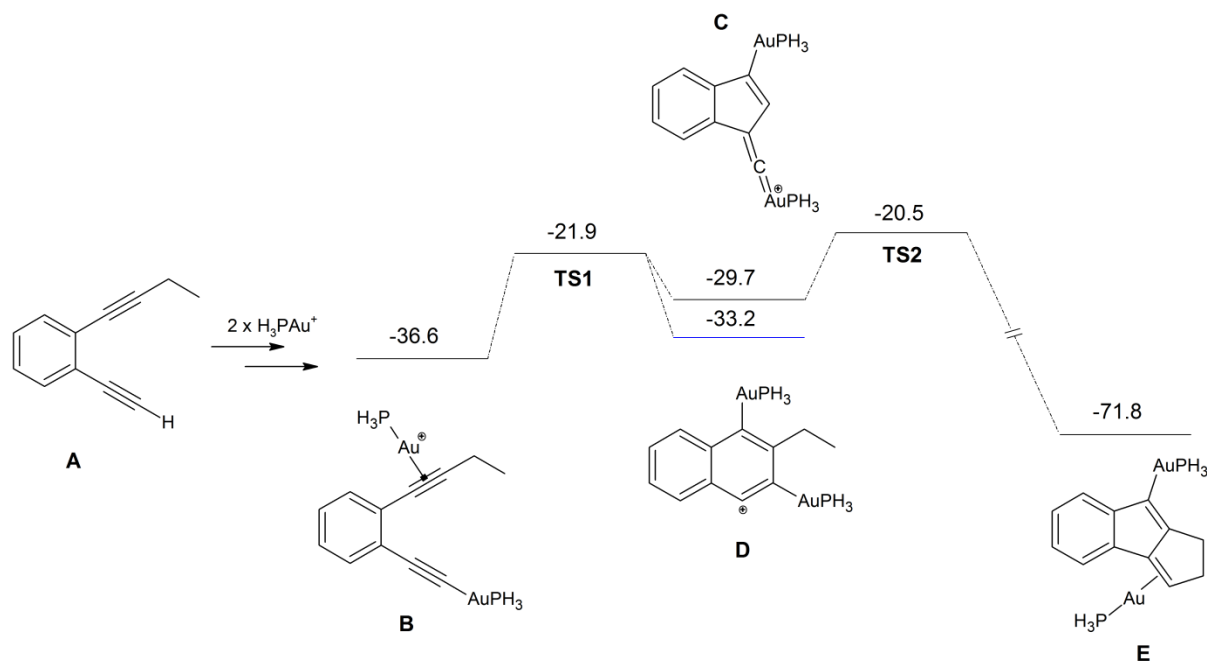


Figure 6.1.2: Free energy diagram for the reaction in chloroform. All energy levels in kcal/mol. TS1 is transition state 1 and TS2 is transition state 2. Adapted from reference 28.²⁸

The authors found that the cyclo-isomerisation of benzene -1,2-dialkynes occurs with the aid of two BrettPhosAuNTf₂ molecules working synergistically with each other and a gold vinylidene structure (C) as the most likely intermediate (as opposed to structure D).

6.2 Objectives

The objectives of the computational work were: (1) to delineate the gas phase structures of all compounds and compare them to the solid state structures in order to determine the accuracy of the computational methods used as well as to determine the influence crystal packing effects have on the solid state structures, (2) to calculate the d-orbital electron distributions in order to gain insight on the electronic structure of the compounds, (3) to calculate IR, NMR and energy values for each complex and compare and contrast them to the respective experimentally obtained values in order to determine the accuracy of the computational methods used, (4) to use the calculated IR, NMR, time-dependent DFT (TD-DFT) data to guide the assignment

6.3 Experimental

There are different approximation methods, also known as levels of theory that can be used to determine the required parameters of a calculation. In our case DFT and TD-DFT²⁹ calculations were performed with Gaussian09 using the full Heyd-Scuseria-Ernzerhof functional (HSE06)¹⁰⁻¹³ and the double- ζ basis set 6-311G(d,p)¹⁴⁻¹⁶ for all atoms except Au, for which the Los Alamos ECP basis set (LanL2DZ)¹⁷⁻¹⁹ was implemented. An additional f-type polarisation function ($\alpha = 0.20$)^{30, 31} was used for the Au atom. X-ray co-ordinates of the cations [Au(HL1)Cl₂]-[Au(L9)Cl](PF₆), [Au(L11)Cl](PF₆)-[Au(L13)Cl](PF₆) and [Au(L15)Cl] were used as a starting point for each respective geometry optimisation while the X-ray co-ordinates of [Au(L11)Cl](PF₆), [Au(L12)Cl](PF₆) and [Au(L15)Cl] were modified accordingly and used as the starting point geometry for compounds [Au(L10)Cl](PF₆), [Au(L14)Cl](PF₆) and [Au(L16)Cl], respectively. The calculations excluded the counterions (anions). No negative eigenvalues were calculated for the stationary point structures located by geometry optimisation, consistent with location of minima on the potential energy surface for each gold(III) chelate. Solvent effects were added using the conductor-like polarisable continuum model (C-PCM)³² for TD-DFT energy calculations. Root-mean-square deviation (RMSD) fits between calculated and experimental structures for all complexes were calculated using Mercury 3.0³³. NMR chemical shifts were calculated and analysed relative to tetramethylsilane using the GIAO³⁴⁻³⁷ method at the same level of theory as stated above. All of the Gaussian job files can be found in Appendix C.

6.4 Results and discussion

GEOMETRY OPTIMISATIONS:

The geometries of all compounds were optimised to energy minima on potential energy surface. The calculations were performed at the level of theory discussed above and the results compared to the experimental single crystal X-ray structures where possible. Where comparison was not possible (X-ray structure not available) the results were simply reported for the stationary point structure determined from the geometry optimisation.

Considering the calculations were performed in *vacuo*, the calculated structures are not exposed to any intermolecular forces which are able to distort the solid state structure quite

significantly from the energy minimised structures. The intermolecular forces involved may comprise conventional and unconventional hydrogen bonding, van der Waals forces as well as ring-ring interactions. The preference for the co-ordination sphere of all the compounds to adopt a square planar geometry was confirmed through the geometry optimisation results. In addition, the metal ion, the conjugated aromatic system of the pyridine, quinoline and isoquinoline rings, as well as the amide functionality further serve to enforce a square planar geometry of the co-ordination sphere.

Superposition of the co-ordination spheres between single crystal X-ray structures and DFT calculated structures was performed by least squares minimisation of the differences between non-H atoms of the amido compounds. The RMSD values obtained (0.0405-0.133) reflect a good agreement between the experimental solid state structures and the gas phase optimised structures. This reflects, in part, the minimal influence of crystal packing effect on the planar co-ordination sphere. The least squares fit between calculated and X-ray structures for compounds $[\text{Au}(\text{HL1})\text{Cl}_2]$ – $[\text{Au}(\text{L4})\text{Cl}_2]$, $[\text{Au}(\text{L7})\text{Cl}](\text{PF}_6)$, $[\text{Au}(\text{L9})\text{Cl}](\text{PF}_6)$, $[\text{Au}(\text{L12})\text{Cl}](\text{PF}_6)$ and $[\text{Au}(\text{L13})\text{Cl}](\text{PF}_6)$ are displayed in Figure 6.4.1. The compounds represented in Figure 6.4.1 were chosen because their auxiliary structures are susceptible to distortion via intermolecular forces and crystal packing effects while the balance of the compounds are included in Appendix C as they displayed exemplary all-atom fits. Without exception, all cation structures showed the co-ordination sphere of the compounds to be planar. As was the case for the X-ray structures, the DFT-calculated geometry of $[\text{Au}(\text{HL3})\text{Cl}_2]$, displayed an obvious increase in the Au–N1 and Au–N2 bond lengths over those for $[\text{Au}(\text{HL1})\text{Cl}_2]$, $[\text{Au}(\text{HL2})\text{Cl}_2]$ and $[\text{Au}(\text{L4})\text{Cl}_2]$ (Table 6.4.1). Both the Au–Cl1 and Au–Cl2 bond lengths were overestimated for compounds $[\text{Au}(\text{HL1})\text{Cl}_2]$ – $[\text{Au}(\text{L4})\text{Cl}_2]$ on average, by 0.052(4) and 0.034(14) Å, respectively (Table 6.4.1). For compounds $[\text{Au}(\text{L5})\text{Cl}](\text{PF}_6)$ – $[\text{Au}(\text{L9})\text{Cl}](\text{PF}_6)$ and $[\text{Au}(\text{L11})\text{Cl}](\text{PF}_6)$ – $[\text{Au}(\text{L13})\text{Cl}](\text{PF}_6)$ the computational method overestimated the Au–N1, Au–N2, Au–N3 and Au–Cl1 bond lengths on average by 0.021(7), 0.03(2), 0.025(8) and 0.05(2) Å, respectively. A similar trend was observed for $[\text{Au}(\text{L15})\text{Cl}]$, with the exception that the Au–C1 distance was underestimated by 0.007 Å.

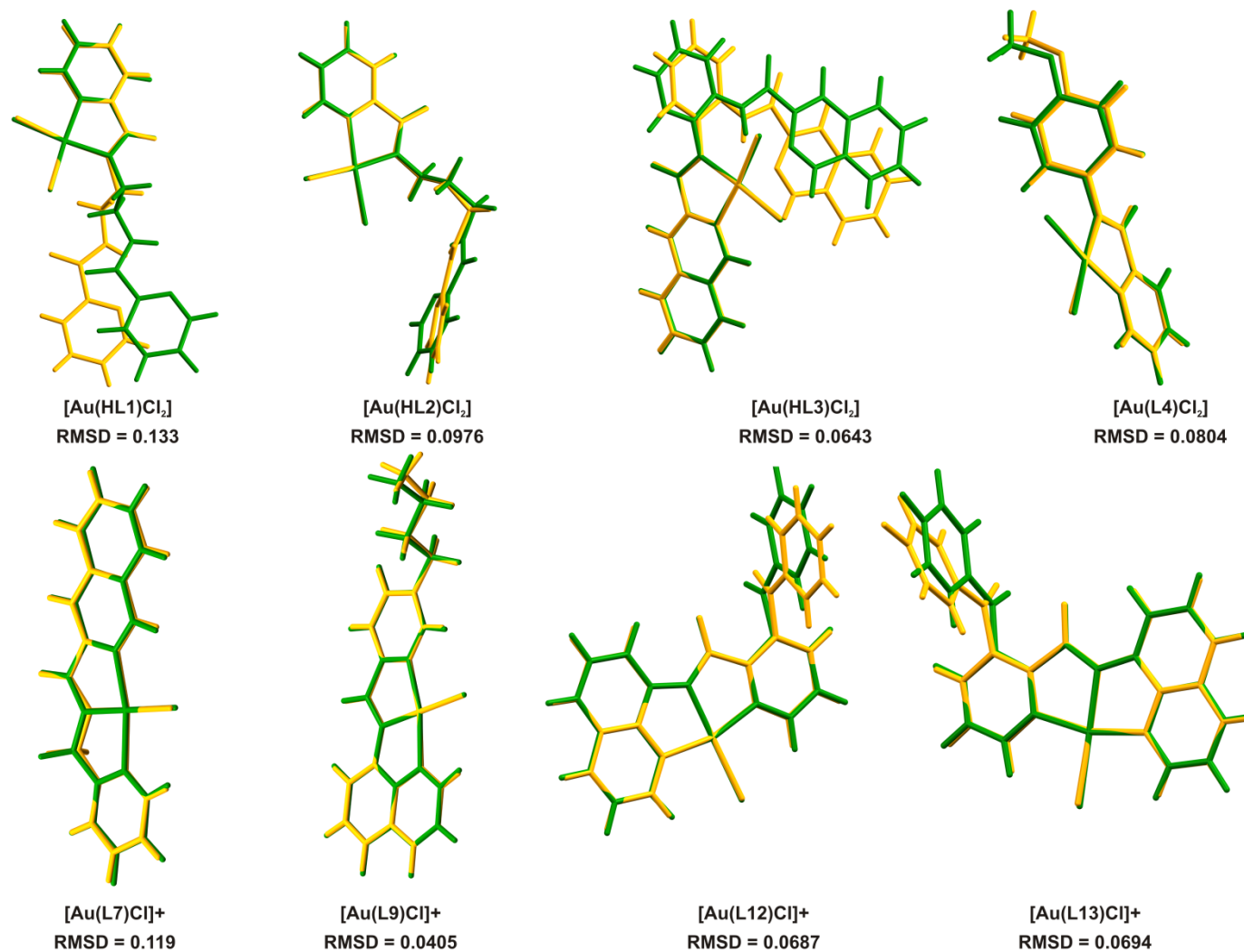


Figure 6.4.1: Least squares fit of the non-H atoms involved in the co-ordination sphere of the selected DFT (green) and X-ray (yellow) structures studied in this work. RMSD values (Å) are indicated in the diagram.

Computational

The co-ordination bond angles for all compounds were accurately calculated to within 2.5% of the single crystal X-ray structures for all of the compounds investigated. Although compounds $[\text{Au}(\text{HL1})\text{Cl}_2]$ – $[\text{Au}(\text{L4})\text{Cl}_2]$, $[\text{Au}(\text{L9})\text{Cl}](\text{PF}_6)$, $[\text{Au}(\text{L12})\text{Cl}](\text{PF}_6)$ and $[\text{Au}(\text{L13})\text{Cl}](\text{PF}_6)$ displayed good co-ordination sphere fits between the calculated and X-ray structures, they also contain auxiliary functional groups that contain many torsional degrees of freedom and are hence able to adopt distorted conformations associated with crystal packing effects when compared to the *in vacuo* calculated structures. For chelate $[\text{Au}(\text{HL1})\text{Cl}_2]$ the N1–C7–C8–C9 torsion angle for the DFT-calculated structure is 6.1° while the equivalent torsion angle in the X-ray structure is 12.2° . This, along with the dissimilar N1–C7–C8 bond angles for the DFT calculated (111.8°) and X-ray determined (108.1°) structures, is a direct result of the intermolecular hydrogen bonding as well as π – π stacking interactions prevalent in the solid state. Compounds $[\text{Au}(\text{HL2})\text{Cl}_2]$ – $[\text{Au}(\text{L4})\text{Cl}_2]$ follow similar trends with intermolecular forces accounting for deviations of the auxiliary functional group positions between the calculated and observed structures. Chelate $[\text{Au}(\text{L7})\text{Cl}](\text{PF}_6)$ contains no auxiliary functional group, yet has the highest RMSD value (0.119 \AA). This is due to the methylene carbon and amide group puckering out of the co-ordination plane in opposite directions due to unconventional C–H \cdots O and C–H \cdots Cl hydrogen bonding (Figure 6.4.2). Compound $[\text{Au}(\text{L9})\text{Cl}](\text{AuCl}_2)$ contains a butyl group, which has many degrees of freedom, and therefore significant deviations between the calculated and observed structures is both expected and inevitable. Compounds $[\text{Au}(\text{L12})\text{Cl}](\text{PF}_6)$ and $[\text{Au}(\text{L13})\text{Cl}](\text{PF}_6)$ each contain a phenyl ketone "side-chain" functional group which are involved C–H \cdots X (where X = Cl, F or O) unconventional hydrogen bonding interactions as well as van der Waals interactions. These lattice interactions are absent in the gas phase simulations and readily account for the deviations between the calculated and observed complex conformations.

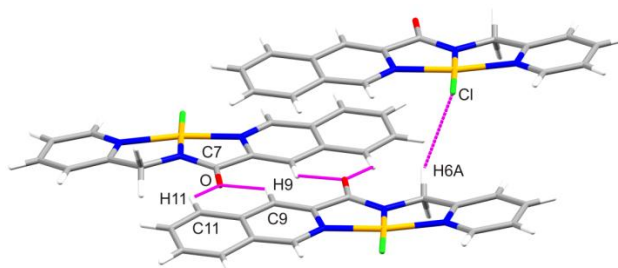


Figure 6.4.2: Unconventional hydrogen bonding interactions responsible for the large RMSD (0.199 \AA) value between the experimental and calculated structures of $[\text{Au}(\text{L7})\text{Cl}](\text{PF}_6)$.

Computational

Table 6.4.1: Comparisons of the mean bond lengths and angles of the calculated and experimental structures of the gold(III) compounds : [Au(HL1)Cl₂]-[Au(L9)Cl](PF₆), [Au(L11)Cl](PF₆)-[Au(L13)Cl](PF₆) and [Au(L15)Cl].

Parameter	[Au(HL1)Cl ₂]			[Au(HL2)Cl ₂]			[Au(HL3)Cl ₂]			[Au(L4)Cl ₂]		
	Calc.	Exp.	Diff.	Calc.	Exp.	Diff.	Calc.	Exp.	Diff.	Calc.	Exp.	Diff.
Bond Length / Å												
Au–N1	2.073	2.036(5)	0.037	2.071	2.037(3)	0.034	2.073	2.048(3)	0.025	2.075	2.031(4)	0.044
Au–N2	2.035	2.019(4)	0.016	2.035	2.014(3)	0.021	2.069	2.035(3)	0.034	2.063	2.009(5)	0.054
Au–Cl1	2.337	2.290(2)	0.047	2.339	2.287(1)	0.052	2.355	2.303(1)	0.052	2.352	2.295(2)	0.057
Au–Cl2	2.299	2.285(2)	0.014	2.302	2.263(1)	0.039	2.306	2.270(1)	0.036	2.309	2.261(2)	0.048
C=O	1.220	1.211(7)	0.009	1.220	1.230(5)	-0.010	1.213	1.232(4)	-0.019	1.215	1.21(1)	0.005
C–N	1.349	1.345(8)	0.004	1.348	1.341(5)	0.007	1.365	1.362(5)	0.003	1.358	1.343(9)	0.015
Bond Angle / °												
N1–Au–Cl1	94.5	94.0(1)	0.5	94.5	94.85(9)	-0.35	94.3	95.68(8)	-1.38	94.5	95.3(1)	-0.8
Cl1–Au–Cl2	89.6	89.11(7)	0.49	89.3	89.00(4)	0.3	90.2	89.42(2)	0.78	89.7	88.87(6)	0.83
Cl2–Au–N2	95.3	95.8(1)	-0.5	95.6	94.90(9)	0.7	94.8	93.83(9)	0.97	95.4	94.4(1)	1
N2–Au–N1	80.6	81.0(2)	-0.4	80.6	81.3(1)	-0.7	80.7	81.1(1)	-0.4	80.5	81.5(2)	-1
Parameter	[Au(L5)Cl](PF ₆)			[Au(L6)Cl](PF ₆)			[Au(L7)Cl](PF ₆)			[Au(L8)Cl](PF ₆)		
	Calc.	Exp.	Diff.	Calc.	Exp.	Diff.	Calc.	Exp.	Diff.	Calc.	Exp.	Diff.
Bond Length / Å												
Au–N1	2.039	2.024(5)	0.015	2.044	2.013(5)	0.031	2.042	2.031(6)	0.011	2.022	2.001(4)	0.021
Au–N2	1.972	1.918(5)	0.054	1.962	1.933(5)	0.029	1.970	1.888(6)	0.082	1.989	1.969(4)	0.02
Au–N3	2.044	2.013(5)	0.031	2.042	2.015(6)	0.027	2.038	2.000(5)	0.038	2.035	2.024(4)	0.011
Au–Cl1	2.330	2.292(1)	0.038	2.332	2.298(2)	0.034	2.334	2.286(2)	0.048	2.385	2.283(1)	0.102
C=O	1.208	1.206(7)	0.002	1.211	1.223(9)	-0.012	1.210	1.231(8)	-0.021	1.246	1.220(6)	0.026
C–N	1.354	1.390(7)	-0.036	1.353	1.360(9)	-0.007	1.357	1.360(8)	-0.003	1.375	1.340(6)	0.035
Bond Angle / °												
N1–Au–N2	81.7	81.4(2)	0.3	82.0	82.8(2)	-0.8	81.7	82.5(2)	-0.8	82.9	83.2(2)	-0.3
N2–Au–N3	81.9	83.1 (2)	-1.2	81.0	80.7(2)	0.3	82.0	82.5(2)	-0.5	82.2	81.9(2)	0.3
N3–Au–Cl1	97.7	96.8(1)	0.9	99.0	99.3(2)	-0.3	97.6	96.8(1)	0.8	97.5	97.6(1)	-0.1
Cl1–Au–N1	98.6	98.8(1)	-0.2	98.0	97.2(2)	0.8	98.6	98.4(2)	0.2	97.4	97.3(1)	0.1

Computational

Table 6.4.1: Continued...

Parameter	[Au(L9)Cl](AuCl ₂)			[Au(L11)Cl](PF ₆)			[Au(L12)Cl](PF ₆)			[Au(L13)Cl](PF ₆)		
	Bond Length / Å	Calc.	Exp.	Diff.	Calc.	Exp.	Diff.	Calc.	Exp.	Diff.	Calc.	Exp.
Au–N1	2.033	2.021(4)	0.012	2.032	2.010(2)	0.022	2.032	2.005(2)	0.027	2.032	2.005(3)	0.027
Au–N2	1.987	1.975(4)	0.012	1.987	1.969(2)	0.018	1.985	1.971(3)	0.014	1.985	1.971(3)	0.014
Au–N3	2.042	2.021(5)	0.021	2.037	2.013(2)	0.024	2.044	2.022(2)	0.022	2.044	2.013(3)	0.031
Au–Cl1	2.326	2.272(1)	0.054	2.328	2.282(5)	0.046	2.326	2.283(1)	0.043	2.325	2.278(1)	0.047
C=O	1.208	1.223(6)	-0.015	1.209	1.223(3)	-0.014	1.208	1.225(5)	-0.017	1.208	1.224(4)	-0.016
C–N	1.367	1.354(7)	0.013	1.370	1.364(3)	0.006	1.365	1.352(4)	0.013	1.365	1.353(5)	0.012
Bond Angle / °												
N1–Au–N2	82.3	83.0(2)	-0.7	82.3	83.0(1)	-0.7	82.4	83.1(1)	-0.7	82.4	83.1(4)	-0.7
N2–Au–N3	82.0	82.3(2)	-0.3	82.3	83.0(1)	-0.7	81.9	83.1(1)	-1.2	81.9	82.1(3)	-1.2
N3–Au–Cl1	97.8	97.7(1)	0.1	97.6	96.4(1)	1.2	98.0	96.3(1)	1.7	98.0	97.6(1)	1.7
Cl1–Au–N1	97.8	96.9(1)	0.9	97.8	97.4(1)	0.4	97.7	97.4(1)	0.3	97.7	96.8(1)	0.3
Parameter	[Au(L15)Cl]											
Bond Length / Å	Calc.	Exp.	Diff.									
Au–N1	2.151	2.116(4)	0.035									
Au–N2	2.003	1.970(4)	0.033									
Au–C16	2.010	2.017(4)	-0.007									
Au–Cl1	2.331	2.290(2)	0.041									
C=O	1.215	1.221(6)	-0.006									
C–N	1.381	1.356(5)	0.025									
Bond Angle / °												
N1–Au–N2	80.2	81.7(1)	-1.5									
N2–Au–C16	82.9	82.6(2)	0.3									
C16–Au–Cl1	98.6	96.5(1)	2.1									
Cl1–Au–N1	98.3	99.2(1)	-0.9									

Computational

The complexes $[\text{Au}(\text{L10})\text{Cl}](\text{PF}_6)$, $[\text{Au}(\text{L14})\text{Cl}](\text{PF}_6)$ and $[\text{Au}(\text{L16})\text{Cl}]$ could not be crystallised and their structures were therefore calculated (Figure 6.4.3) by modifying existing structures $[\text{Au}(\text{L8})\text{Cl}](\text{PF}_6)$, $[\text{Au}(\text{L12})\text{Cl}](\text{PF}_6)$ and $[\text{Au}(\text{L15})\text{Cl}]$, respectively. The small RMSD values obtained for the co-ordination spheres for the compounds studied by X-ray crystallography, indicate that the calculated structures are likely to be a fairly accurate reflection of the unknown experimental structures.

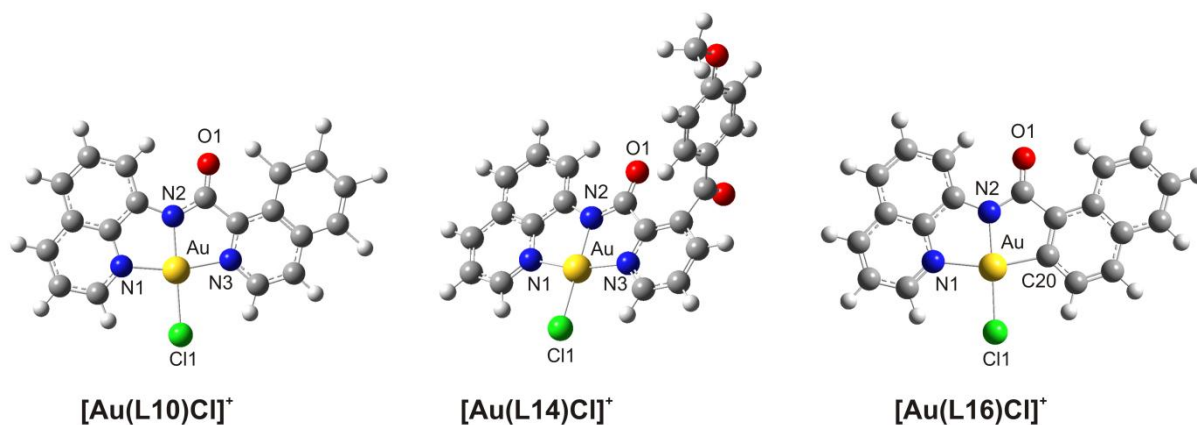


Figure 6.4.3: Partially labelled diagram for calculated structures $[\text{Au}(\text{L10})\text{Cl}]^+$, $[\text{Au}(\text{L14})\text{Cl}]^+$ and $[\text{Au}(\text{L16})\text{Cl}]^+$.

The bond lengths and bond angles for the compounds above are tabulated below (Table 6.4.2). The data is in good agreement with the analogous data for the structurally related complexes that have been studied in this work.

Table 6.4.2: Summary of calculated bond lengths and angles for complexes $[\text{Au}(\text{L10})\text{Cl}]^+$, $[\text{Au}(\text{L14})\text{Cl}]^+$ and $[\text{Au}(\text{L16})\text{Cl}]^+$.

Structural Features	$[\text{Au}(\text{L10})\text{Cl}]^+$	$[\text{Au}(\text{L14})\text{Cl}]^+$	$[\text{Au}(\text{L16})\text{Cl}]$
Bond Length / Å			
Au–N1	2.040	2.033	2.148
Au–N2	1.978	1.985	1.992
Au–N3	2.033	2.044	2.011
Au–Cl1	2.326	2.326	2.334
C=O	1.210	1.207	1.217
C–N	1.366	1.367	1.382
Bond Angle / °			
N1–Au–N2	82.7	82.4	80.6
N2–Au–N3	81.3	81.8	82.1
N3–Au–Cl1	98.9	98.1	99.4
Cl1–Au–N1	97.1	97.7	97.8

* For compound $[\text{Au}(\text{L16})\text{Cl}]$, atom N3 is replaced by atom C20.

FREQUENCY CALCULATIONS:

The vibrational frequencies for all compounds were calculated for two purposes: (1) to determine if the geometry optimised structures reached a pure minimum on the potential energy surface and (2) to compare the calculated frequencies against the experimentally obtained results. The frequencies were compared by plotting the experimental values against the calculated ones and observing the trend. The slope obtained from the plot would give a scaling factor that could be used to correct for any systematic errors in the calculations. Figure 6.4.4 shows an overlay of the calculated and experimental frequency data for complex $[\text{Au}(\text{HL}3)\text{Cl}_2]$, which is used as a representative for the compounds discussed in this work.

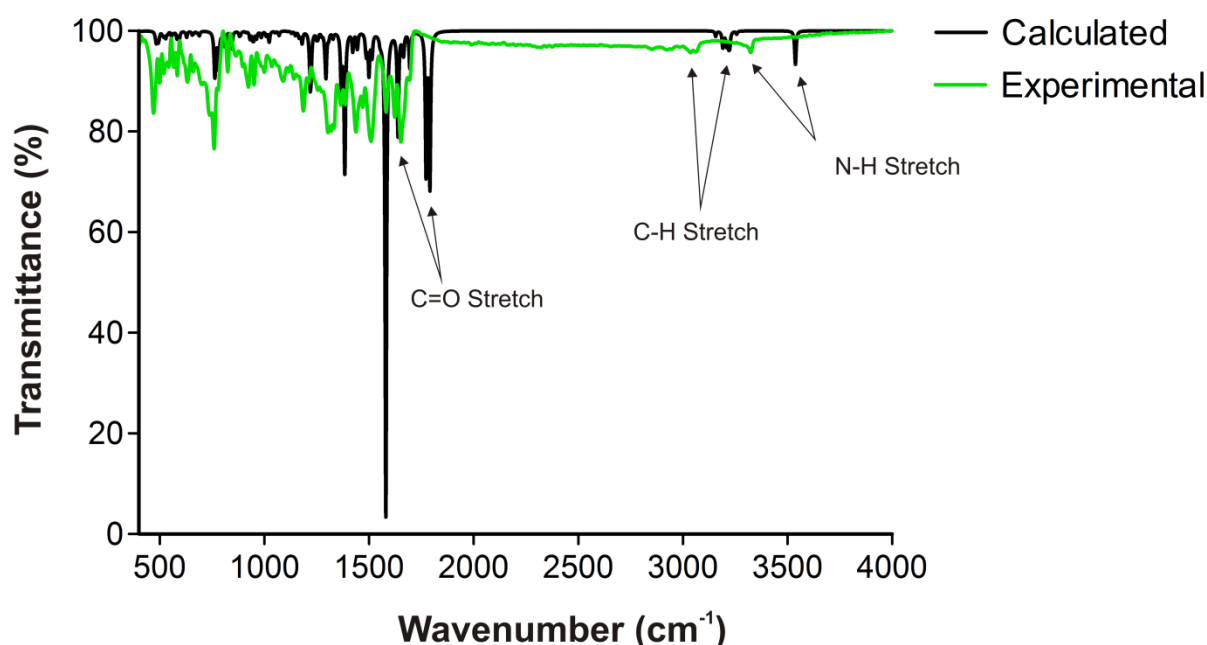


Figure 6.4.4: Overlay of calculated and experimental frequency data for the gold(III) chelate $[\text{Au}(\text{HL}3)\text{Cl}_2]$.

The relative intensities of the peaks show reasonable correlation between the calculated and experimental results. There is, however, some discrepancy between the absolute values of the calculated and experimental peak amplitudes. The functional group that is common to all compounds is the amide carbonyl C=O which exhibits a characteristic stretch in the $\approx 1600 \text{ cm}^{-1}$ region. The data for this particular stretching frequency were analysed by plotting the experimental versus calculated points (Figure 6.4.4). With the data for $[\text{Au}(\text{L}8)\text{Cl}](\text{PF}_6)$ removed as an outlier the plot suggests that the error observed in the prediction of the

amide carbonyl stretching frequency is systematic and a correction could be applied to the calculated values to afford more accurate predictions of vibrational mode energies.

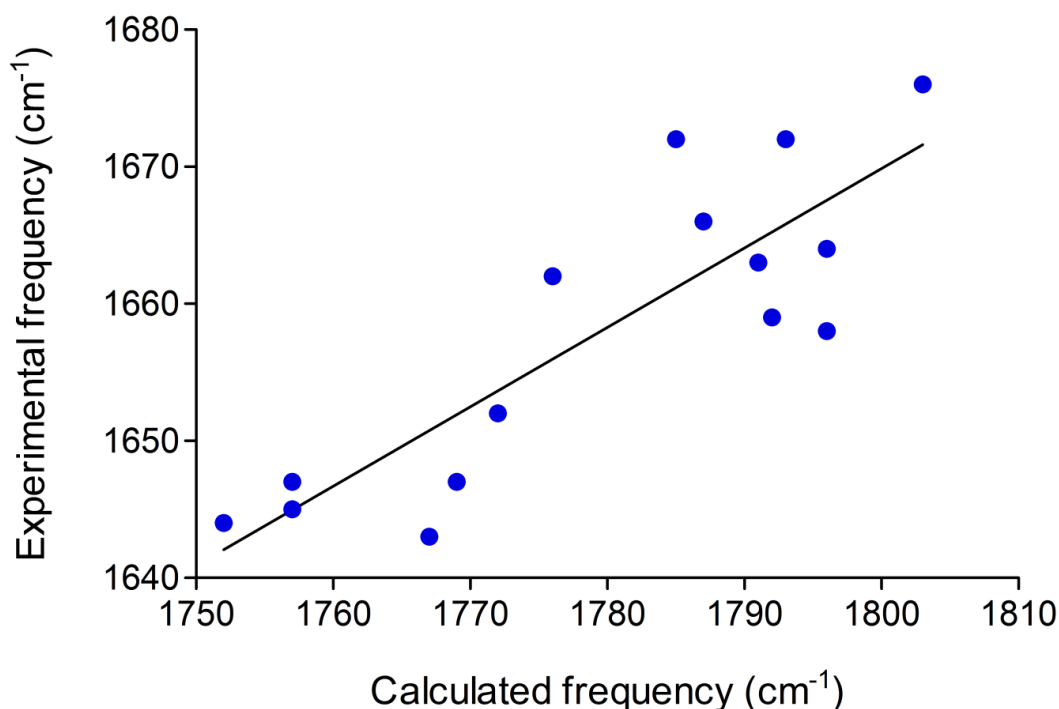


Figure 6.4.5: Plot of experimental versus calculated amide carbonyl stretching vibrations for all compounds discussed in the work except [Au(L8)Cl](PF₆) (removed as an outlier). The correlation coefficient of the fit is 0.854.

Equation 6.4.1 gives the mathematical relationship between the calculated and the experimental data of the amide C=O stretching vibration. There was no such relationship observed for any other vibration that was common throughout the series. The experimental and calculated vibrational frequencies are displayed in Table 6.4.3

$$\nu_{\text{C=O}}^{\text{exp}} = 0.579 \times \nu_{\text{C=O}}^{\text{calc}} + 627 \text{ cm}^{-1} \quad 6.4.1$$

The data in Table 6.4.3 show that the calculated C=O stretching frequency was overestimated in all cases. Although the correlation between the experimental and the calculated spectral frequencies was not ideal, the error was below 9% in all cases.

Computational

Table 6.4.3: Summary of experimental and calculated frequencies for the amide C=O stretch for all gold(III) compounds studied in this work.

	$\nu(\text{C=O})/\text{cm}^{-1}$		
	Calc.	Exp.	Diff.
[Au(HL1)Cl ₂]	1757	1647	155
[Au(HL2)Cl ₂]	1757	1645	114
[Au(HL3)Cl ₂]	1772	1652	150
[Au(L4)Cl ₂]	1767	1643	174
[Au(L5)Cl](PF ₆)	1803	1676	127
[Au(L6)Cl](PF ₆)	1785	1672	113
[Au(L7)Cl](PF ₆)	1796	1664	132
[Au(L8)Cl](PF ₆)	1687	1655	32
[Au(L9)Cl](PF ₆)	1791	1663	128
[Au(L10)Cl](PF ₆)	1776	1662	114
[Au(L11)Cl](PF ₆)	1787	1666	121
[Au(L12)Cl](PF ₆)	1796	1658	138
[Au(L13)Cl](PF ₆)	1793	1672	121
[Au(L14)Cl](PF ₆)	1792	1659	133
[Au(L15)Cl]	1769	1647	122
[Au(L16)Cl]	1752	1644	108

ENERGY CALCULATIONS:

Excited state energy calculations were performed for the gold(III) compounds in this work at the HSE06/LanL2DZ (Au) and HSE06/6-311G(d,p) (all other atoms) level of theory using the TD-SCF method, solving for $N = 30$ states. The additional f type polarisation function was added since it has been shown to be necessary for heavy atoms to obtain reasonable geometry optimisations and spectroscopic properties.³⁸ The LanL2DZ basis set used makes use of effective core potentials and only takes into account the valence electrons. As core electrons are not involved in electronic transitions, this should not affect the accuracy of the calculations. The calculated results were compared to the experimental data by overlaying the respective spectra (Figure 6.4.6).

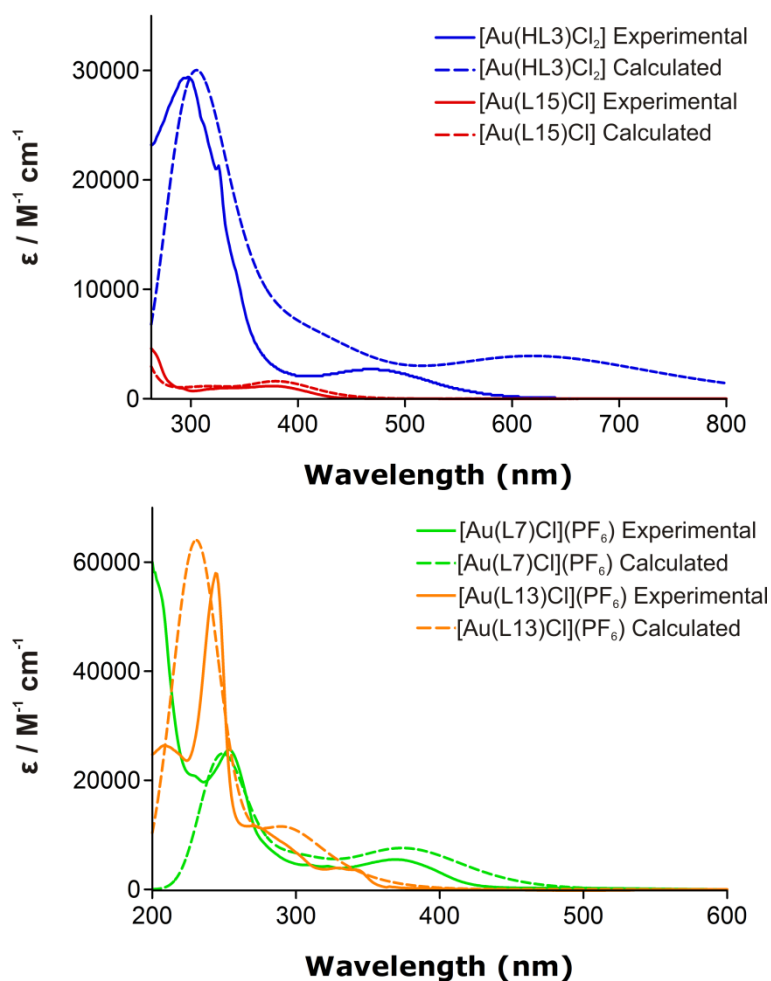


Figure 6.4.6: Overlay of experimental and calculated UV-vis spectra for compounds [Au(HL3)Cl₂], [Au(L7)Cl](PF₆), [Au(L13)Cl](PF₆) and [Au(L15)Cl]. Extinction coefficient scaling factors of 0.2 and 0.75 were applied to the calculated data for compounds [Au(L13)Cl](PF₆) and [Au(L15)Cl] respectively. Bandwidth of 2600 cm⁻¹ was used to generate the calculated spectra.

In general, the correlations between the experimental and calculated data were satisfactory. The purpose of the energy calculations was not only to compare experimental data against observed data, but also to provide insight into the orbital parentage of the transitions responsible for the observed UV-Vis spectra. Metal compounds [Au(HL3)Cl₂], [Au(L7)Cl](PF₆), [Au(L13)Cl](PF₆) and [Au(L15)Cl] are used as representative complexes in the discussion below. The calculated spectra shown in Figure 6.4.6 are the result of several electronic transitions between various molecular orbitals, not only the HOMO and the LUMO. The energy levels for the major orbitals as well as the orbital plots for the frontier orbitals for compounds [Au(HL3)Cl₂], [Au(L7)Cl](PF₆), [Au(L13)Cl](PF₆) and [Au(L15)Cl] are displayed in Figure 6.4.7.

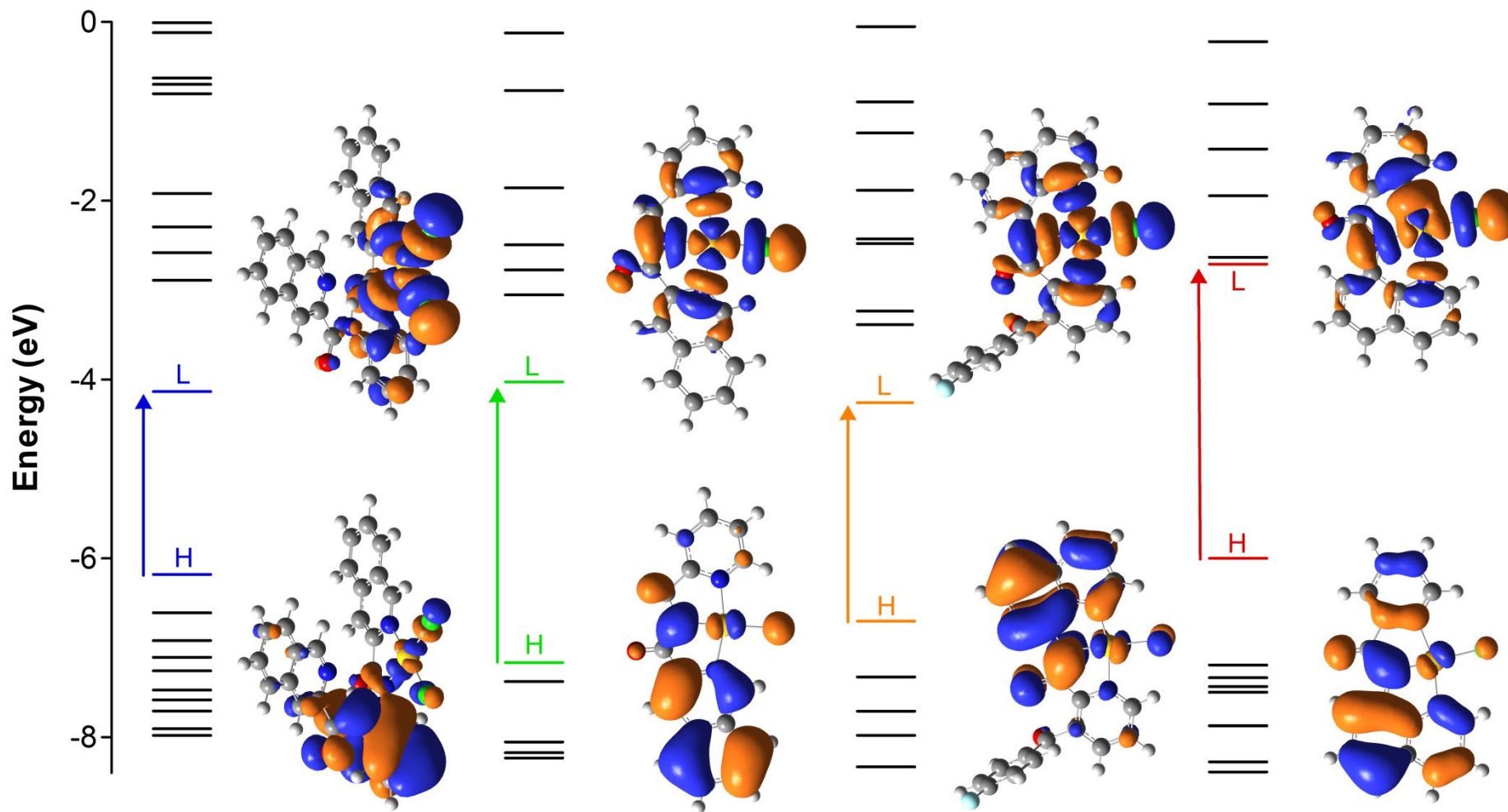


Figure 6.4.7: Energy level diagram for complex cations (from left to right) of compounds $[\text{Au}(\text{HL3})\text{Cl}_2]$, $[\text{Au}(\text{L7})\text{Cl}](\text{PF}_6)$, $[\text{Au}(\text{L13})\text{Cl}](\text{PF}_6)$ and $[\text{Au}(\text{L15})\text{Cl}]$, depicting the HOMO(H) \rightarrow LUMO(L) electronic transition as well as the frontier orbital plots for each complex.

Computational

The method and basis set used in the calculations achieves a respectable level of accuracy in determining the major absorption bands as can be seen from the overlaid spectra in Figure 6.4.6. In some cases, such as for [Au(L13)Cl](PF₆) and [Au(L15)Cl], a scaling factor needs to be applied to the extinction coefficient. The band that was most accurately predicted was the higher energy π - π^* band in the 200-300 nm range while the lower energy mixed transition band was less accurately predicted. A summary of the predicted and experimental absorption bands for compounds [Au(HL3)Cl₂], [Au(L7)Cl](PF₆), [Au(L13)Cl](PF₆) and [Au(L15)Cl] is given in Table 6.4.4. Since the remainder of the gold(III) compounds studies were all similar to one of the representative examples described in detail above.

The HOMO plot for all representative compounds is dominated by a π -symmetry MO centred over the ligand with slight metal d orbital character. In the case of [Au(HL3)Cl₂] the π -symmetry MO is centred over the phenylenediamine ring and the ligand-based MO is slightly admixed with the d_{xz} (or d_{yz}) orbital of the gold(III) ion. A large percentage of the HOMO for compounds [Au(L7)Cl](PF₆), [Au(L13)Cl](PF₆) and [Au(L15)Cl] relates to a π -symmetry MO located over the quinoline ring with slight metal d character relating to a d_{yz} MO. The LUMO plot for all representative compounds is dominated by d orbital metal character and for all cases the d orbital corresponds to the $d_{x^2-y^2}$ orbital. In all cases, the lowest energy transition occurs between the HOMO and the LUMO and can therefore be ascribed as a ligand-to-metal charge transfer (LMCT) transition. Interestingly, these transitions are calculated to be very weak with almost negligible oscillator strengths. The lower energy transitions with more appreciable oscillator strengths generally occur from lower lying orbitals with mixed π - and σ -character to the LUMO and LUMO+1. Since the calculated molecular orbitals are generally mixed with contributions from both ligand and metal it is impossible to assign a single transition to a corresponding experimentally observed peak. The experimental peaks, rather, have to be assumed to be the sum of several transitions between several different mixed orbitals. The predicted HOMO, LUMO and ligand field splitting energies (LFSE Δ_o) for compounds [Au(HL3)Cl₂], [Au(L7)Cl](PF₆), [Au(L13)Cl](PF₆) and [Au(L15)Cl] are -6.179, -4.135, 2.004; -7.166, -4.027, 3.139; -6.701, -4.258, 2.433 and -6.000, -2.710, 3.290 eV, respectively. Compound [Au(L15)Cl] has the largest LFSE at 3.290 eV consistent with a strong ligand field and reflective of the ligand's powerful C₆H₅⁻ σ -donor group.

Computational

Table 6.4.4: Summary of calculated and experimental transitions for the major peaks of the representative gold(III) compounds [Au(HL3)Cl₂], [Au(L7)Cl](PF₆), [Au(L13)Cl](PF₆) and [Au(L15)Cl].

Compound	Exp. (nm)	Calc. (nm)	MOs*	<i>f</i> *	Transition assignment
[Au(HL3)Cl ₂]	468	635	135(H)→136(L)	0.0910	π→σ*
		520	130, 133, 134→136(L)	0.0216	π, π, π→σ*
	297	448	132→136(L)		π→σ*
		301	134→139; 134→140; 135(H)→140	0.2307	π→π*, π→π*, π→π*
		295	133→138	0.0966	π→π*
[Au(L7)Cl](PF ₆)	342	342	81, 84→87(L)	0.0323	σ, σ→σ*
		318	81, 84→87(L) 85→88	0.0243	σ, σ→σ*, π→π*
	244	244	80, 82, 83→88	0.0493	π, π, π→π*
		236	82,83→88; 83→89	1.0647	π, π→π*, π→π*
		231	80→88; 83→89; 85→91	0.3198	π→π*, π→π*, π→π*
[Au(L13)Cl](PF ₆)	369	388	113(H)→115,116; 108→114(L)	0.0744	π→π*, π* σ→σ*
		376	113(H)→115,116; 110→114(L)	0.1403	π→π*, π* σ/π→σ*
	255	256	107→115; 110→118; 112→117	0.2665	π→π*, σ/π→π* π→π*
		246	109→116; 112→117; 113(H)→119	0.3447	π→π* π→π*, π→π*
	[Au(L15)Cl]	376	382	82(H)→84	0.1709
322			79→83(L); 82(H)→85	0.0980	σ→σ*, π→π*

*MO, molecular orbital; *f*, oscillator strength; H, HOMO; L, LUMO.

The presence of the C₆H₅- σ-donor group significantly raises the energy of the LUMO (-2.710 eV) while a similar, but less significant, effect is observed for the HOMO. Compound [Au(L7)Cl](PF₆) has the second largest splitting energy at 3.139 eV which is consistent with the fact that it comprises a less aromatic ligand with reduced pi-donor capacity (and thus more sigma-donor character) relative to [Au(HL3)Cl₂] and [Au(L13)Cl](PF₆). The energy of the HOMO is also noticeably lower in energy than the HOMOs [Au(HL3)Cl₂], [Au(L13)Cl](PF₆) and [Au(L15)Cl]. This trend is not only applicable to compound [Au(L7)Cl](PF₆) but also to the

Computational

sister compounds $[\text{Au}(\text{L5})\text{Cl}](\text{PF}_6)$ and $[\text{Au}(\text{L6})\text{Cl}](\text{PF}_6)$ (available in Appendix C). This indicates an intrinsic electronic difference between the non-aromatic aminomethyl-based ligands and the balance of the ligands discussed in this work.

CALCULATED NMR DATA:

The ^1H and ^{13}C NMR spectra were calculated using the same level of theory that was used for the geometry optimisation, frequency and energy calculations. Since a split basis set has been used with C, H, N, O, F and Cl atoms described the large 6-311G(d,p) basis set and the gold(III) ion by the ECP basis set LanL2DZ, we expected the results on a whole to be fairly accurate. This was found to be true for both calculated ^1H and ^{13}C chemical shifts. Interestingly, the ^1H and ^{13}C calculated shifts obtained for both compounds $[\text{Au}(\text{L5})\text{Cl}](\text{PF}_6)$ and $[\text{Au}(\text{L13})\text{Cl}](\text{PF}_6)$ were extremely poor and hence have been left out of all comparisons as outliers.

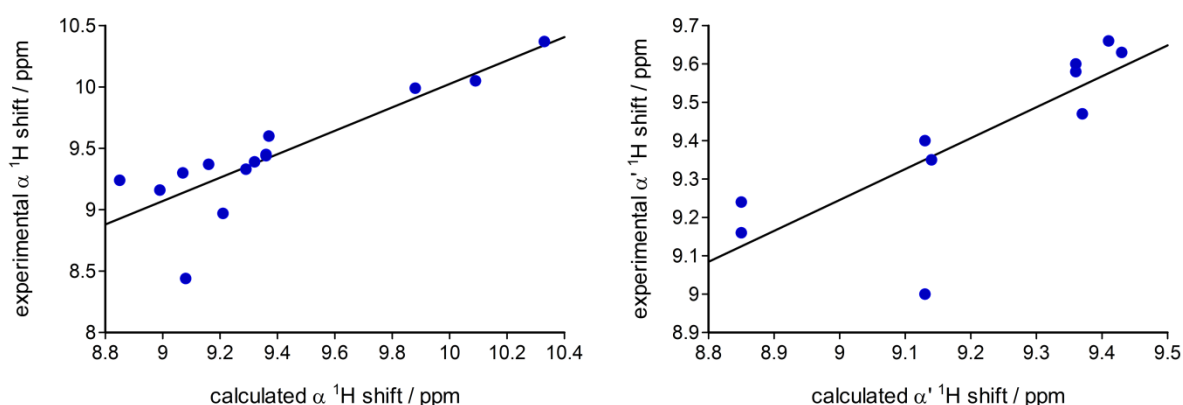


Figure 6.4.8: Plot of experimental versus calculated α - (left) and α' - (right) ^1H chemical shifts for compounds discussed in the work. Chemical shifts for compounds $[\text{Au}(\text{L5})\text{Cl}](\text{PF}_6)$ and $[\text{Au}(\text{L13})\text{Cl}](\text{PF}_6)$ have been removed as outliers. The correlation coefficients of the respective fits are 0.876 and 0.800. Compounds $[\text{Au}(\text{HL1})\text{Cl}_2]$ – $[\text{Au}(\text{L4})\text{Cl}_2]$ do not contain an α' -proton and hence were not included in the respective plot.

Since the compounds presented in this work are structurally quite diverse there are few proton and carbon signals that are common to all compounds and thus available for a systematic comparison. One such set of signals are the α - and α' -proton signals (see Chapter 4). The computational method performs admirably when predicting the α - and α' -proton chemical shifts for all compounds. The predicted values were generally overestimated, but within 7% of the experimental values (Table 6.4.5). A plot of experimental versus calculated

Computational

chemical shifts for both α - and α' -protons reveals that the error seems to be systematic and therefore a correction factor could be determined in order to apply an empirical correction (Figure 6.4.8).

Equations 6.4.2 and 6.4.3 below, represent the linear relationships between the experimental and the calculated chemical shift data for the α - and α' -protons, respectively.

$$\sigma_{\alpha \text{ proton}}^{\text{exp}} = 1.087 \times \nu_{\alpha \text{ proton}}^{\text{calc}} - 0.821 \text{ ppm} \quad 6.4.2$$

$$\sigma_{\alpha' \text{ proton}}^{\text{exp}} = 0.805 \times \nu_{\alpha' \text{ proton}}^{\text{calc}} + 1.991 \text{ ppm} \quad 6.4.3$$

Table 6.4.5: Comparison of experimental and calculated ^1H NMR data for the gold(III) compounds studied in this work.

Complex	Exp.	Calc.	Diff.*	Exp.	Calc.	Diff.*
	$\delta(^1\text{H}) \alpha /$ ppm	$\delta(^1\text{H}) \alpha /$ ppm	ppm	$\delta(^1\text{H}) \alpha /$ ppm	$\delta(^1\text{H}) \alpha' /$ ppm	ppm
[Au(HL1)Cl ₂]	9.32	9.39	-0.07	N/A	N/A	N/A
[Au(HL2)Cl ₂]	9.29	9.33	-0.04	N/A	N/A	N/A
[Au(HL3)Cl ₂]	10.33	10.37	-0.04	N/A	N/A	N/A
[Au(L4)Cl ₂]	9.36	9.45	-0.09	N/A	N/A	N/A
[Au(L5)Cl](PF ₆)	9.12	7.12	2	9.08	6.95	2.13
[Au(L6)Cl](PF ₆)	9.07	9.30	-0.23	9.13	9.40	-0.27
[Au(L7)Cl](PF ₆)	9.88	9.99	-0.11	9.14	9.35	-0.21
[Au(L8)Cl](PF ₆)	9.21	8.97	0.24	9.13	9.00	0.13
[Au(L9)Cl](PF ₆)	8.99	9.16	-0.17	9.36	9.58	-0.22
[Au(L10)Cl](PF ₆)	9.16	9.37	-0.21	9.41	9.66	-0.25
[Au(L11)Cl](PF ₆)	10.09	10.05	0.04	9.43	9.63	-0.20
[Au(L12)Cl](PF ₆)	9.37	9.60	-0.23	9.37	9.47	-0.10
[Au(L13)Cl](PF ₆)	9.38	-0.71	10.09	9.38	0.45	8.93
[Au(L14)Cl](PF ₆)	9.36	9.44	-0.18	9.36	9.60	-0.24
[Au(L15)Cl]	9.08	8.44	0.64	8.85	9.16	0.31
[Au(L16)Cl]	8.85	9.24	0.39	8.85	9.24	0.39

*Diff.: Exp. – Calc.

As was mentioned in Chapter 4, proton *f* for compounds [Au(L6)Cl](PF₆) and [Au(L10)Cl](PF₆) was the furthest downfield resonance due to the deshielding effect of the unconventional

C–H···O hydrogen bond present. This assignment was confirmed by the similar prediction obtained from the calculated results. The accuracy of the prediction, however, was lower than for the other proton signals. The experimental chemical shifts were 9.85 and 9.86 ppm, respectively, while the calculated chemical shifts were predicted to be further downfield at 10.62 and 10.73 ppm, respectively.

The analogous calculated carbon chemical shifts, α and α' , were similarly compared to the experimental data (Table 6.4.6). The results were encouraging with the majority of the calculated shifts falling within 5% of the experimental chemical shifts (Figure 6.4.9).

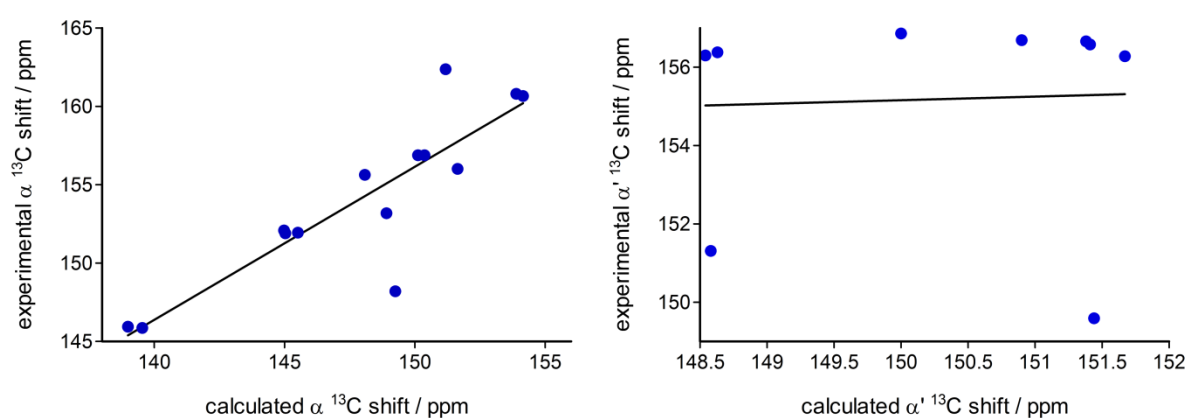


Figure 6.4.9: Plot of experimental versus calculated α -(left) and α' -(right) ^{13}C chemical shifts for compounds discussed in the work. Chemical shifts for compounds [Au(L15)Cl] and [Au(L16)Cl] have been left out as the corresponding experimental values could not be determined. The correlation coefficient of the respective fits are 0.868 and 0.046 respectively.

$$\sigma_{\alpha \text{ carbon}}^{\text{exp}} = 0.805 \times \nu_{\alpha \text{ carbon}}^{\text{calc}} + 1.991 \text{ ppm} \quad 6.4.4$$

$$\sigma_{\alpha' \text{ carbon}}^{\text{exp}} = 0.092 \times \nu_{\alpha' \text{ carbon}}^{\text{calc}} + 141.3 \text{ ppm} \quad 6.4.5$$

The plot shows that there is a linear relationship between the experimental and the calculated values for the α -carbon chemical shifts. The mathematical relationship is depicted by equation 6.4.4 above. A similar relationship was not observed for the α' -carbon chemical shifts (equation 6.4.5).

Computational

Table 6.4.6: Comparison of experimental and calculated ^{13}C NMR data for the gold(III) compounds studied in this work.

Complex	Exp.	Calc.	Diff.*	Exp.	Calc.	Diff.*
	$\delta(^{13}\text{C}) \alpha /$ ppm	$\delta(^{13}\text{C}) \alpha /$ ppm	ppm	$\delta(^{13}\text{C}) \alpha /$ ppm	$\delta(^{13}\text{C}) \alpha' /$ ppm	ppm
[Au(HL1)Cl ₂]	145.51	151.94	-6.43	N/A	N/A	N/A
[Au(HL2)Cl ₂]	145.03	151.90	-6.87	N/A	N/A	N/A
[Au(HL3)Cl ₂]	150.37	156.88	-6.51	N/A	N/A	N/A
[Au(L4)Cl ₂]	144.98	152.08	-7.1	N/A	N/A	N/A
[Au(L5)Cl](PF ₆)	148.91	153.18	-4.27	148.58	151.31	-2.73
[Au(L6)Cl](PF ₆)	138.99	145.94	-6.95	148.63	156.38	-7.75
[Au(L7)Cl](PF ₆)	154.15	160.66	-6.51	148.54	156.30	-7.76
[Au(L8)Cl](PF ₆)	149.25	148.20	1.05	151.44	149.59	1.85
[Au(L9)Cl](PF ₆)	148.08	155.63	-7.55	151.41	156.58	-5.17
[Au(L10)Cl](PF ₆)	139.54	145.86	-6.32	151.38	156.66	-5.28
[Au(L11)Cl](PF ₆)	153.89	160.80	-6.91	150.90	156.69	-5.79
[Au(L12)Cl](PF ₆)	150.12	156.88	-6.76	151.67	156.28	-4.61
[Au(L13)Cl](PF ₆)	151.18	162.37	-11.19	149.68	103.29	46.39
[Au(L14)Cl](PF ₆)	151.64	156.01	-4.37	150.00	156.86	-6.86

*Diff.: Exp. – Calc.

6.5 References

1. F. Jensen, *Introduction to Computational Chemistry*, Wiley and Sons, New York, 1999.
2. J. B. Foresman and Frisch, *Exploring Chemistry with Electronic Structure Methods*, Gaussian Inc., Pittsburgh, 1996.
3. D. Young, *Computational Chemistry: A practical guide for applying techniques to real world problems*, Wiley and Sons, New York, 2001.
4. C. J. Cramer, *Essentials of Computational Chemistry*, Wiley and Sons, London, 2002.
5. E. G. Lewars, *Computational Chemistry: Introduction to the Theory and Applications of Molecular and Quantum Mechanics*, 2nd Edition edn., Springer, 2011.
6. C. Lee, W. Yang and R. G. Parr, *Phys. Rev. B*, 1988, **37**, 785-789.
7. A. D. Becke, *J. Chem. Phys.*, 1993, **98**, 5648-5652.
8. P. J. Stephens, F. J. Devlin, M. J. Frisch and C. F. Chabalowski, *J. Chem. Phys.*, 1994, **98**, 11623-11627.
9. C. Adamo and V. Barone, *J. Chem. Phys.*, 1999, **110**, 6158-6159.
10. J. Heyd, J. E. Peralta, G. E. Scuseria and R. L. Martin, *J. Chem. Phys.*, 2005, **123**, 174101-174108.
11. J. Heyd and G. E. Scuseria, *J. Chem. Phys.*, 2004, **120**, 7274-7280.
12. J. Heyd and G. E. Scuseria, *J. Chem. Phys.*, 2004, **121**, 1187-1192.
13. J. Heyd, G. E. Scuseria and M. Ernzerhof, *J. Chem. Phys.*, 2006, **124**, 219906/219901.
14. A. D. McLean and G. S. Chandler, *J. Chem. Phys.*, 1980, **72**, 5639-5648.
15. R. Krishnan, J. S. Binkley, R. Seeger and J. A. Pople, *J. Chem. Phys.*, 1980, **72**, 650-654.
16. T. Clark, J. Chandrasekhar, G. W. Spitznagel and P. v. R. Schleyer, *J. Comput. Chem.*, 1983, **4**, 294-301.
17. P. J. Hay and W. R. Wadt, *J. Chem. Phys.*, 1985, **82**, 299-310.
18. P. J. Hay and W. R. Wadt, *J. Chem. Phys.*, 1985, **82**, 270-283.
19. W. R. Wadt and P. J. Hay, *J. Chem. Phys.*, 1985, **82**, 284-298.
20. P. Schwerdtfeger, M. Dolg, W. H. E. Schwarz, G. A. Bowmaker and P. D. W. Boyd, *J. Chem. Phys.*, 1989, **91**, 1762-1774.
21. V. K.-M. Au, W. H. Lam, W.-T. Wong and V. W.-W. Yam, *Inorg. Chem.*, 2012, **51**, 7537-7545.
22. A. Castineiras, S. Dehnen, A. Fuchs, I. Garcia-Santos and P. Sevillano, *Dalton Trans*, 2009, 2731-2739.
23. A. Djekovic, B. Petrovic, Z. D. Bugarcic, R. Puchta and E. R. van, *Dalton Trans.*, 2012, **41**, 3633-3641.
24. C. Gabbiani, A. Casini, L. Messori, A. Guerri, M. A. Cinellu, G. Minghetti, M. Corsini, C. Rosani, P. Zanello and M. Arca, *Inorg Chem*, 2008, **47**, 2368-2379.
25. T. Marino, N. Russo, M. Toscano and M. Pavelka, *Dalton Trans.*, 2012, **41**, 1816-1823.
26. D. V. Partyka, T. J. Robilotto, M. Zeller, A. D. Hunter and T. G. Gray, *Proc. Natl. Acad. Sci.*, 2008, **105**, 14293-14297.
27. E. L. Noey, Y. Luo, L. Zhang and K. N. Houk, *J. Am. Chem. Soc.*, 2012, **134**, 1078-1084.
28. L. Ye, Y. Wang, D. H. Aue and L. Zhang, *J. Am. Chem. Soc.*, 2012, **134**, 31-34.
29. R. E. Stratmann, G. E. Scuseria and M. J. Frisch, *J. Chem. Phys.*, 1998, **109**, 8218-8224.
30. P. Pyykkoe and F. Mendizabal, *Inorg. Chem.*, 1998, **37**, 3018-3025.
31. Q.-J. Pan and H.-X. Zhang, *Inorg. Chem.*, 2004, **43**, 593-601.
32. M. Cossi, N. Rega, G. Scalmani and V. Barone, *J. Comput. Chem.*, 2003, **24**, 669-681.
33. *Mercury*, (2012) Cambridge Crystallographic Data Centre, Cambridge, UK.

Computational

34. J. R. Cheeseman, G. W. Trucks, T. A. Keith and M. J. Frisch, *J. Chem. Phys.*, 1996, **104**, 5497-5509.
35. R. Ditchfield, *Mol. Phys.*, 1974, **27**, 789-807.
36. F. London, *J. Phys. Radium*, 1937, **8**, 397-409.
37. K. Wolinski, J. F. Hinton and P. Pulay, *J. Am. Chem. Soc.*, 1990, **112**, 8251-8260.
38. B.-Z. Yang, X. Zhou, T. Liu, F.-Q. Bai and H.-X. Zhang, *J. Phys. Chem. A*, 2009, **113**, 9396-9403.

7. Biological studies

7.1 Introduction

Gold compounds have received much attention in recent years related to their potential use as chemotherapeutic agents.^{1, 2} The use of gold compounds as anti-cancer agents is varied with both gold(I) and gold(III) compounds being investigated as potential candidates.^{3, 4} Gold(I) compounds are linear in geometry and therefore are generally unable to target DNA via intercalation. Gold(III) compounds, on the other hand, are generally square planar in nature (due to the vacant $d_{x^2-y^2}$ orbital) and are therefore ideal candidates for the preparation of DNA-targeted intercalators.¹ Since gold(III) complexes are highly electron deficient this enables them to form favourable axial Au- π interactions between the gold(III) ion and the DNA base pairs which stabilise the gold(III) centre. The fact that the gold ion is in the +3 oxidation state similarly allows for the generation of positively charged compounds that are able to interact electrostatically with the negatively charged phosphate backbone of DNA. All these properties allow for gold(III) compounds to be potential chemotherapeutic drugs.

Currently the treatment of cancer is based on three major approaches depending on the type, location and health of the patient in question. The first two, surgery and radiation therapy, are locoregional and largely successful if the cancer is non-metastatic, accessible, and the patient is of good health and the cancer is caught early.⁵ Both are however fairly aggressive approaches with surgery being invasive and radiation causing burns. Both of these approaches are highly developed compared to chemotherapy which still has great potential for further development.⁵ Chemotherapy is a systematic treatment that is mainly used for the treatment of metastatic cancers. Combinatorial chemotherapy is most often used with multiple different drugs being administered simultaneously in order to maximise the efficacy of the treatment.⁶ The major problem associated with chemotherapy are the side-effects experienced by the patients; therefore there is a major drive in the development of new chemotherapeutics that are targeted and have far fewer and less severe side effects.

The gold(III) compounds synthesised in this work have been designed to be chemotherapeutic agents via the intercalation of DNA. This process is anticipated to induce

apoptosis through the inhibition or poisoning of the topoisomerase group of enzymes. The cytotoxicity profiles of the gold(III) compounds have been assessed by the *in vitro* screening process administered by the National Cancer Institute (NCI)⁷ in association with the Developmental Therapeutics Program (DTP).⁷ These organisations are both part of the American National Institute of Health (NIH) and a key goal of these research-led entities is to screen synthetic compounds and natural products against their library of 60 common human cancer cell lines and to prioritise the development of successful candidates into commercial anti-cancer agents. The ranges of tumour cell lines include leukaemia, melanoma, lung, colon, central nervous system, ovary, breast, prostate and kidney. An application for the screening of a compound is submitted to the NCI and upon review is either denied or accepted into the first phase of testing. This phase consists of a single dose (10^{-5} M) screen across all 60 NCI human cancer cell lines. The results of this screening process then determine whether the compound proceeds to the second phase of testing. This takes the form of a 5-dose screen (ranging from 10^{-9} to 10^{-5} M in order of magnitude increments), from which three dose response parameters can be calculated:

- 1) GI₅₀, the concentration of the compound at which there is a 50% growth inhibition compared to the control.⁸
- 2) TGI or IC₅₀, the concentration of the compound at which there is total growth inhibition.⁸
- 3) LC₅₀, the concentration of the compound at which there is a 50% reduction in growth.⁸

If the candidate compound performs well in the 5-dose phase of testing, the process is repeated, known as repeat 5-dose, in order to determine the reproducibility of the results. Once a compound has successfully passed the repeat 5-dose phase it is submitted to a biological evaluation committee who assess the candidate's results and make a decision on whether the candidate is suitable for *in vivo* testing. Lead compound [Au(L12)Cl](PF₆) made it to this stage of testing (an *in vivo* hollow fibre assay),⁹ where the candidate's ability to effect the net cell growth of a respective cancerous cell line contained within a subcutaneously and/or intraperitoneally implanted hollow fibre. This is after dosage via intraperitoneal injection of the candidate drug in mice.

There are several advantages to having a drug candidate screened against a wide range of cell lines, as is the case for compounds screened at the NCI. The first advantage is that any specificity that a test compound may express towards a particular cell line or class of cell lines can be detected. This may allow for the more specific treatment of individual cancer cell lines. Secondly, it allows for the statistical comparison of the activity profile of the candidate against the activity profile of a series of well-known chemotherapeutic agents that have identified mechanisms of action (MOA). This analysis allows for the indication of a MOA for the drug candidate and therefore reduces the valuable time and money that would otherwise be required for such a determination. A large data set for comparison would tend to increase the reliability of the statistical analysis.

7.2 Experimental

7.2.1 *In vitro* cell screening⁸

The *in vitro* cell screening was performed by the DTP within the NCI and therefore the screening protocol has been directly acquired from their website.

The human tumour cell lines of the cancer screening panel are grown in Roswell Park Memorial Institute Media (RPMI) 1640 medium containing 5% fetal bovine serum and 2 mM L-glutamine. For a typical screening experiment, cells are inoculated into 96 well microtiter plates in 100 μ L at plating densities ranging from 5,000 to 40,000 cells/well depending on the doubling time of individual cell lines. After cell inoculation, the microtiter plates are incubated at 37 °C, 5% CO₂, 95% air and 100% relative humidity for 24 h prior to addition of the experimental drugs.

After 24 h, two plates of each cell line are fixed *in situ* with tricarboxylic acid (TCA), to represent a measurement of the cell population for each cell line at the time of drug addition (Tz). Experimental drugs are solubilised in dimethyl sulfoxide at 400-fold the desired final maximum test concentration and stored frozen prior to use. At the time of drug addition, an aliquot of frozen concentrate is thawed and diluted to twice the desired final maximum test concentration with complete medium containing 50 μ g/mL gentamicin. Additional four, 10-fold or ½ log serial

Biological Studies

dilutions are made to provide a total of five drug concentrations plus a control. Aliquots of 100 μL of these different drug dilutions are added to the appropriate microtiter wells already containing 100 μL of medium, resulting in the required final drug concentrations.

Following drug addition, the plates are incubated for an additional 48 h at 37 °C, 5% CO_2 , 95% air, and 100% relative humidity. For adherent cells, the assay is terminated by the addition of cold TCA. Cells are fixed *in situ* by the gentle addition of 50 μL of cold 50% (w/v) TCA (final concentration, 10% TCA) and incubated for 60 minutes at 4 °C. The supernatant is discarded, and the plates are washed five times with tap water and air dried. Sulforhodamine B (SRB) solution (100 μL) at 0.4% (w/v) in 1% acetic acid is added to each well, and plates are incubated for 10 minutes at room temperature. After staining, unbound dye is removed by washing five times with 1 % acetic acid and the plates are air dried. Bound stain is subsequently solubilised with 10 mM trizma base, and the absorbance is read on an automated plate reader at a wavelength of 515 nm. For suspension cells, the methodology is the same except that the assay is terminated by fixing settled cells at the bottom of the wells by gently adding 50 μL of 80% TCA (final concentration, 16% TCA). Using the seven absorbance measurements [time zero, (Tz), control growth, (C), and test growth in the presence of drug at the five concentration levels (Ti)], the percentage growth is calculated at each of the drug concentrations levels. Percentage growth inhibition is calculated as:

$$[(\text{Ti}-\text{Tz})/(\text{C}-\text{Tz})] \times 100 \text{ for concentrations for which } \text{Ti} \geq \text{Tz}$$

$$[(\text{Ti}-\text{Tz})/\text{Tz}] \times 100 \text{ for concentrations for which } \text{Ti} < \text{Tz}.$$

Three dose response parameters are calculated for each experimental agent. Growth inhibition of 50% (GI_{50}) is calculated from $[(\text{Ti}-\text{Tz})/(\text{C}-\text{Tz})] \times 100 = 50$, which is the drug concentration resulting in a 50% reduction in the net protein increase (as measured by SRB staining) in control cells during the drug incubation. The drug concentration resulting in total growth inhibition (TGI) is calculated from $\text{Ti} = \text{Tz}$. The LC_{50} (concentration of drug resulting in a 50% reduction in the measured

protein at the end of the drug treatment as compared to that at the beginning) indicating a net loss of cells following treatment is calculated from $[(T_i - T_z)/T_z] \times 100 = -50$. Values are calculated for each of these three parameters if the level of activity is reached; however, if the effect is not reached or is exceeded, the value for that parameter is expressed as greater or less than the maximum or minimum concentration tested.

7.2.2 *In vivo* testing⁹

The *in vivo* cell screening was performed by the DTP within the NCI and therefore the screening protocol has been directly acquired from their website.

MAXIMUM TOLERATED DOSE DETERMINATION:

Generally, maximum tolerated dose MTD determinations are done in a way that conserves compound and limits the number of animals used to the barest minimum possible. Thus, a single mouse is given a single injection intraperitoneally, intravenously, subcutaneously, intramuscularly or orally (IP, IV, SC, IM or PO) of 400 mg/kg (or lower if the compound is anticipated to be extremely potent, e.g. natural products); a second mouse receives a dose of 200 mg/kg and a third mouse receives a single dose of 100 mg/kg. The mice are observed for a period of 2 weeks. They are sacrificed if they lose more than 20% of their body weight or if there are other signs of significant toxicity. If all 3 mice must be sacrificed, then the next 3 dose levels (50, 25, 12.5 mg/kg) are tested in a similar way. This process is repeated until a tolerated dose is found. This dose is then designated the maximum tolerated dose and is used to calculate the amount of material given to experimental mice during anti-tumour testing. The mice are allowed *ad libitum* feed and water. Injections are most commonly administered IP, but SC, PO, and IV dosing may be required upon occasion. Dose volumes are generally 0.01 mL gm⁻¹ body weight but may be up to 0.02 mL gm⁻¹ body weight for the IP, IV, SC and PO routes of administration.

HOLLOW FIBRE ASSAY:

A standard panel of 12 tumour cell lines is used for the routine hollow fibre screening of the in vitro actives. These include NCI-H23, NCI-H522, MDA-MB-231, MDA-MB-435, SW-620, COLO 205, LOX, UACC-62, OVCAR-3, OVCAR-5, U251 and SF-295. In addition, alternate lines can be used for specialised testing of compounds on a non-routine basis. The cell lines are cultivated in RPMI-1640 containing 10% foetal bovine serum (FBS) and 2 mM glutamine. On the day preceding hollow fibre preparation, the cells are given a supplementation of fresh medium to maintain log phase growth. For fibre preparation, the cells are harvested by the standard trypsinization technique and resuspended at the desired cell density ($(2-10 \times 10^6 \text{ cells/mL})$). The cell suspension is flushed into 1 mm (internal diameter) polyvinylidene fluoride hollow fibres with a molecular weight exclusion of 500,000 Da. The hollow fibres are heat-sealed at 2 cm intervals and the samples generated from these seals are placed into tissue culture medium and incubated at 37 °C in 5% CO₂ for 24 to 48 hours prior to implantation. A total of 3 different tumour lines are prepared for each experiment so that each mouse receives 3 intraperitoneal implants (1 of each tumour line) and 3 subcutaneous implants (1 of each tumour line). On the day of implantation, samples of each tumour cell line preparation are quantitated for viable cell mass by a stable endpoint MTT assay so that the time zero cell mass is known. Mice are treated with experimental agents starting on day 3 or 4 following fibre implantation and continuing daily for 4 days. Each agent is administered via IP injection at 2 dose levels. The doses are based on the MTD determined during prior acute toxicity testing. The fibres are collected from the mice on the day following the fourth compound treatment and subjected to the stable endpoint MTT assay. The optical density of each sample is determined spectrophotometrically at 540 nm and the mean of each treatment group is calculated. The percent net growth for each cell line in each treatment group is calculated and compared to the percent net growth in the vehicle treated controls. A 50% or greater reduction in percent net growth in the treated samples compared to the vehicle control samples is considered a positive result. Each positive result is given a score of 2 and all of the

scores are totalled for a given compound. The maximum possible score for an agent is 96 (12 cell lines X 2 sites X 2 dose levels X 2 [score]). A compound is considered for xenograft testing if it has a combined IP + SC score of 20 or greater, a SC score of 8 or greater, or produces cell kill of any cell line at either dose level evaluated. This scoring system has been validated by Division of Cancer Treatment, Diagnosis and Centres (DCTDC) statisticians in Cancer Therapy Evaluation Program (CTEP) to represent a level of detection expected to score current "standard" agents as active.

7.2.3 Mechanism of action elucidation

The set of 60 GI₅₀ values measured for [Au(HL3)Cl₂], [Au(L6)Cl](PF₆), [Au(L10)Cl](PF₆) and [Au(L12)Cl](PF₆) were compared (in negative log format) to the analogous publically available DTP data for 25 well-known anti-cancer drugs that have established MOAs. More specifically, the data were analysed using KyPlot 5.0 with a statistical multivariate cluster analysis algorithm (group average method, Minkowski distances) to calculate a dendrogram on which the analysed set of anti-cancer drugs cluster according to similarities in their GI₅₀ profiles and thus mechanisms of action.

7.2.4 Gel electrophoresis experiments

TOPOISOMERASE IB and II α INHIBITION ASSAYS:¹⁰

Human topoisomerase II α (topo II α) catalysed dsDNA decatenation reactions were performed with purified kinetoplast DNA (kDNA) and purified enzyme (TopoGen Inc., Port Orange, FL) essentially following the manufacturer's published method. Experiments were performed by Alex Fagenson or Wanvipa Ruangpradit under the supervision of Professor Mark T. Muller at the School of Medicine, Biomolecular Research Annex, University of Central Florida. Briefly, 200 ng/ μ L of kDNA was prepared as a master mix in a topo II α cleavage assay buffer containing 30 mM Tris-HCl (pH 7.6), 60 mM NaCl, 8 mM MgCl₂, 15 mM dithiothreitol, 3 mM ATP, and 30 μ g mL⁻¹ BSA (TopoGen product code TG4040). Aliquots of the master mix solution (29 μ L) were used for separate reactions in 1 mL polyethylene microcentrifuge tubes by additions (1.0 μ L) of appropriate standard solutions of compound and etoposide (topo II α interfacial poison control) dissolved in DMSO. All reaction tubes

contained 0.5% DMSO and DMSO was thus used as the zero-drug control in one reaction tube. Reactions were incubated with 2 units of topo II α for 30 minutes at 37 °C, stopped with 3.0 μ L of 10% sodium dodecyl sulfate (SDS) and digested with Proteinase K (0.5 mg mL⁻¹) for another 30 minutes at 37 °C. (One unit of topo II α is defined as the amount of enzyme required to fully decatenate 0.1 μ g of kDNA in 15 min at 37 °C.) The reaction solutions were then mixed with 6.0 μ L of 6X electrophoresis loading dye (50% aqueous glycerol, 0.025% bromophenol blue). Aliquots from each dyed solution (5.0 μ L) were loaded on a freshly-cast 1% agarose gel containing 0.5 μ g mL⁻¹ ethidium bromide (EB, a cationic DNA intercalator control) and electrophoresed in 1X TBE buffer (88 mM boric acid, 88 mM Tris base, 10 mM EDTA, pH 7.8) containing 0.5 μ g mL⁻¹ EB at 50 V for 60 min. The gel was destained in deionised water for 15 min and imaged with UV transillumination (302 nm) on a Syngene ChemGenius system.

Inhibition of topo IB-catalysed relaxation of negatively super-coiled pHOT1 plasmid DNA was studied by two methods: (1) conventional DNA unwinding assays as designed, marketed, and distributed by TopoGen Inc. and (2) a new assay contrived to discriminate between a topo IB catalytic inhibitor and a topo IB interfacial poison, where similar conditions to the conventional unwinding are used except for the use of a 5-10 fold increase in enzyme concentration as well as the absence of sodium chloride.

DNA MOBILITY SHIFT ASSAY:

The significant cytotoxicity profile of [Au(HL3)Cl₂], [Au(L12)Cl](PF₆) and [Au(L13)Cl](PF₆) and the presence of chelated and metal-free isoquinoline moieties in their structures (i.e. known DNA intercalator groups) warranted an assessment of their DNA-binding affinity. Standard spectroscopic titrations of the metal complexes with calf thymus DNA in phosphate-buffered 5% DMSO solutions (pH 7.0, 25 °C) gave irreproducible binding isotherms as a result of concomitant demetallation of the complex for [Au(HL3)Cl₂] and possible diverse modes of interaction with DNA for [Au(L12)Cl](PF₆) and [Au(L13)Cl](PF₆). Electrophoretic gel mobility shift assays (EMSAs) were required to reproducibly detect an interaction between the compounds and DNA. These experiments were performed by Prof Orde Munro or Wanvipa Ruangpradit in Prof Mark T. Mullers laboratory at the School of Medicine, Biomolecular Research Annex, University of Central Florida. The method below is given for

Biological Studies

the sake of completeness. For these experiments, $6.3 \text{ ng } \mu\text{L}^{-1}$ of negatively supercoiled pHOT1 plasmid DNA (TopoGen, Inc.) was used as the dsDNA substrate. Reaction solutions were prepared by mixing $1.0 \text{ } \mu\text{L}$ of a $188 \text{ ng } \mu\text{L}^{-1}$ pHOT1 stock solution, $3.0 \text{ } \mu\text{L}$ pH 7.9 1X TGS buffer (100 mM Tris-HCl, 10 mM EDTA, 1.5 M NaCl, 1 mM spermidine, 1% BSA, 50% v/v glycerol), and $25.0 \text{ } \mu\text{L}$ of deionised water in 1 mL polyethylene microcentrifuge tubes. To these solutions were added $1.0 \text{ } \mu\text{L}$ aliquots of standard solutions of EB, or mAMSA (a neutral DNA intercalator control) in DMSO (molecular biology-grade, Sigma) to give final control compound concentrations of 500 nM, $5.0 \text{ } \mu\text{M}$, and $50 \text{ } \mu\text{M}$. For all compounds, additions of $1.0 \text{ } \mu\text{L}$ aliquots of appropriate freshly-made standard solutions of the test compound in DMSO were made to an analogous series of pHOT1-containing reaction solutions ($29.0 \text{ } \mu\text{L}$ total volumes) to give final compound concentrations of 5.0 nM, 50 nM, 100 nM, 500 nM, $1.0 \text{ } \mu\text{M}$, $5 \text{ } \mu\text{M}$, $10 \text{ } \mu\text{M}$, $25 \text{ } \mu\text{M}$ and $50 \text{ } \mu\text{M}$ for $[\text{Au}(\text{HL3})\text{Cl}_2]$. Concentration ranges including $0.5 \text{ } \mu\text{M}$, $1 \text{ } \mu\text{M}$, $5 \text{ } \mu\text{M}$, $15 \text{ } \mu\text{M}$, $50 \text{ } \mu\text{M}$, $150 \text{ } \mu\text{M}$ and $500 \text{ } \mu\text{M}$ were prepared and used in the experiment. The solutions were incubated at $37 \text{ } ^\circ\text{C}$ for 15 min before adding $6.0 \text{ } \mu\text{L}$ of 6X electrophoresis loading dye (50% aqueous glycerol, 0.025% bromophenol blue) and mixing by vortex centrifugation. Aliquots from each dyed solution ($5.0 \text{ } \mu\text{L}$) were loaded on a freshly cast 1% agarose gel and electrophoresed in 1X TBE buffer (88 mM boric acid, 88 mM Tris base, 10 mM EDTA, pH 7.8) at 50 V for 60 min. The gel was rinsed in deionised water and stained for 10 min in an aqueous 1X TBE-buffered EB solution ($0.5 \text{ } \mu\text{g mL}^{-1}$) prior to imaging with UV transillumination (302 nm) on a Syngene ChemGenius system.

7.3 Results and Discussion

7.3.1 NCI-60 *in vitro* cytotoxicity screens

In this work sixteen novel gold(III) compounds have been synthesised and applications for all compounds were sent to the NCI for screening against their 60 human cancer cell lines. All compounds with the exception of [Au(HL1)Cl₂] were accepted since the latter complex was deemed structurally too similar to [Au(HL2)Cl₂]. Compounds [Au(HL2)Cl₂]-[Au(L15)Cl] all underwent one-dose screening at a concentration of 10⁻⁵ M. Compound [Au(L16)Cl] had limited solubility and was thus rejected by the NCI after multiple attempts at the one-dose screening process without success. In general, the results for the compounds that successfully underwent one-dose screening were extremely promising. The results of the one-dose screen for compound [Au(L12)Cl](PF₆) are shown below in Figure 7.3.1.1.

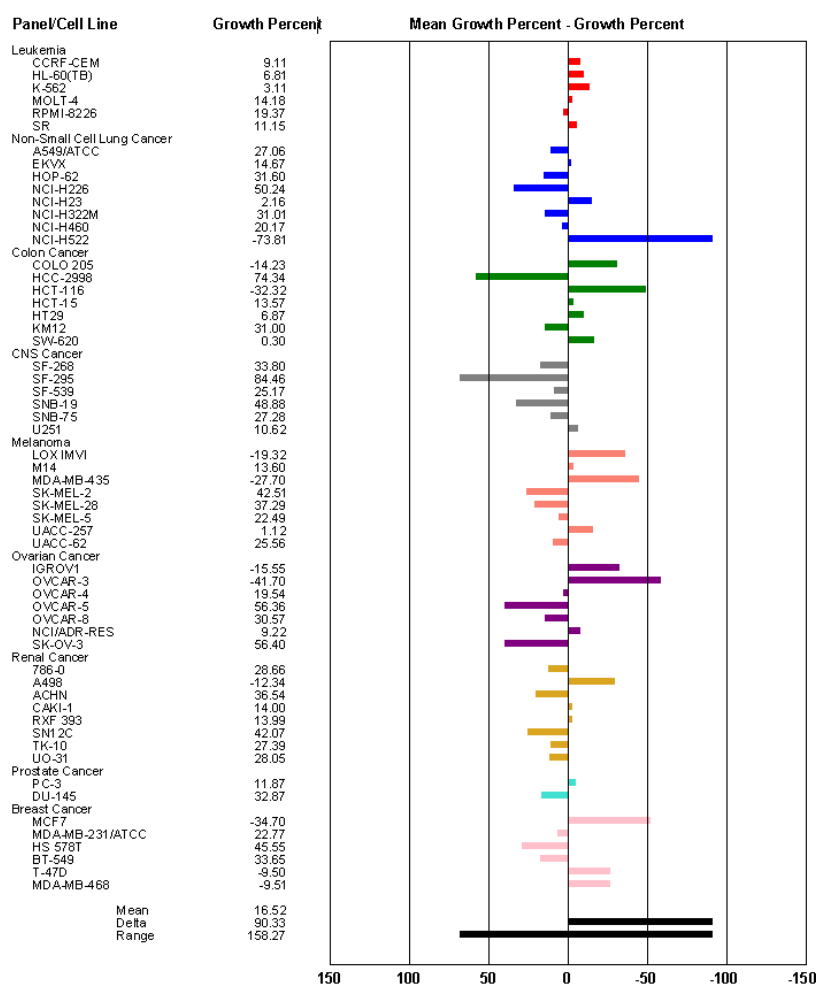


Figure 7.3.1.1: One-dose screening results for compound [Au(L12)Cl](PF₆) over 60 human cancer cell lines. The bars have been coloured according to the cell line panel.

Biological Studies

Figure 7.3.1.1 shows the preliminary one-dose screening results obtained for compound $[\text{Au}(\text{L12})\text{Cl}](\text{PF}_6)$ over the full 60 cell line panel against which the NCI screens all new candidate compounds. This preliminary data gives the NCI an idea of the cytotoxicity of the compound and whether it should be considered for further testing. It also gives an indication as to the relative susceptibility of the cell lines towards the compound. In the case for $[\text{Au}(\text{L12})\text{Cl}](\text{PF}_6)$, the one-dose screen indicates that the compound exhibits inherent specificity towards certain cell lines. This indicates that the compound is not just a non-specific poison, but rather a potential chemotherapeutic agent with a well-defined mode of action through which it exerts its cytotoxic activity. Similar data for the balance of the compounds was obtained and available in appendix D. The one-dose results for compound $[\text{Au}(\text{L12})\text{Cl}](\text{PF}_6)$ indicate that the compound is most effective against leukaemia, colon and breast cancer cell lines. Compound $[\text{Au}(\text{L12})\text{Cl}](\text{PF}_6)$ is also effective against a few isolated melanoma and ovarian cancer cell lines while it is least effective against non-small cell lung, central nervous system and renal cancer cell lines. A summary of the single dose screening data for all compounds is displayed in Figure 7.3.1.2

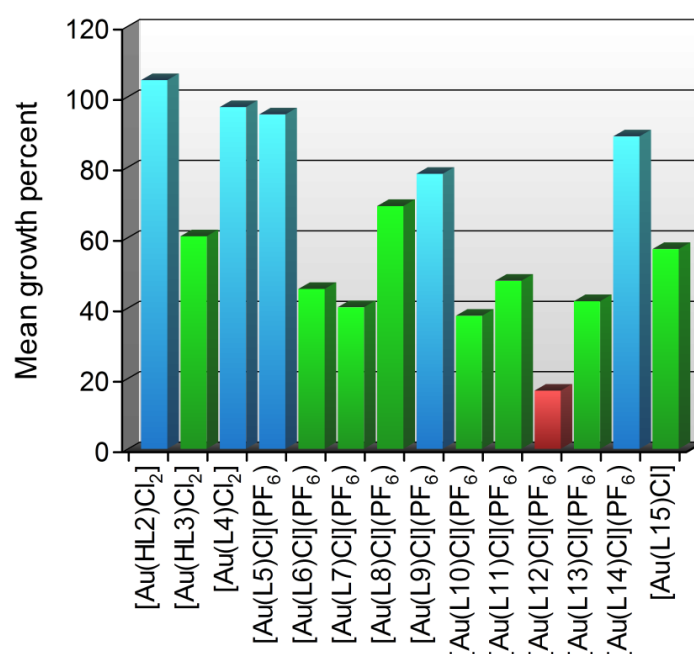


Figure 7.3.1.2: Mean growth percent for all compounds submitted for one-dose testing against the NCI-60 cell lines. The blue bars represent compounds that failed the one-dose screen, green bars represent compounds that were accepted to 5-dose screening and the red bar indicates the compound that was accepted through to the *in vivo* phase of testing.

Based on the results of the one-dose screening process for compounds [Au(HL2)Cl₂]-[Au(L15)Cl], nine compounds were further selected for the second stage 5-dose screening process, from which, dose-response parameters could be determined. Of the nine compounds, [Au(L12)Cl](PF₆), was further selected for the initial *in vivo* phase of testing. Some interesting trends were observed when analysing the mean growth percentage results as a function of structural parameters for the complexes. Compounds [Au(HL2)Cl₂], [Au(L4)Cl] and [Au(L5)Cl](PF₆) contain only pyridine rings within the compound structure compared to the nine compounds proceeding through to 5-dose which all contain at least one quinoline ring system indicating that the presence of a quinoline ring system is of vital importance to the biological activity of the compounds studied in this work. This is not surprising as many chemotherapeutic agents contain quinoline ring systems such as topotecan,¹¹ a topoisomers I poison; amsacrine,^{12, 13} a topoisomerase II poison, and ciprofloxacin, a broad spectrum antibiotic that inhibits DNA gyrase in prokaryotes.¹⁴ Compound [Au(L9)Cl](PF₆) is identical to [Au(L8)Cl](PF₆) except for the fact that it has a butyl substituent in the *para* position of the pyridine ring. This bulky *para* substitution evidently plays an important role in the ability of the compound to affect its cytotoxic behaviour as it was not selected to progress through to 5-dose testing, unlike the unsubstituted compound [Au(L8)Cl](PF₆). An interesting trend in cytotoxicity was also observed between similar compounds [Au(L12)Cl](PF₆) – [Au(L14)Cl](PF₆). Compound [Au(L12)Cl](PF₆) is the most active compound in the one-dose screen with a mean growth percent of 16.52% and contains an unsubstituted phenyl ketone moiety off the 3' position of the pyridine ring, whereas compounds [Au(L13)Cl](PF₆) and [Au(L14)Cl](PF₆) contain bulkier fluoro and methoxy *para*-substituted phenyl ketone moieties. This increased bulk introduced by the substituent group evidently results in a poorer performance in their cytotoxicity profiles. So much so that the methoxy-substituted compound, [Au(L14)Cl](PF₆), did not proceed past the one-dose phase of testing while compound [Au(L13)Cl](PF₆) was accepted through to the 5-dose phase but did not perform to the level of [Au(L12)Cl](PF₆). Compounds [Au(L15)Cl] and [Au(L16)Cl] were synthesised isostructurally to compounds [Au(L8)Cl](PF₆) and [Au(L10)Cl](PF₆) except for the change in chelating rings from N-donor pyridine and isoquinoline to C-donor phenyl and naphthyl. The anionic carbon donor introduces the neutral compounds compared to the cationic complexes which are the main focus of this work. This was performed to assess the ability of the neutral compounds to similarly perform as possible chemotherapeutic agents

Biological Studies

without the presence of a positive charge. Compound [Au(L16)Cl] was unable to be assessed due to poor solubility which was to be expected as similar neutral cyclometallated gold(III) compounds are generally only soluble in non-polar solvents such as DCM and CHCl₃. Compound [Au(L15)Cl] was soluble enough to progress through the one-dose phase and into the 5-dose phase of testing. Interestingly it outperformed its analogous cationic compound, [Au(L8)Cl](PF₆), in both single dose and 5-dose screens. This indicates that the cationic charge on the compounds is not necessarily required for the compound to be biologically active. This may be due to the ability of the electron deficient gold(III) centre being able to form strong Au- π interactions between the compound and the base pairs of DNA without an overall cationic charge. Further analogous compounds with a similar neutral charge need to be synthesised and screened in order to confirm this trend.

Table 7.3.1.1: Summary of the average cytotoxicity data over the 60 human cancer cell lines for each of the nine compounds: [Au(HL3)Cl₂], [Au(L6)Cl](PF₆)-[Au(L8)Cl](PF₆), [Au(L10)Cl](PF₆)-[Au(L13)Cl](PF₆) and [Au(L15)Cl] as well as some commercially available chemotherapeutic agents for comparison.

Drug	Log High Conc / M	GI ₅₀ / μ M	TGI / μ M	LC ₅₀ / μ M
[Au(HL3)Cl ₂]	-4	9.85	38.86	>100
[Au(L6)Cl](PF ₆)	-4	2.52	36.92	>100
[Au(L7)Cl](PF ₆)	-4	2.54	39.47	>100
[Au(L8)Cl](PF ₆)	-4	13.83	51.04	>100
[Au(L10)Cl](PF ₆)	-4	1.79	19.56	>100
[Au(L11)Cl](PF ₆)	-4	2.73	37.66	>100
[Au(L12)Cl](PF ₆)	-4	0.80	11.36	80.64
[Au(L13)Cl](PF ₆)	-4	2.41	33.86	>100
[Au(L15)Cl]	-4	9.85	87.02	>100
Etoposide*	-4	4.11	60	>100
Topotecan*	-4	0.62	26	79.6
Cisplatin*	-4	4.67	27	>100
Daunorubicin*	-4	0.20	1.4	18.9

*Data obtained from NCI DTP database.¹⁵

Nine compounds from the fifteen selected for one-dose screening were further selected for 5-dose screens. These compounds were [Au(HL3)Cl₂], [Au(L6)Cl](PF₆)-[Au(L8)Cl](PF₆), [Au(L10)Cl](PF₆)-[Au(L13)Cl](PF₆) and [Au(L15)Cl]. A summary of the average cell growth

response parameters for each of these three complexes against the full NCI 60 cell line panel is displayed in Table 7.3.1.1. This data has been compiled for 60 human cancer cell lines from the NCI database for the commercial drugs etoposide, topotecan, cisplatin and daunorubicin as well as the compounds presented in this work.¹⁵ The data show that, in general, the GI₅₀ values for compounds derived from this work compare fairly well with the commercially available chemotherapeutic drugs. In particular, compound [Au(L12)Cl](PF₆) performs extremely well with its average GI₅₀ value being 0.80 μM compared to the GI₅₀ values of daunorubicin and topotecan at 0.20 and 0.62 μM, respectively. The GI₅₀ values of [Au(L6)Cl](PF₆), [Au(L7)Cl](PF₆), [Au(L10)Cl](PF₆), [Au(L11)Cl](PF₆) and [Au(L13)Cl](PF₆) at 2.52, 2.54, 1.79, 2.73 and 2.41 μM, respectively, were similarly encouraging, being less potent than daunorubicin and topotecan but slightly more potent than cisplatin and etoposide. Compounds [Au(HL3)Cl₂], [Au(L8)Cl](PF₆) and [Au(L15)Cl] were the least active compounds that made it to the 5-dose phase of testing; however, their activities were still notable.

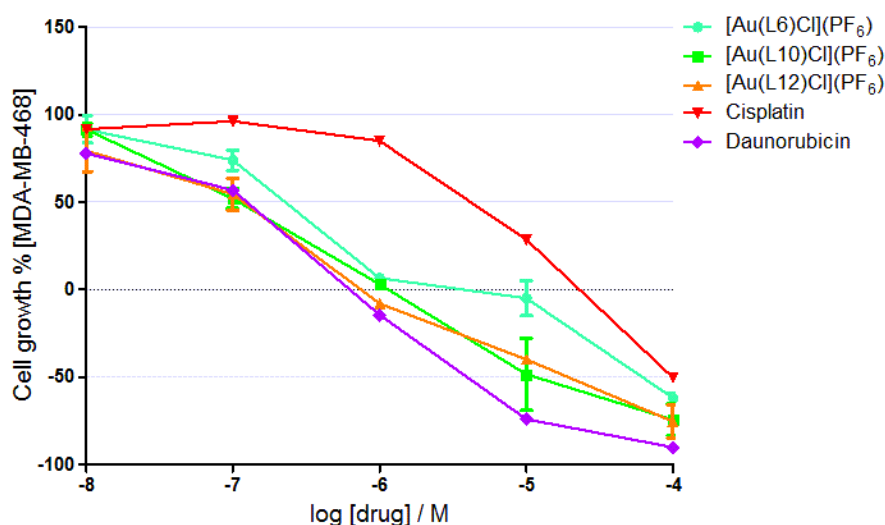


Figure 7.3.1.3: Dose-response data for the commercial anti-cancer drugs, cisplatin and daunorubicin as well as the gold(III) compounds [Au(L6)Cl](PF₆), [Au(L10)Cl](PF₆) and [Au(L12)Cl](PF₆) synthesised in this work. The data measures the response of the Colon cancer cell line HCT-116 to varying concentrations of the compounds mentioned above. The data for the commercial drugs, cisplatin and daunorubicin, were obtained from the DTP drug repository database.¹⁵

The dose-response data exhibited in Figure 7.3.1.3, above, shows the growth response of the human colon cancer cell line, HCT-116, in response to varying concentrations of compounds [Au(L6)Cl](PF₆), [Au(L10)Cl](PF₆) and [Au(L12)Cl](PF₆) as well as the commercial

anti-cancer agents cisplatin and daunorubicin. The response of the HCT-116 cell line to the three compounds synthesised in this work is interesting as it is fairly linear in nature and in fact, very similar to the comparative commercially available drugs. A consequence of this type of response is that one generally requires a significant increase in concentration to effect a 50% cell death (LC_{50}) from 50% growth inhibition (GI_{50}). A more traditional response is a sigmoidal, S-shaped response. This type of response has the characteristic that it requires a fairly high concentration to initiate 50% cell growth inhibition (GI_{50}), however, a relatively small increase in concentration allows for the progression to effect a 50% cell death (LC_{50}).

Five representative compounds from this work were selected and a bar graph, depicting the $-\log GI_{50}$ values for the above mentioned compounds as well as some commercially available drugs, generated (Figure 7.3.1.4).

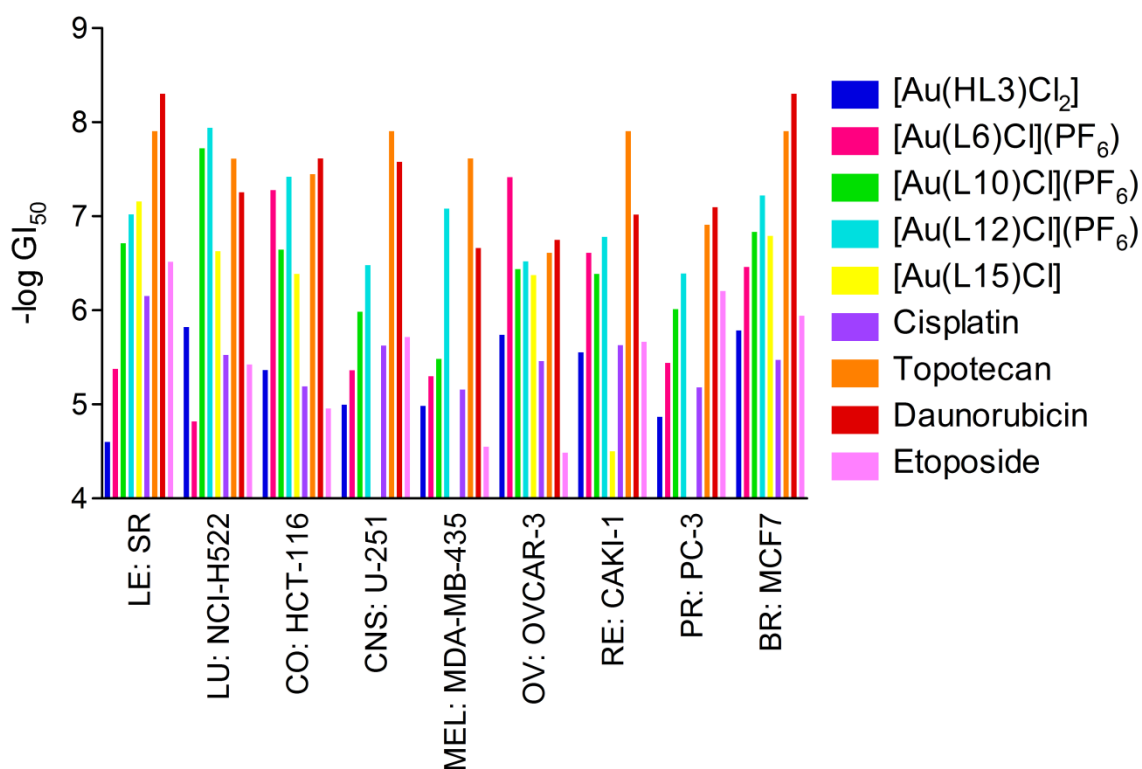


Figure 7.3.1.4: Comparison of the $-\log GI_{50}$ values for complexes $[Au(HL3)Cl_2]$, $[Au(L6)Cl](PF_6)$, $[Au(L10)Cl](PF_6)$, $[Au(L12)Cl](PF_6)$ and $[Au(L15)Cl]$ against some commercially available anti-cancer drugs for some specific cancer cell lines.

The comparison was performed to graphically assess and compare the cytotoxicity of the compounds synthesised in this work against some reference chemotherapeutic agents. From Figure 7.3.1.4 one can see that compound $[Au(L12)Cl](PF_6)$ (blue bar) is more cytotoxic

than the commercial chemotherapeutic agents cisplatin and etoposide in every cell line represented on the graph and, in most cases, quite significantly more active. The cytotoxicity profile of compound $[\text{Au}(\text{L12})\text{Cl}](\text{PF}_6)$ can even compete with, and in some cases is more active than, the ultra high activity chemotherapeutic drugs topotecan and daunorubicin. Compounds $[\text{Au}(\text{L6})\text{Cl}](\text{PF}_6)$ and $[\text{Au}(\text{L10})\text{Cl}](\text{PF}_6)$ are less active than compound $[\text{Au}(\text{L12})\text{Cl}](\text{PF}_6)$, however, are still more potent than cisplatin and etoposide in most cases and are therefore still promising candidates. $[\text{Au}(\text{HL3})\text{Cl}_2]$ and $[\text{Au}(\text{L15})\text{Cl}]$ are the least active compounds but are still competitive against cisplatin and etoposide. Considering $[\text{Au}(\text{L12})\text{Cl}](\text{PF}_6)$ is the most active compound synthesised in this work, it was further compared to cisplatin, which is currently the most widely used inorganic anti-cancer agent worldwide. A comparison of the efficacy of the two compounds against all common cell lines in the NCI-60 screen was conducted by plotting the $-\log \text{GI}_{50}$ values for $[\text{Au}(\text{L12})\text{Cl}](\text{PF}_6)$ against the equivalent data for cisplatin (Figure 7.3.1.5).

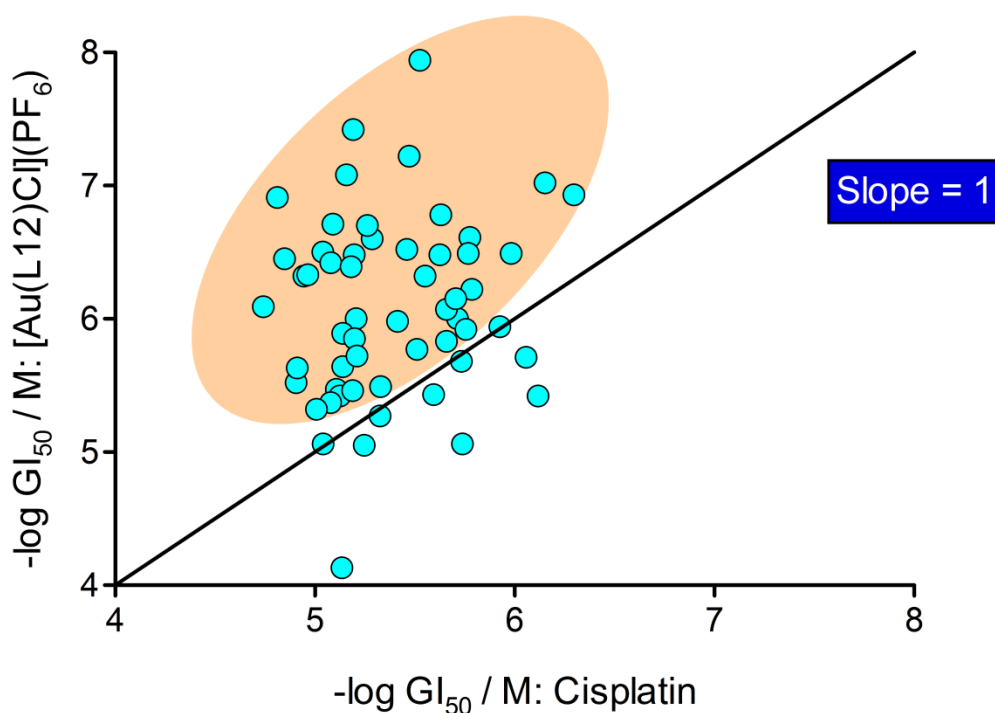


Figure 7.3.1.5: Plot of $-\log \text{GI}_{50}$ values for $[\text{Au}(\text{L12})\text{Cl}](\text{PF}_6)$ versus the same data for cisplatin for all common cell lines in the NCI-60 screen.

As can be seen in Figure 7.3.1.5, a line (black) with a slope of 1 depicts the border where the activity for each respective compound would be equal, hence any data point positioned on that line indicates that the activity of compound $[\text{Au}(\text{L12})\text{Cl}](\text{PF}_6)$ and cisplatin for that

specific cell line are equal. Any data points above the line indicate that compound [Au(L12)Cl](PF₆) is more active and any data points below the line indicate that cisplatin is more active, for each specific cell line in question. From the figure one can immediately see that compound [Au(L12)Cl](PF₆) is significantly more active than cisplatin across almost all the cell lines tested (highlighted oval), with the majority (82%) of the data points (light blue) residing above the equal activity line. There are a few datapoints (7%) on the line, indicating equal activity, while there are only a handful of datapoints (11%) below the equal activity line where cisplatin is the more active drug. Interestingly there were no correlations observed between cytotoxicity, log P_{o/w} and DNA binding affinity other than the counterintuitive correlation between log P_{o/w} and one-dose mean growth percentage for the phenyl ketone based compounds (see Chapter 3). Compound [Au(L12)Cl](PF₆) obtained the most negative log P_{o/w} value (-1.41) but was most active while [Au(L14)Cl](PF₆) exhibited the lowest log P_{o/w} value (-1.00) but did not make it past the one-dose phase. This is interesting as a more positive log P_{o/w} value is generally associated with higher cytotoxic activity due to the compound being able to traverse cellular membranes more efficiently than those with a more negative log P_{o/w} value. The cytotoxicity data presented above for the gold(III) complexes, screened by the NCI, indicate that this class of gold(III) compounds has a potentially bright future in the emerging field of metallo-drug discovery.

7.3.2 NCI *in vivo* testing

The next phase of testing once a drug candidate has displayed significant potential during the *in vitro* screening process is a series of *in vivo* studies designed to determine the toxicity and efficacy of the lead compound in live animals. This involves the testing of a candidate in one or more animal models of neoplastic disease. The *in vivo* phase of testing is crucial to the advancement of a candidate drug that demonstrates *in vitro* activity through to preclinical development. Most above mentioned animal models require substantial materials in terms of laboratory animals and test compounds as well as substantial amounts of time and cost to determine whether a drug or series of drugs has even minimal *in vivo* activity. The hollow fibre assay conducted with mice, described in the Experimental Section 7.2.2, has demonstrated the ability to provide a quantitative guide to drug efficacy with minimal expenditure of time and materials and hence is the initial *in vivo* experience for agents found to have reproducible activity during the *in vitro* drug screens.

Biological Studies

Overall the cytotoxicity profiles of compounds [Au(L6)Cl](PF₆), [Au(L10)Cl](PF₆) and [Au(L12)Cl](PF₆) were deemed to be effective enough to be considered for *in vivo* testing and were hence put forward to an evaluation committee at the NCI where they were assessed as to their potential as chemotherapeutics and hence further investigation through the initial *in vivo* hollow fibre assay. Compound [Au(L12)Cl](PF₆) was the only compound selected, from of the three put forward for biological evaluation, to undergo initial *in vivo* testing.

The first step of this process is to assess the MTD of the drug candidate in mice and the procedure is fully described in the Experimental Section 7.2.2. The reason for conducting this experiment is to conserve time and materials in the long term as one needs be certain that during the hollow fibre assay the mice are not killed by the drug due to a high dose, which would be wasteful in terms of time, money and mice.

The results of the MTD test were reported as follows by the technician from the NCI performing the experiment:

Day 0, [Au(L12)Cl](PF₆): Several minutes after dosing, all mice became sedated. All mice had a very bright pink skin, the 400 mg/kg/injection mouse was dead, and the 200 mg/kg /injection mouse was sedated but very cold and had laboured breathing (sacrificed). The 100 mg/kg/injection mouse was sedated and had a cool body temperature. The next morning, it was still sedated, had red urine, was very cold, and very delayed breathing (sacrificed). The mice that received the 12.5 mg/kg/injection dose and the 50 mg/kg/injection dose were sedated with some movement several minutes after dosing. The 12.5 mg/kg/injection mouse acted normally. The 50 mg/kg/ injection mouse had very pink skin and was still sedated several hours later while the other mice acted normally.

Day 1, all the mice appeared normal. The maximum tolerated dose was therefore determined to be 50 mg/kg/injection.

The hollow fibre assay was then performed using the 12 cell lines as indicated in the experimental section at a high dose concentration of 37.5 mg/kg/dose through IP injection. The NCI states that in order to progress from the hollow fibre assay to the next stage of *in vivo* testing, the xenograft, a drug candidate has to obtain a combined IP + SC score of 20 or

greater, a SC score of 8 or greater, or produces cell kill of any cell line at either dose level evaluated (see Experimental). Compound [Au(L12)Cl](PF₆) performed poorly in this regard, with an IP score of 0 out of 48 and an SC score of 0 out of 48. This data indicates that compound [Au(L12)Cl](PF₆) was ineffective against all cell lines tested. The obvious rationale for this result is that the compound is unable to progress from the injection site to the hollow fibre. The compound would therefore not be able to effect cell growth within the hollow fibre. There are several ways in which the compounds transport may have been affected. The calculated log P_{o/w} value for the compound is -1.41. This indicates that the compound is highly hydrophilic. Drugs with hydrophilic log P_{o/w} values have been shown to be less effective chemotherapeutic agents as they find it significantly more difficult to cross cellular membranes than chemotherapeutics with a more positive log P_{o/w}.¹⁶ Therefore since the drug was administered via intraperitoneal injection, it would have to traverse numerous cellular membranes before reaching the hollow fibre target and hence compound [Au(L12)Cl](PF₆) may not be capable of doing so. Another suggestion as to the poor performance of the compound in the hollow fibre assay is that [Au(L12)Cl](PF₆) has been shown to be susceptible to reductive demetallation through a cellular reducing agent, glutathione. This is a common problem with gold(III)-based drugs.^{3, 17} Therefore [Au(L12)Cl](PF₆) may have a significantly short half-life in the *in vivo* cellular environment which has been shown to be reducing in nature. The last suggestion as to why compound [Au(L12)Cl](PF₆) performed poorly is that it may irreversibly bind to serum albumin proteins found in the blood, such as human serum albumin (HSA). This would prevent the compound from progressing from the blood to the intended target. Drugs that bind to HSA irreversibly have also been shown to be less effective chemotherapeutic agents than those that do not.¹⁸ Overall the result was disappointing but not uninformative. The drug discovery pipeline is a long and arduous process with many setbacks expected. This gives us vital information which we can use to investigate further the means by which the compounds are inactivated. This would then allow us to design new compounds of a second generation that are structurally related with the view of being more potent than the first generation

7.3.3 Mechanism of Action

Although the *in vivo* testing results of compound [Au(L12)Cl](PF₆) were poor, this does not discount this class of compounds from further development. The *in vitro* results of the

gold(III) amide compounds described in this work were nonetheless still extremely exciting and further development of this class of compounds may yet progress through the hollow fibre assay and into the xenograft assay. The next stage in development is to determine how the drugs effect their cytotoxic action. This is crucial as there is often little known about the mode of action of many chemotherapeutic drugs, in particular gold-based metallothrapeutic drugs.

The major advantage of having the drug candidates screened for their cytotoxicity at the NCI is that they are tested against a vast range of cell lines. A substantial body of data are generated for a single compound in that three dose-response parameters, GI₅₀, TGI and LC₅₀, are generated for each cell line tested. This large amount of data makes it possible for a fairly accurate comparison between a drug candidate and several well-known chemotherapeutic drugs with well-known mechanisms of action. This is possible because the NCI have made available the cytotoxic data for numerous commercial chemotherapeutic agents that have been screened according to the same process as the compounds in this work. Due to the significant amount of data for each of the drug candidates as well as commercially available drugs, a fairly accurate and reliable hierarchical cluster analysis can be performed between the cytotoxicity profiles of the respective drugs. There are several established methods for affecting this type of analysis; however, irrespective of the method chosen a similar grouping together of compounds with similar mechanisms of action is obtained. Therefore if drug candidates, [Au(HL3)Cl₂] and [Au(L12)Cl](PF₆) in this case, with unknown mechanisms of action are clustered with well-known drugs that have experimentally determined mechanisms of action, one is able to get an idea of the mechanism of action of the new drug candidate by observing the grouping of the drugs presented as a dendogram. One such dendogram using the group average method and Minkowski distance is displayed in Figure 7.3.3.1. Minkowski metrics are non-Euclidean metrics which are frequently used in applications of multidimensional scaling in statistical analysis.¹⁹ Compounds [Au(HL3)Cl₂] and [Au(L12)Cl](PF₆) were chosen due to their structural dissimilarity and therefore different mechanisms of action. The dendogram displayed in Figure 7.3.3.1 shows the clustering of compounds [Au(HL3)Cl₂] and [Au(L12)Cl](PF₆) according to the probable mechanisms of action. As can be seen, compound [Au(HL3)Cl₂] clearly has a direct link to the commercially available topoisomerase II poison etoposide

(highlighted in red typeface).²⁰ Compound $[\text{Au}(\text{HL3})\text{Cl}_2]$ also has a direct link, although more distant, to daunorubicin and zorubicin, which are similarly potent topoisomerase II poisons.²¹ There is also a distant but direct link to cisplatin. Cisplatin is a well-known DNA cross linker but has also shown to be an effective topoisomerase II inhibitor.²²

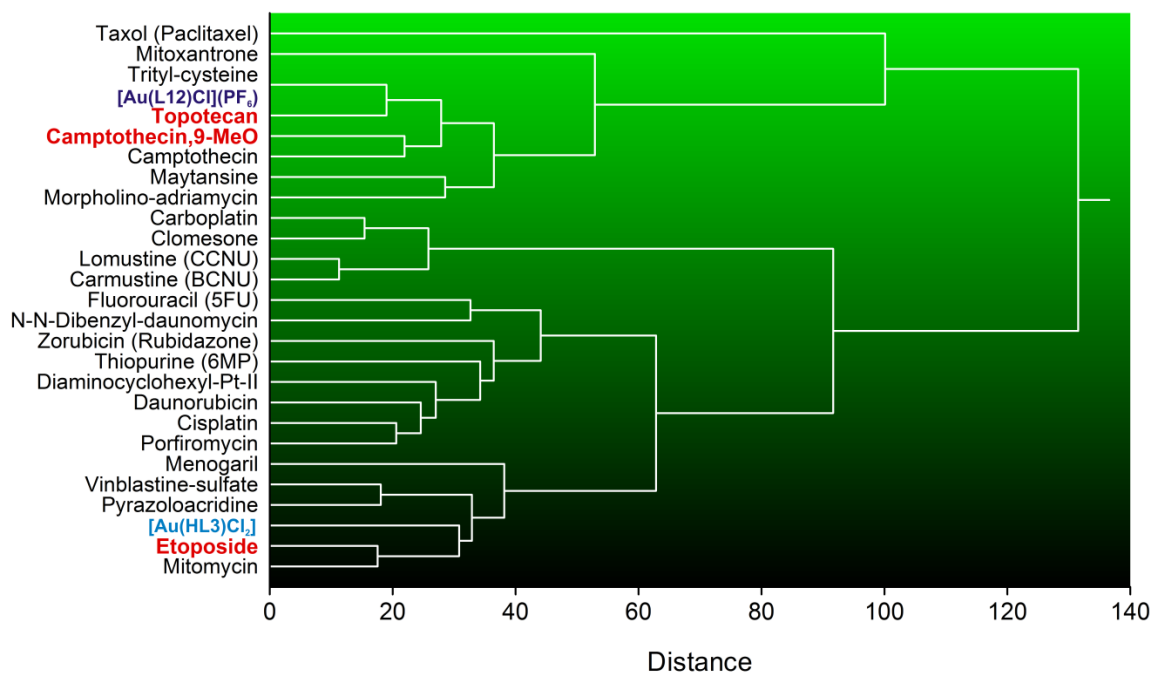


Figure 7.3.3.1: Statistical comparison between the $-\log \text{GI}_{50}$ values of 25 commercially available chemotherapeutic drugs with known mechanisms of action and the gold(III) amide compounds, $[\text{Au}(\text{HL3})\text{Cl}_2]$ (light blue) and $[\text{Au}(\text{L12})\text{Cl}](\text{PF}_6)$ (purple), synthesised in this work.

The isostructural *cis*-chloride ligands present in compound $[\text{Au}(\text{HL3})\text{Cl}_2]$ along with the possibility that they may undergo ligand substitution reactions suggests that $[\text{Au}(\text{HL3})\text{Cl}_2]$ may be able to behave as a DNA cross-linker. This grouping characteristic strongly suggests that compound $[\text{Au}(\text{L12})\text{Cl}](\text{PF}_6)$ is likely to perform as either a topoisomerase II poison or inhibitor, or DNA cross-linker, or both in effecting its cytotoxic activity. $[\text{Au}(\text{L12})\text{Cl}](\text{PF}_6)$, on the other hand, clusters heavily with commercially available topoisomerase I poisons topotecan, camptothecin and 9-MeO-camptothecin (highlighted in red typeface). This clustering behaviour indicates that compound $[\text{Au}(\text{L12})\text{Cl}](\text{PF}_6)$ may perform its cytotoxic activity as either a topoisomerase I poison or inhibitor. Based on this statistical analysis, gel electrophoresis experiments were designed to ascertain whether in fact compounds $[\text{Au}(\text{HL3})\text{Cl}_2]$ and $[\text{Au}(\text{L12})\text{Cl}](\text{PF}_6)$ target topoisomerase II and I, respectively.

DNA topoisomerases are abundant nuclear enzymes that control the topology of DNA and are essential to cell viability.²³ In eukaryotes this group of enzymes is divided into two distinct classes based on their interaction with DNA. Type I topoisomerases are a monomeric unit that cleave one strand of the DNA and perform a controlled rotation, followed by re-ligation on the cleaved strand. There are two major topoisomerase I subtypes, being type IA and type IB. Topoisomerase IB (topo IB), an essential enzyme that acts on the chromatin, making single-strand DNA breaks to relax supercoiled DNA during various genetic events such as transcription, recombination and replication.²⁴ It is therefore a validated target in cancer therapy.²⁵ Type II topoisomerases are homo dimeric and hence are capable of effecting a short-lived double stranded DNA break.²⁶ The enzyme then religates the double-stranded break after passing a distant strand through it. There are two isoforms of topoisomerase type II enzymes, namely topoisomerase II α and topoisomerase II β .²⁷ Topoisomerase II α (topo II α) is similarly essential for cell propagation and essential for the decatenation of catenated DNA.²⁶ It is therefore a validated target in cancer therapy.^{27,}

28

There are two major mechanisms through which a small molecule drug can disrupt the function of both topo IB and II α : (i) catalytic inhibition and (ii) interfacial poisoning.^{20, 29} Most drugs in clinical use today act as interfacial poisons in that they allow the enzyme to make the single- or double- stranded break for topoisomerase I and II, respectively, but then form a stable enzyme-DNA-Drug ternary 'cleavage complex' which inhibits the enzyme from religating the DNA. This results in DNA damage that signals for cell death (apoptosis). Examples of such drugs are camptothecin and etoposide which act as interfacial poisons of topoisomerase I and II, respectively.^{20, 23} In gel electrophoresis experiments the enzyme-catalysed reaction may be followed by the disappearance of supercoiled and catenated DNA and the emergence of nicked open circular and linear DNA for topoisomerase I and II, respectively. Catalytic inhibitors are less well-characterised in literature, but are of great interest in drug design since they are able to effect cell death with minimal DNA damage.^{30,}
³¹ Such catalytic inhibitors exert their catalytic activity by either interacting with the enzyme directly, such as bisdioxopiperazine,^{12, 30} or interacting with the DNA substrate in such a way the topoisomerase enzyme is 'blocked' from interacting and locking onto the DNA to perform its site-specific cleavage. In reaction followed by gel electrophoresis the supercoiled

and catenated DNA remain unchanged as the enzyme is not given a chance to interact with the DNA substrate.

Compounds $[\text{Au}(\text{HL3})\text{Cl}_2]$, $[\text{Au}(\text{L7})\text{Cl}](\text{PF}_6)$ and $[\text{Au}(\text{L13})\text{Cl}](\text{PF}_6)$ were assessed for their ability to inhibit/poison the activity of both topo IB and II α . Topo IB activity was assessed using a commercially available topoisomerase relaxation assay kit available from TopoGEN.¹⁰ The assay makes use of purified topo IB, supercoiled DNA, a linear DNA marker, the drug in question and a control drug, in this case camptothecin. Camptothecin is a commercially available chemotherapeutic agent that is widely used in the treatment of colorectal, small cell lung, ovarian and cervical cancers.⁶ The choice of camptothecin as a control is based on the fact that it is a powerful poison, but a weak inhibitor of topo IB. Comparison of the results of camptothecin with the gold(III) drug in question will give a good indication of whether the gold(III) drug is a poison or a catalytic inhibitor of topo IB. The results for the topoisomerase relaxation assay for compound $[\text{Au}(\text{HL3})\text{Cl}_2]$ are shown below in Figure 7.3.3.2

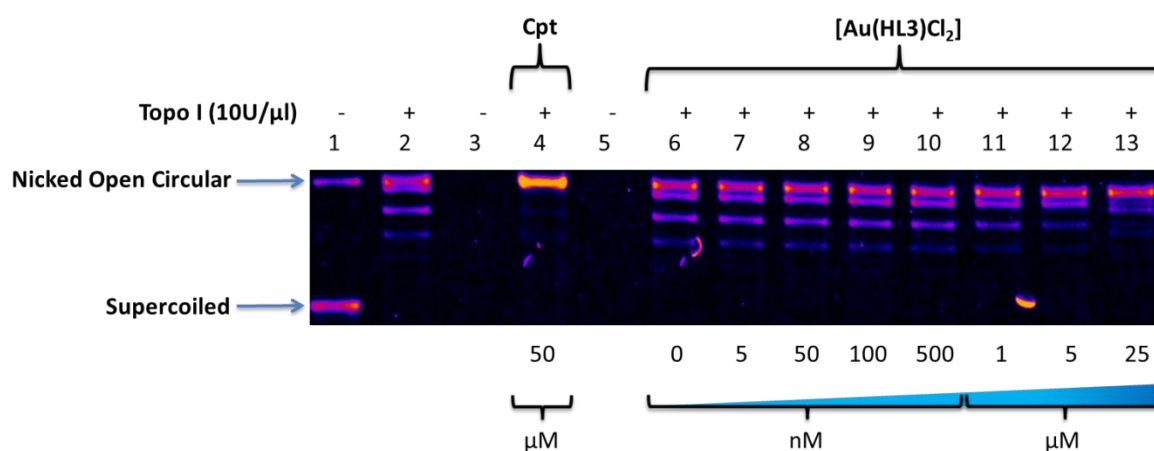


Figure 7.3.3.2: Non-EB gel showing the ineffective poisoning or inhibition of topoisomerase IB by compound $[\text{Au}(\text{HL3})\text{Cl}_2]$ through all concentrations tested.

Lane 1 of the gel (Figure 7.3.3.2) is the DNA control lane. It indicates the presence of both nicked open circular DNA (NOC-DNA) and supercoiled DNA (SC-DNA) without the topo IB enzyme. Lane 2 contains topo IB enzyme but no drug; therefore we see the supercoiled DNA being relaxed into its topoisomers. Lane 4 contains the commercially available topo IB poison, camptothecin, as a control. One can clearly see that the camptothecin control is working correctly since there is no evidence of SC-DNA and a heavy banding of NOC DNA. The remaining lanes as indicated in Figure 7.3.3.2 contain the gold(III) drug $[\text{Au}(\text{HL3})\text{Cl}_2]$

(concentration range 0-25 μM). Evidently the compound tested has a slight inhibitory effect on the functioning of the enzyme as we can see a decreasing concentration of the DNA topoisomers, with increasing drug concentration. The effect is most pronounced at the highest drug concentration of 25 μM . It may be concluded that compound $[\text{Au}(\text{HL3})\text{Cl}_2]$ is a poor to moderate topo IB inhibitor or poison. This result was in agreement with the statistical results which suggested that compound $[\text{Au}(\text{HL3})\text{Cl}_2]$ would be a more effective topo II α inhibitor than a topo IB inhibitor.

Compounds $[\text{Au}(\text{L12})\text{Cl}](\text{PF}_6)$ and $[\text{Au}(\text{L13})\text{Cl}](\text{PF}_6)$ were similarly tested for their ability to act as topo IB poisons or inhibitors. The results for $[\text{Au}(\text{L12})\text{Cl}](\text{PF}_6)$ are shown below as a representative example (Figure 7.3.3.3).

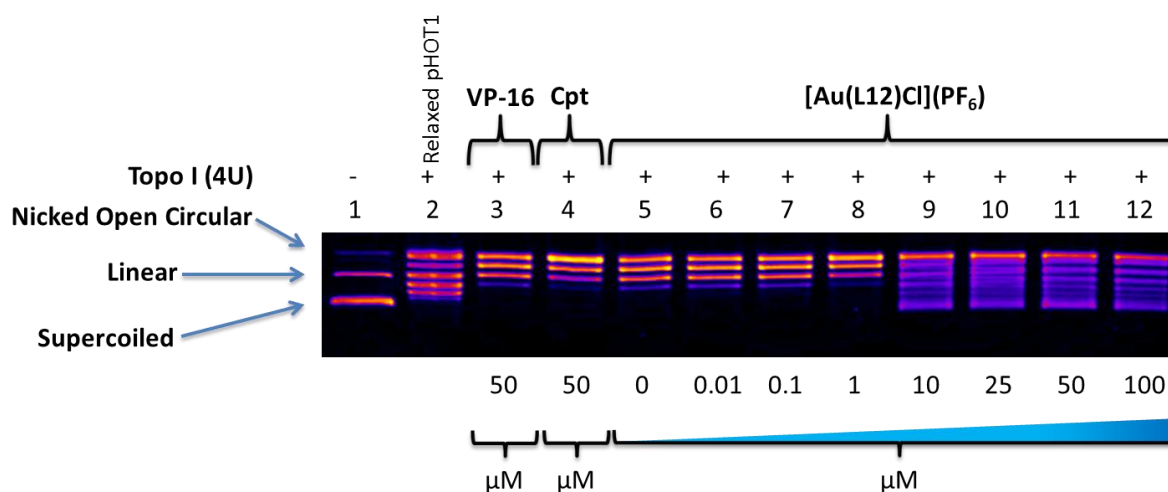


Figure 7.3.3.3: Non-EB gel showing the effective poisoning or inhibition of topoisomerase IB by compound $[\text{Au}(\text{L12})\text{Cl}](\text{PF}_6)$ between metal compound concentrations of 1 and 10 μM .

Lane 1 is the DNA control lane, containing bands of SC-, NOC and linear DNA. Lane 3 contains VP-16 (etoposide which is a topoisomerase II poison and non-intercalator of DNA). We would therefore expect no inhibition of the enzyme, topo IB, by VP-16. We do however see a slight poisoning of the enzyme which may be due to contamination of the control. Lane 4 contains the topo IB control, camptothecin, which displays an increased banding of NOC DNA. This confirms the control is working as expected. Lanes 5-12 contain the gold(III) compound $[\text{Au}(\text{L12})\text{Cl}](\text{PF}_6)$ from concentrations 0-100 μM . The test compound, $[\text{Au}(\text{L12})\text{Cl}](\text{PF}_6)$, acts as a weak interfacial poison of the enzyme, particularly towards a compound concentration of 1 μM , as the DNA banding profile is similar to that seen in the

presence of camptothecin. There is, however, significant catalytic inhibition of the enzyme from a concentration 10 μM onwards, revealed by the heavy banding of SC-DNA and a marked decrease in the concentration of DNA topoisomers. This is because the enzyme is unable to relax the SC-DNA and therefore it remains unchanged and runs as such on the gel. From this gel one can conclude that compound $[\text{Au}(\text{L12})\text{Cl}](\text{PF}_6)$, in all likelihood, acts as a dual mode interfacial poison (at low concentration) and a catalytic inhibitor (at higher concentration) of topo IB. This is further confirmed by a new, topo IB cleavage assay, developed by Professor Mark Muller at the University of Central Florida. In this assay almost all conditions are the same as for the commercially available topo IB relaxation assay except for the fact that there is a large increase in the amount of enzyme units present in the reaction, typically a 5-10 fold increase, and the absence of NaCl. Since there is no NaCl and a large amount of enzyme present in the reaction, DNA anion sites are unsaturated allowing for multiple enzymes to 'lock' onto the DNA making single-stranded breaks at numerous points along the DNA polymer. Supercoiled DNA is effectively linearised under such conditions and detected as a linear DNA band on the gel. In the presence of a topoisomerase poison, such as camptothecin, this results in the generation of linear DNA fragments that can be visualised in a gel electrophoresis experiment such as the one shown in Figure 7.3.3.4. Lane 3, in which camptothecin is the control, contains a broad band indicating the presence of linear DNA which therefore confirms that camptothecin is acting as a topoisomerase poison. Lane's 4-12 contain compound $[\text{Au}(\text{L12})\text{Cl}](\text{PF}_6)$ from 0-20 μM in which there is a slight increase in linear DNA observed from 0-5 μM . The presence of linear DNA then decreases from 5-20 μM . This is consistent with weak poisoning of the enzyme at lower concentrations and catalytic inhibition at higher concentrations of the compound. The experiment therefore confirms that the compound $[\text{Au}(\text{L12})\text{Cl}](\text{PF}_6)$ primarily acts as a topoisomerase catalytic inhibitor but also a poison at low concentrations of compound. Once again this result is in agreement with the statistical prediction which suggested compound $[\text{Au}(\text{L12})\text{Cl}](\text{PF}_6)$ would target topoisomerase I by virtue of clustering with camptothecin, and topotecan.

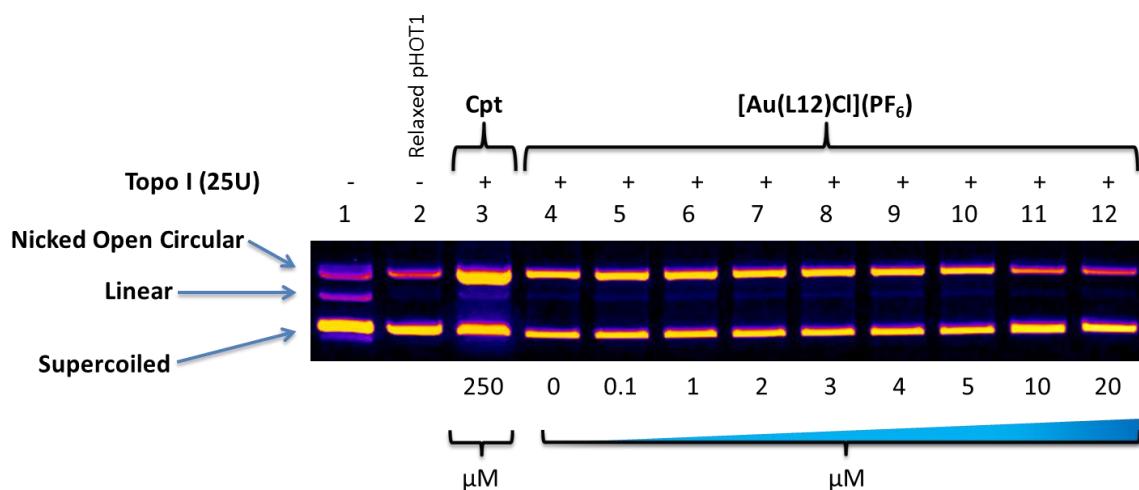


Figure 7.3.3.4: EB gel showing CPT acting as an interfacial poison through its generation of linear DNA. There is a slight increase in linear DNA in presence of compound $[\text{Au}(\text{L12})\text{Cl}](\text{PF}_6)$ from 0-5 μM , after which, a decrease in linear DNA is observed.

Compound $[\text{Au}(\text{L12})\text{Cl}](\text{PF}_6)$ can act as a catalytic inhibitor by either binding to the enzyme or preventing the enzyme binding to the DNA by interacting with DNA in a site-specific manner that is common with the enzyme. The spectroscopic studies (Chapter 4) and DNA mobility shift assays (discussed below) indicate that the compound binds to DNA (specific mechanism unknown) and therefore is able to competitively prevent the enzyme from binding DNA and initiating strand cleavage at a concentration between 1 and 10 μM . This is a comparative result to the one of Che and co-workers presented in 2010 whereby they report the topoisomerase I inhibitory action of a cyclometallated gold(III) compound to be between 3.3 and 10 μM , which is within the same range of activity for $[\text{Au}(\text{L12})\text{Cl}](\text{PF}_6)$.³² Further detailed mechanistic work on this complex has recently been reported by Castelli and co-workers.³³ They describe how the gold(III) compound is able to inhibit the enzyme by preventing it binding to the DNA substrate. Since compound $[\text{Au}(\text{L12})\text{Cl}](\text{PF}_6)$ and $[\text{Au}(\text{C}^{\wedge}\text{N}^{\wedge}\text{C})(\text{IMe})]\text{CF}_3\text{SO}_3$ ³² are similar in structure, we surmise that $[\text{Au}(\text{L12})\text{Cl}](\text{PF}_6)$ may work in a similar way. Overall this is an exciting result as the topoisomerase catalytic inhibition activity correlates well with the cytotoxicity data obtained from the NCI.

All three compounds, $[\text{Au}(\text{HL3})\text{Cl}_2]$, $[\text{Au}(\text{L12})\text{Cl}](\text{PF}_6)$ and $[\text{Au}(\text{L13})\text{Cl}](\text{PF}_6)$ were then tested for their ability to inhibit/poison topo II α via a decatenation assay. From the statistical analysis it was envisaged that compound $[\text{Au}(\text{HL3})\text{Cl}_2]$ would act as a poison or inhibitor while $[\text{Au}(\text{L12})\text{Cl}](\text{PF}_6)$ would not. Etoposide or VP-16 is a well-known topo II α poison, being

able to stabilise the double-stranded enzyme-DNA-cleavage complex thereby blocking DNA strand religation, and was therefore chosen as the control drug. Figure 7.3.3.5 below depicts a wide range topo II α decatenation assay performed with compound [Au(HL3)Cl₂]. From Figure 7.3.3.5, lane 1 contains only catenated DNA. Lane 2 contains catenated DNA and the enzyme, which results in the banding of NOC and closed covalent circular (CCC). Lane 3 contains the linear DNA marker and lane 4 contains catenated DNA with the control drug etoposide. This results in the formation of the linear band shown on the gel, due to poisoning of the enzyme.

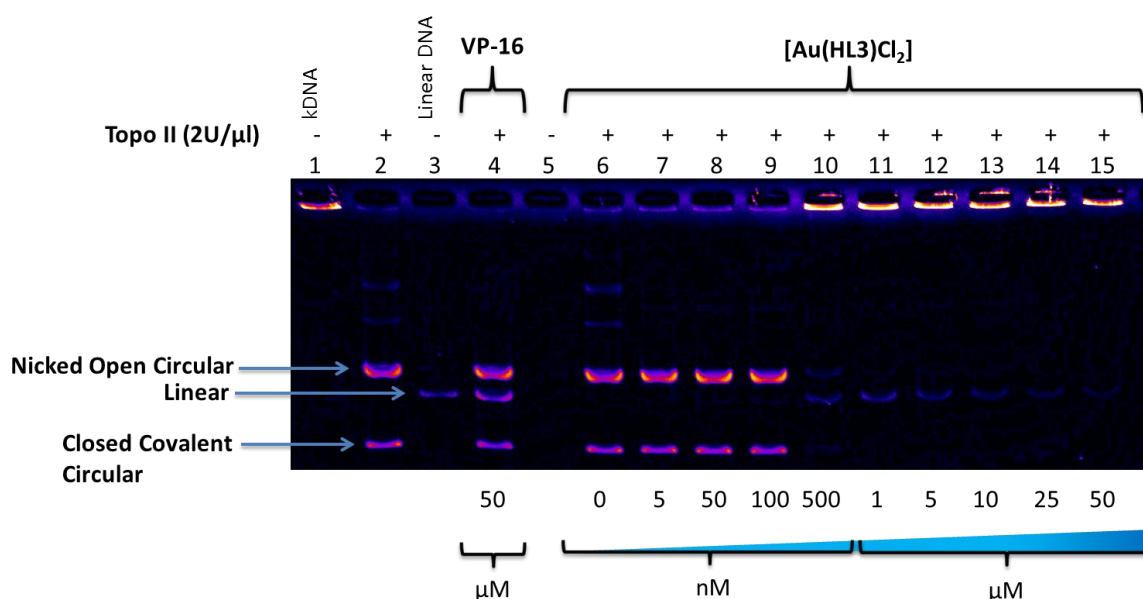


Figure 7.3.3.5: EB gel showing a wide range topoisomerase II α kDNA decatenation assay for compound [Au(HL3)Cl₂]. At low concentrations (50 nM) [Au(HL3)Cl₂] acts as a poison while at higher concentrations [Au(HL3)Cl₂] acts as a catalytic inhibitor.

Lanes 6-15 contain the gold(III) drug [Au(HL3)Cl₂] in the concentration range 0-50 μ M. Upon analysis of the gel one can observe the slight presence of linear DNA in the nM concentration range (5-100 nM), indicating that the compound is behaving as a topo II α poison. The presence of NOC and CCC DNA in this range as well as the similar control result affirms this notion as it indicates the enzyme is being allowed to perform the double stranded cleavage of the DNA. The reaction product profile is, however, markedly different at concentrations greater than 500 nM. One can clearly see the heavy presence of catenated DNA as well as a small amount of linear DNA, indicating dual catalytic inhibition and poisoning modes of activity. The gradual disappearance of linear DNA indicates that

[Au(HL3)Cl₂] predominantly acts as a catalytic inhibitor over this concentration range rather than a poison.

As previously mentioned, a topoisomerase II poison creates a ternary drug-DNA-enzyme 'cleavage complex', effectively trapping the enzyme on the DNA once a double-stranded break has been formed. One is able to test whether this occurs by performing the reaction in duplicate as per the gel in Figure 7.3.3.6. One reaction is treated with proteinase K (PK) and other is not (Figure 7.3.3.6). PK is a broad spectrum serine protease discovered in extracts of the fungus *Engyodontium album*.³⁴ It is able to digest DNA nucleases and is therefore used for the purification of DNA.³⁴ It is for this reason that it was used in the above mentioned experiment to release the linear DNA from the drug-DNA-enzyme 'cleavage complex'.

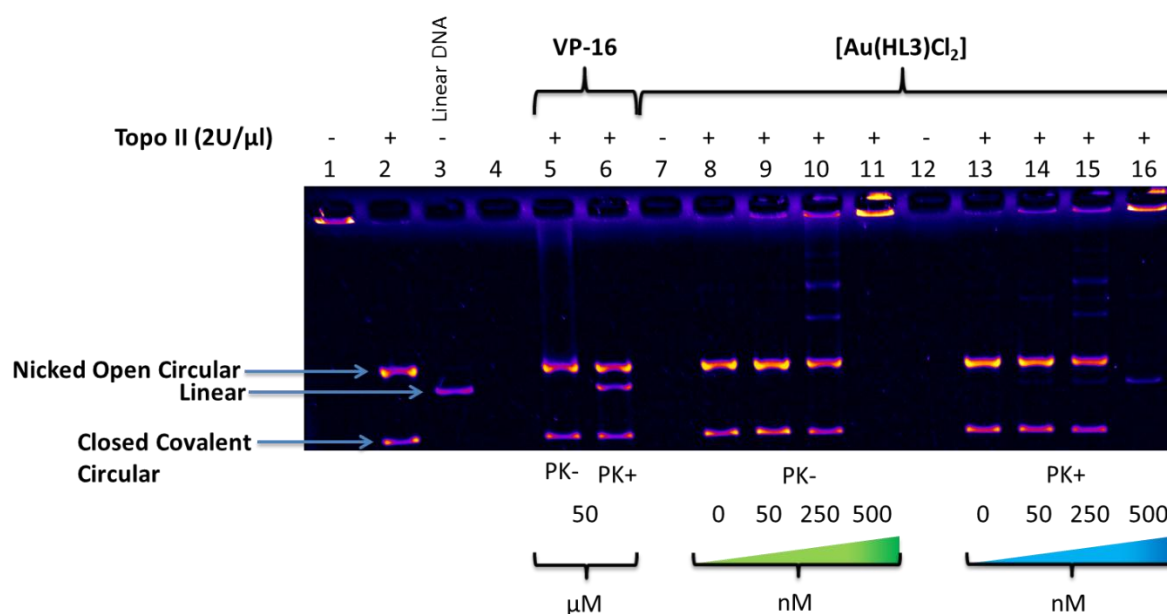


Figure 7.3.3.6: EB gel showing a topoisomerase II α kDNA decatenation assay for [Au(HL3)Cl₂] and the absence and presence of linear DNA before and after treatment with PK, respectively.

As can be seen from Figure 7.3.3.6, lanes 1-3 contain the relevant DNA markers. Lanes five and six contain the topoisomerase poison, etoposide. One can clearly see that in lane 5 where the reaction has not been treated with PK, there is no evidence of linear DNA and furthermore there is slight smearing of the NOC DNA band. This is because the enzyme is still attached to the DNA and therefore increases the total weight and mobility of the DNA. In lane six the reaction has been treated with PK and we can clearly see the presence of a

linear DNA band indicating the 'cleavage complex' has been digested (i.e. the enzyme removed from the DNA) and the linear DNA released. Lanes 8-11 and 13-16, similarly contain varying concentrations of $[\text{Au}(\text{HL3})\text{Cl}_2]$ in the absence and presence of PK respectively. Since $[\text{Au}(\text{HL3})\text{Cl}_2]$ behaves predominantly as a catalytic inhibitor, the presence of linear DNA after treatment with PK is greatly diminished compared to that of etoposide, however its presence indicates that $[\text{Au}(\text{HL3})\text{Cl}_2]$ can act as a poison. This dual mechanism of action is an encouraging result as it is thought that a drug that behaves in such a way could be more effective than a specific poison or inhibitor.

Compound $[\text{Au}(\text{L12})\text{Cl}](\text{PF}_6)$ was similarly tested for its topo II α inhibitory action (Figure 7.3.3.7). In Figure 7.3.3.7 we have similar controls to Figure 7.3.3.6. Lanes 5-12 contain compound $[\text{Au}(\text{L12})\text{Cl}](\text{PF}_6)$ in varying concentrations as indicated.

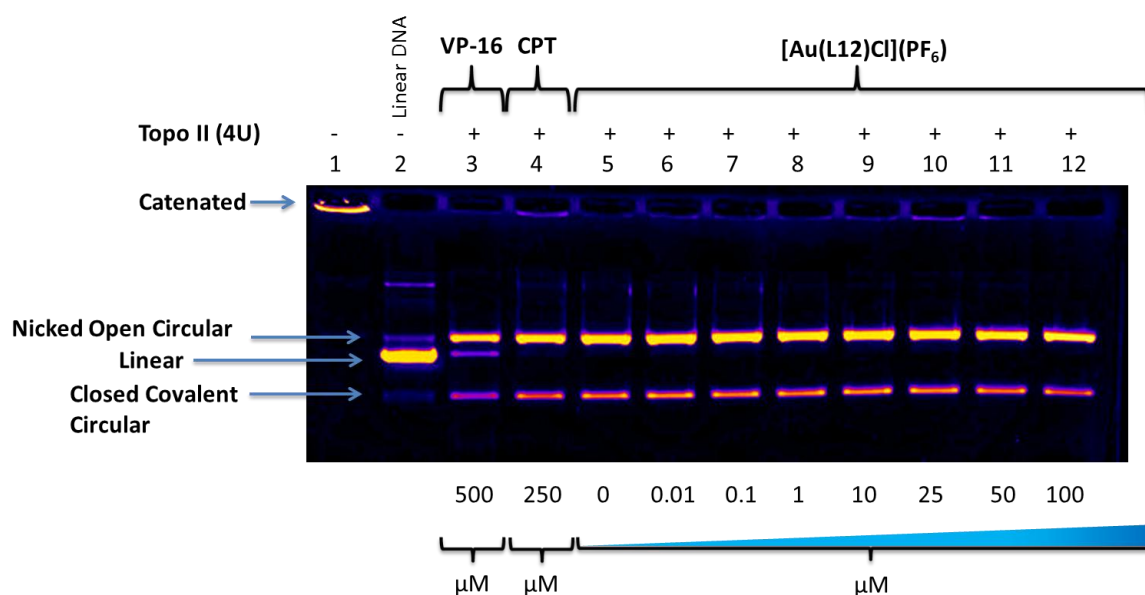


Figure 7.3.3.7: EB gel showing a wide range topoisomerase II α decatenation assay for compound $[\text{Au}(\text{L12})\text{Cl}](\text{PF}_6)$. The compound shows no inhibitory/poisoning activity through the concentration range tested.

As one can clearly see, there is almost no inhibition or poisoning of the enzyme at low concentrations while there is minimal catalytic inhibition from 25 μM up. These results indicate that compound $[\text{Au}(\text{L12})\text{Cl}](\text{PF}_6)$ is an ineffective topo II α inhibitor or poison.

7.3.4 Electrophoretic gel mobility shift assays

An electrophoretic gel mobility shift assay (EMSA) is an alternative from the traditional spectroscopic methods for determining an intercalating or groove binding interaction between a drug and a DNA substrate.^{32, 35} The DNA substrate can take many different forms such as supercoiled or relaxed. In the experiments performed in this work, the supercoiled and nicked open circular form was used as the DNA substrate. EMSA has been frequently used to ascertain the interaction between DNA and gold(III) drugs.^{32, 35} The premise behind an EMSA experiment is that once a drug has been incubated with the DNA substrate and had sufficient time to equilibrate, it alters the tertiary structure of the DNA by unwinding the helix slightly (most notably when intercalated). This causes the DNA to become more bulky and hence not as mobile through the agarose gel when a current is applied, resulting in the DNA-drug band traveling a lesser distance down the gel than the pure DNA band. This mobility shift is generally a concentration-dependant effect since the more drug molecules that are available to intercalate the DNA, the greater the effect on the tertiary structure of the DNA and hence a greater effect on the mobility of the DNA.

EMSA experiments were only performed for compounds $[\text{Au}(\text{HL3})\text{Cl}_2]$, $[\text{Au}(\text{L12})\text{Cl}](\text{PF}_6)$ and $[\text{Au}(\text{L13})\text{Cl}](\text{PF}_6)$. This was because $[\text{Au}(\text{HL3})\text{Cl}_2]$ displayed variable solution stability and standard spectroscopic titrations of the metal compound with ctDNA in TBS gave irreproducible binding isotherms as a result of concomitant demetallation of the complex. Compounds $[\text{Au}(\text{L12})\text{Cl}](\text{PF}_6)$ and $[\text{Au}(\text{L13})\text{Cl}](\text{PF}_6)$ were selected as representative examples from the three phenyl ketone derivatives to perform EMSA experiments because, despite their stability in biological media, they similarly gave irreproducible binding isotherms (see Chapter 4) with traditional spectroscopic methods. The EMSA results for compound $[\text{Au}(\text{HL3})\text{Cl}_2]$ are shown in Figure 7.3.4.1.

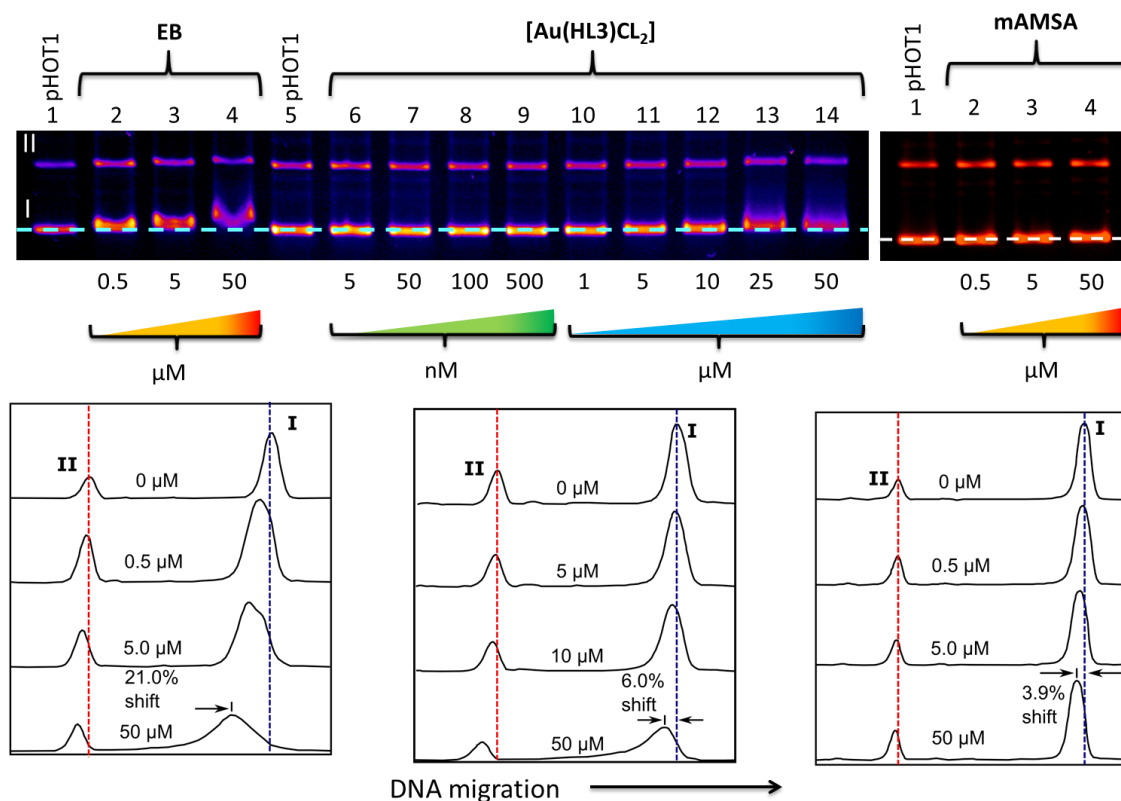


Figure 7.3.4.1: EMSA gel for EB (top left), [Au(HL3)Cl₂] (top middle) and mAMSA (top right) at various indicated drug concentrations. Two dimensional peak deconvolution for EB (bottom left), [Au(HL3)Cl₂] (bottom middle) and mAMSA (bottom right). DNA band identities: I, supercoiled DNA; II, nicked open-circular DNA.

From the figure we can see that the top left hand gel contains the known intercalator EB as well as compound [Au(HL3)Cl₂] from this work, while the top right hand gel contains the commercially available neutral anti-cancer drug, 4'-(acridinylamino)methanesulfon-m-anisidide (mAMSA). The cationic intercalator, EB lanes 2-4, exhibits a large mobility shift of 21% at 50 μM compared to compound [Au(HL3)Cl₂], lanes 6-14, which displays a significantly lower mobility shift of 6% at 50 μM. This large observable difference in mobility shift is understandable as EB is cationic and therefore has an electrostatic attraction to the negatively charged backbone of the DNA. To obtain a more accurate comparison another EMSA assay was performed using mAMSA, which is a proven neutral intercalator. The mobility shift of mAMSA was observed at 3.9% at 50 μM complex concentration which was less than that of [Au(HL3)Cl₂] at an equivalent concentration. This result indicates that compound [Au(HL3)Cl₂] is able to intercalate DNA therefore inducing a mobility shift, however, what this assay does not tell us is the intercalation mode. There are two possible ways in which [Au(HL3)Cl₂] is able to intercalate DNA, the first is via the unco-ordinated

isoquinoline ring and the second is through the gold(III) chelated isoquinoline ring. One would presume $[\text{Au}(\text{HL3})\text{Cl}_2]$ would intercalate through the co-ordinated isoquinoline ring as the π - π interactions between the isoquinoline ring and the base pairs of the DNA, coupled with the Au(III)- π interactions between the electron deficient gold(III) centre and the base pairs of the DNA, would encourage this mode of interaction.

EMSA experiments were similarly performed with compounds $[\text{Au}(\text{L12})\text{Cl}](\text{PF}_6)$ and $[\text{Au}(\text{L13})\text{Cl}](\text{PF}_6)$ to further try and elucidate whether they are able to bind DNA since the spectroscopic data was indicative of this but inconclusive. Compound $[\text{Au}(\text{L12})\text{Cl}](\text{PF}_6)$ is used as a representative example. EMSA assays using both relaxed and SC-DNA were used. As seen above in Figure 7.3.4.1, when using SC-DNA one is able to detect a mobility shift of a respective band, however, when using relaxed DNA the effect is slightly different with the topoisomers displaying a smudging effect in the presence of an intercalator such as EB and total immobility in the presence of a minor groove binder such as Hoechst-33258 (Figure 7.3.4.2).

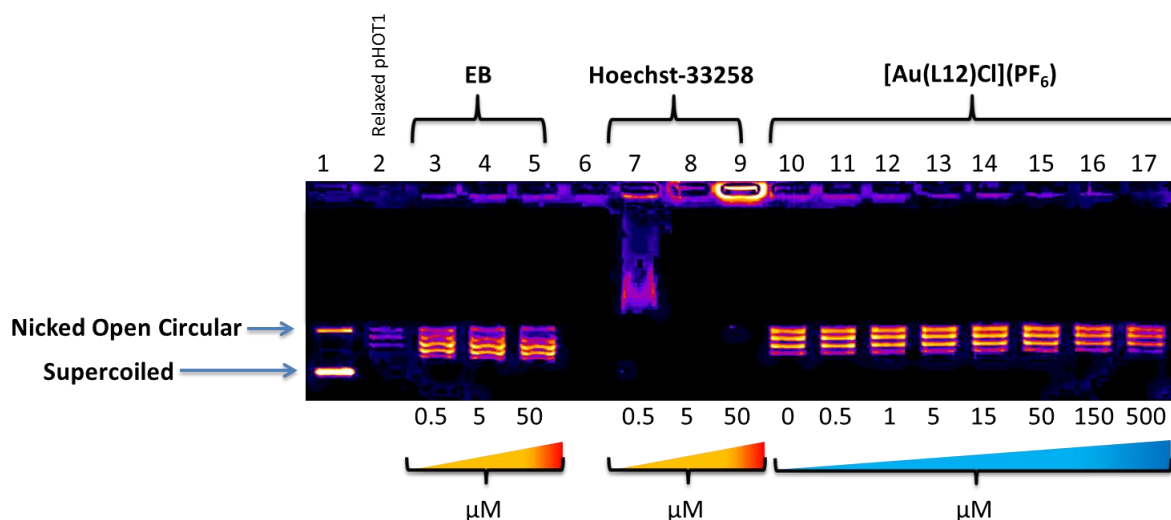


Figure 7.3.4.2: EMSA gel for EB, Hoechst-33258 and $[\text{Au}(\text{L12})\text{Cl}](\text{PF}_6)$ using relaxed DNA as the substrate. The gel shows no evidence for DNA intercalation by compound $[\text{Au}(\text{L12})\text{Cl}](\text{PF}_6)$.

From the figure it is evident that $[\text{Au}(\text{L12})\text{Cl}](\text{PF}_6)$ does not interact with DNA as an intercalator since the smudging of the relaxed topoisomer bands is not observed even at a high concentration of 500 μM . This result is interesting as it is contradictory to the spectroscopic data obtained in Chapter 4. Groove binding has been removed as a possible

mode of interaction as Hoechst-33258 was used as a control and almost completely immobilised the DNA at 0.5 μM , while $[\text{Au}(\text{L12})\text{Cl}](\text{PF}_6)$ did not show any such effect.

A similar EMSA experiment was performed, where the DNA substrate was SC- and NOC DNA. The results of this assay showed that there was in fact an increase in mobility shift for both the SC- and NOC DNA bands for compounds $[\text{Au}(\text{L12})\text{Cl}](\text{PF}_6)$ and $[\text{Au}(\text{L13})\text{Cl}](\text{PF}_6)$. This increase in mobility shift was very small for compound $[\text{Au}(\text{L12})\text{Cl}](\text{PF}_6)$ (1%), however, for compound $[\text{Au}(\text{L13})\text{Cl}](\text{PF}_6)$ the increased mobility shift was quite prominent (25%). (Figure 7.3.4.3)

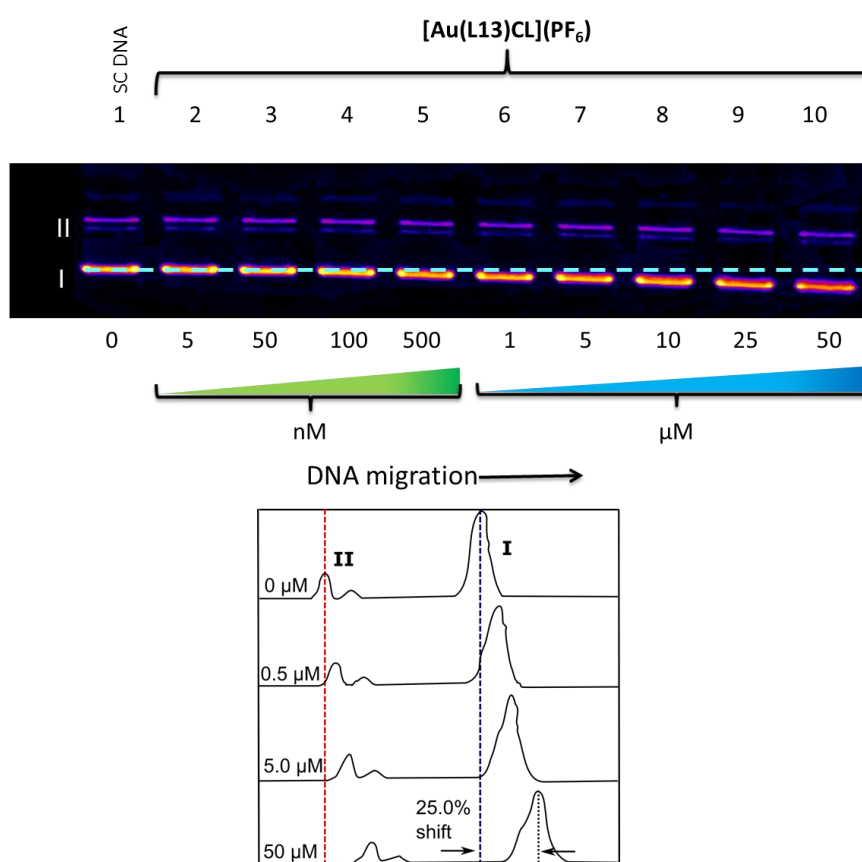


Figure 7.3.4.3: EMSA gel for $[\text{Au}(\text{L13})\text{Cl}](\text{PF}_6)$ (top) at various indicated drug concentrations. The two dimensional peak deconvolution for $[\text{Au}(\text{L13})\text{Cl}](\text{PF}_6)$ is shown below. DNA band identities: I, supercoiled DNA; II, nicked open-circular DNA.

This result effectively means that the compound is ‘coiling’ the DNA further, which causes less drag in the EMSA experiment and therefore the DNA runs with a greater mobility than for standard SC-DNA. There are very few cases in the literature where a metal compound has this effect on DNA. One such case was reported by Hannon and co-workers in 2001, where an Fe(II) based supramolecular cylinder is shown to extensively coil DNA by

microscopy.³⁶ These supramolecular cylinders have since been proven to be DNA 3-way junction binders.^{37, 38} Compounds $[\text{Au}(\text{L12})\text{Cl}](\text{PF}_6)$ and $[\text{Au}(\text{L13})\text{Cl}](\text{PF}_6)$ comprise an asymmetric non-cylindrical shape and are therefore envisaged not to behave in a manner akin to that of the cylinders. One way in which we believe the compound may interact with DNA is through electrostatic interactions since the compounds are positively charged. It is well known that by removing/replacing the cationic sodium ions within the DNA structure, one is able to affect its tertiary structure.³⁹ We therefore propose that the metal compound binds to the surface of the DNA through electrostatic interactions and displaces the sodium ions present (Figure 7.3.4.4). This change in cation within the DNA helix would therefore result in a conformational change of the DNA. In this case, enhanced supercoiling of the DNA, allowing for the increased mobility observed in the EMSA. This structural change could also negatively influence the binding of EB to DNA, forcing the equilibrium between the free and bound EB towards the free EB (Figure 7.3.4.4). This would account for the decrease in emission intensity observed in the EB displacement titrations.

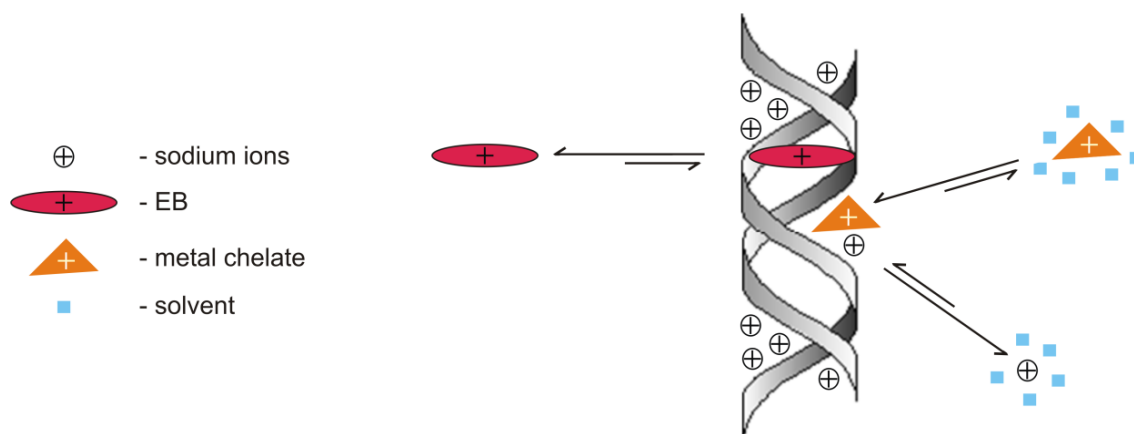


Figure 7.3.4.4: Schematic representation of the hypothetical electrostatic interaction between $[\text{Au}(\text{L12})\text{Cl}](\text{PF}_6)$ and a DNA molecule. The diagram shows the displacement of EB and sodium ions from helical DNA structure by $[\text{Au}(\text{L12})\text{Cl}](\text{PF}_6)$.

The bathochromic shift and decrease in LMCT band intensity observed during the UV-vis ctDNA titrations could also be accounted for using this hypothesis. When the compound is free in solution it is uniformly surrounded by solvent molecules of a certain dielectric constant, however, when the compound electrostatically binds to DNA it is no longer uniformly surrounded by solvent molecules and hence the dielectric constant surrounding the molecule is different (Figure 7.3.4.4). This change in dielectric constant may cause the

spectral perturbations observed in the UV-vis spectra. In both the EB displacement titration and ctDNA binding experiments the spectral changes become more pronounced as the concentration of compound increases since the equilibrium between bound compound and unbound compound shifts towards the former. This would allow for a steady drop in emission intensity as the EB is displaced from the DNA as well as a change in the UV-vis spectrum as more and more compound becomes electrostatically bound to the DNA.

7.3.5 Summary and Conclusions

Overall, the compounds studied in this work were found to be effective chemotherapeutic agents *in vitro* but lack the same efficacy *in vivo*. Although beyond the scope of the work in this thesis, the lack of *in vivo* efficacy may be due to irreversible binding of the compounds to serum proteins such as HSA. The mechanism by which the more cytotoxic gold(III) complexes exert their cytotoxicity has been determined to be via the catalytic inhibition of the topoisomerase family of enzymes. Compounds $[\text{Au}(\text{HL}3)\text{Cl}_2]$ and $[\text{Au}(\text{L}8)\text{Cl}](\text{PF}_6)$ – $[\text{Au}(\text{L}11)\text{Cl}](\text{PF}_6)$ were shown to intercalate DNA. Compounds $[\text{Au}(\text{L}12)\text{Cl}](\text{PF}_6)$ – $[\text{Au}(\text{L}14)\text{Cl}](\text{PF}_6)$ display spectral properties consistent with DNA intercalation, however, EMSA studies suggest that the interaction between the compounds and DNA is not intercalation, but rather another mode of interaction (perhaps electrostatic) as evidenced by a gel mobility shift.

7.4 References

1. R. W.-Y. Sun, C. K.-L. Li, D.-L. Ma, J. J. Yan, C.-N. Lok, C.-H. Leung, N. Zhu and C.-M. Che, *Chem.–Eur. J.*, 2010, **16**, 3097-3113, S3097/3091-S3097/3030.
2. R. W.-Y. Sun and C.-M. Che, *Coord. Chem. Rev.*, 2009, **253**, 1682-1691.
3. U. Abram, K. Ortner, R. Gust and K. Sommer, *Dalton Trans.*, 2000, 735-744.
4. R. Rubbiani, I. Kitanovic, H. Alborzinia, S. Can, A. Kitanovic, L. A. Onambele, M. Stefanopoulou, Y. Geldmacher, W. S. Sheldrick, G. Wolber, A. Prokop, S. W€olfli and I. Ott, *J. Med. Chem.*, 2010, **53**, 8608-8618.
5. I. Kostova, *Anti-Cancer Agents Med. Chem.*, 2006, **6**, 19-32.
6. D. E. Thurston, *Chemistry and Pharmacology of Anticancer Drugs*, Taylor and Francis Group, 2007.
7. http://dctd.cancer.gov/ProgramPages/dtp/tools_drug_discovery.htm, 2012.
8. <http://dtp.nci.nih.gov/branches/btb/ivclsp.html>, 2012.
9. <http://dtp.nci.nih.gov/branches/btb/hfa.html>, 2012.
10. <http://www.topogen.com>, 2012.
11. B. L. Staker, K. Hjerrild, M. D. Feese, C. A. Behnke, A. B. Burgin, Jr. and L. Stewart, *Proc. Natl. Acad. Sci.*, 2002, **99**, 15387-15392.
12. L. H. Jensen, A. Renodon-Corniere, K. C. Nitiss, B. T. Hill, J. L. Nitiss, P. B. Jensen and M. Sehested, *Biochem. Pharmacol.*, 2003, **66**, 623-631.
13. W. S. El-Hamouly, J. C. Ruckdeschel and S. Archer, *Eur. J. Med. Chem.*, 1993, **28**, 913-916.
14. T. Karoli, S. K. Mamidyala, J. Zuegg, S. R. Fry, E. H. L. Tee, T. A. Bradford, P. K. Madala, J. X. Huang, S. Ramu, M. S. Butler and M. A. Cooper, *Bioorg. Med. Chem. Lett.*, 2012, **22**, 2428-2433.
15. http://dtp.nci.nih.gov/docs/dtp_search.html, 2012.
16. L. Fetzer, B. Boff, M. Ali, X. Meng, J.-P. Collin, C. Sirlin, C. Gaiddon and M. Pfeffer, *Dalton Trans.*, 2011, **40**, 8869-8878.
17. U. Abram, J. Mack, K. Ortner and M. Muller, *J. Chem. Soc., Dalton Trans.*, 1998, 1011-1020.
18. A. Yasgar, S. D. Furdas, D. J. Maloney, A. Jadhav, M. Jung and A. Simeonov, *PLoS One*, 2012, **7**, e45594.
19. B. Everitt and G. Dunn, *Applied Multivariate Data Analysis*, 2nd Edition edn., Arnold, London, 2001.
20. C.-C. Wu, T.-K. Li, L. Farh, L.-Y. Lin, T.-S. Lin, Y.-J. Yu, T.-J. Yen, C.-W. Chiang and N.-L. Chan, *Science* 2011, **333**, 459-462.
21. Y. Pommier, E. Leo, H.-L. Zhang and C. Marchand, *Chem. Biol.*, 2010, **17**, 421-433.
22. F. Ali-Osman, M. S. Berger, S. Rajagopal, A. Spence and R. B. Livingston, *Cancer Res.*, 1993, **53**, 5663-5668.
23. Y. Pommier, *Nat. Rev. Cancer*, 2006, **6**, 789-802.
24. E. Kiselev, S. DeGuire, A. Morrell, K. Agama, T. S. Dexheimer, Y. Pommier and M. Cushman, *J. Med. Chem.*, 2011, **54**, 6106-6116.
25. Y. Pommier, E. Leo, H. Zhang and C. Marchand, *Chem Biol*, 2010, **17**, 421-433.
26. J. M. Berger, S. J. Gamblin, S. C. Harrison and J. C. Wang, *Nature* 1996, **379**, 225-232.
27. J. L. Nitiss, *Nat. Rev. Cancer*, 2009, **9**, 327-337.
28. J. L. Nitiss, *Nat. Rev. Cancer*, 2009, **9**, 338-350.

29. T. Andoh and R. Ishida, *Biochim. Biophys. Acta, Gene Struct. Expression*, 1998, **1400**, 155-171.
30. T. Andoh, *Biochimie*, 1998, **80**, 235-246.
31. P. B. Jensen and M. Sehestedt, *Biochem. Pharmacol.*, 1997, **54**, 755-759.
32. J. J. Yan, A. L.-F. Chow, C.-H. Leung, R. W.-Y. Sun, D.-L. Ma and C.-M. Che, *Chem. Commun.*, 2010, **46**, 3893-3895.
33. S. Castelli, O. Vassallo, P. Katkar, C.-M. Che, R. W.-Y. Sun and A. Desideri, *Arch. Biochem. Biophys.*, 2011, **516**, 108-112.
34. W. Ebeling, N. Hennrich, M. Klockow, H. Metz, H. D. Orth and H. Lang, *Eur. J. Biochem.*, 1974, **47**, 91-97.
35. R. G. Buckley, A. M. Elsome, S. P. Fricker, G. R. Henderson, B. R. C. Theobald, R. V. Parish, B. P. Howe and L. R. Kelland, *J. Med. Chem.*, 1996, **39**, 5208-5214.
36. M. J. Hannon, V. Moreno, M. J. Prieto, E. Moldrheim, E. Sletten, I. Meistermann, C. J. Isaac, K. J. Sanders and A. Rodger, *Angew. Chem., Int. Ed.*, 2001, **40**, 880-884.
37. D. R. Boer, J. M. C. A. Kerckhoffs, Y. Parajo, M. Pascu, I. Uson, P. Lincoln, M. J. Hannon and M. Coll, *Angew. Chem., Int. Ed.*, 2010, **49**, 2336-2339, S2336/2331-S2336/2313.
38. C. Ducani, A. Leczkowska, N. J. Hodges and M. J. Hannon, *Angew. Chem., Int. Ed.*, 2010, **49**, 8942-8945, S8942/8941-S8942/8945.
39. S. R. Gadre, S. S. Pundlik, A. C. Limaye and A. P. Rendell, *Chem. Commun.*, 1998, 573-574.

8. Summary, conclusions and future work

8.1 Summary and conclusions

Since the ability of cisplatin to arrest cell division was discovered in 1965, there has been a steady rise in the number of literature articles reporting the use of metal complexes as potential chemotherapeutic agents. One particular field which has garnered much interest is the investigation of gold(I/III) compounds as anti-cancer agents, particularly gold(III) compounds, since they possess isoelectronic and isostructural properties to platinum(II) compounds. However, the inherent problem with gold compounds, particularly gold(III) compounds, is their instability in biological media as well as towards cellular reducing agents such as GSH. Consequently, ligand design is crucial to stabilising the gold(III) ion and hence the structural integrity of gold(III) compounds in solution. Therefore the main objective of the research presented in this thesis was to synthesise a series of novel, potentially stable, gold(III) compounds and to assess their cytotoxicity profiles towards human cancer cell lines.

In summary, this work describes the synthesis, characterisation, computational and biological studies of sixteen (fifteen novel) quinoline- and pyridine-amide-based gold(III) compounds. The preliminary stages of the project involved the synthesis of a tetradentate dianionic bis(amide) ligand (H_2L1), via literature methods, as a scaffold for incorporating the gold(III) ion with a view of forming a cationic, tetradentate, metal complex analogous to that synthesised by Che and co-workers.¹ This phase of the project was initiated principally to investigate the synthetic procedures surrounding the chelation of the gold(III) ion by bis(amide) ligands, since there are very few specific methodologies in the literature regarding this. Initial synthetic attempts involved the reflux of a gold(III) salt ($H[AuCl_4]$, $K[AuCl_4]$, $Na[AuCl_4]$, or $[Bu_4N][AuCl_4]$), with the bis(amide) ligand, H_2L1 , in a solvent (DCM, MeOH or a 1:1 binary mixture of these solvents). This resulted in the isolation of the respective starting materials with no metal complex formation. The synthesis was then performed using similar conditions with the addition of a base (NaMeO, NaEtO or NaOAc) which resulted in the formation of a cis-dichloro tris-chelate where the gold(III) ion was only bound to half the bis(amide) ligand. Irrespective of the combination between solvent and base (*vide supra*) the cis-dichloro tris-chelate ($[Au(HL1)Cl_2]$) was invariably isolated. Due to the interesting co-ordination mode between the gold(III) ion and the bis(amide) ligand, the investigation into the formation of the tetradentate mono-chelate was abandoned and two

Summary, Conclusions and Future Work

additional bis(amide) ligands (H₂L2 and H₂L3) were synthesised followed by their tris-chelates ([Au(HL2)Cl₂] and [Au(HL3)Cl₂]). Upon review of the literature it became apparent that the use of bi- and tridentate amide ligands and the synthesis of their gold(III) complexes may, in fact, afford potentially cytotoxic compounds. To this end, ligands HL4–H₂L16 were synthesised using literature methods. The chelation of the respective ligands to gold(III) was initially performed using the same methods to produce [Au(HL1)Cl₂]. These methods afforded the correct gold(III) chelate cation for all ligands, however, the incorrect [AuCl₂]⁻ and/or [AuCl₄]⁻ anion(s) were always encountered. This problem was solved by encouraging the formation of the [AuCl₄]⁻ anion while refluxing in acetic acid with a 3-fold molar excess of NaOAc. The [AuCl₄]⁻ anion was subsequently metathesised to the Cl⁻ and then to the PF₆⁻ anion via literature methods.

All metal complexes synthesised were fully characterised by standard IR, NMR, UV-vis as well as mass spectrometry. The IR spectrum for all ligands was characterised by an amide N-H stretch between 3272 and 3359 cm⁻¹ and an amide C=O stretch between 1646 and 1689 cm⁻¹. Upon chelation of ligands H₂L1–H₂L3 to a gold(III) ion, an amide N-H and C=O stretch remain at a similar stretching frequency to the free ligand due to the unusual co-ordination mode of the gold(III) ion to the ligand allowing for an unbound amide group, while the bound amide C=O stretches shifted to lower wavenumbers (from 1650-1685 cm⁻¹ to 1645-1652 cm⁻¹). Ligands HL4– H₂L16 all contain only one amide group which lost their respective amide N-H stretches upon chelation to gold(III), while the amide C=O stretching band shifted to higher wavenumbers upon chelation of gold(III) for ligands HL5–HL7 (1646-1664 cm⁻¹ to 1664-1676 cm⁻¹). Ligands HL4 and HL8-H₂L16 all displayed a decrease in amide C=O stretching frequency similar to that observed upon chelation of gold(III) to ligands H₂L1–H₂L3. The ¹H and ¹³C spectra for all ligands synthesised displayed characteristic downfield shifts for the amide N-H (between 8.55 and 12.46 ppm) and C=O (between 162.98 and 166.26 ppm) resonances respectively, while ligands HL12–HL14 all contained an extra ketone C=O resonance downfield (≈ 190 ppm) in the ¹³C spectrum. Upon chelation of the respective ligands to gold(III), there is a general downfield shift for both ¹H and ¹³C chemical shifts due to the deshielding effect of the gold(III) ion. This effect is particularly evident for the α- and α' ¹H signals where a maximum 0.97 ppm downfield shift is observed after chelation of a gold(III) ion to the free ligand. The UV-vis spectrum for all complexes was

Summary, Conclusions and Future Work

characterised by a strong π - π^* absorption band situated between 200 and 300 nm and a LMCT band situated between 300 and 500 nm.

All compounds were evaluated for their solubility in a wide range of solvents with [Au(HL1)Cl₂] and [Au(HL2)Cl₂] being soluble only in polar solvents such as DMSO and MeNO₂, while [Au(HL3)Cl₂] and [Au(L4)Cl₂] displayed additional solubility in organic solvents such as DCM and THF. The chloride salts of compounds [Au(L5)Cl](PF₆)-[Au(L14)Cl](PF₆) displayed good solubility in H₂O while the corresponding PF₆⁻ salts were more soluble in MeOH and/or MeCN. The neutral chelates [Au(L15)Cl]-[Au(L16)Cl] were soluble in DMSO and only sparingly soluble in DCM. Solution stability plays a vital role with gold(III) compounds and their potential as chemotherapeutic agents since they can be highly susceptible to decomposition. The compounds were therefore further evaluated for their solution stability in a biologically relevant media, TBS (50 mM Tris-HCl, NaCl 10 mM, pH 7.34, 37 °C). Compound [Au(HL3)Cl₂] was found to be susceptible to reductive demetallation, presumably through chloride substitution. Compounds [Au(L5)Cl](PF₆)-[Au(L7)Cl](PF₆) were all unstable in solution with a large decrease in both π - π^* and LMCT absorption bands observed over a period of 12 h. Compounds [Au(L8)Cl](PF₆)-[Au(L14)Cl](PF₆) were similarly evaluated for their stability in TBS and found to be stable over 24 h with a less than 2.5% drop in absorbance for both π - π^* and LMCT absorption bands, while complexes [Au(L15)Cl]-[Au(L16)Cl] were also found to be stable. Compound [Au(L12)Cl](PF₆) was further tested for its reactivity towards biologically relevant nucleophiles (imidazole and glutathione; 10-fold higher concentration relative to the concentration of the complex). [Au(L12)Cl](PF₆) was found to be stable in the presence of imidazole with a < 5% drop in absorbance of the LMCT absorption band over 24 h while in the presence of glutathione, the complex displayed an effective 100% reduction in LMCT band intensity over a 12 h period. In order to try and ascertain the ability of the stable complexes, [Au(L8)Cl](PF₆)-[Au(L14)Cl](PF₆), to cross cellular membranes, their log P_{o/w} values were assessed via the 'shake flask' method. All complexes were found to have fairly large negative log P_{o/w} values (-0.80-2.16) indicating that the compounds are hydrophilic in nature and may encounter difficulties traversing cellular membranes. Due to the planar nature and appropriate solubility and stability of the chloride salts of compounds [Au(L8)Cl](PF₆)-[Au(L14)Cl](PF₆) in TBS, their ability to interact with ctDNA was explored via

Summary, Conclusions and Future Work

traditional UV-vis spectroscopic methods. Compounds [Au(L8)Cl](PF₆)–[Au(L11)Cl](PF₆) all displayed characteristic spectral changes associated with ctDNA intercalation upon sequential addition of ctDNA to a $\approx 10^{-5}$ M concentration of respective complex in TBS at 37 °C. The resulting data from the UV-vis ctDNA binding experiments strongly indicated that all four compounds bound ctDNA via an intercalative method with binding affinities (K_b) ranging from $2.7(5) \times 10^5$ to $4.7(6) \times 10^5$ M⁻¹. Compounds [Au(L12)Cl](PF₆)–[Au(L14)Cl](PF₆) gave irreproducible UV-vis ctDNA binding isotherms with large errors in ctDNA binding constants, characteristic of multiple modes of ctDNA binding. EB competitive binding assays using emission spectroscopy were then performed for compounds [Au(L12)Cl](PF₆)–[Au(L14)Cl](PF₆) to try and further elucidate the mode of interaction between the complexes and ctDNA. These results indicated that the compounds were able to bind ctDNA via intercalation with the highest apparent binding constant (K_{app}) being $8.4(6) \times 10^5$ M⁻¹ for compound [Au(L14)Cl](PF₆).

Solid state structures for all chelates except [Au(L10)Cl](PF₆), [Au(L14)Cl](PF₆) and [Au(L16)Cl] were determined by X-ray crystallography. Analysis of the structures confirmed the co-ordination mode of the gold(III) ion to each respective ligand is, as expected, a distorted square planar geometry. For chelates [Au(HL1)Cl₂]–[Au(L4)Cl₂], the ligand donates two binding sites while a pair of *cis* chloride ions completes the square planar geometry. The Au–Cl1 and Au–Cl2 bond lengths average 2.293(6) and 2.260(13) Å, respectively, with the former bond length indicative of a structural *trans* effect manifested through the anionic amide nitrogen. The Cl–Au–Cl and N–Au–N co-ordination bond angles are 89.1(2)° and 81.2(2)°, respectively, of which the latter represents the geometric constraints imposed on the metal ion co-ordination geometry by the five-membered chelate ring. For chelates [Au(L5)Cl](PF₆)–[Au(L15)Cl](PF₆) the ligand donates three binding sites and a single chloride ion in the fourth co-ordination site completes the square planar geometry. A similar *trans* effect is observed for the tridentate chelates with the longest Au–Cl bond length (2.298(2) Å) being recorded for [Au(L6)Cl](PF₆). The bond angles for compounds [Au(L5)Cl](PF₆)–[Au(L15)Cl](PF₆) similarly deviate from the ideal square planar geometric angle of 90° due to the geometric constraints imposed by the ligand system. The mean N–Au–Cl bond angle is fairly obtuse (97.8(9)°) while the mean N–Au–N angle is quite acute, measuring 82.1(9)°. The supramolecular interactions present for chelates [Au(HL1)Cl₂]–[Au(HL3)Cl₂] were fairly

Summary, Conclusions and Future Work

significant, owing to their polyfunctional nature. The extended structures are dominated by C–H···O and C–H···Cl hydrogen bonding which culminates in 1D hydrogen-bonded chains in the solid state. The balance of the chelates only contain non-traditional hydrogen bond capabilities and therefore their supramolecular structures were accordingly less diverse. Due to the presence of extended aromatic ring systems present in most chelates, π -stacking was a prevalent feature, with the majority of the compounds exhibiting this effect. A particularly strong π -stacking effect was observed for the compound [Au(L12)Cl](PF₆), where the MPS between quinoline rings was measured to be 3.307 Å.

The main aim of the project was the development of novel gold(III) metallotherapeutic drugs. An obvious requirement is therefore the assessment of the compounds *in vitro* and, more specifically, their ability to act as cytotoxic agents towards human cancer cell lines. The cytotoxicity of all compounds except for [Au(HL1)Cl₂] was therefore evaluated at the NCI in their initial (single-dose screen) against 60 human cancer cell lines. During this screening process the chelates were assessed at a concentration of 1 x 10⁻⁵ M across their 60 human cancer cell lines in order to determine mean growth percentage values. Compound [Au(L12)Cl](PF₆) exhibited the lowest mean growth percentage value (17%) while compound [Au(HL2)Cl₂] displayed the highest (105%). From these values, compounds [Au(HL3)Cl₂], [Au(L6)Cl]PF₆–[Au(L8)Cl](PF₆), [Au(L10)Cl](PF₆)–[Au(L13)Cl](PF₆) and [Au(L15)Cl] were deemed sufficiently cytotoxic to progress through to the 5-dose phase of testing where the dose-response parameters, GI₅₀, TGI and LC₅₀ were determined. Chelate [Au(HL3)Cl₂] performed fairly well with GI₅₀, TGI and LC₅₀ values averaging 10, 23 and 78 μM, respectively against the NCI's 60 human cancer cell lines. Compounds [Au(L6)Cl](PF₆)–[Au(L8)Cl](PF₆), [Au(L10)Cl](PF₆)–[Au(L13)Cl](PF₆) and [Au(L15)Cl] performed well with [Au(L12)Cl](PF₆) being the outstanding performer, exhibiting GI₅₀, TGI and LC₅₀ values averaging 0.80, 11.36 and 80.64 μM, respectively against the NCI's 60 human cancer cell lines. The cytotoxicity of compound [Au(L12)Cl]PF₆ was deemed sufficient enough to progress through to the initial *in vivo* phase of testing, namely, the hollow fibre assay. The compound unfortunately performed poorly with a score of 0 out of 96. This may be attributed to several problems such as poor trans-membrane cellular transport, irreversible binding to serum proteins and/or the decomposition of the drug *in vivo*.

Summary, Conclusions and Future Work

After the compounds were shown to have anti-cancer activity, the next step was to try and determine the MOA by which they effect their cytotoxic action. This was performed by taking the $-\log GI_{50}$ values for compounds $[Au(HL1)Cl_2]$ and $[Au(L12)Cl](PF_6)$ (due to their structural diversity) and applying a statistical cluster analysis with the $-\log GI_{50}$ values of 25 commercially available chemotherapeutic agents with established MOA's. This results in a dendogram with the test compound clustering with commercial compounds that display a similar cytotoxicity profile with the premise that the test compound may exert its cytotoxic ability through the same MOA. The results revealed that compound $[Au(HL3)Cl_2]$ and $[Au(L12)Cl](PF_6)$ probably target topoisomerase II and I, respectively. This was confirmed by topo IB relaxation and topo II α decatenation assays, respectively. The experiments were performed in Prof Mark Muller's laboratory at the University of Central Florida. Chelate $[Au(HL3)Cl_2]$ was determined to be a dual-mode poison and catalytic inhibitor of topo II α . Poisoning of the topo II α enzyme occurred between 5-100 nM and catalytic inhibition between 500 nM and 50 μ M. Compound $[Au(L12)Cl]PF_6$ was also determined to be a dual mode poison and catalytic inhibitor of topo IB with weak poisoning of the topo IB enzyme between a complex concentration of 0 and 1 μ M and catalytic inhibition between 1-10 μ M. Since the solution instability of compound $[Au(HL3)Cl_2]$ did not allow for its ctDNA binding ability to be assessed, an EMSA assay was employed to give an indication of whether intercalation of DNA might occur for $[Au(HL3)Cl_2]$. The experiment concluded that $[Au(HL3)Cl_2]$ is able to intercalate DNA, albeit weakly, at a metal concentration of 50 μ M. The EB displacement and UV-vis ctDNA binding assays were inconclusive for compounds $[Au(L12)Cl](PF_6)$ – $[Au(L14)Cl](PF_6)$, therefore a similar assay was performed for $[Au(L12)Cl](PF_6)$ and $[Au(L13)Cl](PF_6)$. The results showed that there was no evidence for intercalation, however, an increase in mobility shift for both chelates was detected which is suggestive of enhanced coiling of the DNA. It is thus postulated that the complexes may in fact bind electrostatically to the DNA helix.

In conclusion, we have synthesised a promising novel class of gold(III) amide chelates as potential chemotherapeutic agents. To this end, the *in vitro* results were encouraging with chelate $[Au(L12)Cl](PF_6)$ proving to be the lead candidate in the series with low μ M GI_{50} and IC_{50} values against several leukaemia, colon, ovarian and breast cancer cell lines. The *in vivo* results were however less encouraging. This is presumably due to the chelate being

Summary, Conclusions and Future Work

reduced, as suggested by spectroscopic glutathione reduction experiments. The stability of the compounds in biological media subsequently needs to be enhanced through structural modifications of the existing group of compounds so that their *in vivo* activity may be enhanced. Further mechanistic detail needs to be elucidated on the topo I/II poisoning and catalytic inhibitory action so that the compounds presented in this work may be optimised in order to increase their cytotoxicity. The ability of $[\text{Au}(\text{L12})\text{Cl}](\text{PF}_6)$ to bind DNA has not been conclusively proven since there is contradicting evidence between the spectroscopic data and EMSA data and the exact nature of the interaction between the complex and DNA needs to be determined in order to try and understand better the mechanism of topo IB inhibition. Overall, a solid platform has been laid from which numerous future experiments can be performed to further develop this area of research.

8.2 Future work

The future for this project is immense as the work presented herein covers only the initial discovery phase of a class of potential chemotherapeutic agents. The future work can be split into two major sections; the first being work that needs to be performed on the current class of compounds presented, and the second being the structural modification of chelates in this thesis (second generation chelates) so that questions raised from the results of this work may be answered.

From the current class of compounds, $[\text{Au}(\text{L6})\text{Cl}](\text{PF}_6)$ and $[\text{Au}(\text{L10})\text{Cl}](\text{PF}_6)$ need to be individually assessed for their ability to inhibit or poison topo IB or II α via the same relaxation and decatenation assays performed for compounds $[\text{Au}(\text{HL3})\text{Cl}_2]$ and $[\text{Au}(\text{L12})\text{Cl}](\text{PF}_6)$. These experiments need to be performed since the complexes mentioned are structurally unique and therefore need to be independently confirmed as topo poisons/inhibitors. The major focus of the future work will obviously centre on $[\text{Au}(\text{L12})\text{Cl}](\text{PF}_6)$ as it was the lead compound in this work. Firstly, the mechanism through which chelate $[\text{Au}(\text{L12})\text{Cl}](\text{PF}_6)$ interacts with DNA needs to be unequivocally determined. The best method by which to do this is X-ray crystallography. In recent years there have been numerous structural reports of Ru(II) and Rh(III) octahedral chelates bound to proteins and synthetic DNA oligomers.²⁻⁵ The crystal growth process usually involves vapour diffusion from sitting drops and the data either collected via synchrotron radiation or via a

Summary, Conclusions and Future Work

diffractometer with a high power source such as a rotating anode.^{3, 4} The results can be incredibly informative with up to three different binding modes present on a single DNA oligomer as was recently reported for Δ -[Ru(bpy)₂dppz]²⁺.^{3, 4} These types of experiments are becoming increasingly crucial to understanding how drugs in general interact with their target.

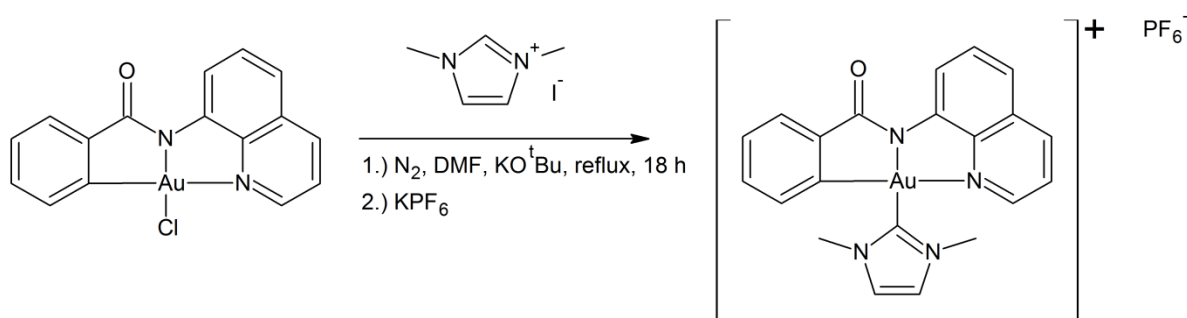
One of the reasons suggested for the failure of [Au(L12)Cl](PF₆) at the hollow fibre assay is that the chelate may bind irreversibly to serum proteins such as HSA. The ability for a drug to bind to HSA can be assessed via the use of a HSA binding kit available from the company SOVICELL.⁶ The kit takes the form of a ready-to-use 96-well microtiter plate, carrying TRANSIL beads with albumin immobilised in random orientations to expose all binding sites. The experiment is performed on a 96-well plate reader and is depicted graphically. The results from such an assay would be greatly informative and lead to a far greater understanding of the transport of the drug *in vivo*.

From the topo I relaxation assays performed in this work we have deduced that [Au(L12)Cl](PF₆) acts as an interfacial poison of the enzyme between a metal complex concentration of 0-1 μ M and a catalytic inhibitor between 1 and 10 μ M. A similar experiment needs to be performed with a metal chelate titration range of 1-10 μ M at 1 μ M increments in order to determine a more accurate inhibitory concentration. The specific mode by which [Au(L12)Cl](PF₆) reduces the activity of topo IB also needs to be further investigated by analysing the effect the complex has on various steps in the enzyme's catalytic cycle, as was completed for a similar gold(III) complex, [Au(C^N^C)(IMe)](CF₃SO₃), in 2011 by Castelli and co-workers.⁷

The first property of the current generation of chelates that needs to be resolved, through synthetic modifications, is their stability towards glutathione. These chelates all have a chloride ion in the fourth co-ordination site which seems to allow for reductive demetallation of the gold(III) centre through its substitution by glutathione. Therefore by substituting the chloride ion with a substitution inert ligand, such as *N,N'*-dimethylimidazolium, we may afford a much more stable chelate towards biological reducing agents. This is an ideal ligand as it allows for the use of neutral cyclometallated chelates [Au(L15)Cl] and [Au(L16)Cl], which after substitution of the chloride ion with *N,N'*-

Summary, Conclusions and Future Work

dimethylimidazolium, offer an ideal positively charged chelate which will be tested for their redox stability towards glutathione in a similar manner to $[\text{Au}(\text{L12})\text{Cl}](\text{PF}_6)$. Literature methods for the substitution of chloride with *N,N'*-dimethylimidazolium in tridentate gold(III) chelates are available, however they have not been performed on tridentate amide chelates.⁸ Nevertheless, we would not expect to encounter any significant difficulties in affording the correct product. Overall, the substitution of the chloride ion coupled with the highly stabilising C–Au bond should afford the desired redox stability. Scheme 8.2.1 shows a reaction sequence depicting a method through which the second generation chelates may be accessed. The Au–C bond represented in scheme 8.2.1 has been shown to impart redox stability in biologically relevant media for similar gold(III) complexes.⁹ The scheme below is a representative example; the method may be employed using any of the first generation chelates presented in this work, namely the derivitisation of compound $[\text{Au}(\text{L12})\text{Cl}](\text{PF}_6)$.

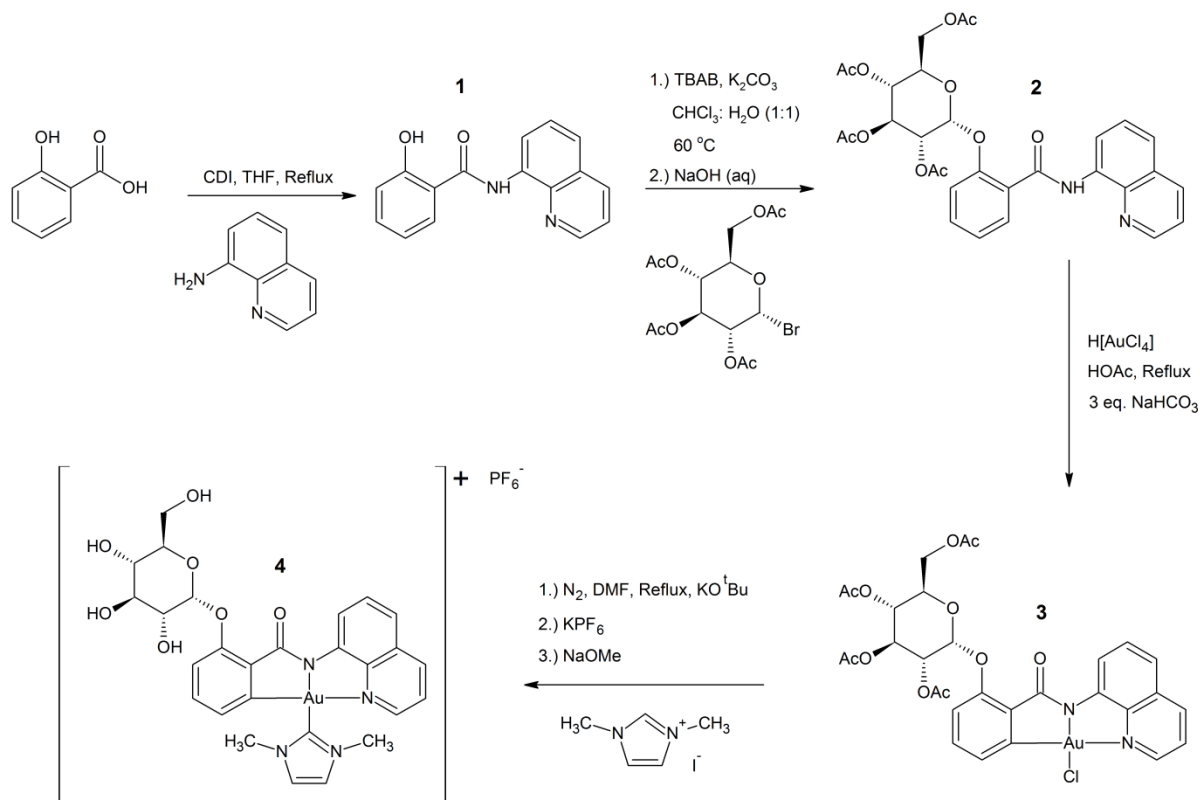


Scheme 8.2.1: Synthetic method that may be employed for the generation of second generation gold(III) amide-based chelates with improved redox stability.

Lastly we propose the modification of the ligand scaffold in such a way that it enhances the cytotoxicity and topo I or II inhibitory action of the chelate. One way in which to do this would be to mimic the structure of commercially available chemotherapeutic topo I or topo II inhibitors. Daunorubicin and etoposide, both commercial topo II poisoning anti-cancer agents, contain sugar-type moieties within their scaffold which are central to their topo II inhibitory activity.^{10, 11} The proposed method for the generation of gold(III) chelates with similar sugar appendages is shown in scheme 8.2.2, and involves a method analogous to the one published by Kumar and co-workers in 2007.¹² The condensation of 2-hydroxybenzoic acid with 8-aminoquinoline via the use of the coupling agent, carbonyldiimidazole (CDI), would afford ligand **1**. The acetylated-sugar ester of compound **1** is then formed via the method published by Bao and co-workers¹³ in 2004 followed by chelation to gold(III) using

Summary, Conclusions and Future Work

the method presented in this thesis to afford compound **3**. The chloride ion of the neutral gold(III) chelate (**3**) would then be substituted via the use of a literature method published by To and co-workers⁸ this year, followed by deacetylation in the presence of NaOMe to afford the target chelate **4**. The generated compound would be expected to have improved redox stability as well as enhanced enzyme inhibitory as well as cytotoxic activity.



Scheme 8.2.2: Proposed synthetic route for the sugar-derivatised gold(III) amide-based second generation chelate.

8.3 References

1. R. W.-Y. Sun and C.-M. Che, *Coord. Chem. Rev.*, 2009, **253**, 1682-1691.
2. B. M. Zeglis, V. C. Pierre and J. K. Barton, *Chem. Commun.*, 2007, 4565-4579.
3. H. Niyazi, J. P. Hall, K. O'Sullivan, G. Winter, T. Sorensen, J. M. Kelly and C. J. Cardin, *Nat. Chem.*, 2012, **4**, 621-628.
4. H. Song, J. T. Kaiser and J. K. Barton, *Nat. Chem.*, 2012, **4**, 615-620.
5. G. E. Atilla-Gokcumen, L. D. Costanzo and E. Meggers, *J. Inorg. Biochem.*, 2011, **16**, 45-50.
6. <http://www.sovicell.com/products-protein-binding.asp>, 2012.
7. S. Castelli, O. Vassallo, P. Katkar, C.-M. Che, R. W.-Y. Sun and A. Desideri, *Arch. Biochem. Biophys.*, 2011, **516**, 108-112.
8. W.-P. To, G. S.-M. Tong, W. Lu, C. Ma, J. Liu, A. L.-F. Chow and C.-M. Che, *Angew. Chem., Int. Ed.*, 2012, **51**, 2654-2657, S2654/2651-S2654/2630.
9. J. J. Yan, A. L.-F. Chow, C.-H. Leung, R. W.-Y. Sun, D.-L. Ma and C.-M. Che, *Chem. Commun.*, 2010, **46**, 3893-3895.
10. C.-C. Wu, T.-K. Li, L. Farh, L.-Y. Lin, T.-S. Lin, Y.-J. Yu, T.-J. Yen, C.-W. Chiang and N.-L. Chan, *Science* 2011, **333**, 459-462.
11. Y. Pommier, E. Leo, H.-L. Zhang and C. Marchand, *Chem. Biol.*, 2010, **17**, 421-433.
12. A. Kumar, B. Narasimhan and D. Kumar, *Bioorg. Med. Chem.*, 2007, **15**, 4113-4124.
13. C. Bao, R. Lu, M. Jin, P. Xue, C. Tan, Y. Zhao and G. Liu, *Carbohydr. Res.*, 2004, **339**, 1311-1316.